

Available online at www.sciencedirect.com



Structural and mechanical properties of polymer nanocomposites

S.C. Tjong*

Department of Physics & Materials Science, City University of Hong Kong, Tat Chee Avenue, Kowloon, Hong Kong

Available online 4 August 2006

Abstract

Recently, polymer nanocomposites reinforced with lower volume fraction of nanoceramics and carbon nanotubes have attracted steadily growing interest due to their peculiar and fascinating properties as well as their unique applications in commercial sectors. The incorporation of nanoceramics such as layered silicate clays, calcium carbonate or silica nanoparticles arranged on the nanometer scale with a high aspect ratio and/or an extremely large surface area into polymers improves their mechanical performances significantly. The properties of nanocomposites depend greatly on the chemistry of polymer matrices, nature of nanofillers, and the way in which they are prepared. The uniform dispersion of nanofillers in the polymer matrices is a general prerequisite for achieving desired mechanical and physical characteristics. In this review article, current development on the processing, structure, and mechanical properties of polymer nanocomposites reinforced with respective layered silicates, ceramic nanoparticles and carbon nanotubes will be addressed. Particular attention is paid on the structure–property relationship of such novel high-performance polymer nanocomposites.

© 2006 Elsevier B.V. All rights reserved.

Keywords: Structural properties; Mechanical properties; Polymer nanocomposites; Clay; Carbon nanotubes; Nanoparticles

1. Introduction

Fillers play important roles in modifying the desirable properties of polymers and reducing the cost of their composites. In conventional polymer composites, many inorganic filers with dimensions in the micrometer range, e.g. calcium carbonate, glass beads and talc have been used extensively to enhance the mechanical properties of polymers. Such properties can indeed be tailored by changing the volume fraction, shape, and size of the filler particles [1–3]. A further improvement of the mechanical properties can be achieved by using filler materials with a larger aspect ratio such as short glass fibers [4–6]. It is logical to anticipate that the dispersion of fillers with dimensions in the nanometer level having very large aspect ratio and stiffness in a polymer matrix could lead to even higher mechanical performances. These fillers include layered silicates and carbon nanotubes. Carbon nanotubes (CNTs) have a substantially larger aspect ratio (~1000) in comparison with layered silicates (~200) [7,8]. Moreover, flexible CNTs also possess very high strain to failure [9,10]. Rigid inorganic nanoparticles with a smaller aspect ratio are also promising reinforcing and/or toughening materials for the polymers. The dispersion of nanofillers in the polymers is rather poor due to their incompatibility with polymers and large surface-to-volume ratio. Therefore, organic surfactant and compatibilizer additions are needed in order to improve the dispersion of these nanofillers in polymeric matrices. For example, layered silicate surfaces are hydrophilic and proper modification

* Tel.: +852 27887702; fax: +852 27887830.

E-mail address: aptjong@cityu.edu.hk.

of the clay surfaces through the use of organic surfactants is needed. The obtained product is known as ‘organoclay’. In this context, organoclays can be readily delaminated into nanoscale platelets by the polymer molecules, leading to the formation of polymer–clay nanocomposites. These nanocomposites belong to an emerging class of organic–inorganic hybrid materials that exhibit improved mechanical properties at very low loading levels compared with conventional microcomposites [11–24]. CNTs are recognized to agglomerate and entangle easily during processing of the nanocomposites, leading to poor mechanical properties. Several techniques such as ultrasonic activation, *in situ* polymerization and surfactant addition are commonly used to disperse CNTs in polymer matrices.

The discovery of multi-walled carbon nanotubes produced by the arc evaporation of graphite in an atmosphere of helium by Iijima has attracted scientific and technological interest worldwide [25]. Carbon nanotubes can be classified into single-walled nanotubes (SWNTs), multi-walled nanotubes (MWNTs) and carbon nanofibers (CNFs). SWNT with a diameter of 1–2 nm consists of a single graphene layer wrapped into a cylindrical shape, and hemispherical caps seal both ends of the tube. SWNT can be further divided into three classes, i.e. armchair, zigzag and chiral depending on the arrangement of hexagons in their structures (Fig. 1) [26]. In most cases, SWNTs tend to assemble into ‘ropes’ structure. In contrast, MWNT comprises a number of graphene layers coaxially roll together to form a cylindrical tube. Each carbon atom within the atomic layer of a grapheme sheet is covalently bonded to three neighboring carbon atoms. Three sp^2 orbitals on each carbon form σ -bonds to three other carbon atoms. One 2p orbital remains unhybridized on each carbon; these orbitals perpendicular to the plane of the carbon ring combine to form the π -bonds. The atomic interactions between the neighboring layers are the van der Waals forces. The outer diameter of MWNTs is about 3–10 nm [27]. Vapor grown CNFs have a larger diameter ranging from 50 to 200 nm, and contain more defects than MWNTs. Compared to SWNTs and MWNTs, CNFs such as Pyrograf-III can be produced in higher volumes and at a lower cost by Applied Sciences, Inc. (ASI) [28].

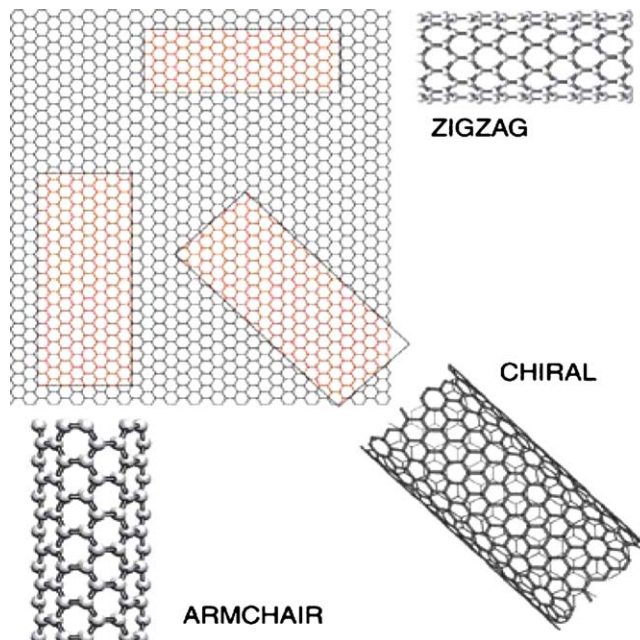


Fig. 1. Schematic diagram showing SWNT formed by rolling-up of rectangular strips of hexagonal graphite monolayers. The short side of the rectangle becomes the tube diameter and, therefore, is ‘quantized’ by the requirement that the rolled-up tube must have a continuous structure. Similarly, the rectangle must be properly oriented with respect to the flat hexagonal lattice, which allows only a finite number of roll-up choices [26].

CNTs exhibit a great range of remarkable properties, including unique mechanical and electrical characteristics. These remarkable high modulus and stiffness properties have led to the use of CNTs to reinforce polymers in the past few years [9,10,29,30]. Both theoretical (e.g. molecular structural mechanics and tight-binding molecular dynamics) and experimental studies have shown SWNTs to have extremely high elastic modulus (~ 1 TPa) [31–33]. The tensile strength of SWNT estimated from molecular dynamics simulation is ~ 150 MPa [34]. The experimental measurement of 150 MPa was found for the break strength of MWNTs [35]. Theoretical calculation reveals that the electrical properties of carbon nanotubes can range from metallic to semiconducting behavior, depending on the chirality and diameter of the nanotubes. Biggest near-term opportunities in the development of polymer–CNT nanocomposites by far are electrical improvement rather than the mechanical. Based on the unique electrical properties of CNTs, many commercial products in development would use the nanotubes to replace carbon black particles. In terms of the mechanical property consideration, thermoplastic polyolefin–clay nanocomposite has been recently commercialized by General Motors, Basel and Southern Clay as the ‘step-assist’ for GMC Safari cars in 2002 [36,37]. PolyOne has established a partnership with Nanocor for the production of nanocomposites with matrices of ethylene–propylene–diene monomer (EPDM), ethylene vinyl acetate (EVA), PP, etc. [38].

Recent developments in nanotechnology have provided several routes to prepare nanoparticles. These include sol–gel, flame spraying, inert gas condensation, chemical vapor deposition and ball milling [39]. Thermoplastics and elastomers filled with nanoparticles such as silica and calcium carbonate exhibit simultaneous improvements in stiffness and toughness [40–45]. However, nanocrystalline spherical alumina particle additions to an amorphous polymethyl methacrylate (PMMA) do not lead to an enhancement of stiffness. Instead, a slight decrement in tensile modulus is observed. The rigid nanoparticles improve the tensile ductility of brittle PMMA significantly [46–48].

The behavior of polymer–nanofiller composites is directly related to their hierarchical microstructures. Therefore, the mechanical properties of polymer–nanofiller composites are controlled by several microstructural parameters such as properties of the matrix, properties and distribution of the filler as well as interfacial bonding, and by the synthetic or processing methods. The interfaces may affect the effectiveness of load transfer from the polymer matrix to nanofillers. Thus surface modification of nanofillers is needed to promote better dispersion of fillers and to enhance the interfacial adhesion between the matrix and fillers. Fabrication of homogeneous polymer nanocomposites remains a major scientific challenge for materials scientists. Fig. 2 shows representative relative modulus as a function of filler content for semi crystalline PA6 reinforced with organoclays, MWNT, and silica nanoparticles [49–51]. It can be seen that the addition of very small amounts of carbon nanotube can produce the largest modulus enhancement for PA6. Although organoclays stiffen the PA6 matrix, however, its addition is detrimental to the tensile ductility of PA6. A drastic reduction in the elongation at break is commonly observed in semicrystalline thermoplastics associated with the clay additions [12,13,49]. On the other hand, addition of CNTs having a very high strain to failure only leads to a small reduction in tensile ductility for the thermoplastics [50]. Despite their lowest modulus enhancement compared to the MWNTs and organoclays, inorganic silica nanoparticles are found to toughen the PA6 matrix dramatically [51]. The effects of adding different reinforcement materials on the modulus of glassy PMMA are shown in Fig. 3. Both the SWNT and organoclays stiffen glassy PMMA with the exception of alumina nanoparticles [52,53]. The alumina nanoparticles act as toughening agents rather than reinforcing materials for brittle PMMA [47]. For elastomers, the stiffening effect of CNTs in polyurethane (PU) and poly(dimethylsiloxane) (PDMS) is well documented in literature [54,55]. Furthermore, functionalised SWNTs provide higher modulus stiffening in elastomeric PU than the pristine counterparts (Fig. 4). The remarkable reinforcing effect of functionalised SWNTs is related to better dispersion of nanotubes and stronger interfacial interaction

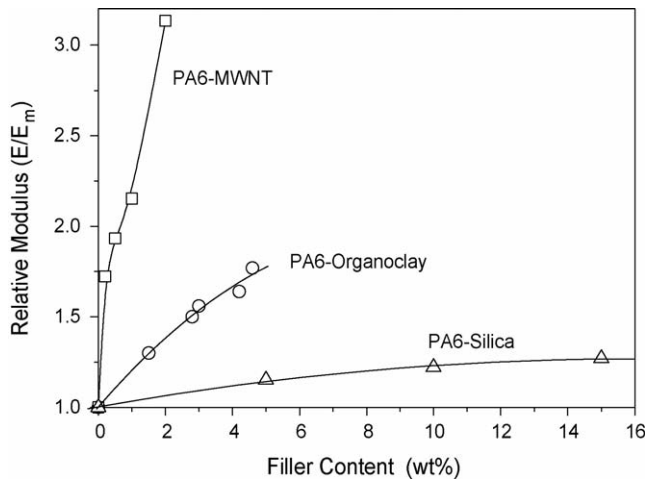


Fig. 2. Relative modulus (E/E_m) vs. filler content for PA6 reinforced with organoclay [49], functionalised MWNT [50] and modified silica [51] nanoparticles. E and E_m are Young's modulus of the nanocomposite and matrix, respectively.

between the PU and SWNTs. Fig. 4 also reveals that the organoclay additions are also effective to reinforce PU. The incorporation of 1 wt.% organoclay enhances the strain at break from 2100 to 2500%. Further clay additions lead to a reduction in tensile ductility [56]. Wang and Pinnavaia also reported that the strain at break of PU tends to increase with increasing clay loadings [57]. This implies that the elongation at break of PU elastomer is similar or not impacted by nanofiller loading. The poor tensile ductility of semicrystalline thermoplastics filled with organoclays is not fully understood. Therefore, understanding the structure–mechanical relationship is essential to the formation and design of polymer nanocomposites with enhanced mechanical strength and toughness. This article provides a comprehensive review on the structure and mechanical properties of various polymer resins (semicrystalline and glassy thermoplastics, elastomers as well as epoxies) reinforced with nanofillers of different aspect ratios and properties. Because of a wide diversity of polymer resins, it would be difficult to cover all areas of interest. In this review article, we address and focus the discussions on

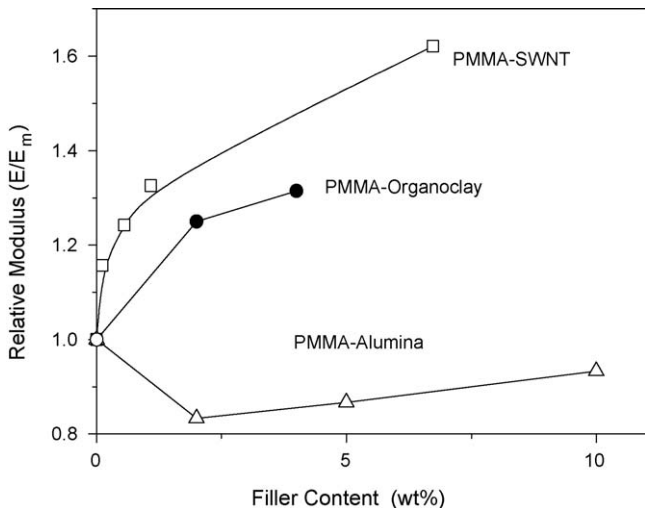


Fig. 3. Relative modulus (E/E_m) vs. filler content for PMMA reinforced with organoclay [52], doped SWNT [53] and alumina [47] nanoparticles. E and E_m are Young's modulus of the nanocomposite and matrix, respectively.

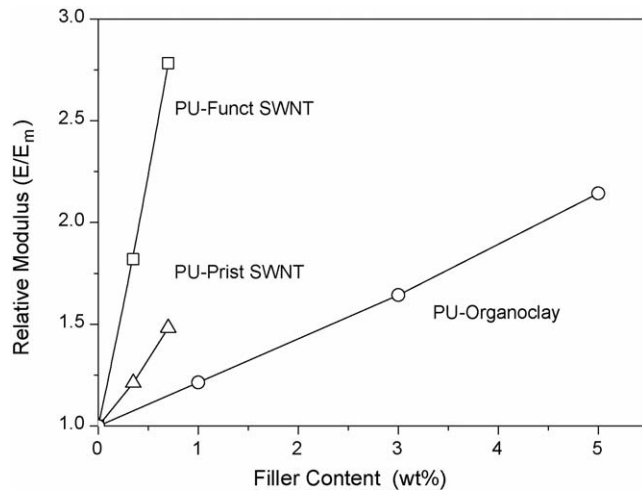


Fig. 4. Relative modulus (E/E_m) vs. filler content for PU reinforced with pristine SWNT [54], functionalised SWNT [54] and organoclay [56] nanoparticles. E and E_m are Young's modulus of the nanocomposite and matrix, respectively.

the synthesis–structure–property relationship of several polymer resins with great technological importances.

2. Silicate clay reinforcement

2.1. Organically modified clay

Clay minerals are hydrous aluminum silicates and are generally classified as phyllosilicates, or layered silicates. Framework layers of natural clays are generated by a combination of tetrahedral and octahedral sheets. Silica is a main component of a tetrahedral sheet whilst octahedral sheet comprises diverse elements such as Al, Mg, and Fe. A natural stacking of tetrahedral and octahedral sheet occurs in the specific ratios and modes, leading to the formation of the 2:1 layer silicates. The phyllosilicate 2:1 layer clays include mica, smectite, vermiculite, and chlorite. Smectite group can be further divide into montmorillonite (MMT), nontronite, saponite and hectorite species [58,59]. A tetrahedral sheet of smectites is composed of corner-linked tetrahedral, whose central ions are Si^{4+} or Al^{3+} and sometimes Fe^{3+} . The basal oxygens of a tetrahedron are shared by the neighboring tetrahedral, forming hexagonal pattern. Thus the crystal lattice of 2:1 phyllosilicate consists of 1 nm thin layers, with an octahedral alumina sheet sandwiched between two tetrahedral silica sheets. The stacking of the platelets leads to a Van der Walls gap or gallery between the platelets. The layer charge can easily be generated by the replacement of cations in the alumina sheet with cations of different charges. Replacement of Al^{3+} by Mg^{2+} or Fe^{2+} produces negatively charged to the layers. This negative charge is balanced by alkali cations (Na^+ , Li^+ or Ca^{2+}) positioned in the gallery between the aluminosilicate layers. The gallery height of pristine clay is determined by the type of cations positioned in the gallery and the degree of hydration (Fig. 5). Generally, the pristine silicate surface is modified with organic compound to make the platelets more compatible with the polymer matrix. When the hydrated cations are ion-exchanged with organic cations such as bulky alky ammonium, it generally results in a larger interlayer spacing. The cation exchange capacity (CEC), expressed as mequiv/100 g clay is used to characterize the degree of isomorphous substitution. Typical CEC values of 2:1 phyllosilicates are listed in Table 1. Vermiculite (VMT) is a clay mineral which has a similar crystalline structure to MMT. However, the

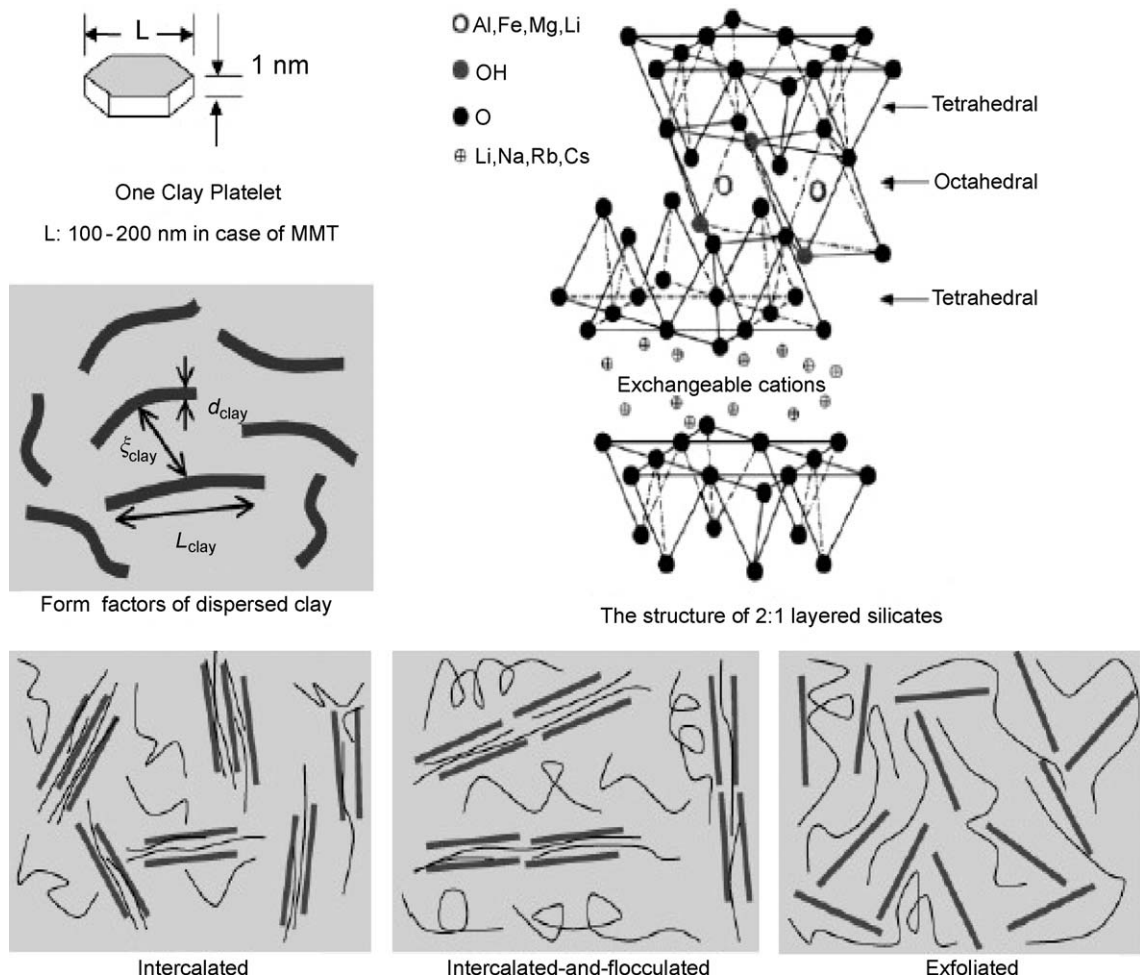


Fig. 5. Schematic diagram showing the structure of 2:1 phyllosilicates and the polymer clay nanocomposites (reprinted from [62] with permission from The American Chemical Society).

electrostatic charge of the VMT layer is larger than that of MMT due to a higher substitution of Si atoms with Al and Mg atoms.

Among these layered silicates, MMT is particularly attractive as reinforcement for the polymer-clay because it is environmentally friendly, readily available in large quantities with relatively low cost and its intercalation chemistry is well understood. The Na-MMT clay is hydrophilic and expands the interlayer spaces readily when immersed in water. The clay surface can be converted from hydrophilic

Table 1
Chemical formula and cation exchange capacity of 2:1 phyllosilicates

Silicate	Formula	CEC (mequiv/100 g)
Montmorillonite	$M_x(Al_{4-x}Mg_x)Si_8O_{20}(OH)_4$	92.6–120
Hectorite	$M_x(Mg_{6-x}Li_x)Si_8O_{20}(OH)_4$	120
Saponite	$M_xMg_6(Si_{8-x}Al_x)Si_8O_{20}(OH)_4$	86.6
Vermiculite	$(Mg, Fe, Al)_3[(Al, Si)_4O_{10}](OH)_2M_x \cdot nH_2O$	150

M represents exchangeable cation and x is the layer charge.

to organophilic via cation exchange of Na^+ with alkylammonium ions including primary, secondary, tertiary and quaternary alkylammonium cations under proper conditions [60]. The space between the silicate layers depends greatly on the length of the alkyl chain and the ratio of cross-sectional area to available area per cation [61]. The conversion of hydrophilic inorganic clay to a hydrophobic organoclay also improves the interfacial adhesion properties between the organic and inorganic phases when a hydrophobic polymer matrix is involved. The potential applications of organoclay as an effective reinforcement for polymers have prompted many researchers to investigate its structural behavior.

Depending on the structure of dispersed clay platelets in the polymer matrix, the composites can be classified as intercalated or exfoliated nanocomposites. Intercalated structures are self-assembled, well-ordered multilayered structures where the extended polymer chains are inserted into the gallery space of the clays. This leads to an expansion of the interlayer spacing. In an exfoliated structure, individual silicate sheets lose their layered geometry as a result of delamination, and dispersed as nanoscale platelets in a polymer matrix (Fig. 5) [62]. However, fully exfoliated structure is rarely seen in practice. An exfoliated structure as shown in Fig. 5 is an idealized reference morphology that arises from only looking at local scale. In reality, the morphology is mixed intercalated/exfoliated structure.

X-ray diffraction (XRD) is commonly used for the characterization of the structure of nanocomposites. For an intercalated structure, the (0 0 1) characteristic peak tends to shift to lower angle regime due to the expansion of the basal spacing. Although the layer spacing increases, there still exists an attractive force between the silicate layers to stack them in an ordered structure. In contrast, no peaks are observed in the XRD pattern of exfoliated polymer nanocomposites due to loss of the structural registry of the layers. The absence of Bragg diffraction peaks in the nanocomposites may indicate that the clay has been completely exfoliated or delaminated as shown in Fig. 6 [63]. The absence of Bragg diffraction peaks in the XRD patterns should not be used as the sole evidence for the formation of an exfoliated structure. Morgan and Gilman [64] and Eckel et al. [65] pointed out that XRD analysis alone can lead to false interpretations of the extent of exfoliation. Several factors such as clay dilution, peak broadening and preferred orientation make XRD characterization of polymer nanocomposites susceptible to errors. Clay dilution and peak broadening can yield false result that exfoliation has occurred. Conversely, preferred orientation effects can result in the false conclusion that exfoliation has not occurred. Further transmission electron microscopic observation is needed to confirm formation of exfoliated nanocomposites [65]. XRD does not yield the information relating to the spatial distribution of the silicate in the polymer matrix because all its data are averaged over the whole regions of the specimen. On the other hand, transmission electron microscopy (TEM) can provide useful information in a localized area on the morphology, structure and spatial distribution of the dispersed phase of the nanocomposites. Vaia et al. indicated that the features of the local microstructures from TEM give useful detail to the overall picture that can be drawn from the XRD results [66]. Thus XRD and TEM techniques are regarded as complementary to each other for materials characterization of the clay–polymer nanocomposites.

Nowadays, several pristine and organoclays are available commercially at relatively low cost. Commercial organoclays include Cloisite[®] 10A, 15A, 20A and 30B produced from Southern Clay Products (U.S.A.) [67], Bentone[®] 107, 108, 109 and 2010 from Elementis Specialties Company [68], Nanomer[®] 1.30P, 1.31PS, 1.44P, 1.44PS, 1.44PT and 1.28E from Nanocor, Inc. (U.S.A.) [69], Nanofil[®] 2, 5, 9, SE 3000 and SE 3010 from Sud-Chemie (Germany) [70] as well as Dellite[®] 72T from Laviosa Chimica Mineraria (Italy). Synthetic fluoromica clays (Somasif[®] ME100) are supplied to Asian customers by Co-op Chemicals, Japan.

Cloisite[®] 10A contains dimethyl, benzyl, hydrogenated tallow, quaternary ammonium salt (2MBHT). Cloisite[®] 15A and 20A are apolar Na^+ -MMT clays modified with dimethyl, dihydro-

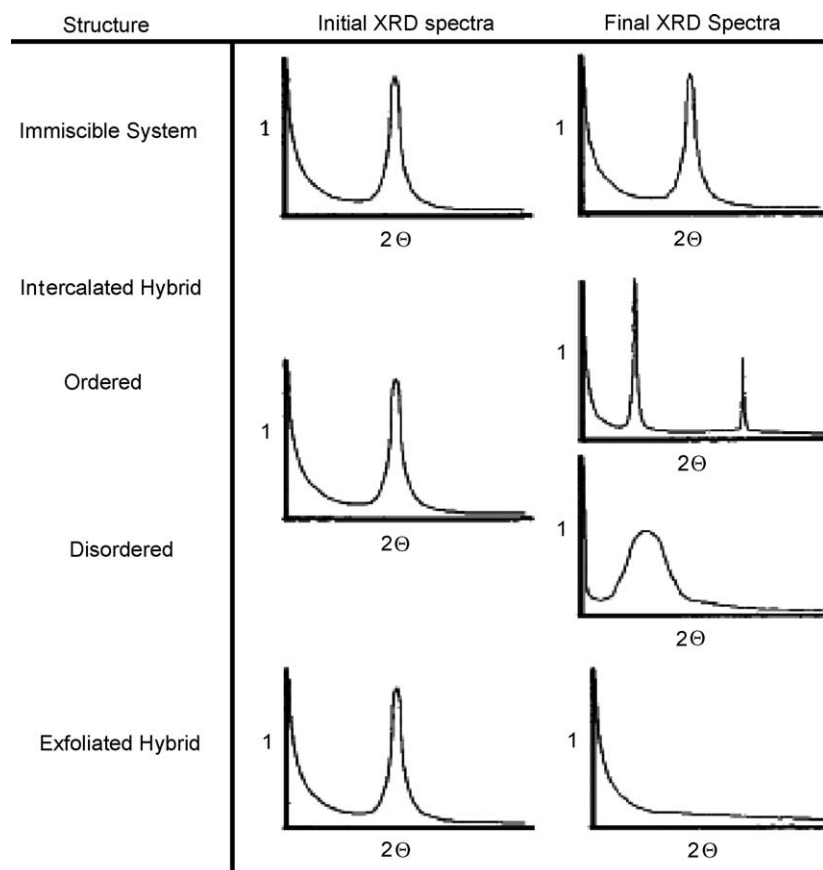
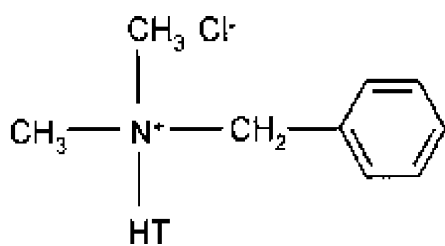
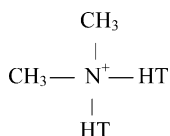


Fig. 6. Schematic illustration depicting the expected XRD patterns for immiscible, intercalated and exfoliated hybrid structures (reprinted from [63] with permission from The American Chemical Society).

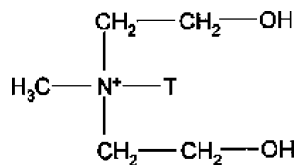
generated tallow, quaternary ammonium (2M2HT). HT stands for a tallow-based compound (~65% C18, ~30% C16, ~5% C14) in which a majority of the double bonds have been hydrogenated. The modifier concentration of Cloisite® 10A, 15A and 20A is 125, 125 and 95 mequiv/100 g clay, respectively. This is reported in the product literature [67]. The molecular structure of Cloisite® 10A contains a benzyl moiety, it is commonly used to promote the intercalation process of styrenics, i.e.



The cation molecular structure of Cloisite® 15A and 20A is:



[66]. Cloisite® 30B is polar organoclay with the organic modifier methyl tallow bis-2-hydroxyethyl ammonium (MT2EtOH) having the formula:



where T stands for tallow. The respective basal spacing (d_{001}) of the Cloisite® 15A, 20A and 30B is 3.23, 2.42 and 1.85 nm [67]. Nanomer® 1.30 and 1.44P series mentioned above are surface modified MMT, intended for use for polyolefin resins.

The 1.30 series utilizes primary amine chemistry and the 1.44 series is based on quaternary ammonium chemistry. The 1.31PS and 1.44PS grades are derivatives containing silane modification. Nanomer® 1.28E is a modified MMT which is formulated for anhydride-cured epoxy resins [69]. Dellite® 72T is a ditallow-dimethyl-ammonium ion modified MMT.

Proper selection of organoclays depends mainly on the type of polymer matrix used. Fornes et al. investigated the effect of the structure of alkylammonium compounds on the dispersion of MMT in polyamide-6 during melt compounding [71]. They reported that the alkylammonium compound consisting of one alkyl tail is more effective than the quaternary cation having two alkyl tails in forming exfoliated nanocomposites. They explained this in terms of the competition between the effects of platelet–platelet interactions and the interaction of the polymer with the organoclay platelet. Polyamide-6 because of its polarity or strong hydrogen-bonding characteristic has some affinity for the pristine surface of the clay. A schematic illustration showing the formation of hydrogen bonds in PA6–pristine MMT is depicted in Fig. 7 [72]. In this case, the organic modifier consisting of two alkyl tails shields more silicate surface than one alkyl tail, thereby precluding desirable interactions between the polyamide and the clay surface [71]. On the other hand, nanocomposites made from a non-polar polymer like linear low density polyethylene (LLDPE) showed complete opposite trends. In that case, the two-tailed organoclay formed nanocomposites exhibit better exfoliation and mechanical properties than a one-tailed organoclay [73]. Manias et al. demonstrated that the polypropylene–MMT nanocomposite formation can be achieved by two ways, i.e. either by using neat polypropylene and semi-fluorinated surfactants for the silicates, or by using functionalised polypropylenes and common organo-montmorillonites [74,75]. In the first case, a semi fluorinated alkyltrichlorosilane

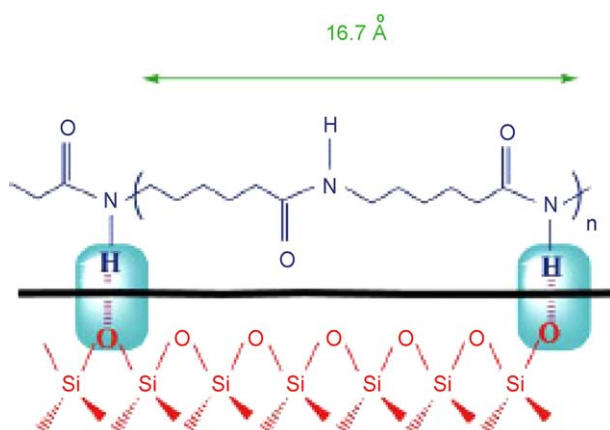


Fig. 7. Schematic illustration showing the formation of hydrogen bonds in PA6–pristine MMT (reprinted from [72] with permission from Elsevier).

$(CF_3-(CF_2)_5-(CH_2)_2-Si-Cl_3)$ was used to modify C18-MMT, rendering it miscible with neat or unfunctionalised PP. This surfactant was tethered to the MMT surface through a reaction of the trichlorosilane groups with hydroxyls in the cleavage plane of the MMT. In the second case, several functional groups were grafted to PP in a random-copolymer fashion. The structure and physical properties of such functionalized PP are listed in Table 2. The functionalized PP samples were aimed to render the polymer–MMT interactions more thermodynamically favorable than the surfactant–MMT interactions. They reported that the necessary level of PP functionalization to form PP nanocomposites is very low, i.e. random copolymers with 0.5 mol% of functionalized comonomers, or diblock copolymers with 1 mol% of non-PP blocks. All the hybrids can be formed by melt intercalation, and the resulting structures are characterized by a coexistence of intercalated and exfoliated MMT layers (Fig. 8). They also demonstrated that the functional group in the form of block copolymer, can also promote the formation of mixed exfoliated/intercalated PP nanocomposite (Fig. 9).

The key issue in the design of polymer–clay nanocomposites is to monitor the dispersion of clay platelets on nanometer scale in a polymer matrix. Accordingly, it is necessary to understand the interaction between the clay surfaces and the intercalants to prepare exfoliated clay–polymer nanocomposites. In other words, understanding the structure of organoclays and the interaction of surfactant–clay is of crucial importance in design, fabrication and characterization of exfoliated nanocomposites. Various structural models have been proposed for the molecular conformation of the surfactants. Lagaly [76] proposed that the alkyammonium ions in 2:1 clay minerals lie either parallel

Table 2
Functionalized PP characteristics (reprinted from [74] with permission from The American Chemical Society)

	Functionalized PP	x (mol%)	M_w	T_m (°C)	
A	Random copolymers 	PP-r-(PP-MS) _x	1.0	200,000	154
B		PP-r-(PP-MA) _x	0.5	200,000	155
C		PP-r-(PP-OH) _x	0.5	200,000	155
D	Diblock copolymer 	PP-b-(PMMA) _x PP-b-(PMMA) _x	5.0 5.0	200,000 220,000	155 154

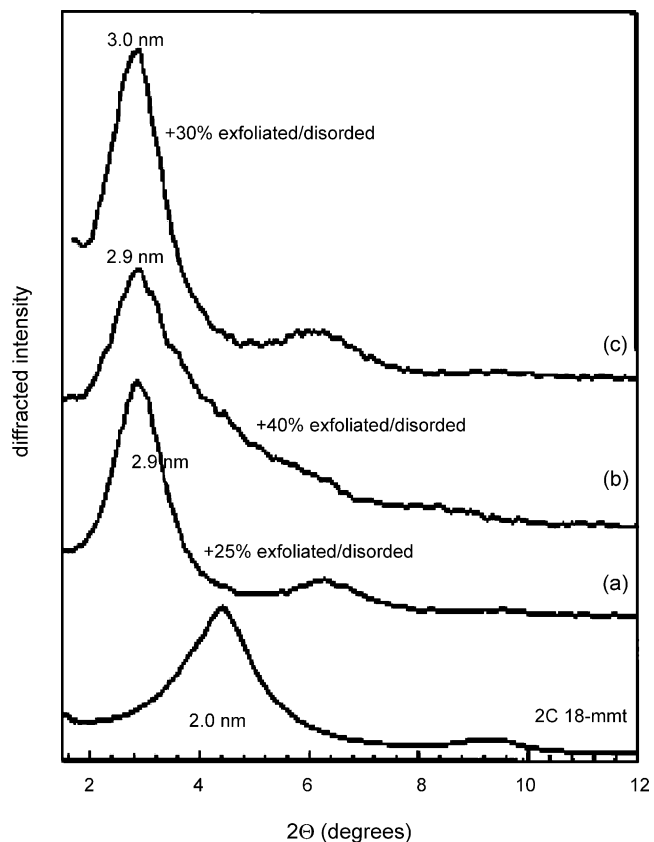


Fig. 8. XRD patterns of a dimethyldioctadecylammonium-modified MMT (2C18-MMT) clay and all of the functionalized PP/2C18-MMT nanocomposites. The functionalized groups used are (a) 1 mol% *p*-methylstyrene (PP-r-MS), (b) 0.5 mol% maleic anhydride (PP-r-MA) and (c) 0.5 mol% hydroxy (PP-r-OH). The content of exfoliated/disordered MMT layers is quantified from image analysis of TEM micrographs (reprinted from [74] with permission from The American Chemical Society).

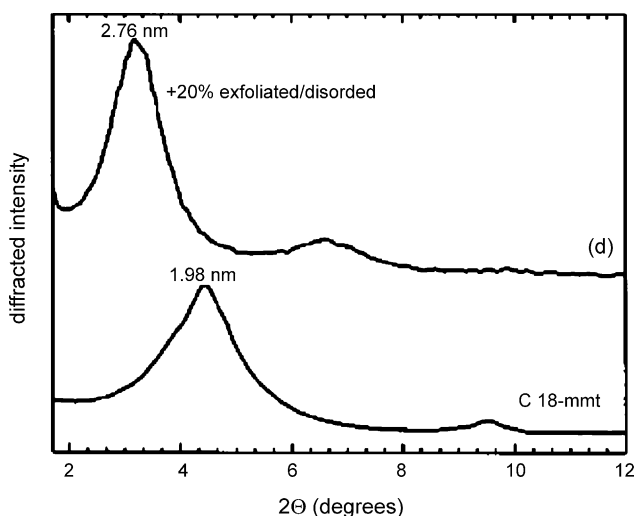


Fig. 9. XRD patterns of octadecylammonium-modified MMT (C18-MMT) and of the PP-b-PMMA/C18-MMT nanocomposite, formed by melt intercalation. The amount of exfoliated/disordered MMT layers is quantified from image analysis of TEM micrographs (reprinted from [74] with permission from The American Chemical Society).

to the silicate surface, forming mono- and bilayers or radiating away from the surface, forming paraffin-type arrangement. In the pseudo trimolecular arrangement, some chain ends are shifted above one another, so that the spacing is determined by the thickness of three alkyl chains (Fig. 10) [76]. Such structural models are considered to be too simple and idealistic. Giannelis and coworkers employed transmission Fourier transform infrared spectroscopy (FTIR) to determine the molecular conformation of intercalated alkylammonium silicates by monitoring frequency shifts of the CH_2 stretching and scissoring vibrations as a function of the interlayer packing density, chain length and temperature [77]. Under most conditions, a wide range of molecular arrangements varying from solidlike to liquidlike or even to intermediate liquid crystalline case, depending on the packing density and chain length (Fig. 11). Increasing the packing density or chain length, improves the ordering of the chains. However, high temperature favors the disordered, liquidlike conformation. When the available surface area per molecule is within a certain range, the chains are not completely disordered but retain some orientational order similar to that in the liquid crystalline state. On the basis of the molecular dynamics (MD) simulation on the static and dynamic properties of 2:1 silicates modified with alkylammonium surfactants, Giannelis and coworkers reported that the organically modified layers self-assemble parallel to each other to form alternating, well-ordered organic/inorganic multilayers [78]. Wang et al. [79] used the nuclear magnetic spectroscopy (NMR) to probe the conformation of alkylammonium surfactant molecules in MMT. They demonstrated that the coexistence of order and disordered conformations. Two main resonance peaks are resolved and associated with the backbone of alkyl chains. The resonance at 33 ppm corresponds to the ordered conformation (all-trans), and the resonance at 30 ppm corresponds to the disordered conformation (mixture of trans and gauche). Osman et al. [60] used IR, NMR XRD and differential scanning calorimetry (DSC) to study the structure and chain dynamics of self-assembled monolayers of mono-, di-, tri- and tetraalkylammonium cations of varying length (C_1 , C_8 and C_{18}) on MMT platelets. At ambient temperatures, alkylammonium monolayers assembled on MMT adopt a two-dimensional order or a disordered state, depending on the cross-sectional area of the molecules, the area/cation available on the substrate and the alkyl length. At low temperatures, the alkyl chains preferentially assume an all-trans conformation. Conformation transformation of the chain takes place with increasing temperature, leading to a disordered phase (liquidlike) in which the chains assume a random conformation. From the XRD measurements, the dependence of the (0 0 1) basal spacing of MMT on the number of alkyl

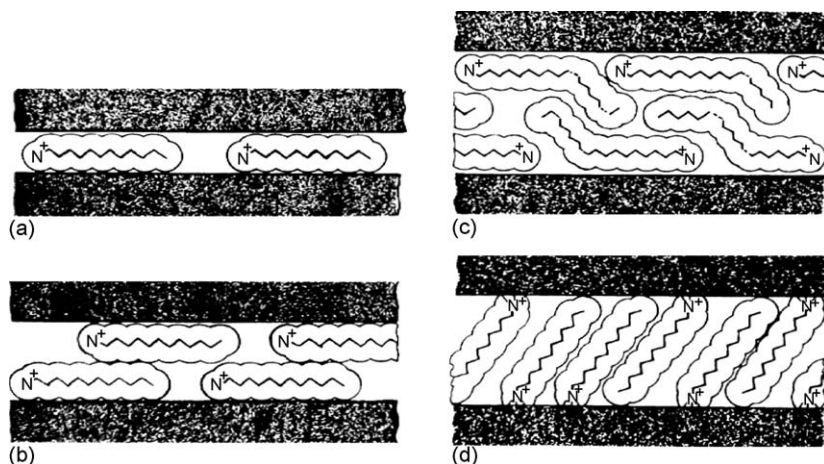


Fig. 10. Alkyl chain aggregations in 2:1 phyllosilicates: (a) monolayer, (b) bilayers and (c) pseudotrimolecular layers of chains lying flat on the surface, and (d) paraffin-type monolayers (reprinted from [76] with permission from Elsevier).

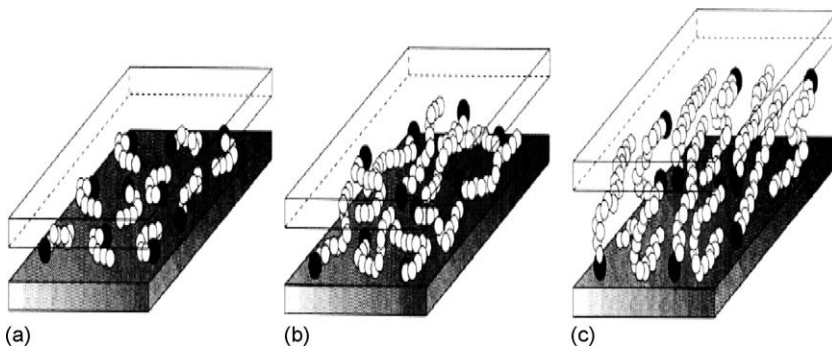


Fig. 11. Alkyl chain aggregation models: (a) the molecules are effectively isolated from each other at the shortest lengths, (b) quasi-discrete layers form with various degree of in plane disorder and interdigitation between the layers at medium lengths, and (c) interlayer order increases leading to a liquid crystalline polymer environment at long lengths. Open circles represent CH_2 segment while cationic head groups are represented by filled circles (reprinted from [77] with permission from The American Chemical Society).

chains of different length is shown in Fig. 10. At a chain length of four carbon atoms (C4), there is nearly no change in the basal-plane spacing of MMT. In the octyl series (C8–4C8), the d -spacing tends to increase linearly with increasing the number of chains. In the octadecyl series (C18–4C18), the d -spacing increases markedly and non-linearly. Such a large increase in the d -spacing of MMT modified with octadecyl series is beneficial in the synthesis of exfoliated polymer nanocomposites (Fig. 12).

As mentioned above, interactions between the PA6 chains and pristine MMT via hydrogen bonding facilitate the intercalation of PA6 molecules into the galleries of MMT. In general, organic molecules can intercalate the galleries of the clays by interacting with the clay surface via ion–dipole, dipole–dipole and hydrogen bonding [80–82]. Recently, Hansen solubility parameters, $\delta_t^2 = \delta_d^2 + \delta_p^2 + \delta_h^2$ [83–85] has been adopted by the researchers to characterize the dispersion of organoclays in

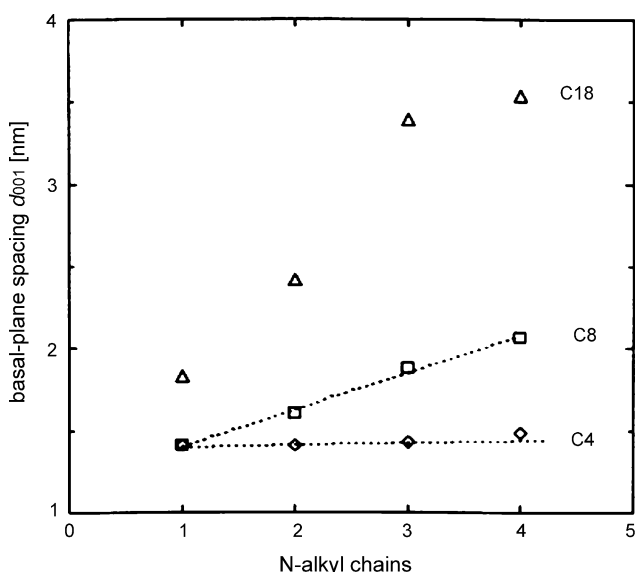


Fig. 12. Dependence of the basal-plane spacing on the number of alkyl chains, of different length, in the organic cation at room temperature (reprinted from [60] with permission from the American Chemical Society).

organic solvents [80–82]. The parameters take the dispersive (δ_d), polar (δ_p) and hydrogen-bonding (δ_h) forces acting together to disperse MMT in various solvents into account. It is noted that Hildebrand and Scott proposed the original definition of solubility parameter, $\delta = (E/V)^{1/2}$ where E is the molar cohesive energy and V is the molar volume. The cohesive energy is the energy associated with the net attractive interactions of the material [85,86]. This is a well established approach for characterizing the inorganic powder (e.g. carbon black) dispersion in solvents [87,88]. Hansen then extended the Hildebrand parameter to polymer–solvent systems, particularly for polar and hydrogen-bonding interactions [82–84]. Ho et al. demonstrated that Cloisite® 15A dispersed in chloroform was fully exfoliated, whereas it formed tactoids in benzene, toluene and *p*-xylene, which possess different values of solvent solubility parameter [79]. They further indicated that the polar (δ_p) and hydrogen bonding (δ_h) forces affect primarily the exfoliated structure or tactoid formation of the suspended platelets in particular solvents [80]. Similarly, Choi et al. reported that that δ_h is an important factor for the dispersion state of Na-MMT in a liquid or solvent. The polar components (δ_p) and hydrogen-bonding components (δ_h) of organic liquids determined the dispersion and basal spacings of Na-MMT in various solvents and monomers [81]. The Hansen solubility parameters are particularly useful for the preparation of polymer–clay nanocomposites via the solution intercalation route [89].

2.2. Synthesis of polymer–clay nanocomposites

2.2.1. Thermoplastic matrices

In general, clay–polymer nanocomposites can be prepared via in situ intercalative polymerization of monomers, polymer intercalation by the solution method and melt intercalation. In situ polymerization involves the insertion of a suitable monomer into the clay galleries followed by polymerization. In the solution route, the organoclay and the polymer are dispersed in a polar organic solvent. The layered silicates owing to their unique feature can be dispersed easily in an adequate solvent. The polymer dissolves in the solvent then adsorbs onto the expanded silicate sheets. When the solvent is evaporated, the sheets reassemble, sandwiching the polymer to form the intercalated structure. This behavior is referred to as the exfoliation-adsorption solution intercalation [11,89]. It is noted that such solvent structures are unstable at processing temperatures, i.e. the polymer effectively dewets the clay. Selection of a proper solvent is the primary criterion to achieve the desired level of exfoliation of organoclays in dispersion into the polymers [81]. Solution intercalation method is not an effective way to prepare commercial nanocomposites because of the high costs of the solvents, which are also environmentally unfriendly. Furthermore, a compatible polymer–clay solvent system is not always available [90]. Melt intercalation is broadly applicable to many commodity and engineering polymers, from non-polar polystyrene, polyolefin, weakly polar PET to strong polar polyamide. These polymers are produced on a large scale and it is desirable to be able to use these materials as they are currently produced. Melt compounding is a flexible and commercial process capable of producing a variety of products on large volume scales. Giannelis and coworkers were the first to conduct the melt intercalation of polystyrene (PS) with MMT [91]. In the process, PS powder was mixed with organoclay followed by pressing into a pellet. It was then heated in vacuum at 165 °C, this temperature is well above the bulk glass transition temperature of PS (96 °C), ensuing the presence of a polymer melt. They reported that intercalated structure was formed in the PS–organoclay hybrid after heating the pellet for 25 h on the basis of XRD results. Since then, the melt intercalation method has become a mainstream technique for the fabrication of polymer–clay nanocomposites in extrusion or injection molding. Moreover, the high shear environment of the melt extruder can assist the delamination or exfoliation of clay platelets [92]. The disadvantage of melt intercalation is related to a low thermal stability of the onium modifiers. Alkylammonium surfactants chemically degraded around 180 °C

[93]. Melt intercalation process commonly occurs in excess of 180–200 °C, leading to the degradation of organic surfactants. According to the literature, water soluble polymers such as poly(ethylene oxide) (PEO) molecular chains can intercalate into the galleries of pristine Na-MMT during melt intercalation without using the organic surfactants [94].

2.2.1.1. Intercalative polymerization. Polyamides are one of the few polymer types that readily form well-exfoliated nanocomposites. Pioneering work in this area was carried out by the Toyota Research group to produce clay/polyamide-6 nanocomposites [95,96]. In the process, MMT was cation exchanged with the ammonium cations of various ω -amino acids $[\text{H}_3\text{N}^+(\text{CH}_2)_{n-1}\text{COOH}, n = 2, 3, 4, 5, 6, 8, 11, 12 \text{ and } 18]$. The modified MMTs were intercalated by ϵ -caprolactam at 100 °C in which ring opening polymerization of ϵ -caprolactam occurred. The number of carbon atoms in ω -amino acids has a strong effect on the swelling behavior of MMT at 100 °C. The (0 0 1) basal spacing of MMT tends to increase dramatically when $n \geq 11$. This implies that a large amount of monomer can be intercalated into the gallery of MMT when the number of carbon atoms in the ω -amino acids is high [95]. From this, they synthesized the 12-aminolauric acid modified MMT (denoted as 12-MMT) and ϵ -caprolactam in a mortar. The content of 12-MMT ranged from 2 to 70 wt.%. The carboxyl end groups of 12-aminolauric acid initiated ring-opening polymerization of ϵ -caprolactam in the presence of a small amount of aminocaproic acid.

Amorphous (glassy) polymers such as polystyrene, PMMA and polycarbonate (PC) are commonly used for many engineering applications because of their excellent transparencies and relative ease of processing. However, PS and PMMA fail in a brittle mode when subject to small deformations. A typical method to prepare the PS-clay and PMMA-clay nanocomposites consists of inserting an organoclay with styrene or MMA monomer and subsequently carried out a free radical polymerization. When the catalyst or the reactive site for polymerization resides in the gallery, in situ polymerization takes place in the gallery space and the system is driven to disperse the silicate platelets by the driving force of polymerization reaction [97]. Fu and Qutubuddin modified Na-MMT and Ca-MMT with vinylbenzyldimethyldecylammonium chloride (VDAC) by cationic exchange between inorganic ions of MMT and ammonium ions of VDAC in an aqueous medium [98]. Dispersion of OrgMMT in styrene monomer and successive polymerization in the presence of free radical initiator result in the formation of highly exfoliated nanocomposites. The exfoliated nanocomposites exhibit higher dynamic modulus and higher thermal degradation temperature than PS as expected. Weimer et al. prepared delaminated PS-silicate nanocomposites by anchoring a living free radical polymerization initiator into silicate layers followed by bulk polymerization [99]. Qu et al. reported that the MMA monomers can be intercalated into the MMT galleries via bulk polymerization method. XRD patterns revealed the absence of (0 0 1) basal reflection in the PMMA-clay nanocomposites. However, TEM image showed a mixed intercalated/exfoliated structure [100].

According to the literature, a one-step emulsion polymerization is a simple and effective method for the synthesis of PS-clay nanocomposites. As mentioned above, the basal spacing expansion of MMT depends on polar components (δ_p) and hydrogen-bonding components (δ_h) of solvents. Thus water with large polar components (δ_p) and hydrogen-bonding components (δ_h) is an ideal solvent to expand the basal spacing of MMT. Emulsion polymerization has shown success in styrenic polymers for the fabrication of PS-clay nanocomposites. Noh and Lee [101] as well as Kim et al. [102] have used water to widen the basal space of clays, and intercalate the styrene monomer into silicate layers via emulsion polymerization. In the process, styrene monomer was dispersed in water under agitation and polymerized with a water soluble radical initiator (e.g. potassium persulfate) in the presence of pristine MMT. An emulsifier (sodium lauryl sulfate) is added to allow the reaction to proceed as emulsion polymerization. Intercalated clay-PS nanocomposites with enhanced thermal and

mechanical properties were produced. The hydrophilicity of pristine MMT impedes the formation of delaminated morphology with hydrophobic styrene polymers. To achieve exfoliated nanocomposites, either a reactive surfactant or organoclay is needed. Chung and coworkers used the ionic comonomer with an amido and sulfonic group in its molecule, i.e., 2-acrylamido-2-methyl-1-propane sulfonic acid (AMPS) to synthesize the exfoliated MMT-PS and MMT-P(S-co-MMA) nanocomposites [103,104]. Qi and coworkers reported that exfoliated clay-PS nanocomposite can be prepared by using organoMMT rather than pristine clay [105]. The Na-MMT was initially cation exchanged with cetyltrimethylammonium bromide (CTAB), and dispersed in styrene monomer. An aqueous mixture of radical initiator (ammonium persulfate) and emulsifying agent (sodium dodecyl sulfate) was added under stirring condition at room temperature. The emulsion was completely precipitated during polymerization at 70–80 °C for 5 h under nitrogen atmosphere. A schematic diagram showing the preparation of MMT-PS nanocomposite is shown in Fig. 13. The XRD pattern (Fig. 14) and TEM examination of the final product revealed the formation of exfoliated nanocomposite [105]. Emulsion polymerization has also been used by the researchers to prepare exfoliated MMT-poly(methyl methacrylate) [106–108].

Despite a widespread use of the polypropylene (PP) and polyethylene (PE) for engineering applications, the synthesis of polyolefin-silicate nanocomposites is still a scientific challenge. Exfoliation of the silicate platelets by non-polar polyolefins is rather difficult to achieve. Thus addition of an appropriate catalyst is required during polymerization. In the process, the monomer and the polymerization initiator or catalyst is intercalated within the silicate layers and the polymerization is initiated either thermally or chemically. O'Hare and coworkers used this technique to intercalate a cationic zirconocene catalyst into synthetic layered silicates. After addition of methylaluminoxane (MAO), propylene was oligomerized. No structural characterization of filled PP was reported [109]. Heinemann et al. prepared HDPE and LLDPE nanocomposites via homo- and copolymerization using layered silicates modified with various quaternary alkyl ammonium cations in the presence of selected catalysts such as MAO-activated zirconocene, nickel and palladium. The presence of *n*-alkyl branches, resulting from 1-olefin copolymerization or migratory insertion polymerization, was reported to enhance compatibility between polyethylene and dispersed organophilic layered silicates. XRD and TEM were used to characterize the structure of nanocomposites. XRD patterns clearly demonstrated the formation of exfoliated structure. Careful examination TEM micrographs of nanocomposites revealed the formation of partially exfoliated nanostructure [110]. Bergman et al. intercalated a cationic palladium-based Brookhart catalyst into the galleries of an organically modified

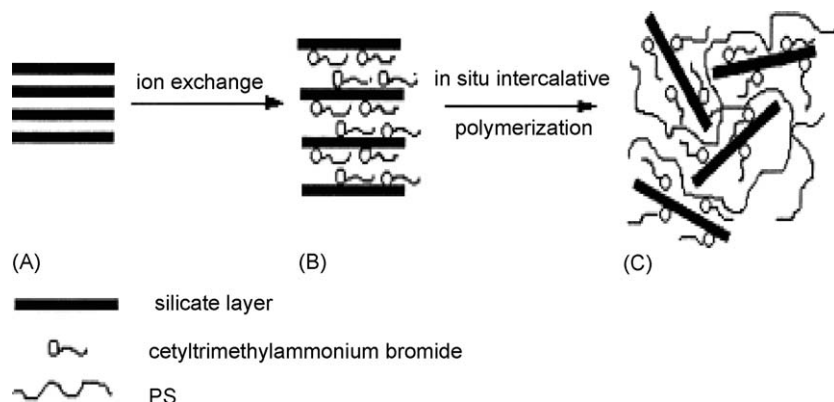


Fig. 13. (A–C) Schematic diagrams showing preparation of MMT-PS nanocomposites via emulsion polymerization (reprinted from [105] with permission from Elsevier).

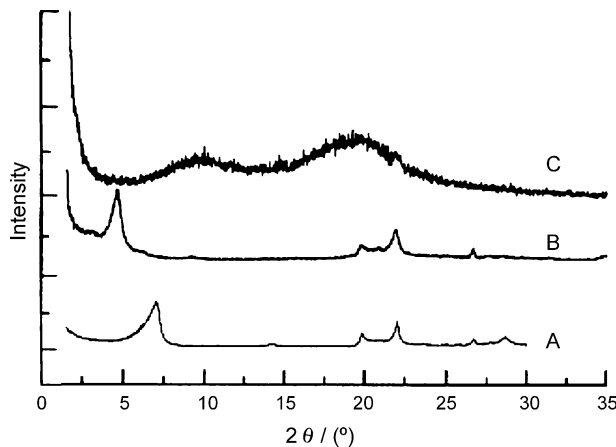


Fig. 14. XRD patterns of: (A) Na-MMT, (B) CTAB exchanged MMT, and (C) exfoliated MMT-PS nanocomposite (reprinted from [105] with permission from Elsevier).

fluorohectorite. An exfoliated polyethylene–silicate nanocomposite was achieved when exposed to olefinic monomer [111].

2.2.1.2. Melt intercalation. Melt compounding is a versatile process to prepare the clay–polymer nanocomposites. Melt intercalation enables the layered silicates mixed with the polymer matrix in molten state. This solvent-free technique requires the polymer to be compatible with the clays. The organic modifier converts the clay surfaces from hydrophilic to organophilic. This facilitates the mixing or intercalation of molecular chains of polymers into the gallery space. The electrostatic interactions between clay layers are already weakened by the presence of the surfactant head groups reside close to the exchange sites. Moreover, the low dielectric constant of the medium reduces the extent of electrostatic coupling [112]. Generally, large amounts of surfactant can shield interactions between the polymer molecules and clay surfaces. Consequently, larger surfactant molecules result in larger shielding effects. Thus, selection of appropriate organoclays is required to achieve intercalation of polymer molecules into the clay galleries. In most cases, compatibilizers such as maleic-anhydride and hydroxyl functional groups are needed to intercalate non-polar polymers into the gallery space of the clay. The purpose of the polymeric compatibilizer is to create the loops and tails on the clay surface to interact with the thermoplastic melt.

In principle, the equilibrium nature of polymer–organoclay nanocomposites is strongly related to the nature of a polymer (polar or apolar), the charge density a layered silicate, the chain length and structure of surfactant molecules. Balazs et al. have used the self-consistent field (SCF) concept to investigate the factors affecting the penetration of polymers into layered silicates [113,114]. They found that an increase in the surfactant length to the length of polymer chains favors the layers separation by allowing the polymer to adopt more conformational degrees of freedom. On the contrary, increase in the length of polymer chains renders the interlayer mixture becoming immiscible. They also reported the effect of the surfactant density on the intercalation process, indicating that excessive density of tethered alkyl chains could impede the formation of intercalated structures [113,114]. Vaia and Giannelis have developed mean filed, lattice-based thermodynamic model for polymer melt intercalation in organically modified mica type silicates [115]. They reported that the outcome of polymer intercalation is determined by an interplay of entropy and energy change in the system. During polymer melt intercalation, the entropy penalty (loss) of polymer confinement in the gallery space can be compensated for by the increased conformational freedom of the surfactant chains as the

layers separate due to the less confined environment. The entropy change associated with the surfactant increases until the interlayer separation is equal to the fully extended length of the surfactant chains. On the other hand, as the interlayer separation increases, more polymers are confined and the total penalty of polymer confinement per unit area continuously increases (Fig. 15). Thus, the penalty for polymer confinement is compensated only up to a critical gallery height, h_c . Since the total entropy change for gallery height less than h_c is about zero, even relatively weak intermolecular interaction can provide the driving force for polymer intercalation. The extent of intermolecular interactions would determine the amount of the intercalated polymer, particularly for gallery heights larger than h_c . At this stage, the penalty of polymer confinement dominates and strong energetic molecular interactions are needed to overcome the unfavorable entropy changes in the system. When the total entropy change is small, small changes in the free energy of the system determine whether intercalation is thermodynamically stable. For alkylammonium-modified silicates, the free energy change is rendered favorable by maximizing the magnitude and number of favorable polymer–surface interaction while minimizing the magnitude the number of unfavorable apolar interactions between the polymer and functionalizing alkyl surfactants (Fig. 16). For most conventional organosilicates, the tethered surfactant chains are apolar, thus the dispersion forces dominate the polymer–surfactant interactions. As the silicate surface is polar, a favorable energy decrease is established because of many favorable polar polymer–surface interactions. From Fig. 16, Type (a) free energy curve is always positive at all gallery heights, indicating polymer intercalation is unfavorable because the polymer and organoclay is immiscible. Type (b) curve displays only one minimum and polymer intercalation is favorable up to a finite layer separation. Type (c) curve displays more than one free energy minimum. Thus Type (c) system exhibits ill-defined intercalated structures or intermediate intercalated structures before complete layered exfoliation. Type (d) curve shows a continuous decrease in the free energy as the gallery height increases. This type corresponds to complete polymer–silicate layer miscibility, leading to the formation of exfoliated structure [115]. Therefore, the melt intercalation process is considered to occur via two stages. In an earlier stage, polymer chains from bulk polymer need to be transported from the bulk melt into the expanded clay galleries. This process does not require high shear force. The driving force is the affinity of the polymer chains for the organoclay surfaces. The enthalpy of mixing could be rendered favorable by maximizing the

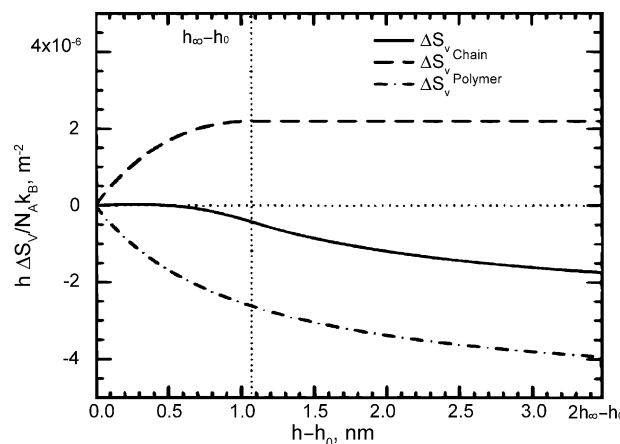


Fig. 15. Entropy change per unit area as a function of the change in gallery height for an arbitrary polymer and a silicate functionalized with octadecylammonium groups. h_0 is the initial gallery space, and $h_\infty - h_0$ is the change in gallery height for fully extended octadecyl chain. Solid curve represents the total entropy change of the system. Dashed and dash point curves represent the entropy change for the tethered chains, and the polymer chains, respectively (reprinted from [115] with permission from The American Chemical Society).

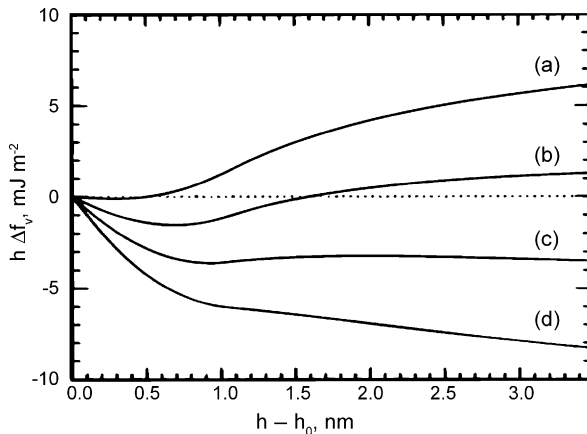


Fig. 16. (a–d) Free energy change per unit area a function of the change in gallery height for an arbitrary polymer and a silicate functionalized with octadecylammonium groups (reprinted from [115] with permission from The American Chemical Society).

polymer–clay interactions. At later stage, the clay tactoids are exfoliated under shear and stacks of clay platelets tend to slide apart from each other. High shear intensity would assist the formation of polymer–clay nanocomposites by breaking up the clay platelets and increasing sample uniformity [92]. The process is thus facilitated by both residence time and screw configuration in the extruder.

Although alkylammonium cations render the layered silicates more organophilic, the main limitation of the organically treated clays is derived from their lower thermal stability during melt processing at high temperatures. This situation becomes more serious for melt-compounding of many high performance polymers such as polyetherimide with high melting point. The onset decomposition temperature of alkylammonium surfactants is ~ 180 °C [93]. Vanderhart et al. studied the thermal stability of MMT modified with dimethyl, dehydrogenated-tallow ammonium during melt blending with PA6 at 240 °C [116]. They reported that most of the organic modifier on the clay surface decomposes, releasing a free amine with one methyl and two tallow substituents. This was caused by the combined effects of the temperature and shear stress during melt blending. Accordingly, melt blending is feasible only if the organic components applied to the clays are stable at the high-temperature processing conditions required.

As mentioned above, water with large polar components (δ_p) and hydrogen-bonding components (δ_h) is a good swelling agent to expand the basal spacing of MMT. In this regard, water can be considered as a possible substitute for alkylammonium surfactant. However, fabrication techniques need to be developed to accommodate the use of water as a swelling agent for the clay minerals. Hasegawa et al. [117] attempted to prepare MMT–PA6 nanocomposite using Na-MMT water slurry via melt compounding. In the process, the slurry was prepared by dispersing the Na-MMT powder into water by using a homogenizer. The inorganic content in the slurry was 2 wt.%. The clay slurry was pumped into the cylinder of the extruder and blended with PA6 in the compounding zone at 240–250 °C under a screw rotation speed of 200 rpm (Fig. 17). The residence time in the cylinder was about 10 min. The water of the slurry was removed from the venting gate by vacuum. The obtained strands were pelletized subsequently. The clay content of the nanocomposite was determined to be 1.6 wt.% by measuring the weights before and after burning its organic part. The XRD pattern (trace c) reveals the formation of an exfoliated structure due to the absence of diffraction peaks of the Na-MMT (Fig. 18). TEM micrograph also reveals that the Na-MMT layers exfoliate and homogeneously disperse at the nanometer level (Fig. 19). For the purpose of comparison, PA6 was blended with

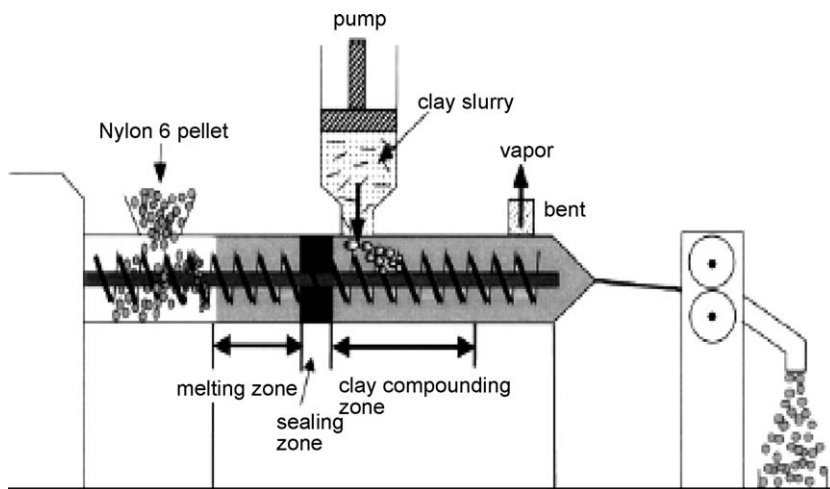


Fig. 17. Schematic diagram showing the compounding process for preparing PA6–MMT nanocomposites using the clay slurry (reprinted from [117] with permission from Elsevier).

Na-MMT without water treatment. XRD pattern demonstrates that this sample exhibits an apparent peak at 7.1° , corresponding to the (0 0 1) diffraction peak of the Na-MMT (trace b). This implies that PA6 molecular chains do not intercalate into the galleries of the Na-MMT during dry-compounding. Fig. 20(a–d) are schematic diagrams showing formation of an exfoliated structure in the MMT–PA6 nanocomposite using the clay slurry. The clay slurry is first pumped into the compounding zone of an extruder under vigorous shear (Fig. 20(a)). The slurry droplets tend to become finer during blending. At the same time, water of the slurry drops begin to evaporate on contact with molten PA6 (Fig. 20(b and c)). The evaporated water was quickly removed by vacuum. During water evaporation, some silicate layers are fixed into molten PA6 and dispersed at monolayer, and some dispersed as few stacking layers (Fig. 20(d)). Hydrolysis of PA6 does not occur in the compounding process using the clay slurry. The tensile and flexural moduli as well as tensile strength of the nanocomposite containing 1.6 wt.% MMT are higher than those of neat PA6. However, the impact strength of the nanocomposite is 12% lower compared to neat PA6 [117].

More recently, Mai and coworkers also used the water as an intercalating/exfoliating agent to prepare the PA6–MMT (5/95) nanocomposites via melt compounding in a twin-screw extruder [118].

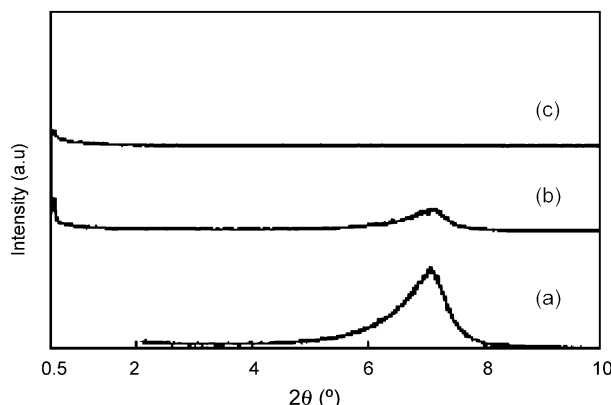


Fig. 18. XRD patterns of: (a) pristine Na-MMT, (b) PA6–MMT (dry) and (c) PA6–MMT (water). In (b), the sample was prepared by compounding PA6 with Na-MMT without water (reprinted from [117] with permission from Elsevier).

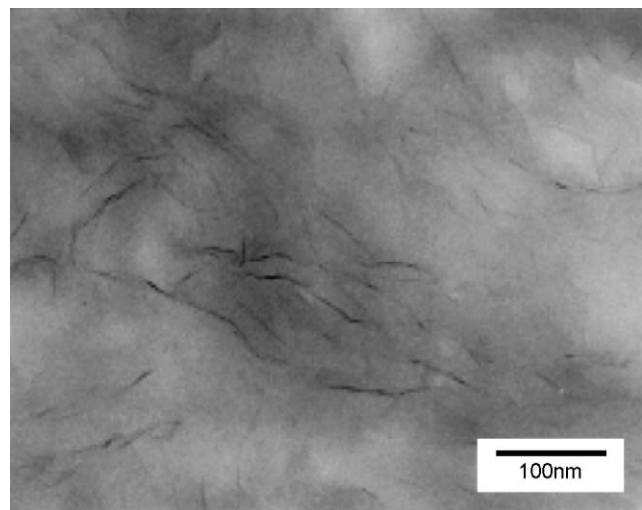


Fig. 19. TEM micrograph of PA6–MMT nanocomposite prepared from the clay slurry (reprinted from [117] with permission from Elsevier).

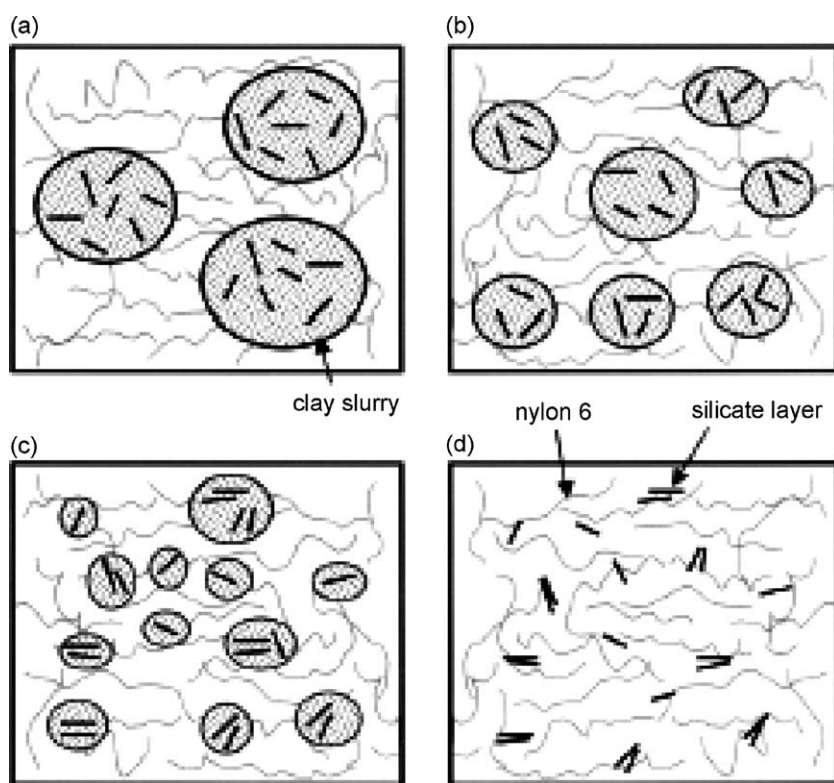


Fig. 20. (a–d) Schematic diagrams showing dispersion of the Na-MMT silicate layers of the slurry into PA6 during compounding (reprinted from [117] with permission from Elsevier).

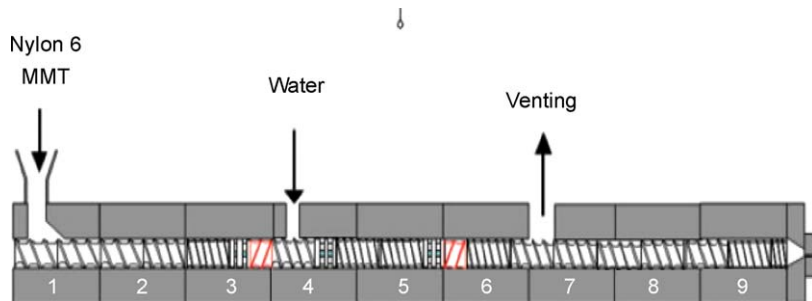


Fig. 21. Schematic diagram showing screw configuration of the twin-screw extruder used for water-assisted preparation of PA6–MMT nanocomposites (reprinted from [118] with permission from Wiley).

A major difference between their design experiments with those of Hasegawa et al. is that clay is not pretreated with water to form the slurry. Commercial PA6 pellets and pristine MMT were directly fed into the hopper of the extruder. Water was then injected into the extruder downstream at a flow rate ranging from 0 to 9 g/min during compounding. After interactions with the PA6 melt and pristine MMT, water was removed from the extruder further downstream via a venting gate (Fig. 21). The contact time between water and the PA6/pristine MMT system inside the extruder was so short that PA6 was subjected to very little hydrolysis. Fig. 22 shows the XRD patterns for the clay–PA6 nanocomposites prepared with or without the aid of water during melt extrusion. When pristine MMT was blended with the PA6 melt without water, its interlayer distance was increased from 1.2 to 1.5 nm (trace c of Fig. 22). This means that PA6 intercalated to a limited extent into the MMT interlayer during melt compounding owing to polar interaction between the PA6 and pristine MMT. However, such polar interaction was not strong enough to significantly intercalate or exfoliate MMT layers. Weakening the electrostatic interaction between MMT layers is needed for MMT exfoliation in a polymer matrix. The weak intensity of the (0 0 1) basal peak does not necessarily imply a high degree

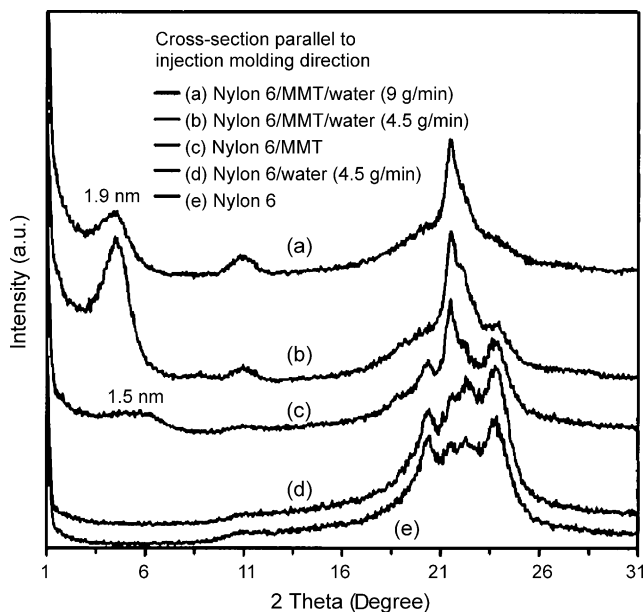


Fig. 22. (a–e) XRD patterns of the PA6–pristine MMT (95/5) composites with or without the aid of water during melt extrusion at a barrel temperature of 200 °C and a screw speed of 300 rpm (reprinted from [118] with permission from Wiley).

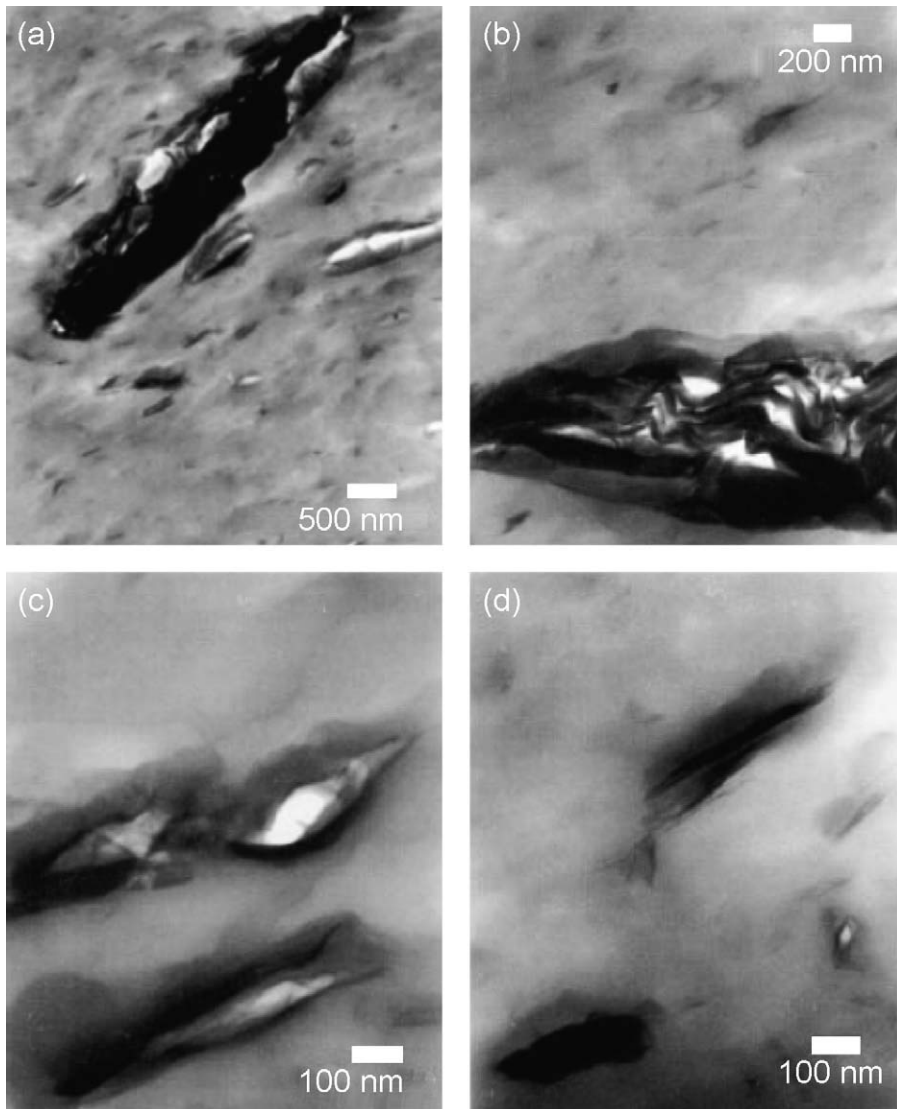


Fig. 23. (a–d) TEM micrographs of the PA6–pristine MMT (95/5) composites prepared by melt extrusion at a barrel temperature of 200 °C and a screw speed of 300 rpm (reprinted from [118] with permission from Wiley).

of exfoliation. If pristine MMT is poorly dispersed in the PA6 matrix, it can also be weak. Water is regarded as a good swelling agent for MMT to weaken the electrostatic interaction between MMT layers. When water is fed into the extruder during compounding, the diffraction peak of MMT was shifted to a lower angle (trace b). A further increase in the water flow rate resulted in a reduction in the intensity of (0 0 1) basal peak, and this implied a higher extent of exfoliation of MMT. Fig. 23(a–d) shows TEM micrographs of the MMT–PA6 composites prepared by melt extrusion without the aid of water. Apparently, most MMT remained as agglomerated tactoids, with the sizes ranging from several hundred nanometers to a few micrometers (Fig. 23(a–c)) and only a limited amount of partially exfoliated MMT layers (Fig. 23(d)). However, pristine MMT with the aid of water exhibited a relatively fine dispersion in the PA6 matrix (Fig. 24(a)), and most of the MMT layers were exfoliated to layers with high aspect ratio (Fig. 24(c and d)). The stiffness and tensile strength as well as the thermal stability of the resultant nanocomposites were greatly enhanced with the aid of water [118].

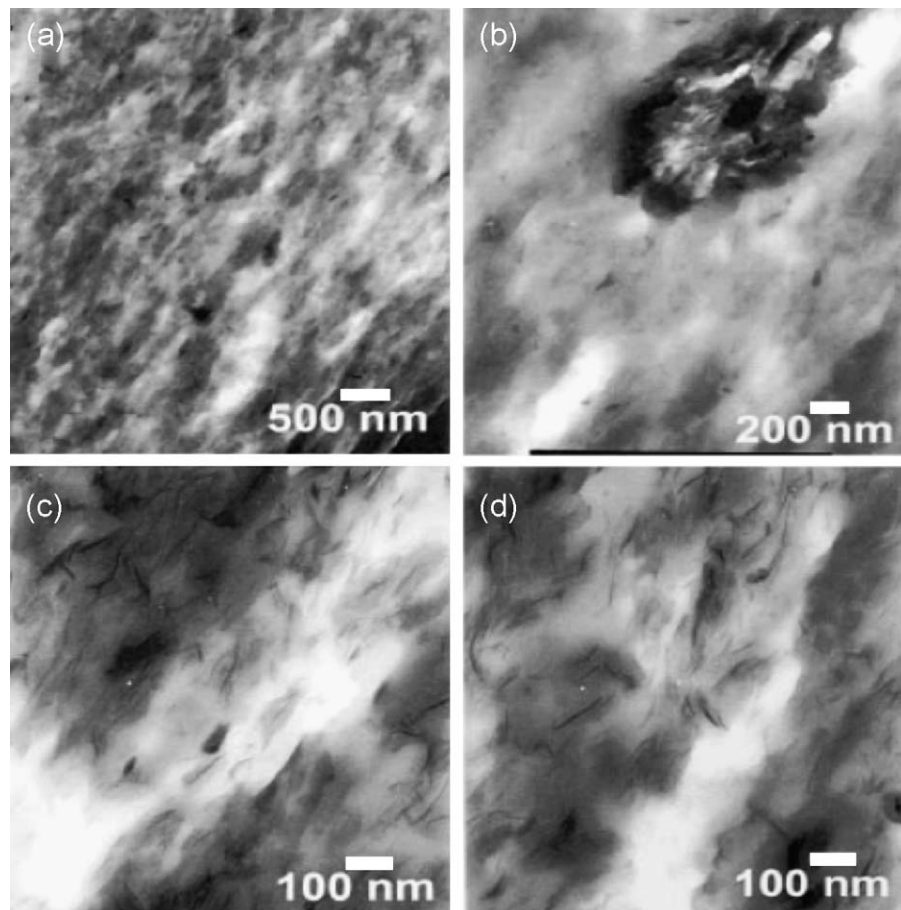


Fig. 24. (a–d) TEM micrographs of the PA6–pristine MMT (95/5) composites prepared by melt extrusion with the injection of water (9 g/min) at a barrel temperature of 200 °C and a screw speed of 300 rpm (reprinted from [118] with permission from Wiley).

It is noted that the fabrication of the polymer–clay nanocomposites using water as a swelling agent for the layered silicates is still in an embryonic stage. Thus, the organic modifiers are the main swelling agents currently used to facilitate the intercalation of polymer chains into the galleries of clays. Paul and coworkers have studied extensively the effect of adding different types of organoclays on the structure and mechanical properties of the melt-compounded polyamide–MMT and low density polyethylene–MMT nanocomposites [61,72,73,119–123]. In one study, various amine surfactants were exchanged for the sodium ion of pristine MMT (CEC = 92 mequiv/100 g clay). These organoclays include commercially available Cloisite® 15A and 20A as well as several laboratories prepared organically modified samples. Such organoclays were then melt blended with PA6 of high and low molecular weights. The degree of exfoliation of silicate platelets blended with PA6 of high molecular weight (HMW) was found to be dependent on three factors: decreasing the number of long alkyl tails from two to one tallow, use of methyl rather than hydroxy-ethyl groups, and use of an equivalent amount of surfactant with the MMT, as opposed to adding excess. The exfoliated nanocomposites exhibited enhanced modulus, higher yield strength and lower elongation at break. It appears that PA6 molecules would react with pristine MMT via a polar interaction. The organic modifier with two alkyl tails shields more silicate surfaces than one alkyl tail, thereby precluding the polar interaction between PA6 and the clay surface. Fig. 25(a) shows that the nanocomposite derived

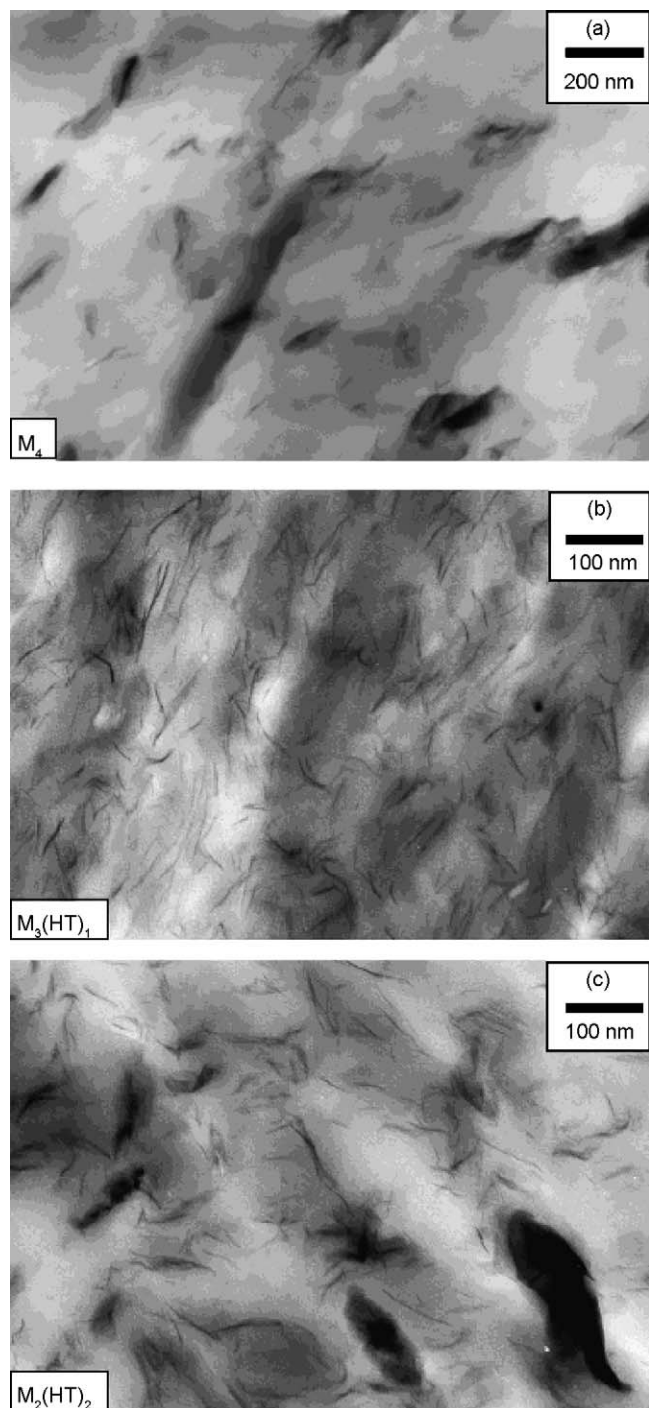


Fig. 25. TEM micrographs of HMW PA6 composites based on the organoclays (a) M₄ (b) M_{3(HT)}₁ and (c) M_{2(HT)}₂ containing 2.7, 2.9 and 3.0 wt.% MMT, respectively (reprinted from [122] with permission from The American Chemical Society).

from an organoclay having no alkyl tails in the quaternary cation results in an immiscible morphology, consisting primarily of unexfoliated clay nanoparticles [122]. In contrast, well-exfoliated nanocomposite is observed in the nanocomposite based on the one tail organoclay (Fig. 25(b)). The nanocomposite based on the two-tail organoclay consists of an intercalated morphology (Fig. 25(c)). The molecular structures of quaternary cation containing different numbers of alkyl tails are shown in Fig. 26. The XRD patterns of these nanocomposites are depicted in Fig. 27(a–c). It is obvious that the XRD trace for the nanocomposite derived from the M₄ organoclay is identical to its organoclay XRD pattern. This means that PA6 molecular chains do not penetrate into the galleries of organoclay during compounding, resulting in immiscible clay tactoids. The XRD trace of nanocomposite derived from organic modifier with one alkyl tail shows the absence of diffraction peaks. In this case, exfoliated structure is produced. For the nanocomposite based on the two-tail modifier, M₂(HT)₂, the basal diffraction peak shifts to lower angle, indicating formation of an intercalated structure. The XRD results generally correlate well with the TEM observations. The extent of mechanical reinforcement parallels the degree of exfoliation [122].

From this, it appears that the use of alkyammonium surfactant or water swelling agent facilitates the intercalation of polar polyamide molecules into the galleries of clays to form exfoliated nanocomposites. It is obvious that polarity of the polymer is required for the insertion of polymer molecules into the Na-MMT. In principle, poly(vinyl chloride) (PVC) would favor formation of the PVC–MMT nanocomposites. The highly electronegative chloride atoms of PVC chains render PVC with strong polarity. And large amount of polar hydroxyl groups reside in the MMT also induce the polarity on the surface of the clay. In this case, the dipole–dipole interaction between PVC molecules and MMT clay would act as a driving force for PVC molecules to intercalate into the gallery space of the clay. However, PVC and its composites are subject to discoloration during melt compounding due to their low thermal stability. Sequences of conjugated double bonds are formed in the molecular

<u>Structure</u>	<u>Designation</u>	<u>No. of Alkyl Tails</u>
$\begin{array}{c} \text{CH}_3 & \text{Cl}^- \\ & \\ \text{H}_3\text{C} - \text{N}^+ - \text{CH}_3 \\ \\ \text{CH}_3 \end{array}$	M ₄	0
$\begin{array}{c} \text{CH}_3 & \text{Cl}^- \\ & \\ \text{HT(C}_{18}\text{)} - \text{N}^+ - \text{CH}_3 \\ \\ \text{CH}_3 \end{array}$	M ₃ (HT) ₁	1
$\begin{array}{c} \text{CH}_3 & \text{Cl}^- \\ & \\ \text{HT(C}_{18}\text{)} - \text{N}^+ - \text{CH}_3 \\ \\ \text{HT(C}_{18}\text{)} \end{array}$	M ₂ (HT) ₂	2

Fig. 26. Molecular structures used to organically modified Na-MMT by ion exchange. The symbols M and HT designate methyl and hydrogenated tallow groups attached to the nitrogen (reprinted from [122] with permission from The American Chemical Society).

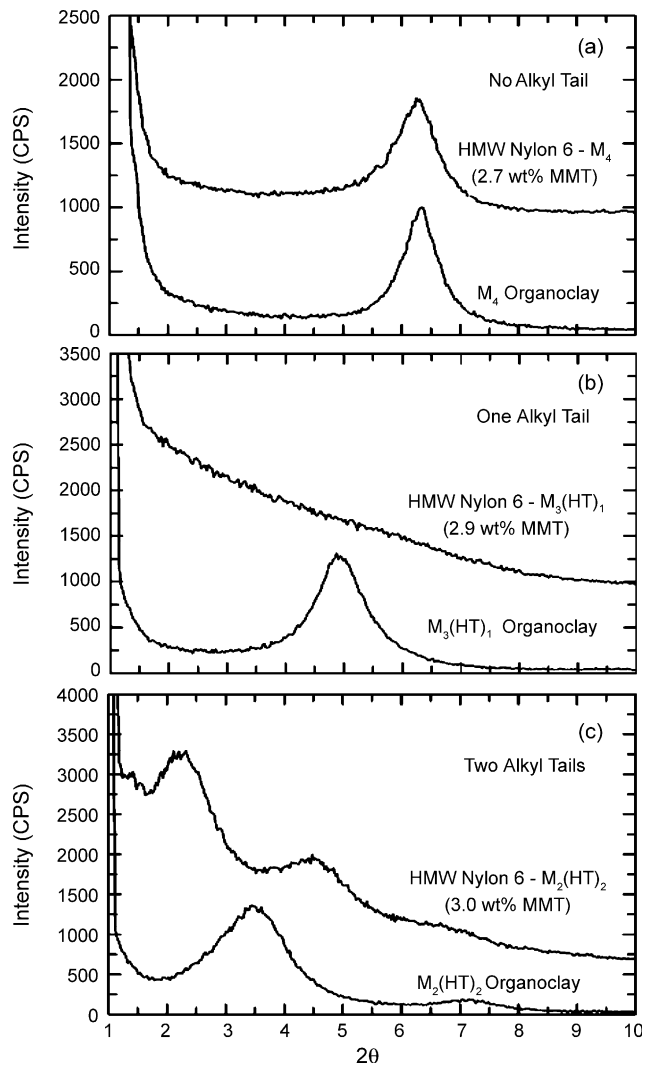


Fig. 27. XRD patterns of the organoclay and corresponding nanocomposites based on HMW PA6 for quaternary ammonium cations having (a) zero (b) one and (c) two alkyl tails (reprinted from [122] with permission from The American Chemical Society).

chains, resulting in the discoloration of the PVC matrix [124]. Furthermore, the thermal stability of PVC degrades considerably in the presence of organoclay. Particular stabilizers such as diethylphthalate (DOP) and epoxy resin are needed to prevent PVC discoloration [125,126]. At a processing temperature of 170 °C, the PVC–organoMMT (OrgMMT) composites exhibit discoloration from light yellow to pink with increasing OrgMMT content, while the PVC–pristine MMT composites do not change color. Wan et al. reported that the decomposition of quaternary alkylammonium modifier and their corresponding catalytic effects on the dehydrochlorination of PVC are the main reasons for the discoloration of the PVC–OrgMMT nanocomposites [127]. After being pretreated the OrgMMT with epoxy resin, the PVC molecules were largely intercalated into the OrgMMT layers, and even exfoliated at high epoxy content [126].

In the case of non-polar polyolefin polymers, the penetration of molecular chains into the gallery space layers of organoclays is limited. Only when in situ polymerization was performed,

Polyethylene-clay nanocomposites showed exfoliated morphology [111]. Therefore, polymer matrix functionalization and/or addition of extra compatibilizers are needed to improve the compatibility between the polymer matrix and the organoclay in order to form the intercalated or exfoliated nanocomposites. Maleic anhydride modified PP (PP-MA) is well known to mix well with certain organoclays to form PP nanocomposites [13,127–135]. Similarly, maleic anhydride grafted PE (MA-PE) also interacts with OrgMMT during melt-compounding to form exfoliated PE-MMT nanocomposites [136,137]. It is considered that the interaction via hydrogen bonding between the oxygen group of the silicates and MA group grafted to PP would assist the desired nanodispersion of organoclay in PP matrix. Hydroxyl-functional PP is also reported to be an effective compatibilizer for PP nanocomposites [138]. However, the extent of exfoliation and dispersion of nanoclays in PP or PE depend on the organic modifier of the organoclay, the initial interlayer spacing, the concentration of functional group in the compatibilizer, the viscosity or molecular weight of polyolefin, and the operating processing conditions. Wang et al. reported an exfoliated structure can be formed in PE nanocomposite when the number of methylene groups in organoclay is larger than 16 and the MA grafting level is higher than 0.1 wt.% [136]. Fig. 28 shows the XRD patterns of extruded MA

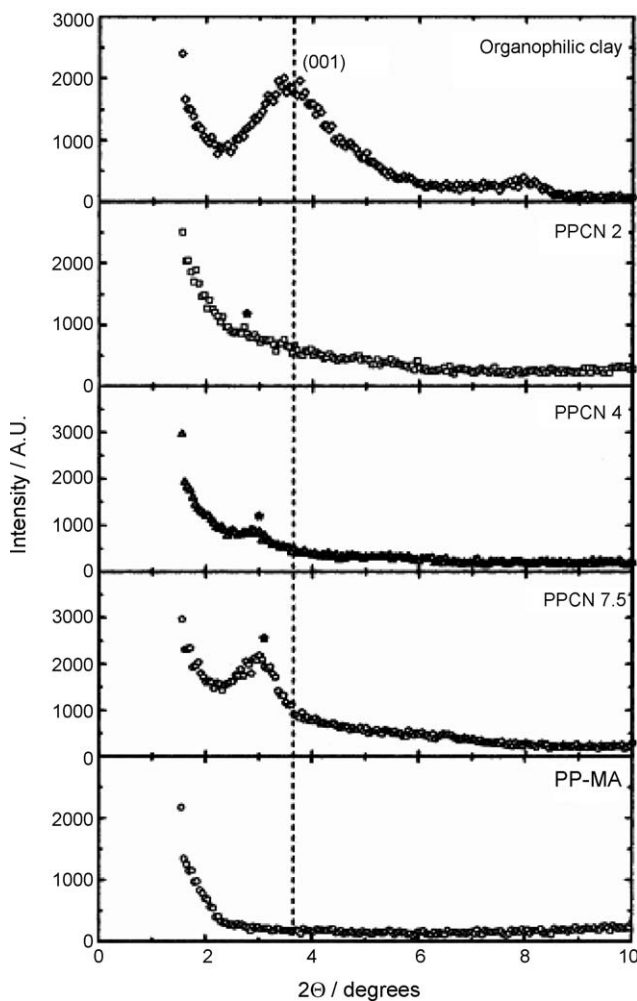


Fig. 28. XRD patterns for organoclay, PP-MA and PPCNs. The dash lines indicate the location of the silicate (0 0 1) reflection of organoclay (reprinted from [131] with permission from Elsevier).

compatibilized PP nanocomposites reinforced with 2, 4 and 7.5 wt.% organoclay (designated as PPCN2, PPCN4 and PPCN7.5). The corresponding TEM micrographs of the nanocomposites are shown in Fig. 29 [131]. It is obvious that the structure and morphology of PPCN2 consist of exfoliated nanostructure. However, a small peak begins to appear at $2\theta = 2.9^\circ$, corresponding to (0 0 1) basal plane of the silicate. For the PPCN7.5, a strong and well-defined diffraction peak is observed at $2\theta = 3.05^\circ$ ($d = 2.89$ nm), implying the formation of an ordered intercalated nanocomposite. TEM micrograph reveals that stacked silicate layers are formed in the PPCN4 and PPCN7.5, indicating formation of an intercalated structure (Fig. 29(b and c)).

Alternatively, Tjong et al. used maleic anhydride as a reactive reagent acting as a modifying additive for the polymeric matrix and a swelling agent for the vermiculite silicate [12]. In the process, vermiculite was initially pretreated with hydrochloric acid solution. The acid-delaminated vermiculite was further treated with MA in the presence of acetic acid to form an organoclay. XRD examination

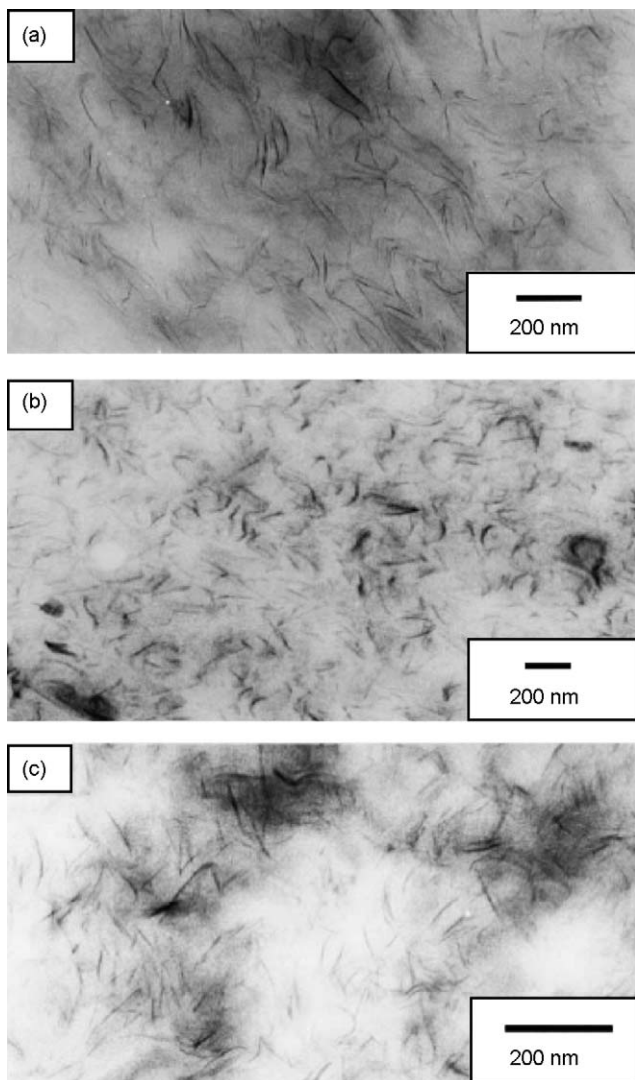


Fig. 29. TEM micrographs for PPCNs containing (a) 2 wt.%, (b) 4 wt.% and (c) 7.5 wt.% organoclay (reprinted from [131] with permission from Elsevier).

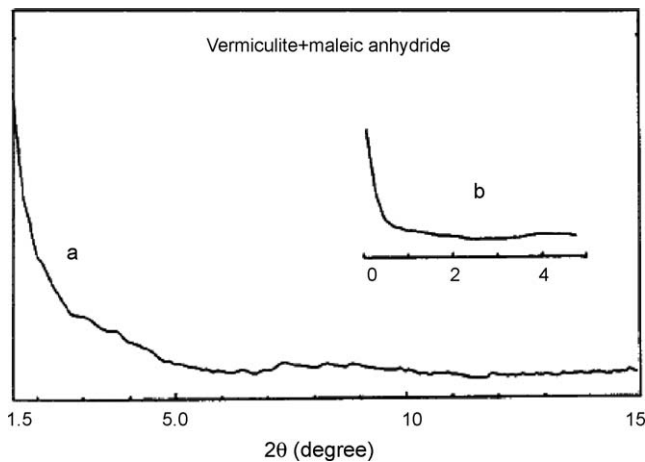


Fig. 30. XRD patterns of MA-treated vermiculite recorded by (a) wide angle ranging from 1.5 to 15° and (b) small angle ranging from 0 to 5° [12].

reveals the absence of diffraction peaks, indicating the formation of an exfoliated structure (Fig. 30). This implies that MA can easily enter the galleries of acid-treated vermiculite because solvent (acetic acid) can act as a carrier to transport MA into hydrophilic vermiculite. MA has a flat molecular structure in which the greatest length is about 5.126 Å, as depicted in Fig. 31. This figure also reveals that the incorporation of excess MA into acid-treated vermiculite extends its gallery spacing. Accordingly, PP-vermiculite nanocomposites with an intercalated or exfoliated structure can be achieved by direct melt mixing of MA-modified vermiculite (MAV) with PP. Fig. 32 shows the XRD patterns of PP nanocomposites prepared by direct melt mixing of MAV with PP. Apparently, the diffraction traces show no XRD peaks, indicating formation of an exfoliated structure. However, TEM micrograph shows the formation of mixed intercalated/exfoliated structures due to the presence of some stacked platelets (Fig. 33) [12]. Tjong et al. then adopted a similar process to prepare polyethylene–MAV nanocomposites. A complete exfoliated structure of vermiculite platelets can be observed in TEM [14].

In the case of glassy PS and PMMA polymers, the nanocomposites can be prepared by melt-blending organoclays with PS or PMMA homopolymers. In general, the PMMA chain can intercalate more easily into the clay galleries than the PS molecule due to its higher polarity. Fig. 34 shows the

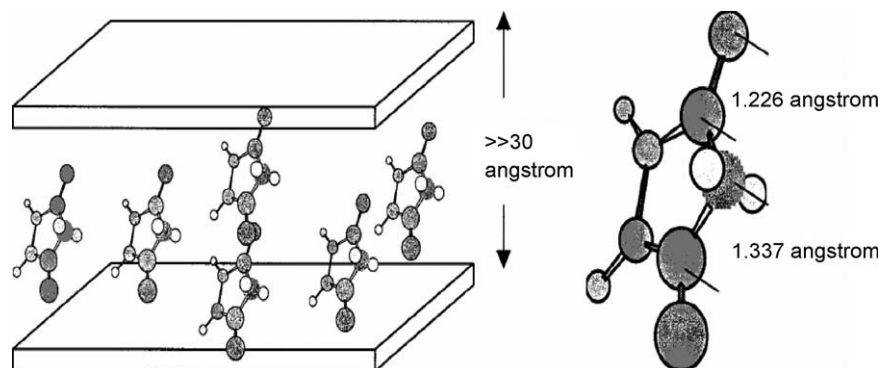


Fig. 31. Structures for energy-minimized maleic anhydride and MA-treated vermiculite [12].

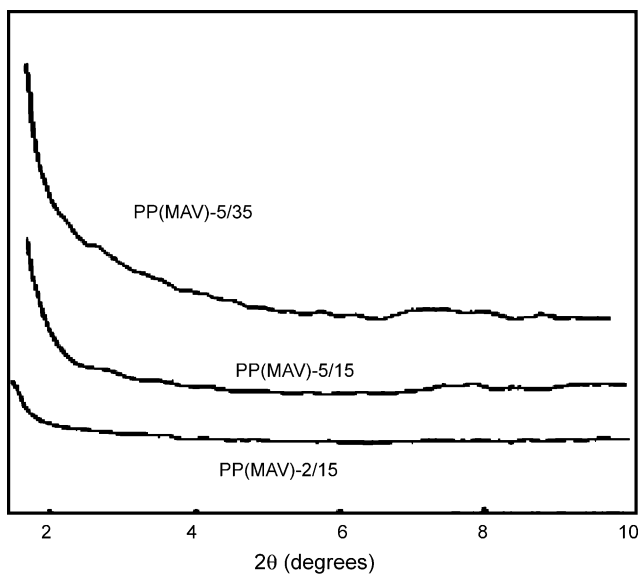


Fig. 32. XRD patterns for PP nanocomposites reinforced with 2 and 5% malleic anhydride-modified vermiculite (MAV) prepared under melt compounding at a screw speed of 15 or 35 rpm [12].

XRD patterns of melt-compounded PMMA–Cloisite 30B nanocomposites reinforced with 1.96, 3.85 and 5.66 wt.% organoMMT. Basal ($0\ 0\ 1$) diffraction peak can be observed at $2\theta = 2.5^\circ$ in the XRD patterns of nanocomposites, corresponding to d -spacing of 3.53 nm [52]. The TEM micrograph (Fig. 35) also reveals the formation of mainly clay tactoid morphology or intercalated structure. For the PC amorphous polymer with better ductility, Paul and coworkers studied the effects of matrix molecular weight on dispersion of organoclays modified with various amine surfactants [139]. They reported that the surfactant having polyoxyethylene and octadecyl alkyl tails shows the most significant improvement in modulus and leads to partially exfoliated platelets in TEM images.

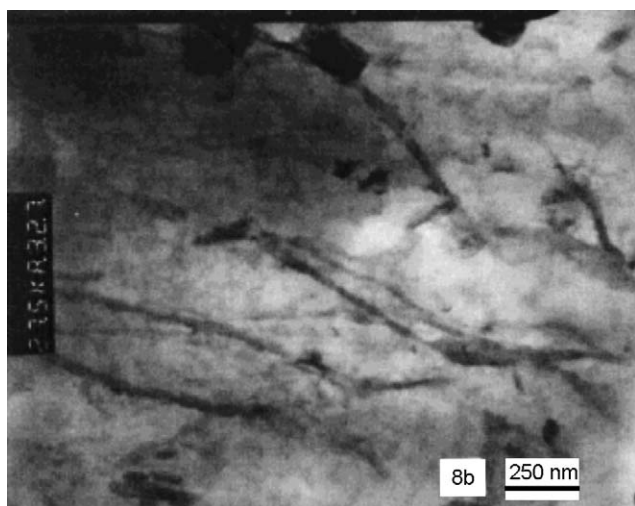


Fig. 33. TEM micrograph showing formation of mixed intercalated/exfoliated structures for PP nanocomposite reinforced with 5% maleic anhydride-modified vermiculite (MAV) [12].

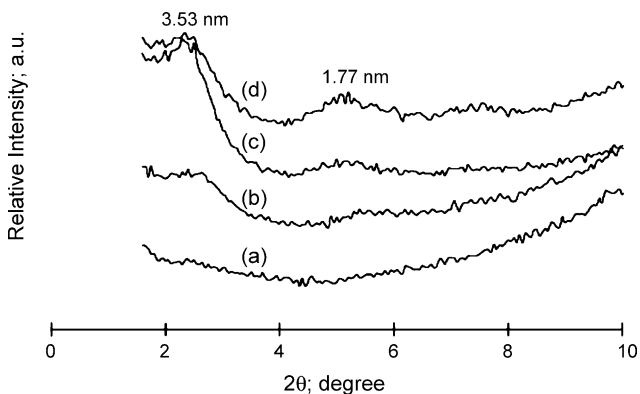


Fig. 34. XRD patterns of melt-blended PMMA–clay composites reinforced with (a) 0, (b) 1.96, (c) 3.85 and (d) 5.66 wt.% Cloisite[®] 30B (reprinted from [52] with permission from Elsevier).

The partial exfoliation of platelets is attributed to miscibility of the poly(ethylene oxide) tail with PC. The clays modified with other amine surfactants yield large aggregate of platelets and tactoids. Moreover, the modulus enhancement is greater for nanocomposites formed from a high molecular weight PC (HMW-PC) than medium molecular weight PC owing to the the higher shear stress generated during melt processing for HMW-PC.

2.2.2. Epoxy matrices

Epoxyresins are an important family of thermosets that find widely applications as matrices of the polymer composites, adhesives in the aerospace industries, and coatings for metals. However, epoxy resins are brittle compared to semicrystalline thermoplastics because of their crosslinked molecular structures; they have poor resistance to crack initiation and growth. The research groups of Pinnavaia [140–145] have carried out extensive research on the effect of clay additions on the structure and property of an epoxy resin, the diglycidyl ether of bisphenol A (DGEBA; Epon-828 resin). They reported that the acidic primary onium ions that are ion-exchanged for the inorganic cations of layered

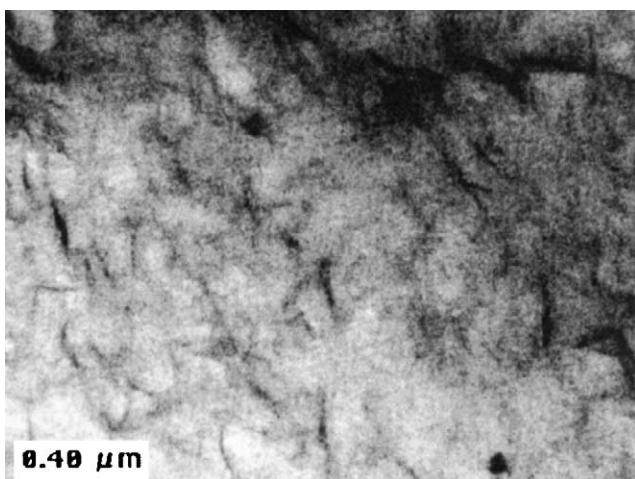


Fig. 35. TEM image of melt-blended PMMA–clay composite reinforced with 3.85 wt.% Cloisite[®] 30B (reprinted from [52] with permission from Elsevier).

silicates, catalyze the intragallery epoxide polymerization process in the presence of diamine curing agent. In other words, the reaction of Epon-828 resin with acidic forms of MMT at temperature at 120–200 °C results in the polymerization of epoxides to produce the polyethers. Moreover, the chain length of the onium ion, its relative acid strength (primary > secondary > tertiary onium ions) and the clay layer charge density play an important role in the exfoliation of clay [140–142]. Fig. 36 shows the XRD patterns for cured epoxy–clay nanocomposites containing 5 wt.% of various alkylammonium exchanged forms of MMTs. Apparently, the XRD patterns of composites formed with $\text{CH}_3(\text{CH}_2)_7\text{NH}_3^+$, $\text{CH}_3(\text{CH}_2)_{11}\text{NH}_3^+$, and $\text{CH}_3(\text{CH}_2)_{15}\text{NH}_3^+$ –MMT show the absence of diffracting peaks, indicating formation of an exfoliated structure. In contrast, the composites formed with shorter alkylammonium cations exhibit an intercalated structure. Long-chain alkylammonium ions allow epoxy monomer to be accommodated in the gallery by adopting a vertical orientation that optimizes solvation interactions with the alkyl chains. Fig. 37 shows the effect of primary, secondary, tertiary and quaternary onium ions with a C₁₈ chain length on the delamination of MMT clay by the epoxy resin.

This figure reveals that the clays with primary and secondary onium ions form exfoliated nanocomposites. The clays with tertiary and quarternary onium ions with decreasing acidity yield intercalated nanocomposites. In the case of primary onium ions, exfoliated nanocomposites can be more readily achieved by using the low charge density clays (MMT and hectorite) rather than using high charge density silicates (fluorohectorite and vermiculite) (Fig. 38). For clays with a high layer charge density, a large number of gallery onium ions are needed to balance the layer charge. Consequently, fewer epoxide monomers can be accommodated in the galleries as the population density of onium ions is increased.

On the basis of DSC measurements, Pinnavaia and coworkers indicated two exothermic catalytic processes occur during the polymerization of epoxy–clay nanocomposites as evidenced by the presence of two peaks at ~130–160 °C (Fig. 39). The lower temperature process is attributed to polymerization of pre-intercalated epoxide on the internal gallery surfaces where the proton concentration is a maximum [142]. The relative intensity of the low temperature peak increases with increasing clay content, implying that this exothermic process is related to the available clay surface area. Polymerization of the extragallery monomer on the external and internal surfaces of the clay

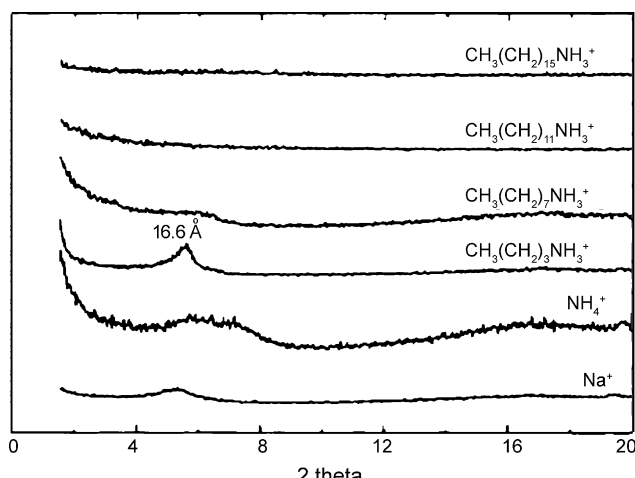


Fig. 36. XRD patterns of epoxy–clay composites formed by the polymerization of a DGEBA resin, with a stoichiometric amount of *m*-phenylenediamine (mPDA) as the curing agent in the presence of various cation exchanged forms of MMT (5 wt.%) (reprinted from [140] with permission from The American chemical Society).

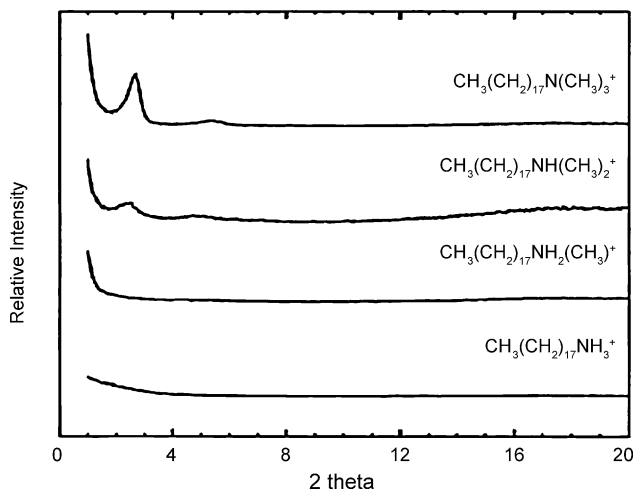
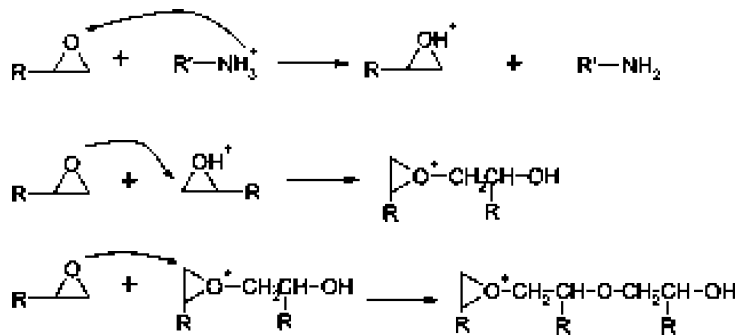


Fig. 37. XRD patterns of amine-cured epoxy–clay nanocomposites formed from MMT clays (5 wt.%) containing primary, secondary, tertiary and quaternary onium ions with a C18 chain length (reprinted from [140] with permission from The American Chemical Society).

platelets occurs at the higher temperature. The proposed mechanism for epoxy polymerization in acidic smectic clay galleries is shown as follows:



The dissociation of $\text{CH}_3(\text{CH}_2)_{n-1}\text{NH}_3^+$ cations in the clay galleries generates protons that attack the epoxy ring, causing acid catalyzed ring opening polymerization.

In order to achieve clay exfoliation in epoxy resins, it is necessary to balance the intragallery and the extragallery polymerization rates by controlling the reaction rates of resin intercalation, chain formation and network crosslinking. This can be controlled by the nature of the clay including the CEC value and the selection of primary alkylammonium ions having long chain length and acidity. However, if the extragallery polymerization is more rapid than the intragallery diffusion, an intercalated structure is produced. In addition, the curing conditions, e.g. the type of curing agents [146–149] and curing temperature [150] also affect the exfoliation of clay layers in epoxy resins. Fig. 40(a and b) show typical TEM micrographs of DGEBA–MMT(C_{18}) nanocomposites cured with

(4,4'-methylenedianiline; MDA) and (4,4'-diaminodiphenyl sulfone; DDS), respectively. For the DGEBA–MMT(C_{18}) nanocomposite cured with MDA, the interlayer distance is about 10 nm or less, and several clay layers are still agglomerated. However, the interlayer distance is larger than 20 nm and the clay layers are exfoliated in the DGEBA–MMT(C_{18}) nanocomposite cured with DDS [146].

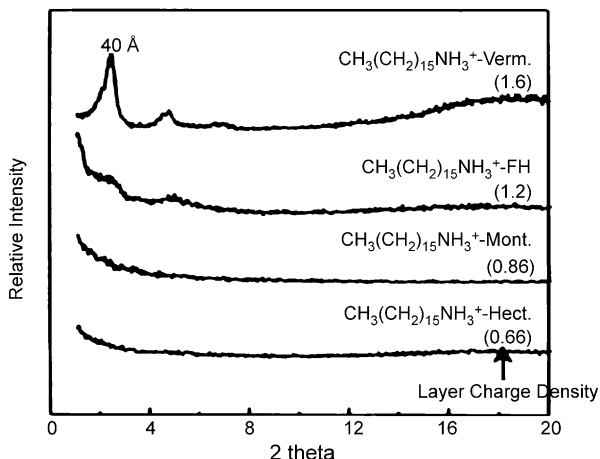


Fig. 38. XRD patterns of amine-cured epoxy–clay composites formed by the polymerization of a DGEBA resin, with stoichiometric amounts mPDA as a curing agent in the presence of various clays with $\text{CH}_3(\text{CH}_2)_{15}\text{NH}_3^+$ as exchanged cations for different layer density clays. Layer density values (mequiv/g) are given in parentheses (reprinted from [140] with permission from The American Chemical Society).

As mentioned previously, water is used as an intercalating/exfoliating agent to swell the clay. Wu and coworkers developed a ‘slurry-compounding’ process to prepare the epoxy–clay nanocomposites. In the process, the MMT clay was first exfoliated and suspended in water [151,152]. This suspension was further treated with acetone to form a clay–acetone slurry followed by chemical modification using silane. The modified slurry was then mixed rigorously with epoxy to form epoxy–clay nanocomposites. Acetone is a good solvent for epoxy, thus the epoxy monomers can easily intercalated into swollen clay galleries due to water treatment. When the acetone is removed by heating, epoxy monomers remain inside the galleries. Epoxy curing then occurs inside and outside galleries after adding the curing agent. Fig. 41(a–d) shows TEM micrographs of epoxy–clay nanocomposite prepared by this process. At lower magnification, exfoliated clay platelets are distributed in the matrix homogeneously and randomly. However, some of the clay platelet stacks consisting of 3–5 layers can be observed in TEM micrographs at higher magnification (Fig. 41(c and d)).

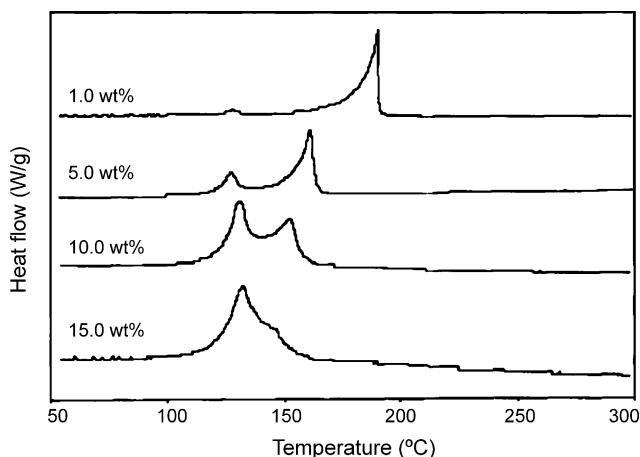


Fig. 39. DSC curves for the self-polymerization of Epon-828 in the presence of different amounts of $\text{C}_{18}\text{H}_{37}\text{NH}_3^+$ –montmorillonite (reprinted from [142] with permission from Elsevier).

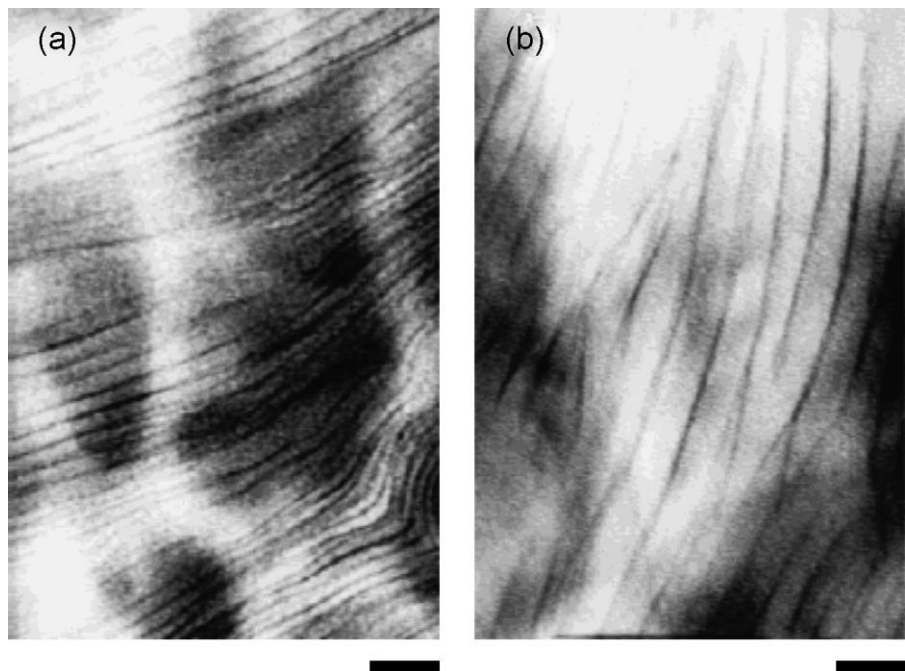


Fig. 40. TEM micrographs of DGEBA–MMT(C_{18}) (10 phr) nanocomposites cured with (a) MDA and (b) DDS agents. Scale bar indicates 20 nm (reprinted from [146] with permission from The American Chemical Society).

2.2.3. Elastomer matrices

Commercial clay (e.g. English India) and carbon black have been used as low cost fillers in rubber industry for many years. The reinforcing capacity of these fillers is poor because of its large particle size and low surface activity [153]. From this aspect, layered silicates are considered as effective reinforcing fillers for rubbers, elastomers and thermoplastic elastomers [154–156]. The enhanced mechanical properties of these nanocomposites have attracted considerable interests and commercial applications in automotive industries.

Karger-Kocsis and coworkers prepared the natural rubber–clay nanocomposites by co-coagulating rubber latex and clay aqueous suspension. The pristine clay was used instead of organoclay. The resulting nanocomposites exhibit enhanced tensile modulus and strength [153,157]. Apart from natural rubbers, other elastomers have also been used as potential matrices for the nanocomposites. These include polyurethane (PU) [158–161], ethylene–propylene–diene monomer (EPDM) [162–164], acrylonitrile–butadiene–styrene (ABS) [165], poly(styrene–(ethylene-co-butylene)–styrene) triblock copolymer (SEBS) [166] and polysiloxane [167–169]. The fabrication methods for the rubber or elastomer–clay nanocomposites are similar to those used for the thermoplastics, i.e. in situ polymerization and melt intercalation.

Very recently, Gatos and Karger-Kocsis investigated the effects of primary and quaternary amine modified MMT as well as MA additions on the structure and mechanical behavior of EPDM–clay nanocomposites [164]. The MMT clays modified with primary octadecylamine (Nanomer® 1.30E; MMT-Prim) and octadecylmethyl-amine (Nanomer® 1.28E; MMT-Quat) were used. The organoclay was introduced in 10 parts per 100 rubber (phr) content during melt-mixing. Curatives and other ingredients (e.g. ZnO, stearic acid, S) were added on the open mill followed by curing in an electrically heated hydraulic press. Fig. 42 shows the XRD pattern of EPDM/MMT-Prim (10 phr) at the different stages of processing. Penetration of non-polar EPDM molecules into the clay galleries is

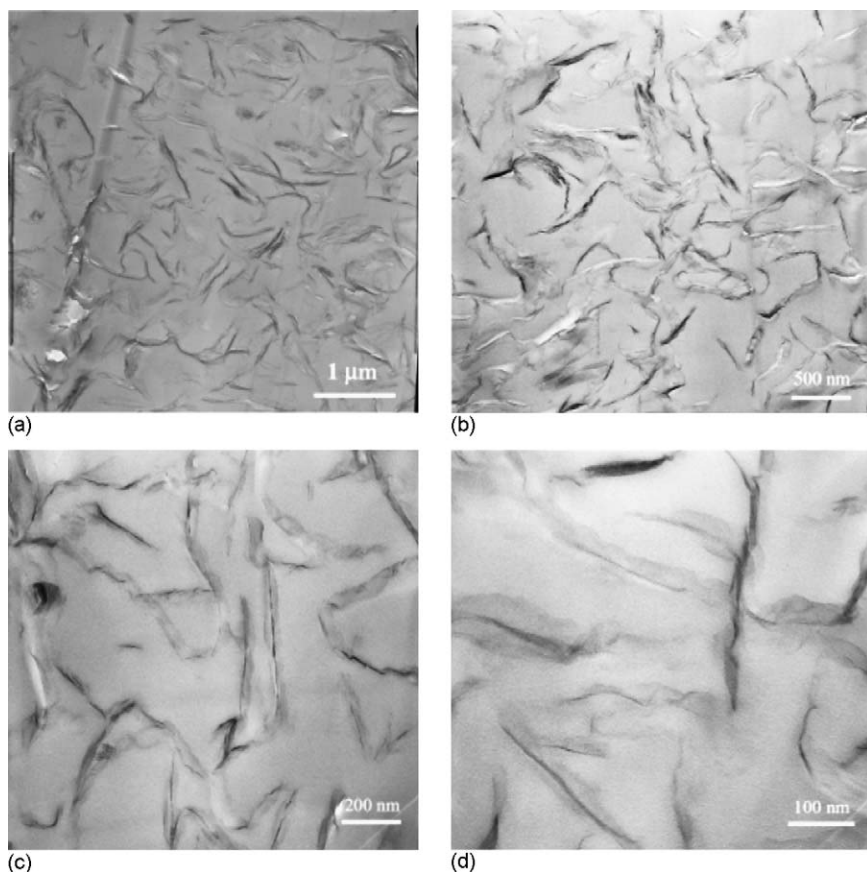


Fig. 41. (a–d) TEM micrographs of epoxy–clay (5 wt.%) nanocomposite prepared by a ‘slurry-compounding’ process at various magnifications (reprinted from [151] with permission from The American Chemical Society).

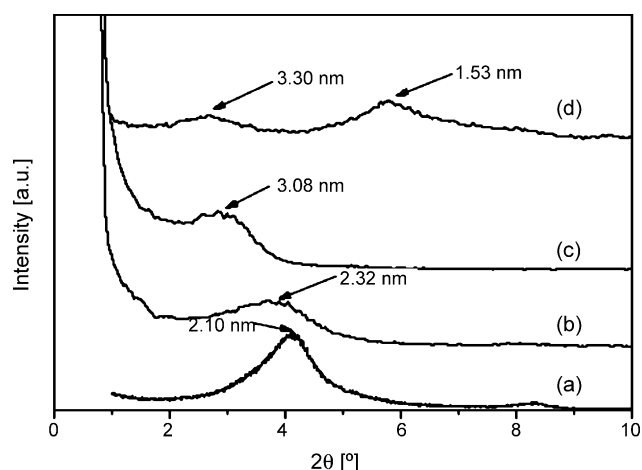


Fig. 42. XRD patterns of EPDM/MMT-Prim (10 phr) nanocomposite at different stages of processing: (a) MMT-Prim, (b) mixing of EPDM and MMT-Prim in the internal mixer, (c) after addition of the curatives on the open mill, and (d) after vulcanization at 160 °C (reprinted from [164] with permission from Elsevier).

limited as evidenced by a small increase of the basal spacing from 2.10 to 2.32 nm. After the second stage of compounding, incorporation of curatives on an open mill leads to a further expansion of the basal spacing to 3.08 nm. However, two diffracting peaks appear in the XRD pattern after vulcanization. The peak at 3.30 nm is associated with the nanocomposite formation whereas the peak at 1.53 nm is attributed to deintercalation of the clay galleries. Deintercalation of the clay during curing is related to the reactivity of primary amine of MMT-Prim with the vulcanization curatives to form a zinc coordination complex. A prominent change occurs in the Zn-complex as the activated sulfur competes with the amines as possible ligand. Fig. 43 shows the effect of grafting MA polar group to EPDM on the structure of nanocomposite. The beneficial effect of MA polar group is evident in the first stage of blending in the internal mixer. At this stage, the basal spacing increases from 2.10 to 3.15 nm. Adding the curatives would not change the degree of intercalation. The TEM images of vulcanized nanocomposites with and without MA compatibilizer are shown in Fig. 44(a and b). It can be seen that the clay platelets are more delaminated or exfoliated in the MA compatibilized nanocomposite. On the other hand, the XRD patterns of EPDM/MMT-Quat and EPDM-MA/MMT-Quat nanocomposites reveal that the basal spacing increases from 2.50 to 4.20 and 4.69 nm, respectively. Additional peaks are associated with higher order reflections of the MMT-Quat (Fig. 45).

As mentioned above, MA is an effective intercalation agent for vermiculite and a modifying additive for the polyolefins [10]. Using the same technique reported by Tjong, Liu et al. employed the MA to treat the vermiculite and to intercalate the EPDM molecules into the clay galleries during melt-compounding [163]. Fig. 46 shows the XRD patterns of EPDM-MAV nanocomposites. The diffracting peaks are absent in the XRD patterns of nanocomposites containing 5 and 7.5 wt.% MAV. However, TEM examination shows the formation of a mixed intercalated/exfoliated structure. At higher clay loading (10 wt.%), a very faint peak appears at $2\theta = 6.12^\circ$ (indicated by an arrow) corresponding to a basal spacing of 1.44 nm, resulting from the aggregation of some clays.

PU elastomer finds a wide range of applications in automotive, textile, paint and furniture industries. It is a linear copolymer consisting of alternating hard and soft segments. The hard segment is composed of alternating diisocyanate and chain extender molecules such as low molecular weight

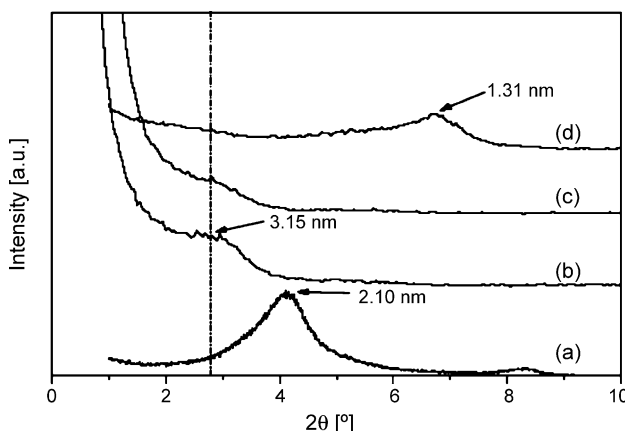


Fig. 43. XRD patterns of EPDM-MA/MMT-Prim (10 phr) nanocomposite at different stages of processing: (a) MMT-Prim, (b) mixing of EPDM-MA XRD patterns of EPDM/MMT-Prim (10 phr) nanocomposite at different stages of processing: (a) MMT-Prim, (b) mixing of EPDM and MMT-Prim in the internal mi MMT-Prim, (b) mixing of EPDM and MMT-Prim in the internal mixer, (c) after addition of the curatives on the open mill and (d) after vulcanization at 160 °C (reprinted from [164] with permission from Elsevier).

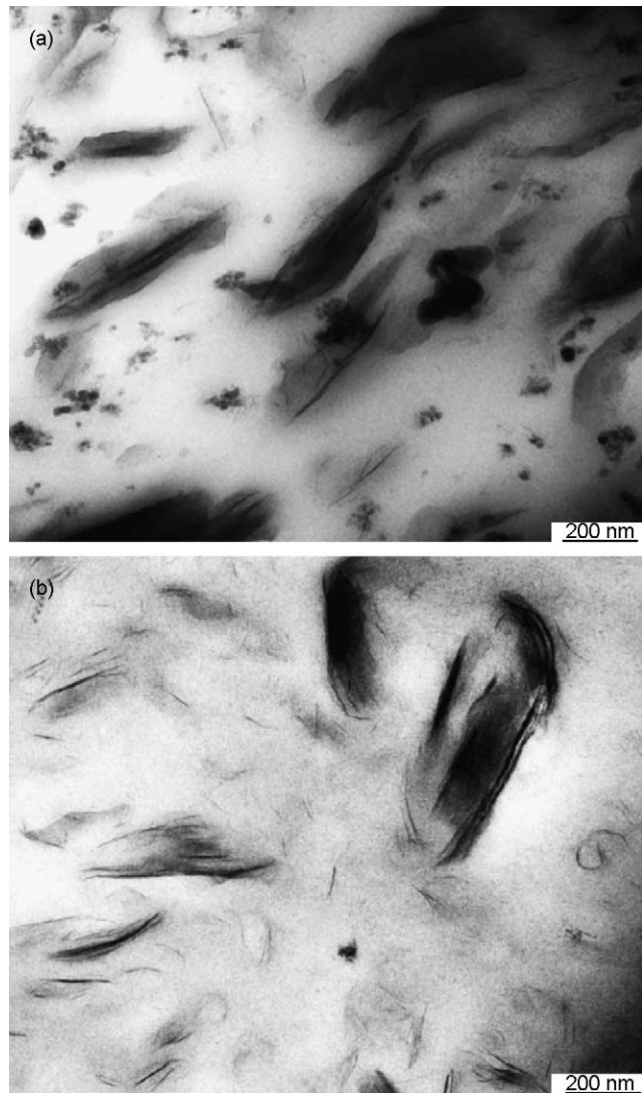


Fig. 44. TEM micrographs of vulcanized (a) EPDM/MMT-Prim and (b) EPDM-MA/MMT-Prim, both in 10 phr clay loading (reprinted from [164] with permission from Elsevier).

diol or diamine, while the soft segment is a high molecular weight polyester or polyether diol. The segments aggregate into microdomains resulting in a structure consisting of glassy and hard domains, as well as rubbery and soft domains, having their glass transition temperatures below and above room temperature. The extent of hard segments primarily determines the modulus of PU. The PU-clay nanocomposites are generally synthesized via in situ polymerization [158,159]. Tien and Wei reported the synthesis of PU-MMT nanocomposites with high tensile strength and elongation at break [159]. In the process, reactive swelling agents having one to three hydroxyl groups and one amine group for modifying the layered silicates were used as pseudo chain extenders for a preurethane prepolymer. The amine group in these swelling agents was converted into onium cations to replace the metal ions of the silicates, while the hydroxyl functional groups can react with the isocyanate groups of the PU monomer. The possible reactions between reactive swelling agents having one to three hydroxyl groups and one amine group are summarized in the following schematic diagram:

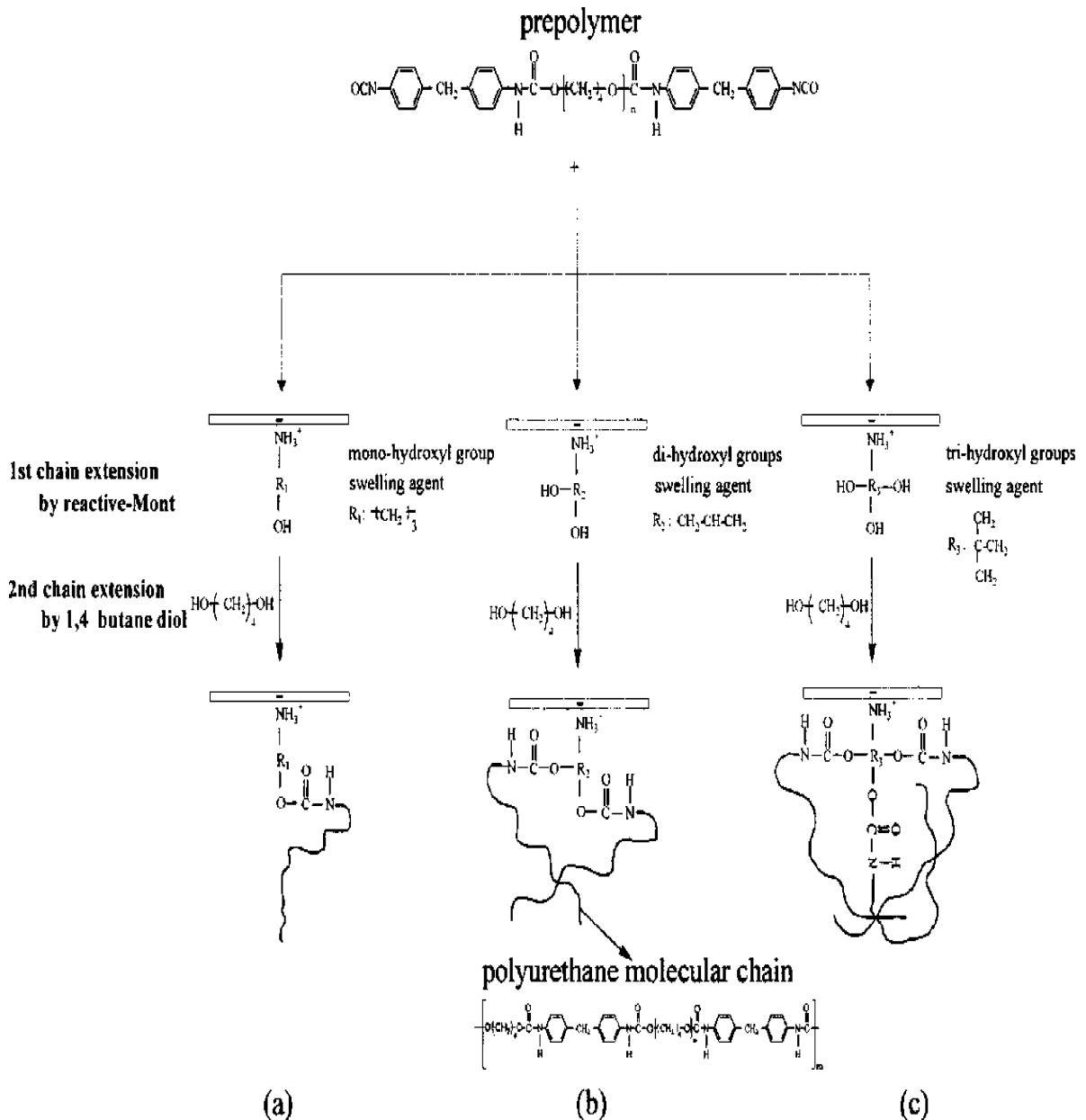


Fig. 47(a–c) shows the XRD patterns of the PU–clay modified with alkyl (C_{12}), monohydroxyl and dihydroxyl groups, respectively. For the nanocomposites containing 3 and 5 wt.% monohydroxyl modified MMT, a diffracting peak at $2\theta = \sim 5.0\text{--}5.2^\circ$ is observed. This peak corresponds to the (0 0 1) basal plane with a spacing of $\sim 1.7\text{--}1.8$ nm. At 1 wt.% clay loading level, this basal reflection diminishes (Fig. 47(b)). For the nanocomposites containing 1 and 3 wt.% dihydroxyl modified MMT, no peaks appear in the XRD pattern from $2\theta = 3$ to 10° (Fig. 47(c)). This implies that the clay galleries are delaminated. However, the basal reflection reappears in the XRD pattern when the clay content is increased to 5 wt.%. Fig. 48(a–c) shows the TEM images of the PU–clay nanocomposites containing 1 wt.% monohydroxyl, dihydroxyl and trihydroxyl modified MMT, respectively. For the MMT modified with monohydroxyl group, stacked clay layers are observed, indicating formation of an

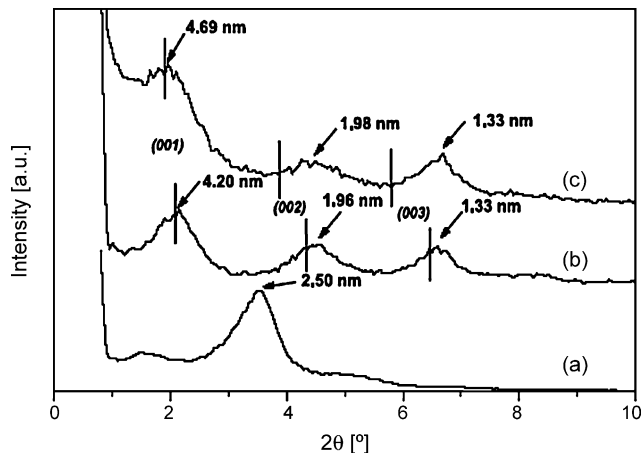


Fig. 45. XRD patterns of (a) MMT-Quat, (b) EPDM/MMT-Quat after vulcanization and (c) EPDM-MA/MMT-Quat after vulcanization (clay loading 10 phr) (reprinted from [164] with permission from Elsevier).

intercalated nanocomposite. However, a mixed intercalated/exfoliated structure is formed in the nanocomposite containing 1 wt.% dihydroxyl modified MMT. More silicate platelets are exfoliated when the MMT is modified with trihydroxyl group. Therefore, the dispersion of silicates in PU changes from an intercalated to an exfoliated structure as the number of hydroxyl functional groups in the modified silicates increases.

2.3. Crystallization

It has been discussed above that the processing conditions have a strong influence of the resulting structures of the polymer–clay nanocomposites. The crystallization kinetics of polymer–clay nanocomposites is important for assessing their microstructure development in melt processing. The process of crystallization can be assessed at a constant temperature, i.e. isothermal crystallization, or at a constant cooling rate, i.e. non-isothermal crystallization. The crystallization of polymers is known to take place non-isothermally during injection molding or extrusion process. This implies that the

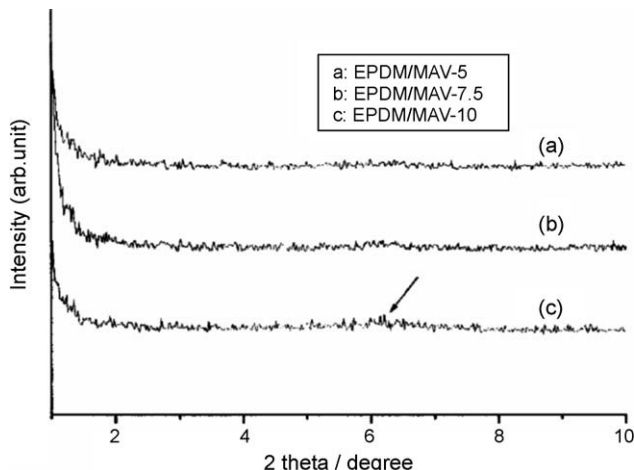


Fig. 46. XRD patterns of EPDM/MAV nanocomposites reinforced with (a) 5, (b) 7.7 and (c) 10 wt.% MAV (reprinted from [163] with permission from Wiley).

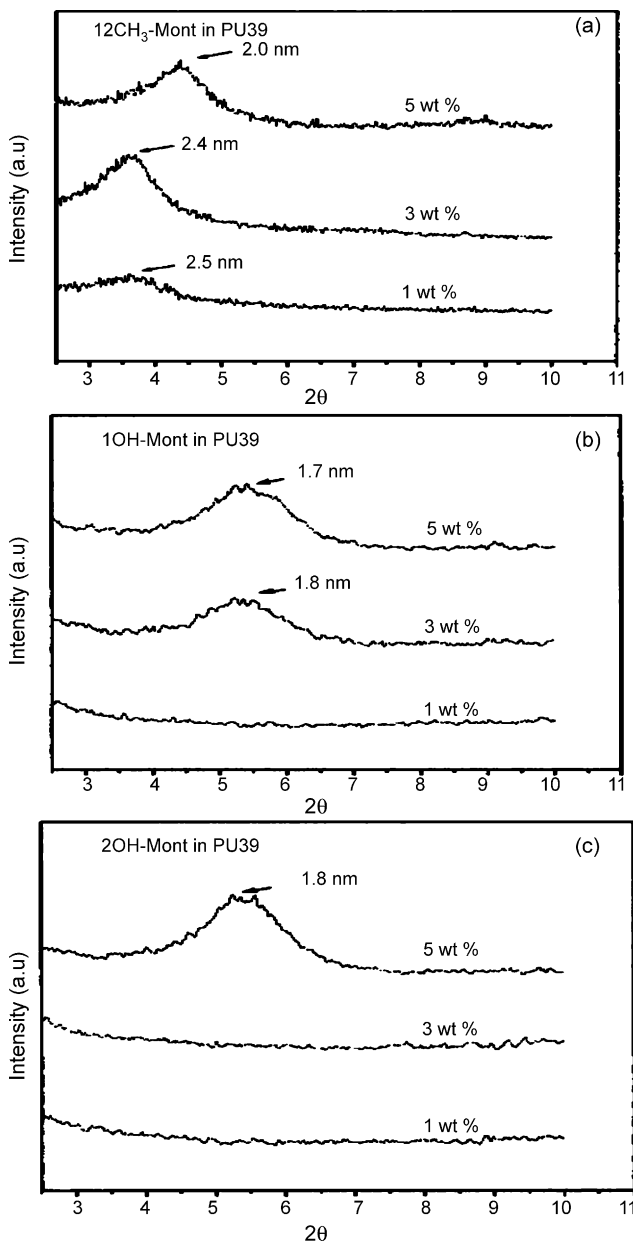


Fig. 47. XRD patterns of PU containing 1, 3 and 5 wt.% MMT modified with (a) alkyl (C_{12}) (b) monohydroxyl (1OH) and (c) dihydroxyl (2OH) groups (reprinted from [159] with permission from The American Chemical Society).

crystallization behavior is influenced by the cooling rate and crystallization rate in polymer processing. An increase in the crystallization rate leads to a decrease in the time of manufacturing cycle, thus enhancing the productivity. The trend in current processing techniques is toward shorter cycle times and high cooling rates [170].

In the polymer–clay nanocomposites, the dispersed clay particles in a polymer matrix always act as a heterogeneous nucleating agent for the spherulites, thereby reducing their sizes considerably. However, such nucleating effect of nanoclays is more pronounced at very low loading levels, ca. 1–5 wt.%. Above these levels, nanoclays may hinder the movement of polymers, thus retarding the

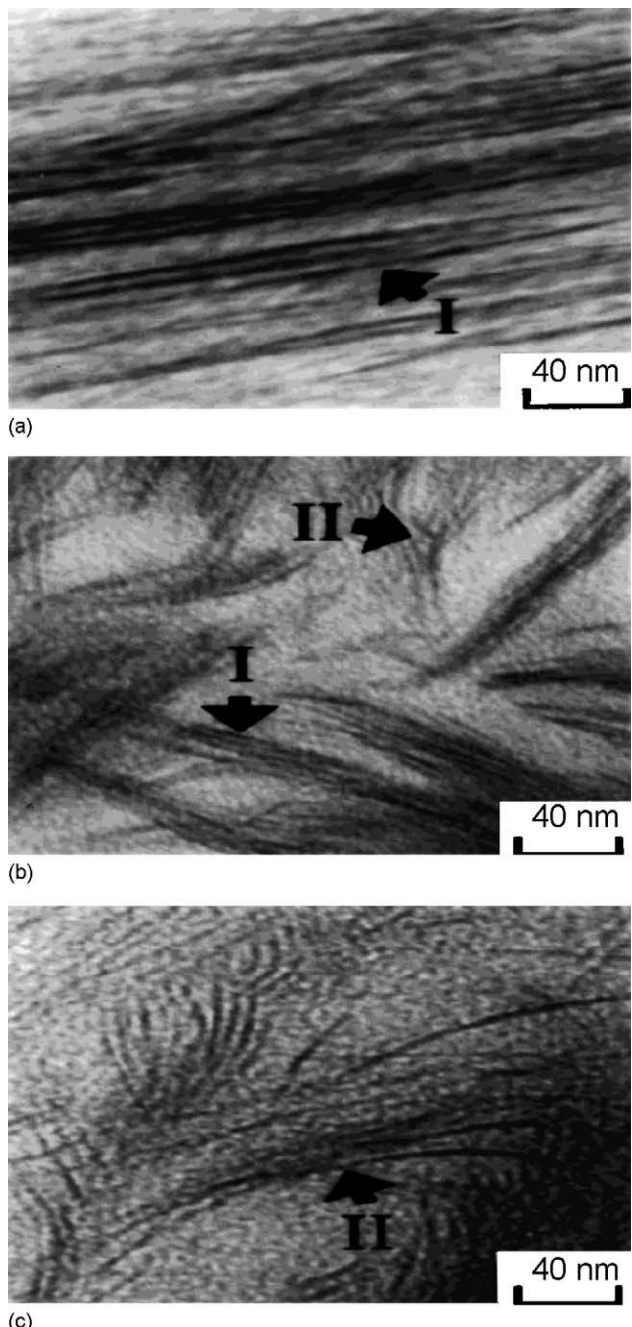


Fig. 48. TEM micrographs of PU containing 1 wt.% MMT modified with (a) monohydroxyl (1OH), (b) dihydroxyl (2OH) and (c) trihydroxyl (3OH) groups. (I) Intercalated structure; (II) exfoliated structure (reprinted from [159] with permission from The American Chemical Society).

crystallization of spherulites. The restricted mobility of the chains imposed by higher clay content would not allow the growth of well developed lamellar crystals [171]. The nanoclays play two roles in the crystallizations, i.e. a nucleating agent to facilitate the crystallization and a physical hindrance to retard the crystallization [172]. For the nanocomposites filled with low loading clay levels, the crystallization of polymers can be either enhanced or inhibited depending on the nature or property of

polymers employed. According to the literature, enhanced crystallization of polymer due to the clay additions includes PA [173,174], PP [175,176], PE [17,177], PET [178], PBT [179,180], syndiotactic PS [181], polyvinylidene fluoride (PVDF) [182–184], etc. In some cases, the introduction of MMT filler hinders the crystallization of poly(ethylene oxide) (PEO). This is evidenced by a decrease of the spherulite growth and crystallization temperature on the basis of optical microscopy and DSC observations [185]. Strawhecker and Manias attributed this behavior to the specific interaction between PEO and Na^+ -MMT, where a strong coordination of PEO to the surface of Na^+ cations promotes non-crystalline PEO conformations. This characteristic PEO/ Na^+ coordination markedly inhibits heterogeneous nucleation of PEO crystallites by the MMT fillers [185].

Apart from enhancing the crystallization rate, nanoclay platelets with large surface areas also enhance polymer–silicate interactions. In this regard, the addition of MMT fillers to polymers can stabilize a metastable phase and induce polymorphism. Typical examples are nanoclays stabilize the γ -phase in polyamides [16,186,187] and the β -phase in PVDF [182–184]. Fig. 49 shows the effect of organoclay additions on the formation of γ -crystalline phase in PA6 [16]. Pure PA6 exhibits a broad peak at $2\theta = \sim 19\text{--}24^\circ$ contributing by α_1 ($2\theta = 20.3^\circ$), α_2 ($2\theta = 23.7^\circ$) and γ ($2\theta = 21.22^\circ$) forms of PA6. The γ -crystalline form is constituted by PA6 molecules having hydrogen bonding in parallel chain arrangement, whereas α -form adopting hydrogen bonding in anti-parallel chain-arrangement [188]. The amide-to-methylene dihedrals are near trans ($164\text{--}168^\circ$) in α -form, whereas they are nearly perpendicular to the peptide plane ($\approx 126^\circ$) in the γ -form. It can be seen from Fig. 49 that the incorporation of MMT content ≥ 2 wt.% leads to huge increase in the intensity of γ -peak. This implies that PA6 crystallizes exclusively in the γ -crystalline phase in the nanocomposites. In other words, the addition of silicate layers disturbs the perfect arrangement of hydrogen bonded sheets of the α -phase, thereby promoting formation of the γ -crystalline structure in PA6. Similarly, Incarnato et al. reported that the presence of silicate layers stabilizes the γ -crystalline phase and promotes the molecular orientation of polymer chains as a consequence of polymer–silicate interaction in a commercial PA6-based copolymer (copolyamide) [187].

Giannelis and coworkers have recently reported on the remarkable enhancement in the toughness of PVDF filled with organoclay (Cloisite[®] 30B) [183]. They attributed this behavior to behavior to the structural and morphological changes induced by the organoMMT particles. XRD and Fourier-transform infrared (FTIR) revealed that the MMT particles induce the formation of β -phase in PVDF (Fig. 50). In general, there are five crystalline forms or polymorphs of PVDF, i.e. α , β , γ , δ and ε [189].

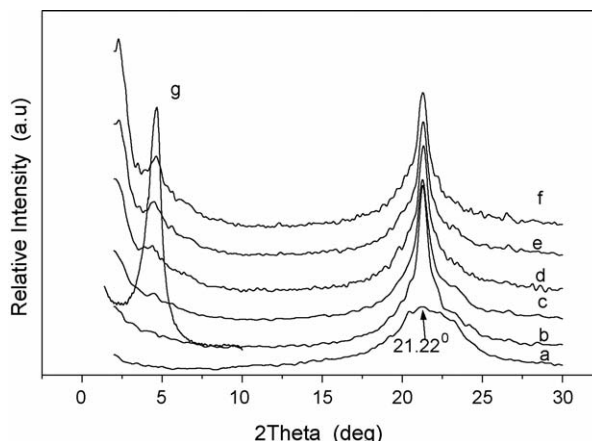


Fig. 49. XRD profiles of pure PA6 and its nanocomposites. (a) Pure PA6, (b) PA6–2%MMT, (c) PA6–4%MMT, (d) PA6–6%MMT, (e) PA6–8%MMT, (f) PA6–10%MMT and (g) OrgMMT [16].

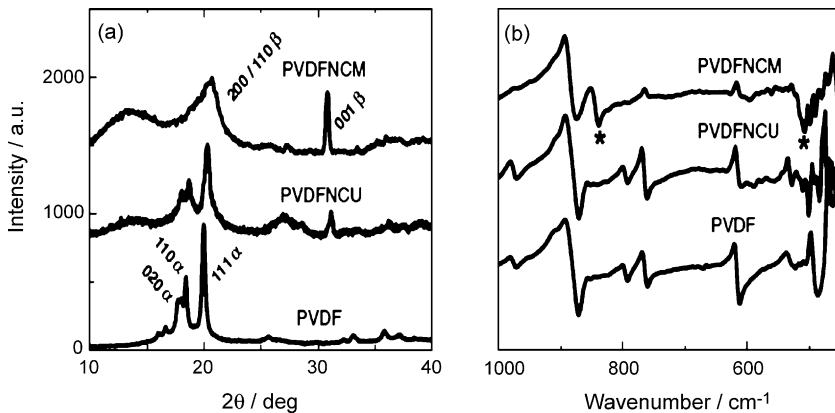


Fig. 50. (a) XRD patterns showing development of the β -phase in PVDF nanocomposites. (b) FTIR curves showing appearance of the β peak (*) in PVDF nanocomposites (reprinted from [183] with permission from Wiley-VCH).

The α -phase is the dominant crystalline form over the β , and γ phases in melt crystallization. From Fig. 50(a), the $(0\ 2\ 0)$, $(1\ 1\ 0)$ and $(1\ 1\ 1)$ reflections of the α -phase can be readily seen in the XRD patterns of pure PVDF, and PVDF filled with unmodified Na^+ -MMT (denoted as PVDFNCU). These α -phase reflections completely disappear and are replaced by the $(2\ 0\ 0/1\ 0\ 0)$ and $(0\ 0\ 1)$ peaks of the β -phase by adding 5 wt.% organoclay to PVDF (PVDFNCM). Similarly, the α -phase peaks at 763 and $796\ \text{cm}^{-1}$ can be readily observed in the FTIR curves of pure PVDF and PVDFNCU. These peaks disappear whilst strong β -phase peaks at 840 and $500\ \text{cm}^{-1}$ are observed in PVDFNCM (Fig. 50(b)). The XRD pattern of PVDFNCM at lower angle regime and TEM image confirm the formation of an intercalated structure. Fig. 51(a–c) is the SEM and POM (inset) micrographs showing the spherulite morphology of pure PVDF and PVDF filled with unmodified MMT and organoMMT, respectively. The presence of large and isotropic spherulites ($\sim 3\ \mu\text{m}$) is reduced considerably by adding MMT fillers. Some isolated β -phase crystallites can be seen in the SEM micrograph (Fig. 51(b)). However, only fiber-like β -phase crystallites (average size $\sim 0.6\ \mu\text{m}$) are formed in PVDFNCM (Fig. 51(c)). This implies that the organoMMT induces a phase transition from ordered α -crystallites to disordered, fiber-like β -phase crystallites. The formation of β -phase is also beneficial to the improvements of stiffness and toughness of PVDF (Fig. 52). The fiber-like β -phase is considered to be much more conductive to plastic flow under applied stress. This could give rise to a more efficient energy-dissipation in the nanocomposites, thereby delaying crack formation. Giannelis and coworkers indicated that the Young's modulus of PVDF increases from 1.3 to 1.8 GPa, while the elongation at break increases from 20 to 140%, giving the organoMMT filled nanocomposite a toughness of $\sim 700\%$ higher than that of the neat polymer [183]. Such concurrent improvements in the stiffness and toughness of semicrystalline PVDF filled with organoclay are considered to be of technological importance. This is because the organoclay additions to most semicrystalline thermoplastics only lead to an enhancement of the stiffness at the expense of their ductility or toughness.

2.4. Mechanical properties

2.4.1. Thermoplastic matrices

Mechanical properties of polymer-clay nanocomposites are highly related to their microstructure which in turn is directly related to the exfoliation and dispersion of clay platelets in the polymer

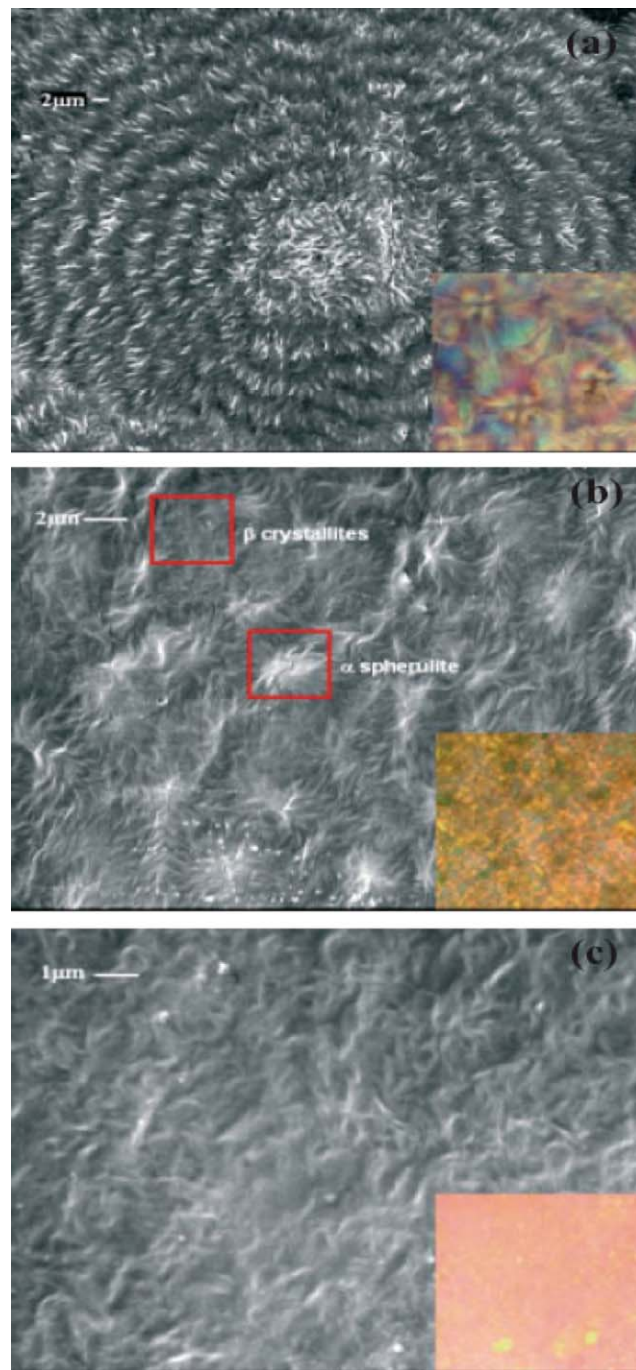


Fig. 51. SEM images with POM insets showing crystal morphology of (a) PVDF, (b) PVDFNCU and (c) PVDFNCM (reprinted from [183] with permission from Wiley-VCH).

matrix. The dispersion of clay platelets in the molten polymer depends on thermal diffusion of polymer molecules in the galleries and on the mechanical shearing action [74]. Thermal diffusion is favored by modifying the clay surfaces with appropriate organic surfactants, rendering the galleries more compatible with the polymer molecules. Good dispersion of the clay platelets in the polymer

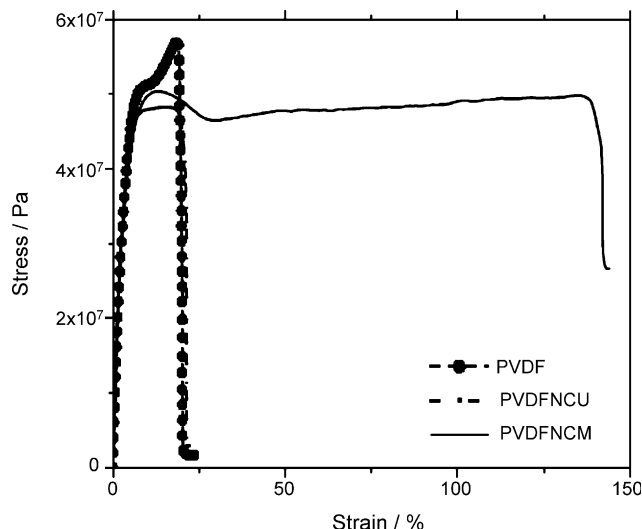


Fig. 52. Stress–strain curves for pure PVDF, PVDFNCU and PVDFNCM showing the dramatic increase in elongation at break for the nanocomposite (reprinted from [183] with permission from Wiley–VCH).

matrix generally yields enhanced Young's modulus, storage modulus and tensile strength, but significantly reduced tensile ductility and impact strength compared to neat polymer [14,190]. Fig. 53(a and b) shows the typical tensile properties of the MA compatibilized PE–organoMMT nanocomposites. Apparently, the tensile strength and modulus tend to increase with increasing clay content. Such an increasing trend is more obvious for the tensile modulus. The increase in the tensile strength is higher at low clay content, indicating that the clay layers are better exfoliated. The reinforcing effect is lower for nanocomposites with higher clay content owing to some clay platelets being partially exfoliated and stacked. From Fig. 53(b), the strain at break decreases with increasing clay content as expected [190]. Osman et al. studied the effect of the degree of exfoliation on tensile properties of the melt-compounded PE–organoMMT [191]. The organic modified cations they used include octadecyltrimethylammonium (C18), dioctadecyldimethylammonium (2C18), methyltriocetyltrimethylammonium (3C18) and tetraoctadecylammonium (4C18). Completely exfoliation was not attained but rather partial exfoliation was achieved without using a compatibilizer. Fig. 54 shows the relative elastic modulus and stress at break of the composite (composite/polymer) as a function of the *d*-spacing of organoclay. Apparently, the modulus steadily increases with increasing *d*-spacing (increasing exfoliation). The relative yield stress and yield strain versus *d*-spacing of the PE–2.8 vol.%MMT are shown in Fig. 55. With increasing exfoliation, a monotonous increase in the yield stress and decrease in the yield strain are observed.

The polymer–clay nanocomposites exhibit extremely large interface polymers due to the confinement of polymer chains within the galleries of clay platelets of large surface area per unit volume. It is considered that the confinement of polymer–clay interactions would affect the local chain dynamics to a certain extent. Since several chemical and physical interactions are governed by surfaces, polymer–clay nanocomposites can have substantially different properties from conventional polymer microcomposites. A key issue arises whether the composite mechanics theories of reinforcement can be applied to explain the mechanical and fracture toughness properties of polymer–clay nanocomposites. Several micromechanical models have been developed to predict the macroscopic behavior of polymer microcomposites. These include Halpin–Tsai, Mori–Tanaka, etc. The models generally include parameters such as the aspect ratio, volume fraction and the orientation of the

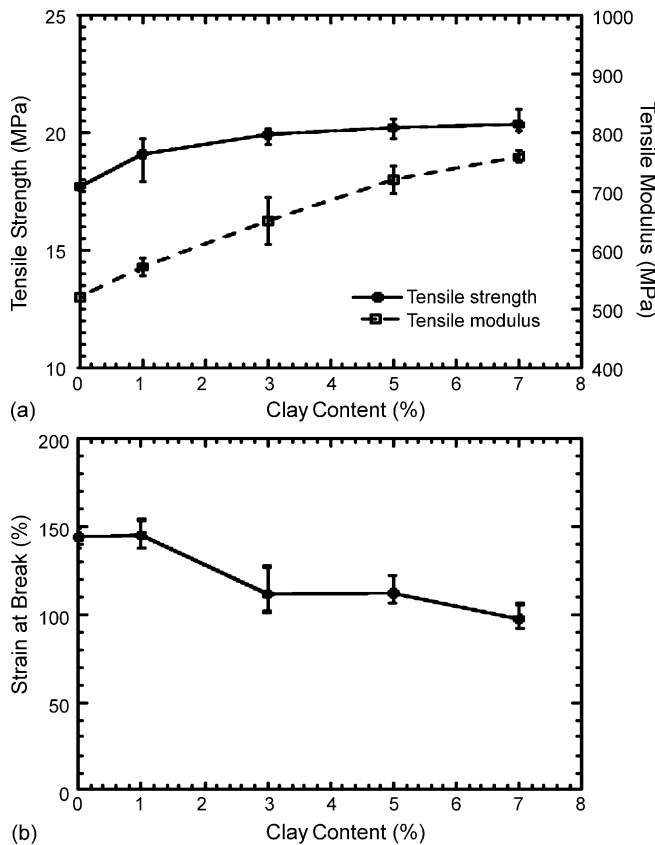


Fig. 53. (a) Tensile modulus and strength and (b) strain at break vs. clay content for the MA compatibilized PE–organoMMT nanocomposites (reprinted from [190] with permission from Elsevier).

reinforcement. It appears that the direct use of micromechanical models for polymer–clay nanocomposites is inappropriate without taking into account the intrinsic hierarchical morphology of intercalated nanoclay with large surface area and expanded gallery spacing.

The elastic modulus of the composite material can be predicted from the Halpin–Tsai equation assuming the fibers are discontinuous and aligned uniaxially [192,193]. The longitudinal elastic modulus of composites E_c , is given by

$$\frac{E_c}{E_m} = \frac{1 + \xi \eta \phi}{1 - \eta \phi} \quad (1)$$

where E_m is the tensile modulus of the matrix and ϕ is the volume fraction of fiber reinforcement. The constants ξ and η are given by

$$\xi = 2 \left(\frac{l}{d} \right) \quad (2)$$

$$\eta = \frac{(E_f/E_m) - 1}{(E_f/E_m) + \xi} \quad (3)$$

where l/d is the aspect ratio (length/diameter) of the reinforcing fibers.

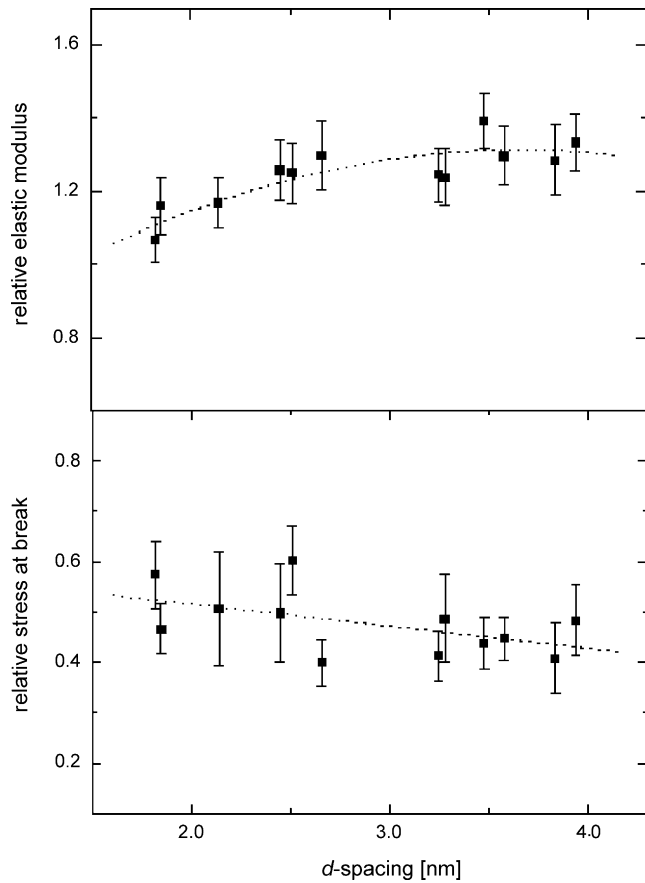


Fig. 54. The relative elastic modulus and stress at break of a PE–2.8 vol.% OrgMMT nanocomposites plotted as a function of their *d*-spacings (reprinted from [191] with permission from Elsevier).

The Mori–Tanaka mean field theory is used to assess the overall properties such as the effective stiffness tensor C^* of the composites. It is based on Elsheby method for estimating stress state in composite reinforced with misfitting inclusions. The composite is assumed to be composed of a continuous matrix and discrete of inclusions of different stiffness. The effective stiffness tensor C^* is given by the following relation [194,195]:

$$C^* = C_1 + V_2 \{(C_2 - C_1)A\} \quad (4)$$

where C_1 is the matrix phase stiffness tensor, C_2 the inclusion stiffness tensor, V_2 the inclusion volume ratio, and A is the concentration tensor.

For a composite consisting of a single, arbitrarily shaped inclusion perfectly bonded inside the matrix, the dilute strain concentration tensor of the effective particle is given by:

$$A^{(\text{dil})} = [I + SC^{-1}(C_2 - C_1)]^{-1} \quad (5)$$

where I is the fourth order unit tensor and S the fourth order Elshelby tensor. As the inclusion volume fraction increases, interaction between the inclusions reduces the accuracy of the dilute approximation. In other words, interactions of the field from other inclusions are expected to influence the evolution of the average fields in the matrix and the reinforcement. The Mori–Tanaka approach includes the effect

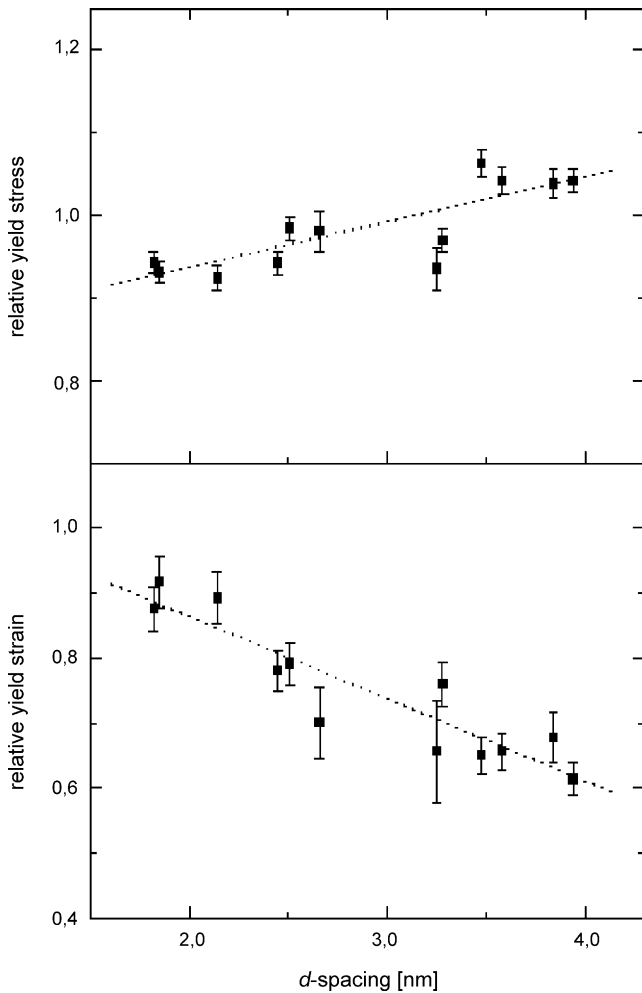


Fig. 55. The relative yield stress and strain of a PE-2.8 vol.% OrgMMT nanocomposites plotted as a function of their d -spacings (reprinted from [191] with permission from Elsevier).

of particle interaction [196]. In this case, A can be expressed as

$$A = A^{(\text{dil})} [V_1 I + V_2 \{A^{(\text{dil})}\}]^{-1} \quad (6)$$

where V_1 is the matrix volume ratio. The Mori–Tanaka model has better predictive capability for fillers with relatively high aspect ratios. Tandon and Weng based on the Mori–Tanaka approach and derived the longitudinal modulus (E_{11}) of the composite reinforced with platelets [197]:

$$\frac{E_{11}}{E_m} = \frac{1}{1 + \phi_f [-2\nu_m A_3 + (1 - \nu_m) A_4 + (1 + \nu_m) A_5 A]/2A} \quad (7)$$

where ν_m is the Poisson's ratio of the matrix, and A , A_3 , A_4 and A_5 are calculated from the matrix and filler properties and the components of the Elshelby tensor.

In polymer–clay nanocomposites, parameters associated with hierarchical morphology of the clay such as the silicate interlayer spacing ($d_{0\ 0\ 1}$), gallery spacing, platelet thickness, etc. should be incorporated into the micromechanics model. Brune and Bicerano [198] developed a micromechanics

model for the prediction of the effects of incomplete exfoliation on the tensile modulus of polymer-clay nanocomposites. They treated the incomplete exfoliate system as composite consisting of a matrix and pseudoparticles which are incompletely exfoliated stacks of individual platelets. They modified the Halpin-Tsai equation for tensile modulus of intercalated (or incompletely exfoliated) nanocomposites as:

$$\frac{E_c}{E_m} = \frac{1 + \xi' \eta' \phi'}{1 - \eta' \phi'} \quad (8)$$

$$\eta' = \frac{E'_r - 1}{E'_r + \xi'} \quad (9)$$

where E'_r the ratio of the modulus of the platelet stack to that of the matrix, ξ' the aspect ratio of the platelet stack and ϕ' is the volume fraction of platelet stacks in the matrix. In each platelet stack, there are N platelet layers, and the platelets within a stack can be at various distances from each other. Assuming t is the thickness of the platelet and s the inter-platelet spacing, then

$$\xi' = \frac{\xi}{\hat{N}} \left[\frac{1}{1 + (1 - 1/\hat{N})(s/t)} \right] \quad (10)$$

$$\phi' = \phi \left(1 + \left(1 - \frac{1}{\hat{N}} \right) \right) \frac{s}{t} \quad (11)$$

$$E'_r = E_r \left[\frac{1}{1 + (1 - 1/\hat{N})(s/t)} \right] + \frac{(1 - 1/\hat{N})(s/t)}{1 + (1 - 1/\hat{N})(s/t)} \quad (12)$$

$$\hat{N} = N + (1 - N) \left(\frac{s}{t} \right) \left(\frac{\phi}{1 - \phi} \right) \quad (13)$$

where E_r is the ratio of the platelet to the matrix modulus. When $N = 1$, there is only one platelet in a stack. In this case, ξ' , ϕ' and E'_r become ξ , ϕ and E_r , thus reverting back to Halpin-Tsai equation. When $s/t = 0$, there is no interplatelet layer, thus ϕ' and E'_r should be equal to ϕ and E_r ; ξ' and ξ should be related by a factor equal to the number of layers. Again, the Halpin-Tsai equation is recovered.

Fig. 56 are the plots showing the ratio of composite modulus to matrix modulus, $f(E)$, as a function of the number N of platelets in a typical stack, for s/t ratios of 1, 2, 3 and 4. The s/t ratio represents the ratio of the distance between the platelets in a stack to the platelet thickness. For well-exfoliated platelets ($N = 1$), $f(E)$ equals the results obtained from the Halpin-Tsai equation. This figure represents combinations of the following parameters: (a) platelet volume fraction (ϕ) values equal to 0.025 and 0.05; (b) platelet aspect ratio (ξ or A_f) values equal to 100 and 200; (c) ratio of platelet to matrix modulus (E_r) equals to 100. Dashed horizontal lines corresponding to the $f(E)$ values calculated for platelets of aspect ratio 1 (cylinders with height = diameter) and 20 (as in conventional unexfoliated fillers). This figure clearly shows the $f(E)$ values tend to decrease as more platelets are incorporated into a stack. Accordingly, incomplete exfoliation has a very significant detrimental

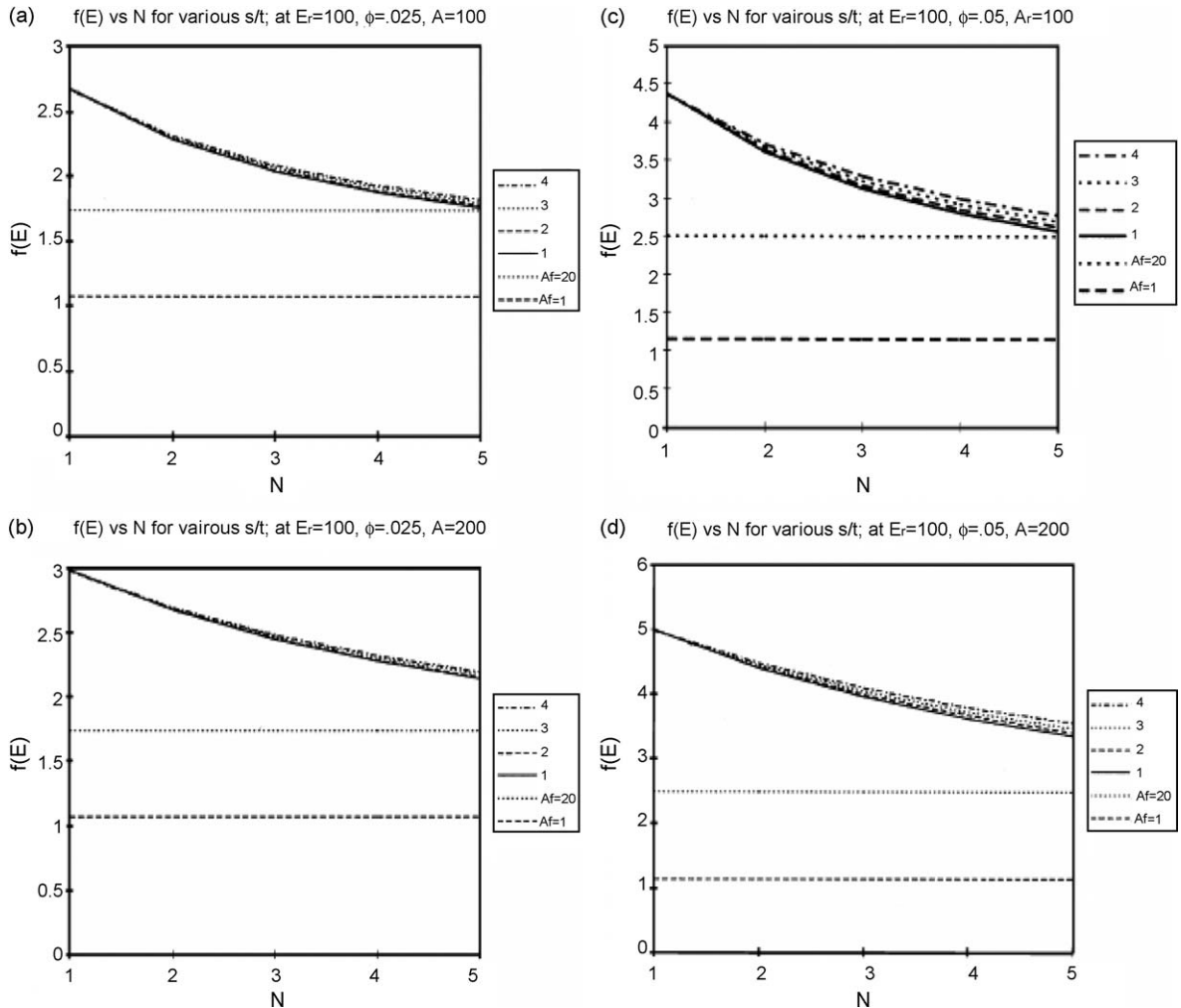


Fig. 56. Ratio of composite modulus to matrix modulus, $f(E)$, as a function of number N of platelets in a typical stack, for s/t ratios of 1, 2, 3 and 4. (a) Platelet volume fraction (ϕ) values equal to 0.025 and 0.05; (b) platelet aspect ratio (ξ or A_f) values equal to 100 and 200; (c) ratio of platelet to matrix modulus (E_r) equals to 100. Dashed horizontal lines corresponding to the $f(E)$ values calculated for platelets of aspect ratio 1 (cylinders with height = diameter) and 20 (as in conventional unexfoliated fillers) (reprinted from [198] with permission from Elsevier).

effect on the reinforcement efficiency [198]. It should be noted that no comparison with experimental data was made to verify the validity of their model.

Recently, Fornes and Paul performed simple calculations on the aspect ratio (l/t) of MMT platelets of the PA6–organoclay nanocomposites [199]. The clay was modified with bis(hydroxyethyl)-(methyl)-rapeseed quaternary ammonium $[(HE)_2M_1R_1]$. Rapeseed is natural product composed predominantly unsaturated C₂₂ alkyl chains (45%). They assumed that the composite consists of a matrix and stacks of clay platelet sheets. For the particle thickness (t) determination, they incorporated several parameters such as the silicate interlayer spacing ($d_{0\ 0\ 1}$), number of platelets per particle and the thickness of a MMT platelet (Fig. 57). From this, the number average particle thickness was determined to be 1.61 nm. On the basis of image analysis from TEM micrographs of nanocomposites, they determined the number average particle length to be 91 nm. This resulted in an

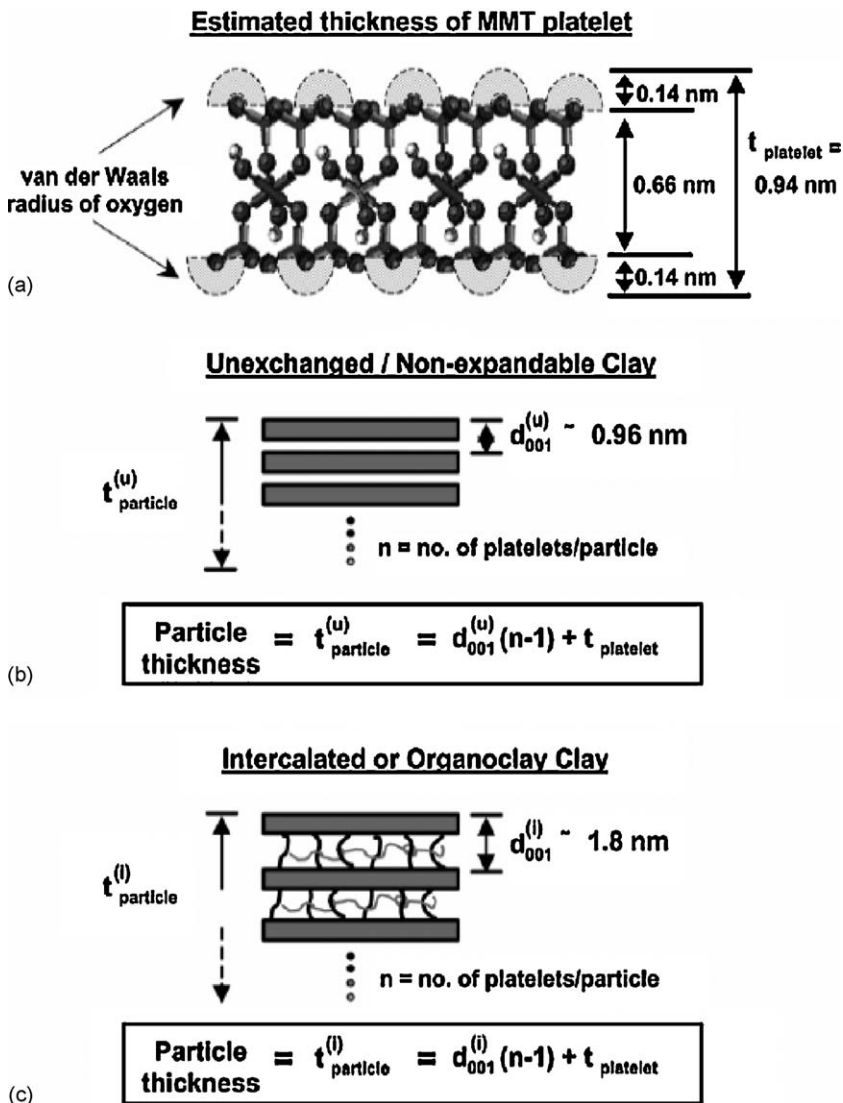


Fig. 57. Schematic diagrams showing the determination of particle thickness of (a) an individual MMT platelet, (b) an unexchanged or non-expandable clay stack, and (c) an organoclay stack intercalated with surfactant and polymer (reprinted from [199] with permission from Elsevier).

aspect ratio of 57. For an exfoliated structure, the platelets were completely delaminated and dispersed independently in the matrix with a thickness of 0.94 nm. Thus an aspect ratio of 97 was determined for an exfoliated structure. They substituted such particle aspect ratio values together with the stiffness of MMT (178 GPa) and PA6 (2.75 GPa) into Halpin–Tsai equation. The theoretical predicted values and experimental results for the stiffness of nanocomposites are shown in Fig. 58(a). Apparently, the experimental results are lower than those of the theoretical prediction, particularly for $l/t = 97$. For the purposes of comparison, elastic modulus prediction from the Mori–Tanaka approach is also shown. The Mori–Tanaka model agrees reasonably with the experimental results at $l/t = 97$ but underpredicts the experimental data at $l/t = 57$. To assess the effect of incompletely exfoliation, the volume fraction ϕ , and stiffness of particle are also modified and evaluated according to geometrical

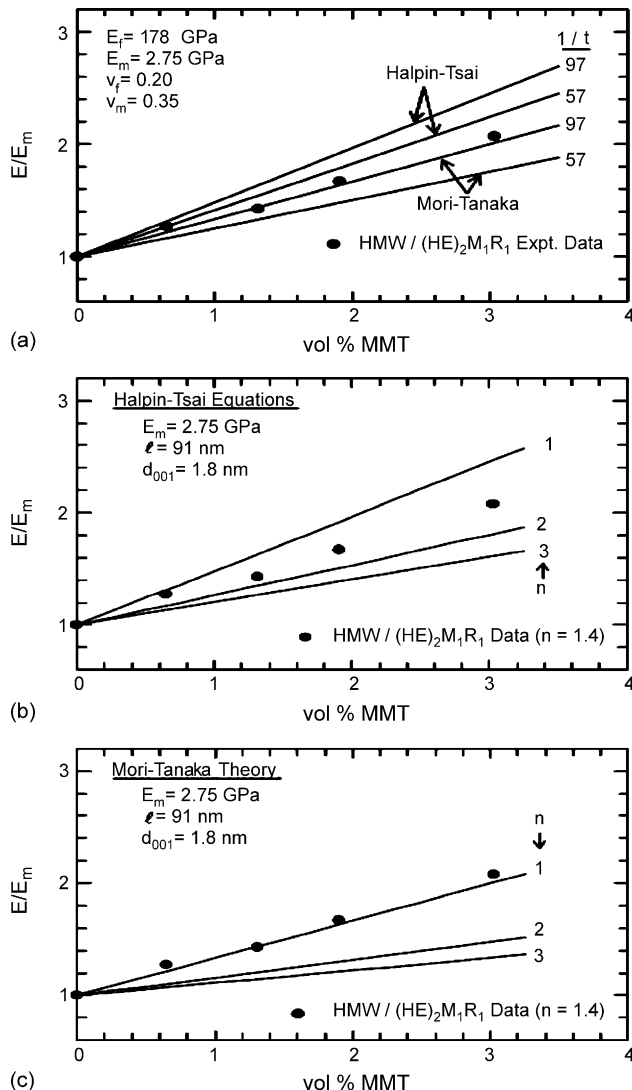


Fig. 58. Experimental and theoretical stiffness data for HMW PA6 nanocomposites; model predictions are based on unidirectional reinforcement of (a) pure MMT having a filler modulus of 178 GPa and aspect ratio of 57 (experimentally determined number average value), and 97, corresponding to complete exfoliation, and (b and c) stacks of clay intercalated with polymer having one or more platelets per stack (reprinted from [199] with permission from Elsevier).

feature and the dispersion of MMT particles in PA6 as shown in Fig. 57. Stack properties were based on the experimental data, i.e. the stacks are 91 nm in length, have a repeat spacing of 1.8 nm, and each individual platelet has a modulus of 178 GPa. They then substituted these values into Halpin-Tsai equation (Fig. 58(b)). The experimental data fall between the Halpin-Tsai curves corresponding to 1 and 2 platelets per stack, which is very close to the experimentally determined value of 1.4. The experimental data agrees reasonably with Mori-Tanaka model when $n = 1$; this corresponds to a completely exfoliated structure (Fig. 58(c)). It is also evident from both theoretical models predicted that increasing the number of platelets per stack results in a decrease of the stiffness of nanocomposite. The composite theories satisfactorily capture the stiffness behavior of the nanocomposites [199].

More recently, Weon and Sue attempted to correlate the experimental stiffness data with those predicted from the Halpin–Tsai and Mori–Tanaka models by incorporating the effective filler structural parameters into the simulations [200]. The thickness of effective filler (Fig. 57) can be expressed as [199]:

$$t_{\text{eff}} = (n - 1)d_{001} + t_p. \quad (14)$$

The effective filler aspect ratio (α_{eff}), volume fraction (ϕ_{eff}) and modulus (E_f^{eff}) can be written as [201]:

$$\alpha_{\text{eff}} = \frac{l}{t_{\text{eff}}} = \frac{l}{(n - 1)d_{001} + t_p} \quad (15)$$

$$\phi_{\text{eff}} = \frac{\psi_{\text{eff}}[(n - 1)d_{001} + t_p]}{nt_p} \frac{\rho_m}{\rho_f} \quad (16)$$

$$E_f^{\text{eff}} = \frac{nt_p E_f}{[(n - 1)d_{001} + t_p]} \quad (17)$$

where ψ_{eff} is effective filler weight fraction, and ρ_f and ρ_m are the densities of the filler and matrix, respectively. From these, the influence of filler aspect ratio on the modulus improvement of the PA6–MMT nanocomposite is shown in Fig. 59. Similarly, the Mori–Tanaka model yields better agreement with the experimental data of PA6–MMT nanocomposite reinforced with the higher aspect ratio fillers.

As mentioned above, the tensile behavior clay reinforced semicrystalline thermoplastics (e.g. PA6, PP, PE, etc.) is characterized by enhanced strength and stiffness but poor elongation at break compared to neat polymers. However, the impact strength of nanocomposites also tends to decrease with increasing clay content [13]. The exceptional case is semi crystalline PVDF reinforced with organoclay due to the formation of tough β -phase as mentioned previously [183]. Despite the fact that the organoclay induces the γ -phase in PA6, however, this phase does not enhance the toughness of

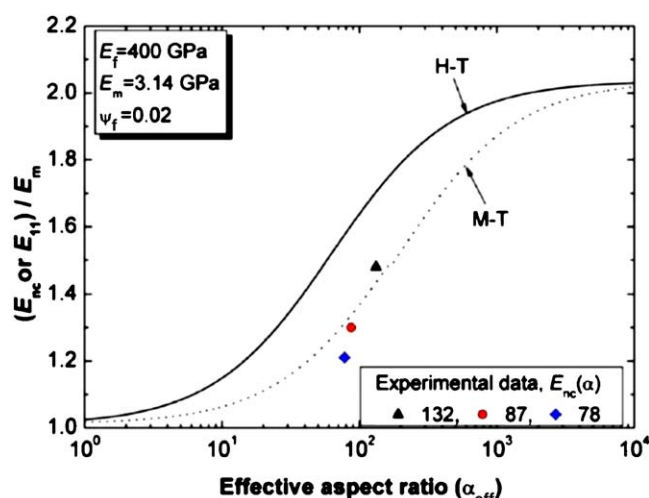


Fig. 59. Effective filler-based model predictions of the Halpin–Tsai and Mori–Tanaka models for the PA6–MMT nanocomposite (reprinted from [200] with permission from Elsevier).

polyamides. It is considered that the incorporation of impact modifiers can improve the tensile ductility and impact strength of the semi crystalline thermoplastic–clay nanocomposites [17,202,203]. Akapeddi reported that the notched Izod and drop-weight strengths of PA6–MMT nanocomposites could be improved dramatically via blending with suitable elastomer particles. However, he did not disclose the type of impact modifier used [202]. Tjong and coworkers reported that the additions of maleated styrene–ethylene butylenes–styrene (SEBS-g-MA) particles to PP–vermiculite and PA6–vermiculite nanocomposites led to significant improvement in their impact strength and tensile ductility [17,203]. For the (PA6–SEBS-g-MA)–vermiculite nanocomposites, the MA group grafted to SEBS reacts with the amine end groups on the PA6 during melt-compounding, thereby improving the compatibility between these phases and resulting in finer dispersion of elastomer particles. SEBS particles have been incorporated previously into the matrices the conventional polymer microcomposites for toughening purposes. For example, Tjong et al. studied the mechanical behavior and fracture toughness of glass fiber-reinforced PP/SEBS hybrids. They reported that the glass fiber reinforced composites toughened with SEBS elastomers exhibit good tensile properties, improved impact strength and fracture toughness. Matrix yielding and fiber pullout are responsible for the toughening mechanism of such hybrids [204]. Fig. 60 shows the variation of the impact strength of (PP–SEBS-g-MA)–vermiculite nanocomposites with the SEBS content. Although the impact strength is improved due to the SEBS additions, but the tensile stiffness and strength of nanocomposites appear to deteriorate considerably.

Very recently, Mai and coworkers used TEM to study the dispersion of clay platelets in PA6 associated with the SEBS additions. They prepared (PA6,6–SEBS-g-MA)–organoclay nanocomposites by varying the blending sequence [205]. Four different blending sequences were adopted: (a) PA6,6, organoclay (Cloisite[®] 30B) and SEBS-g-MA were blended simultaneously (N1 route), (b) PA6,6 and maleated SEBS were blended first, and the mixture was then mixed with organoclay (N2 route), (c) PA66 and organoclay were blended first, and the mixture was then compounded with maleated SEBS (N3 route), and (d) maleated SEBS and organoclay were blended first, and the mixture was blended with PA6,6 later (N4 route). Fig. 61 shows the TEM micrographs of N1–N4 samples. It can be seen that the SEBS particles are finely dispersed in the PA6,6 matrix of N1 and N2 samples. A similar percentage distribution of exfoliated platelets is observed in both the PA6,6 and elastomer phases. However, most of the clay platelets is present in the PA6,6 matrix of N3 sample. In sharp contrast, most of the clay platelets is dispersed in the SEBS-g-MA phase of N4. Owing to the

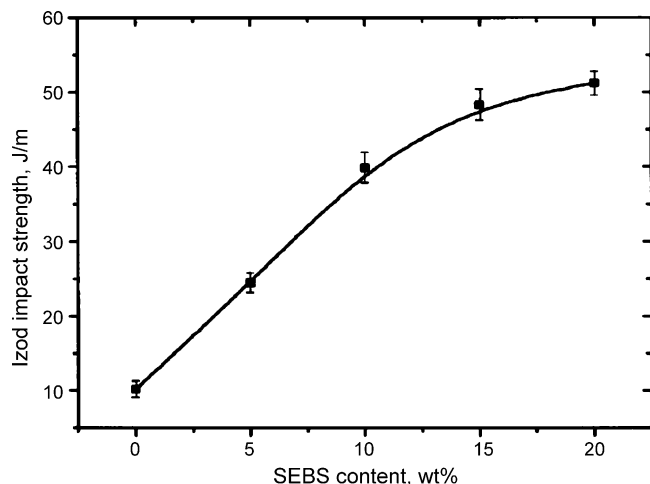


Fig. 60. Izod impact strength vs. maleated SEBS content for the (PP–SEBS-g-MA)–vermiculite nanocomposites [203].

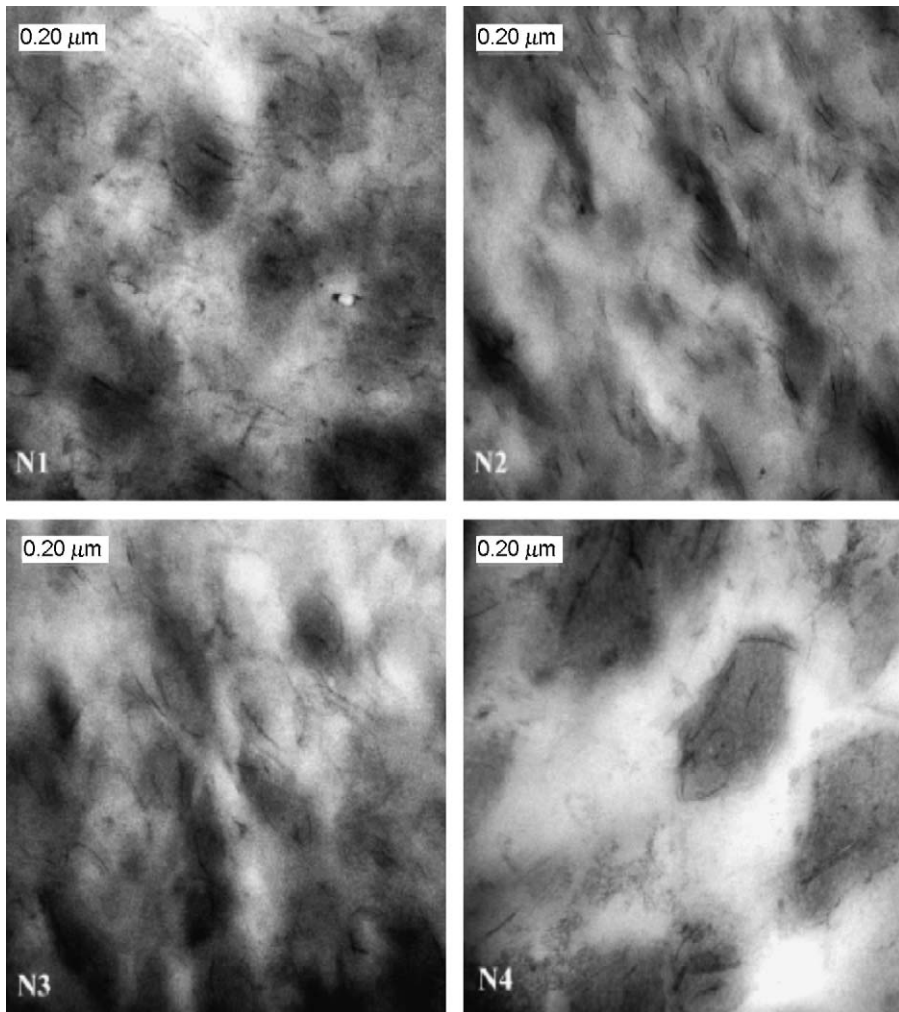


Fig. 61. TEM micrographs of (PA6,6-SEBS-g-MA)-organoclay nanocomposites prepared by different blending sequences, N1, N2, N3 and N4 (reprinted from [205] with permission from Elsevier).

difference in the dispersion of clay platelets in these phases, N3 exhibits the highest impact strength, flexural modulus and strength, and N4 has the lowest impact strength among all the specimens investigated. The lowest impact strength of N4 is attributed to the organoclay stiffens the SEBS-g-MA phase, thereby reducing the cavitation ability of the elastomer particles. The mechanical properties of nanocomposites are summarized in Table 3. Mai and coworkers concluded that the best microstructure for toughness and other mechanical properties is to have the maximum percentage of exfoliated organoclay in the PA6,6 matrix rather than to have it in the dispersed SEBS-g-MA phase. Ahn and Paul [206] reported that the PA6-organomMT composites could be toughened by maleated ethylene/propylene rubber (EPR-g-MA) particles. The nanocomposites were prepared by mixing of PA6 and Cloisite 30B in a twin screw extruder and then blending the extrudates with the rubber in a single screw extruder. In this sequence, the MMT platelets were dispersed in the PA6 matrix. This processing sequence is similar to the N3 route of Mai and coworkers [205]. Impact results indicated that the addition of rubber leads to a shift of ductile-to-brittle transition of the rubber-toughened PA6-MMT nanocomposites to lower temperatures, thereby improving the toughness of nanocomposites.

Table 3

Mechanical properties along with their compositions of ternary nanocomposites (N1–N4) prepared by different blending sequences (reprinted from [205] with permission from Elsevier)

Blending sequence	Notched impact strength (J/m)	Flexural modulus (GPa)	Flexural strength (MPa)
Neat PA66	62.5 ± 3.3	2.95 ± 0.05	129.0 ± 3.8
PA66/organoclay (80/5)	23.9 ± 6.0	3.79 ± 0.10	66.8 ± 5.5
PA66/SEBS-g-MA (80/15)	303.4 ± 56.2	2.06 ± 0.15	92.4 ± 7.3
N1, (PA66 + SEBS-g-MA + organoclay) (80/15/5)	102.9 ± 10.6	2.54 ± 0.11	98.5 ± 2.5
N2, (PA66 + SEBS-g-MA) + organoclay (80/15/5)	78.9 ± 3.9	2.53 ± 0.07	96.8 ± 2.7
N3, (PA66 + organoclay) + SEBS-g-MA (80/5/15)	117.6 ± 16.3	2.65 ± 0.03	100.7 ± 0.2
N4, PA66 + (SEBS-g-MA + organoclay) (80/15/5)	65.9 ± 3.9	2.63 ± 0.02	98.9 ± 1.1

Polymer composites are generally used as structural materials in various engineering applications. They are frequently deformed at high strain rates under impact loading during their service lives. Generally, polymers that are ductile under low strain rate loading can behave in a brittle manner at high strain rates owing to their strain rate sensitivity. Notched Charpy and Izod tests are commonly employed to evaluate the fracture behavior of polymers and composites due to their simplicity. Instrumented drop weight impact test is particularly attractive because it is capable of testing materials at a wide range of velocities. However; the impact strength is not a good parameter to characterize the toughness of ductile polymers because the samples are frequently not fully broken. In addition, impact energy is not a parameter used by the engineers for designing purposes. In this regard, fracture toughness parameters such as K_{IC} , J_{IC} are used to characterize fracture characteristics of the polymers and composites.

In recent years, the essential work of fracture (EWF) concept has been successfully employed to characterize the fracture toughness of ductile polymers and tough composites due to its simplicity over conventional J -integral analysis [207–213]. The EWF approach involves the determination of the total fracture energy of several samples having different initial ligament length. Generally, crack-tip deformation dictates the fracture behavior of polymer nanocomposites. The fracture toughness is related to the localized deformation associated with the extension of a precrack formed in the specimen with a razor blade. Fig. 52(a) shows typical configuration of a double-edge notched tension (DENT) specimen for tensile loading measurement. The work spent to create new surfaces is referred to as the essential work of fracture (W_e). The non-essential work (W_p) involves the plastic work in the volume surrounding the region of a precrack. In other words, W_e is the work required to fracture the polymer in its process zone and surface related. W_p is the energy consumed by various deformation mechanisms in the plastic zone and volume related. Thus, the total fracture work (W_f) can be written as:

$$W_f = W_e + W_p \quad (18)$$

$$W_f = w_e LB + \beta w_p L^2 B \quad (19)$$

$$w_f = \frac{W_f}{LB} = w_e + \beta w_p L \quad (20)$$

where w_f is the specific total fracture work, w_e and w_p are the specific essential fracture work and specific plastic work, respectively; L is the ligament length, B sample thickness, and β is a shape factor

of the plastic zone. An important prerequisite of EWF approach is that crack propagates only after the ligament has fully yielded and the plastic zone is scaled with the square of the ligament length. The validity range of ligament L under plane-stress condition is given by

$$(3-5)B \leq L \leq \min\left(\frac{W}{3}, 2r_p\right) \quad (21)$$

where W is the width of the specimen and $2r_p$ is the size of plastic zone. Apparently, EWF concept is a simple method that consists of testing specimens with different ligament lengths, recording the area under the load–displacement curve (W_f), plotting the w_f versus L diagram and evaluating the best fit linear regression line.

Mai and coworkers [214] have extended the EWF concept to impact testing of polymer blends. Martinatti and Ricco [215] reported that it is valid to apply the EWF method to assess high rate fracture toughness of polypropylene-based materials. Since then, some research has been conducted on the

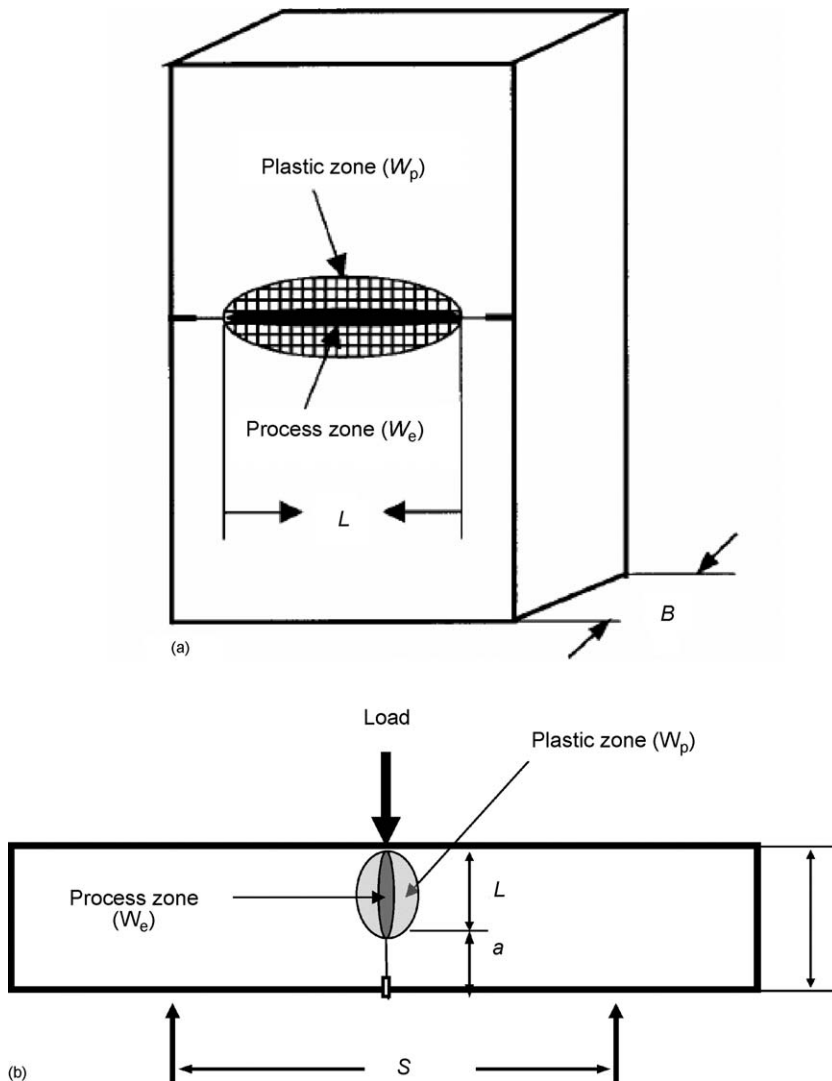


Fig. 62. Geometry of (a) DENT and (b) SENB specimens.

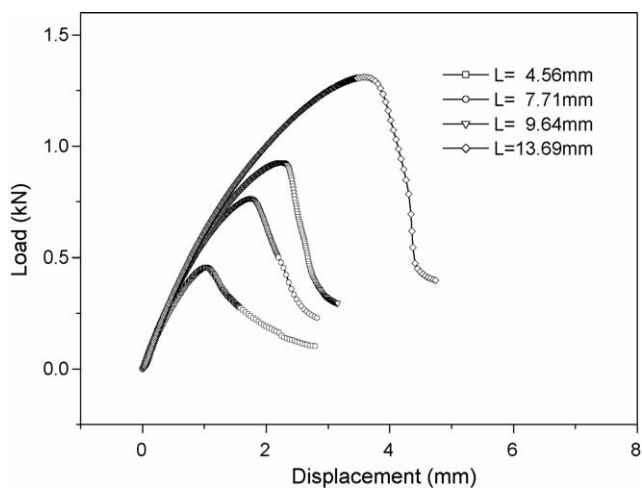


Fig. 63. Load–displacement curve for the (PP–5%SEBS-g-MA)–4%MMT specimen subjected to tensile EWF test [221].

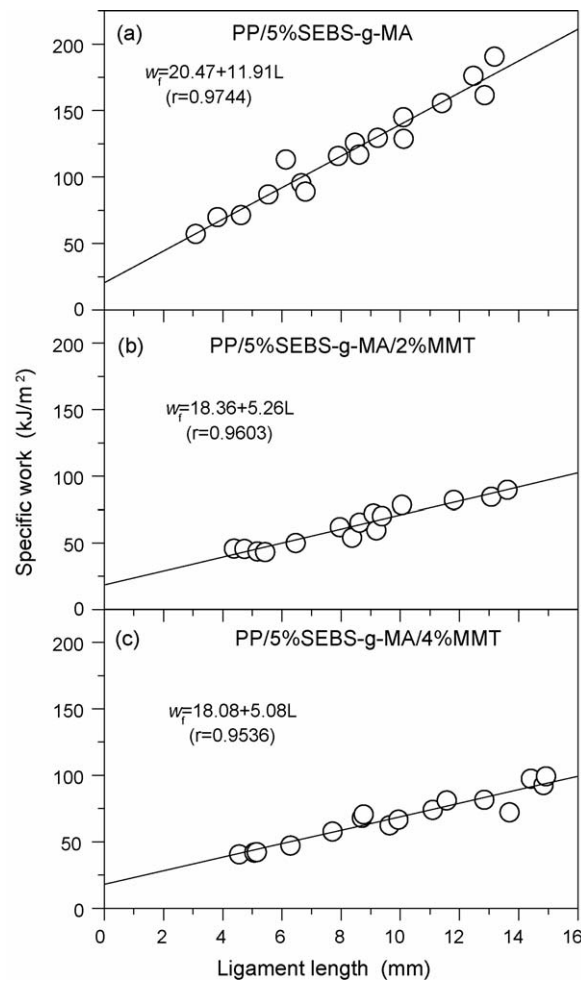


Fig. 64. The w_f vs. L plots for (a) PP–(5%SEBS-g-MA), (b) (PP–5%SEBS-gMA)–2% MMT and (c) (PP–5%SEBS-g-MA)–4%MMT [211].

validity of impact EWF concept to characterize the toughness of polymer blends [216,217] and polymer composites [218–220]. In general, single-edge notched bending (SENB) specimen is used for impact EWF measurement (Fig. 62(b)).

Fig. 63 shows typical load–displacement curves for the (PP–5%SEBS-g-MA)–4% MMT nanocomposite with different ligament lengths. It is apparent that gross yielding and necking occur in this nanocomposite during tensile deformation process. On the other hand, pure PP exhibits typical brittle fracture behavior under employed EWF testing conditions. In this case, the EWF concept cannot be used to determine the fracture toughness of pure PP. The load–displacement curves of PP would show the gross-yielding and necking behavior with the addition of 5% SEBS-g-MA. Fig. 64(a–c) show the plots of w_f versus ligament length for PP–(5%SEBS-g-MA), (PP–5%SEBS-g-MA)–2%MMT and (PP–5%SEBS-g-MA)–4%MMT samples. Good linear regression with a high correlation coefficient between the data of w_f and L is obtained for these samples. The PP–(5%SEBS-g-MA) blend exhibits high w_e value (20.47 kJ/m^2) as expected. It is apparent that the additions of 2 and 4 wt.% OrgMMT to the PP–(5%SEBS-g-MA) blend leads to a decrease of the fracture toughness from 20.47 to $\sim 18 \text{ kJ/m}^2$ [221].

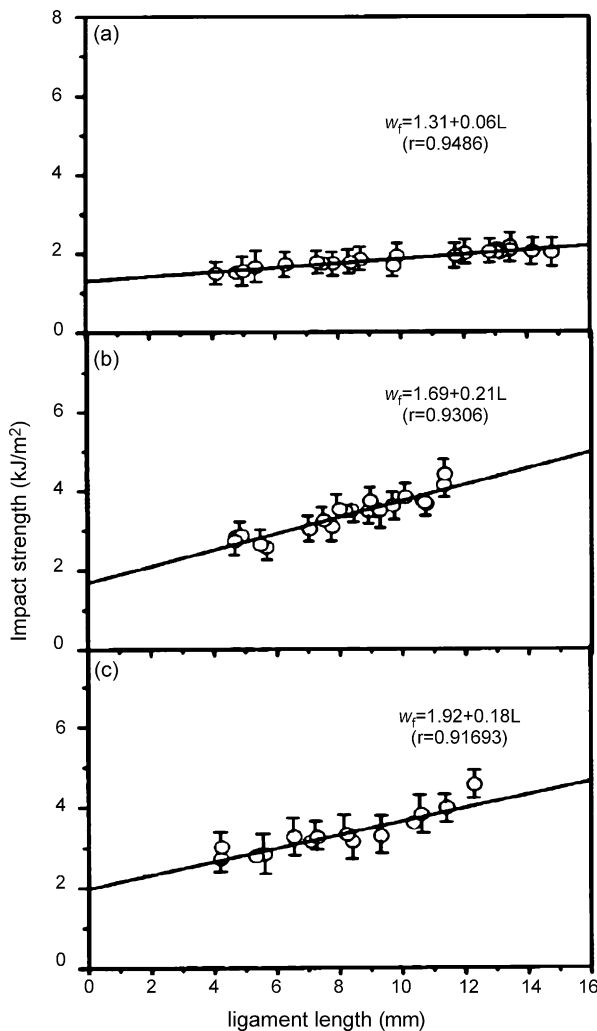


Fig. 65. Impact fracture energy vs. ligament length for (a) (PA6–10%SEBS-g-MA)–4%MMT, (b) (PA6–15%SEBS-g-MA)–4%MMT and (c) (PA6–20%SEBS-g-MA)–4%MMT nanocomposites [222].

Fig. 65(a–c) show the variation of impact fracture energy with ligament length for the (PA6–10%SEBS-g-MA)–4%MMT, (PA6–15%SEBS-g-MA)–4%MMT and (PA6–20%SEBS-g-MA)–4%MMT nanocomposites [222]. The essential fracture work of nanocomposites tends to increase with increasing elastomer content. For the (PA6–10%SEBS-g-MA)–4%MMT nanocomposite, linear regression plot almost yields a horizontal line. The non-essential plastic work (w_p) is extremely small, i.e. 0.06 kJ m^{-2} . This implies that the nanocomposites dissipate very little energy in the outer plastic region of the crack zone. The constraining effect of MMT platelets prevented the matrix to yield or deform under impact loading. Larger positive slopes are attained by increasing the elastomer content to 15% and above (Fig. 65(b and c)). This means that the maleated SEBS can further enhances the energy absorption of crack propagation, thereby enhancing the fracture toughness of the nanocomposites. Therefore, the impact fracture surface of the (PA6–15%SEBS-g-MA)–4%MMT nanocomposite reveals obvious cavitation and shear yielding of the matrix (Fig. 66). The SEBS-g-MA additions are beneficial to increase the impact fracture toughness of the PA6–4%MMT nanocomposite.

In the case of glassy thermoplastics, the clay additions generally enhance their mechanical modulus and strength [52,98,100,139]. However, the tensile ductility and impact toughness of nanocomposites depend on the extent of clay dispersion in the amorphous thermoplastics. For melt-mixed nanocomposites, the clays tend to disperse as intercalated tactoids and agglomerated platelets in the polymer matrices [52,139]. However, a highly exfoliated structure is formed in the nanocomposites prepared via insitu polymerization [100]. Fig. 67 shows the effects of clay loading levels on the tensile and impact behavior of melt-blended PMMA–Cloisite 30B nanocomposites. It can be seen that the stiffness of the nanocomposites increases with increasing clay content at the expenses of their impact strength and tensile ductility [52]. A decreasing trend in the toughness with increasing filler content is related to the poor dispersion of silicate platelets in the PMMA matrix [52]. A similar behavior is observed in the melt-blended PC–MMT nanocomposites [153]. On the other hand, the impact strength of the PMMA–MMT nanocomposites porepared by bulk polymerization tends to increase with increasing clay content (Fig. 68). Highly exfoliated nanocomposites are formed as evidenced by the XRD and TEM

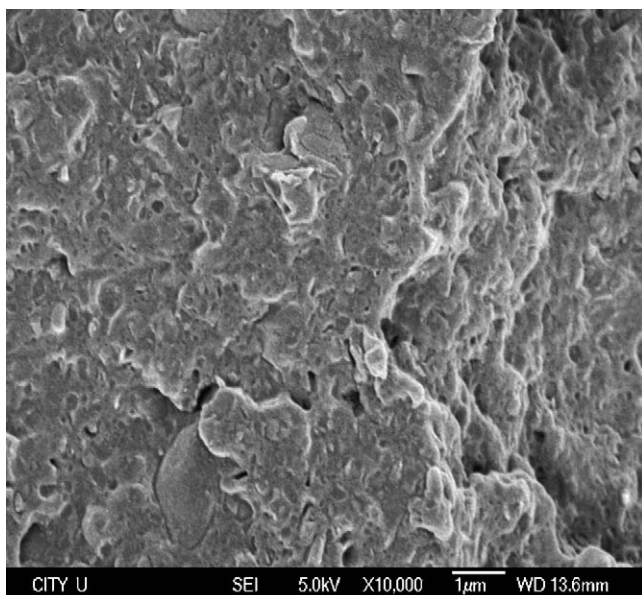


Fig. 66. SEM micrograph showing the fracture surface morphology of (85%PA6–15%SEBS-g-MA)–4%MMT nanocomposite with a ligament length of 5 mm after impact EWF measurement [222].

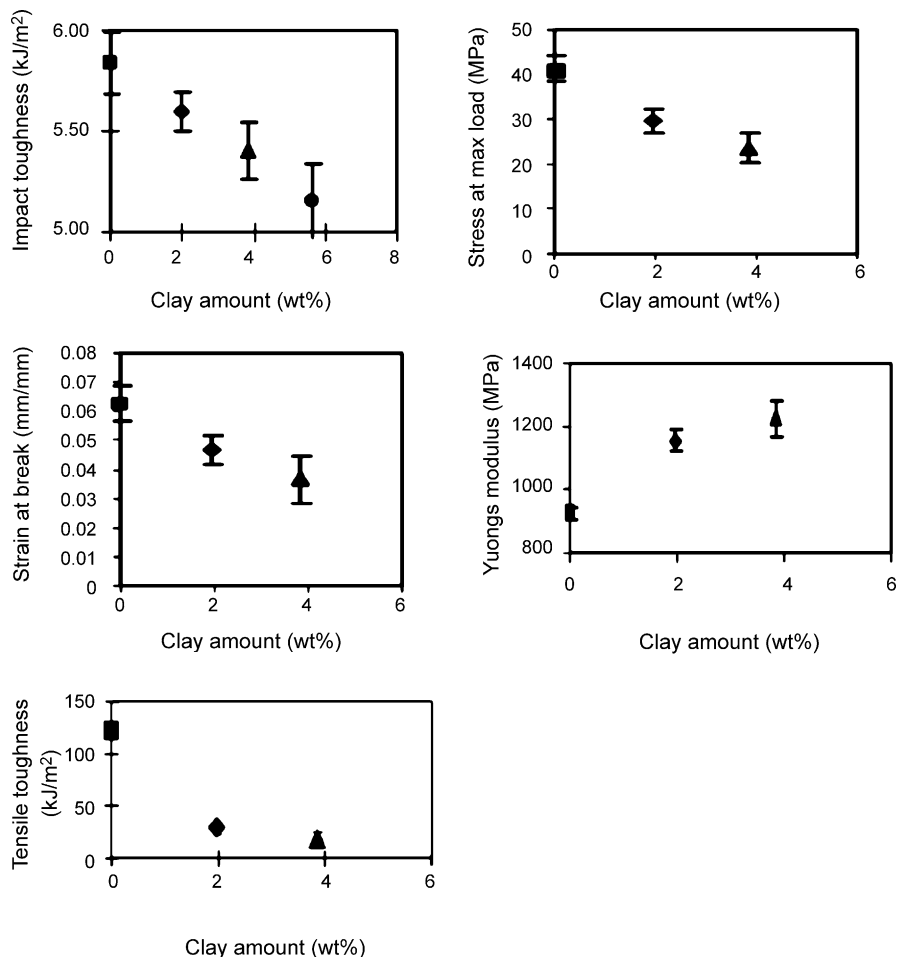


Fig. 67. Effect of clay loading on mechanical properties of melt-blended PMMA–clay nanocomposites (reprinted from [52] with permission from Elsevier).

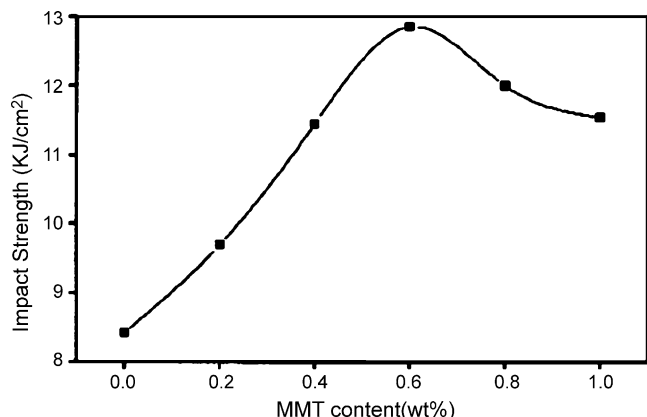


Fig. 68. Effect of clay loading on Charpy impact strength of in situ polymerized PMMA–MMT nanocomposites (reprinted from [100] with permission from Wiley).

examinations [100]. It is considered that the formation of highly exfoliated clay platelets in brittle PMMA matrix can effectively deflect the microcrack propagation, thereby improving its toughness. This behavior has been observed in brittle epoxy nanocomposites having highly exfoliated clay platelets [223].

2.4.2. Epoxy matrices

Epoxy resins are generally known to exhibit a relatively low toughness. The toughness can be improved by the addition of rigid particles such as glass beads [224,225] and elastomers [226,227]. The increase in fracture toughness of a brittle material due to the addition of a rigid particle has been interpreted in terms of the interactions between the moving crack front and the rigid phase [228] and matrix shear yielding mechanism [225]. For the epoxy–clay nanocomposites, the tensile modulus and strength are enhanced associated with the clay additions. Becker et al. [229] studied the morphology and mechanical behavior of DGEBA and other high-functionality epoxy resins such as trifunctional triglycidyl *p*-amino phenol (TGAP) and tetrafunctional tetraglycidyldiaminodiphenylmethane (TGDDM) reinforced with octadecyl ammonium ion-modified MMT.

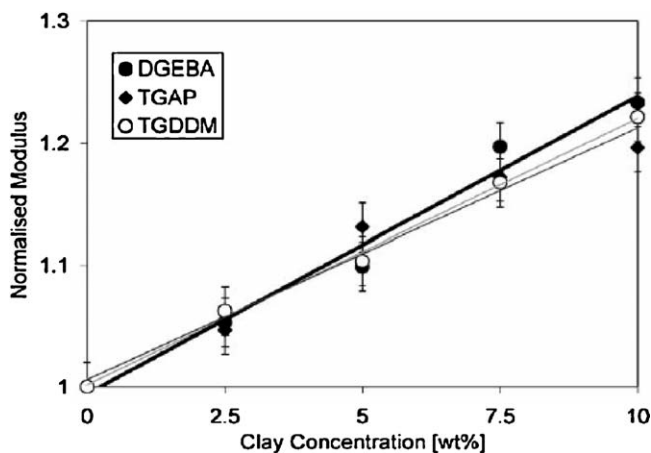
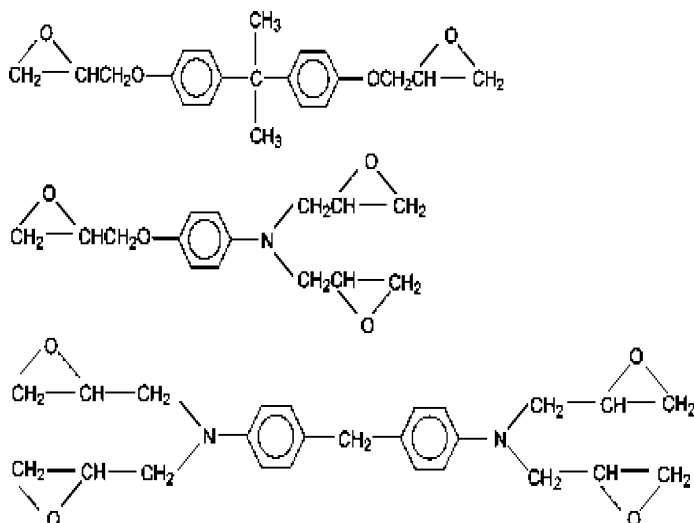


Fig. 69. Normalized modulus with clay content for different epoxy resins containing 0–10% clay. All resins were cured with diethyltoluene diamine (DETDA) (reprinted from [229] with permission from Elsevier).

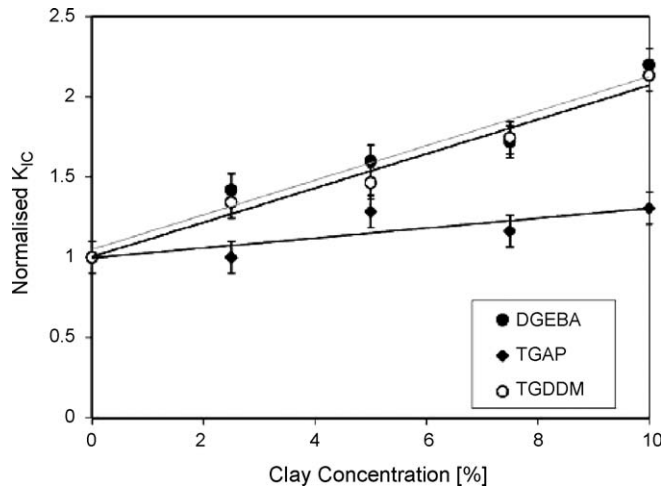


Fig. 70. Normalized fracture toughness with clay content for different epoxy resins containing 0–10% clay. All resins were cured with diethyltoluene diamine (DETDA) (reprinted from [229] with permission from Elsevier).

They reported that improvement in stiffness of the high-functionality epoxy resins is comparable with those for the bifunctional DGEBA system (Fig. 69). All epoxy-clay nanocomposite systems exhibit a mixed intercalated/exfoliated structure on the basis of XRD and atomic force microscopic (AFM) examinations. Furthermore, the fracture toughness (K_{IC}) of nanocomposites tends to increase linearly with increasing clay content. The improvement is much more significant for DGEBA and TGDDM-based nanocomposites (Fig. 70). Therefore, it seems that silicate filler additions are beneficial to improve the stiffness and toughness of epoxy resins. Pluart et al. also reported similar improvements in the tensile strength and stiffness as well as fracture toughness of DGEBA resin resulting from clay additions [230].

More recently, Yee and coworkers attempted to elucidate the mechanisms responsible for improving the fracture toughness of epoxy-clay nanocomposites. They prepared two nanocomposites having

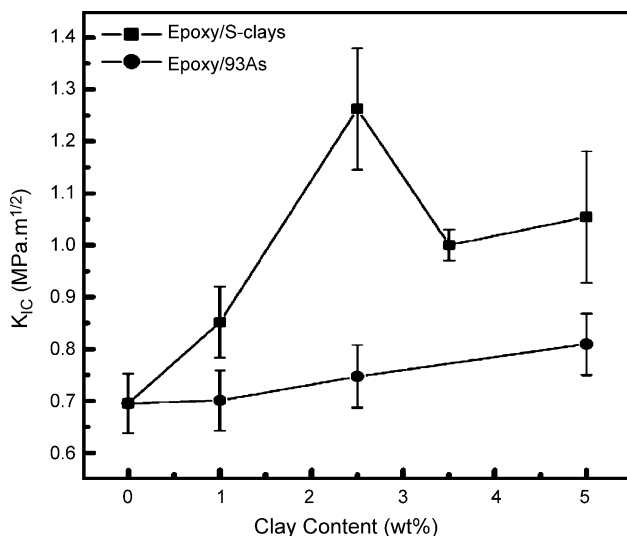


Fig. 71. Fracture toughness of intercalated (Epoxy/93As) and highly exfoliated (Epoxy/S-clays) nanocomposites as a function of clay concentration (reprinted from [223] with permission from The American Chemical Society).

intercalated and highly exfoliated structures, respectively [223]. The highly exfoliated nanocomposite was prepared by a ‘slurry-compounding’ process as mentioned previously. Fig. 71 shows the variation of fracture toughness with clay content for these nanocomposites. The fracture toughness of exfoliated nanocomposite is considerably higher than that of pure epoxy resin, and reaches an apparent maximum at 2.5 wt.% clay. This figure also reveals that the fracture toughness of an intercalated epoxy–clay nanocomposite also improves slowly with increasing clay content. The SEM micrographs can provide useful information regarding the fracture behavior of the nanocomposites. Typical SEM micrographs showing the fracture features of crack initiation and fast-fracture regions of the highly exfoliated nanocomposite are shown in Fig. 72. Rough fracture surfaces having step-like appearances can be readily seen. Under higher magnification, many microcracks (indicated by the arrows) are observed located between these steps. This implies that the nanoclay platelets are very effective to deflect the propagation of microcracks into tortuous paths. In contrast, the fracture surface of the neat epoxy is very smooth as expected. Further TEM observation reveals that the microvoids are initiated inside the clay platelets or along the matrix–clay interface via delamination. Subsequently, microcracks form upon further loading. The microdeformation and toughening mechanisms of the highly exfoliated nanocomposite are

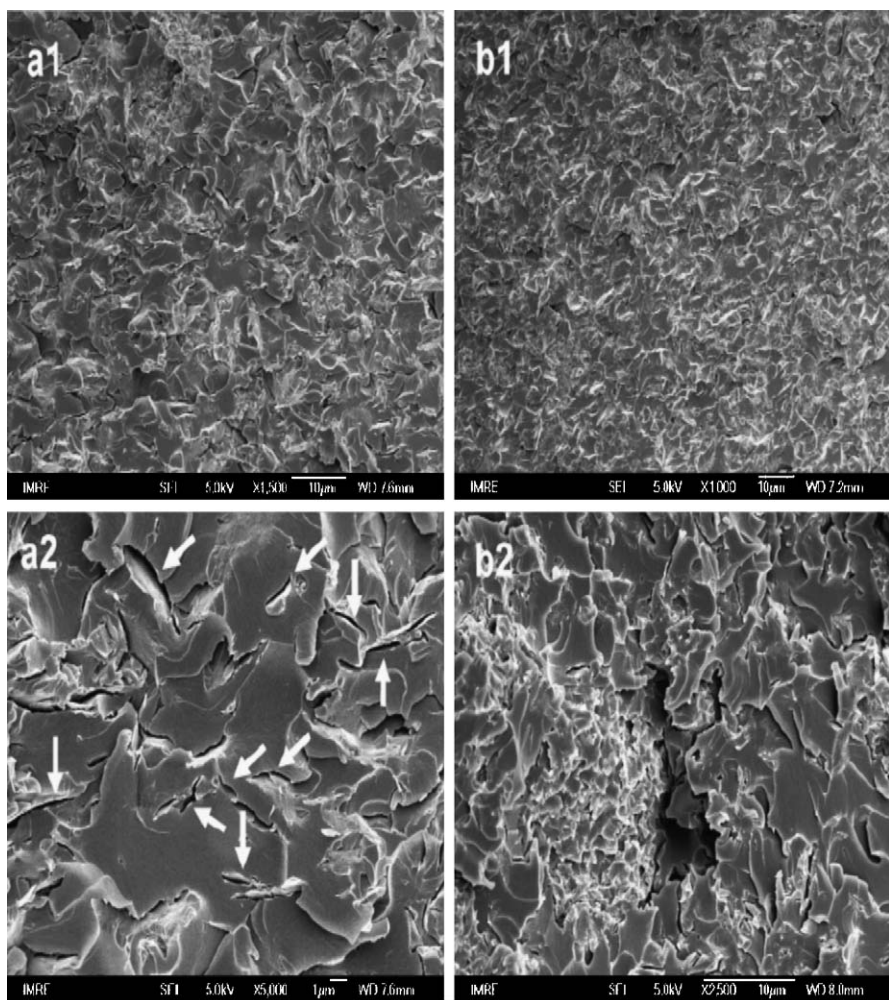


Fig. 72. SEM micrographs of the fracture surface of highly exfoliated Epoxy/S-clay2.5 showing crack initiation (a1 and a2) and fast fracture (b1 and b2) regions (reprinted from [223] with permission from The American Chemical Society).

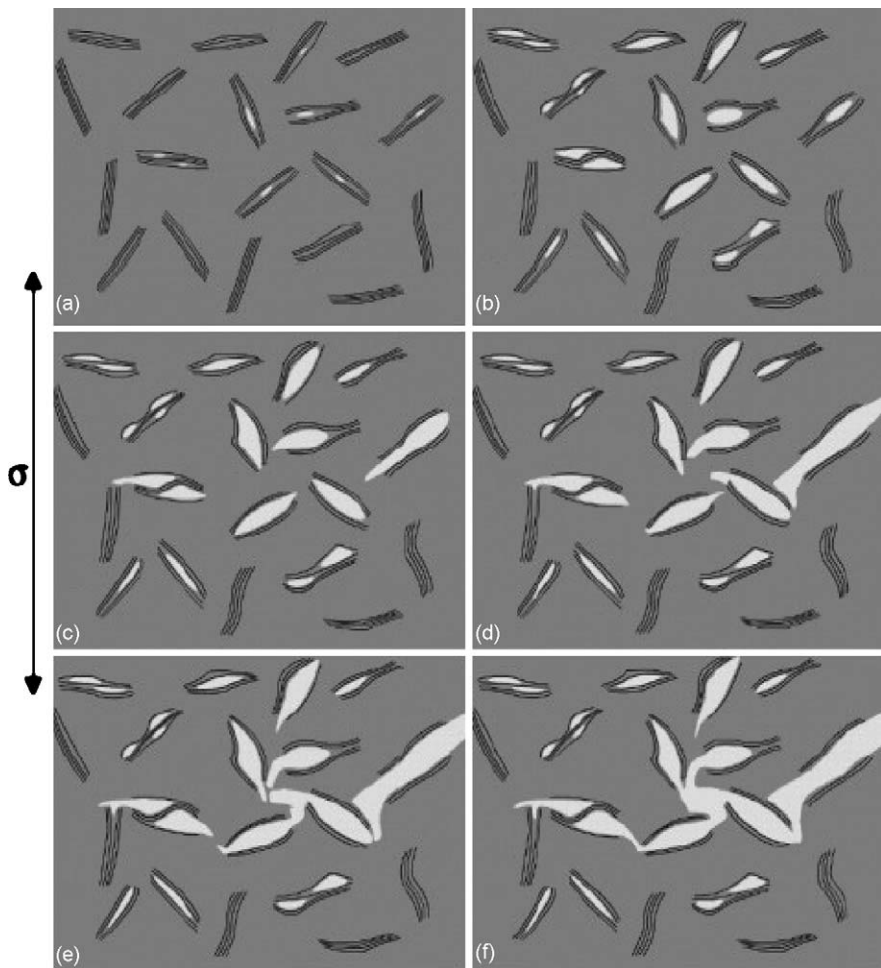


Fig. 73. (a–f) Illustration of the crack initiation and propagation processes in the epoxy/S-clay nanocomposites (reprinted from [223] with permission from The American Chemical Society).

summarized by schematic diagrams as shown in Fig. 73(a–f). Apparently, the microcracks initiated between the clay layers (Fig. 73(a and b)) tend to link together each other and extend into the matrix as the strain increases (Fig. 73(c and d)). The clay platelets then deflect the crack propagation into tortuous paths (Fig. 73(e) and (f)), thereby improving the toughness of brittle epoxy resin. On the other hand, the microcracks developed in the intercalated epoxy–clay nanocomposite tend to break the clay aggregates upon loading. The clay plalets are poorly dispersed and formed aggregates in the intercalated material. Thus, the clay aggregates are less effective to deflect the microcrack propagation. The findings of Yee's research group are in direct contradiction to those of other researchers [231–233]. Zilg et al. indicated that intercalated clay promotes toughness whereas exfoliated clay platelets mainly improve stiffness of the polymer matrix, due to energy-absorbing shearing of intercalated clay layers [231]. Miyagawa and Drzal [232] reported that the exfoliated epoxy–clay materials exhibits higher storage modulus but lower fracture toughness compared to their intercalated counterparts as the clay loading increases (Fig. 74(a and b)). They attributed the improved fracture toughness of intercalated nanocomposites to the effectiveness of crack deflection by stacked clay platelets. The individual clay platelets of exfoliated nanocomposites can break easily, thus are not strong enough to prevent the crack from propagating.

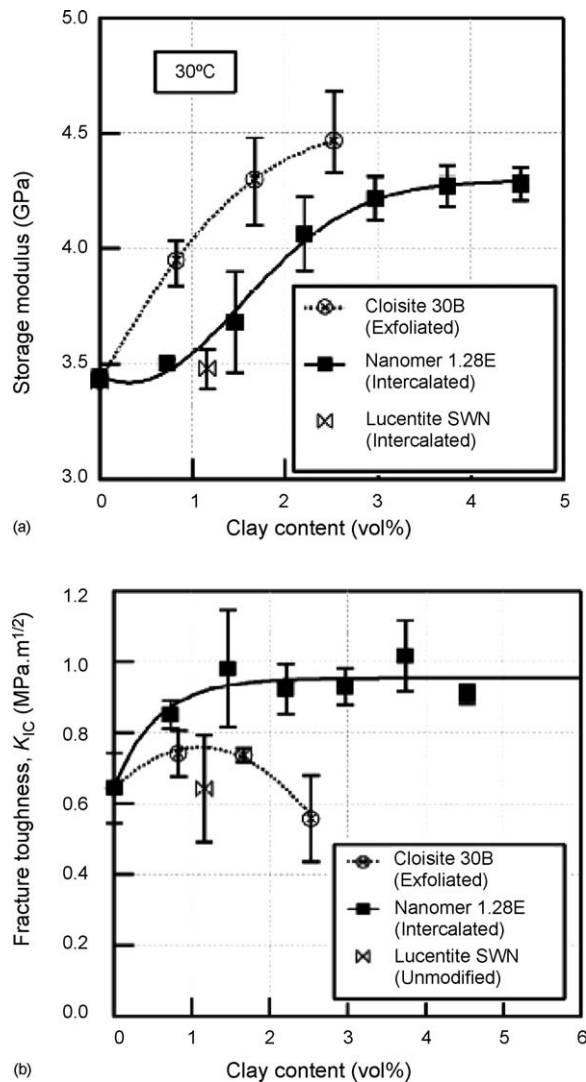


Fig. 74. (a) Storage modulus at 30 °C and (b) fracture toughness vs. clay content for epoxy–clay nanocomposites cured with anhydride agent (reprinted from [232] with permission from VSP Publishers).

2.4.3. Elastomer matrices

Comparing to the thermoplastics, the additions of clay to elastomers generally lead to improvements in toughness, tensile stiffness and strength. It is believed that the clay platelets act as effective reinforcing and toughening agents for the elastomers. For example, LeBaron and Pinnavaia indicated that the organoclay additions improve the tensile stiffness, strength and elongation at break of a silicone rubber (PDMS) significantly. The 5 wt.% organoclay addition to PDMS improves the elongation at break from 11 to 31%, corresponding to about 181% enhancement compared to pure silicone rubber [168]. Song et al. reported that the introduction of clay can improve the tensile strength and elongation of PU. The tensile strength increased by 120% and the elongation at break increased by 100% [161]. Tien and Wei also demonstrated that the addition of only 1 wt.% MMT modified with tris(hydroxymethyl)aminomethane yields a 34% increase in Young's modulus, a 1.7-fold increase in tensile strength and a 1.3-fold increase in the elongation at break, compared to those of the pristine PU [159].

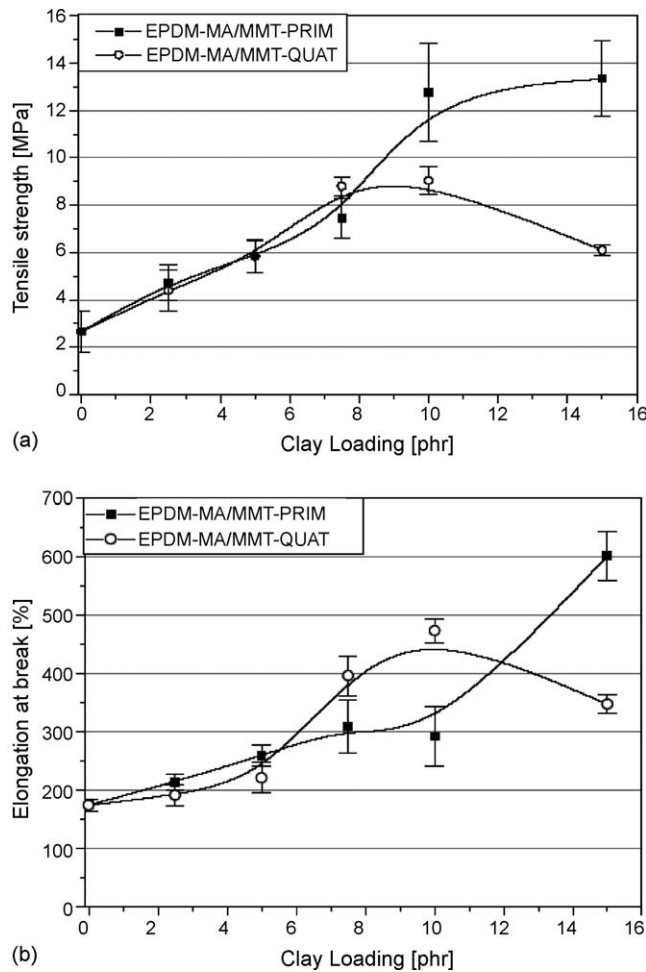


Fig. 75. (a) Tensile strength and (b) elongation at break vs. clay loading for the EPDM-MA/MMT-Prim and EPDM-MA/MMT-Quat nanocomposites (reprinted from [164] with permission from Elsevier).

The effect of clay additions in EPDM is now considered. Fig. 75(a and b) show the variations of tensile strength and elongation at break for the EPDM-MA/MMT-Prim and EPDM-MA/MMT-Quat nanocomposites [164]. The tensile strength and elongation at break for the EPDM-MA/MMT-Prim nanocomposite tend to increase with increasing clay loading. For the EPDM-MA/MMT-Quat nanocomposite, the tensile strength and elongation reach a maximum at ~10 phr organoclay content. Beyond 10 phr clay content, their values reduce considerably as a result of the clay

Table 4
Mechanical properties of the melt-blended EPDM–MAV nanocomposites (reprinted from [163] with permission from Wiley)

	MAV content (%)	Tensile strength (MPa)	Elongation at break (%)	Young's modulus (MPa)
EPDM	0	2.905	2165	1.851
EPDM–MAV(5)	5	4.361	2494	1.942
EPDM–MAV(7.5)	7.5	5.998	2225	2.063
EPDM–MAV(10)	10	3.703	1978	2.473

agglomeration. The beneficial effects of clay additions on the tensile strength and ductility can also be observed in better exfoliated EPDM-MAV nanocomposites prepared by melt-compounding. In this case, the MA functional groups grafted to the vermiculite clays act as the swelling and compatibilizing agents (Table 4).

3. Nanoparticle reinforcement

Conventional polymer microcomposites generally require large amounts of fillers (≥ 20 vol.%) to achieve enhanced stiffness and glass transition temperature [234]. The fabrication of cheaper microcomposites is made feasible by replacing the volume of expensive resins with low cost fillers. However, these gains are usually offset by losses in ductility and toughness. Large amount of filler additions would also detrimentally affect the processability of the polymers and increasing the wear rate of processing facilities. In contrast, nanoparticles such as calcium carbonate and silica filled polymers possess significant improvements in both rigidity and toughness. For example, Qu et al. found that dramatic improvements in the tensile stress (~13%), strain-to-failure (~138%), Young's modulus (~17%) and impact strength (78%) with only 5 wt.% silica nanoparticle addition to PA6 [51]. Similarly, Mai and coworkers reported that optimal properties such as Young's modulus, tensile yield strength, elongation-at-break and Charpy notched impact strength were obtained in PVC by adding only 5 wt.% CaCO_3 nanoparticles with an average size of 44 nm [235]. Furthermore, nanoparticles are also preferred when transparency and surface smoothness are the priorities. PMMA-silica nanocomposites showed no reduction in transparency even reinforced at relatively high loadings unlike the micrometer-sized filled systems [236,237]. Schadler and coworkers studied the glass transition behavior of PS-silica films and composites [238]. They demonstrated that the thermophysical properties of polymer nanocomposites are quantitatively equivalent to the well-documented case of planar polymer films. This means that the changes in glass-transition temperature with decreasing interparticle spacing for the PS-silica nanocomposites are quantitatively equivalent to the corresponding thin film data [238].

The presence of inorganic nanoparticles with large surface areas would alter the local stress state of surrounding matrix. Thus, the polymer chain dynamics in the vicinity of particles is substantially different from that observed in the bulk due to specific polymer-nanoparticle interaction. It is well established that the addition of lower modulus elastomer particles to polymer materials leads to enhancement of both ductility and toughness at the expenses of tensile strength and stiffness. It is believed that cavitation of elastomer particles or debonding at the interface between particles and matrix is responsible for such improvement. The cavities relieve the triaxial stress state present in the matrix, inhibiting bulk polymer void formation and subsequent crazing, and promoting shear yielding of the polymer matrix [239–241]. Rigid inorganic nanoparticles are considered to be more effective than elastomers as they increase both stiffness and toughness of the polymers. It is considered that cavitation of nanoparticles and its successive shear yielding contribute to an improvement in the toughness of nanocomposites.

3.1. Synthesis

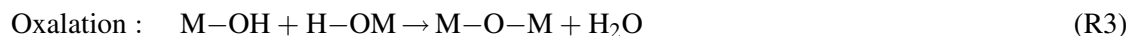
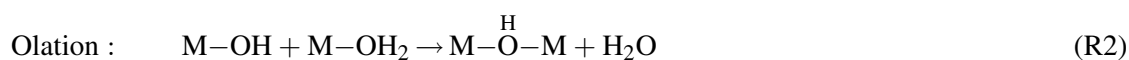
Polymer-particle nanocomposites can be prepared via melt blending, sol-gel and in situ polymerization routes. Melt compounding is an effective route for mass production of nanocomposites with cost effectiveness. However, homogeneous dispersion of nanoparticles is difficult to achieve during melt compounding because the nanoparticles with large surface energy tend to agglomerate.

Proper controlling of the processing parameters and surface treatment of nanoparticles are needed to obtain homogeneous dispersion [242]. Better dispersion of nanoparticles in a polymer matrix can be obtained by means of the sol–gel and in situ polymerization processes. The sol–gel route has been widely used for preparation of inorganic particles and in situ organic–inorganic nanocomposite materials [242–244]. The inorganic particles can then be incorporated ex situ into the polymers to form the nanocomposites. There are several advantages using sol–gel route, including low synthesis temperature, easiness of obtaining high purity materials due to the chemical reactions can be tailored at the molecular level, versatility of control over the nature of the organic–inorganic interface, as well as convenience of introducing new properties into the resulting materials. The preparation of high-purity, homogeneous and nanosized metal oxides at relatively low temperatures involved the hydrolysis of metal alkoxides and subsequent to the covalent network.

Metal alkoxides are metalorganic compounds having an organic ligand attached to a metal or metalloic atom. They are the result of direct or indirect reactions between a metal M and an alcohol ROH. Typical examples are methoxide (OMe ; MOCH_3) and ethoxide (OE_t ; MOC_2H_5). During hydrolysis, the alkoxy groups (OR) are replaced by hydroxo ligands (OH), i.e.

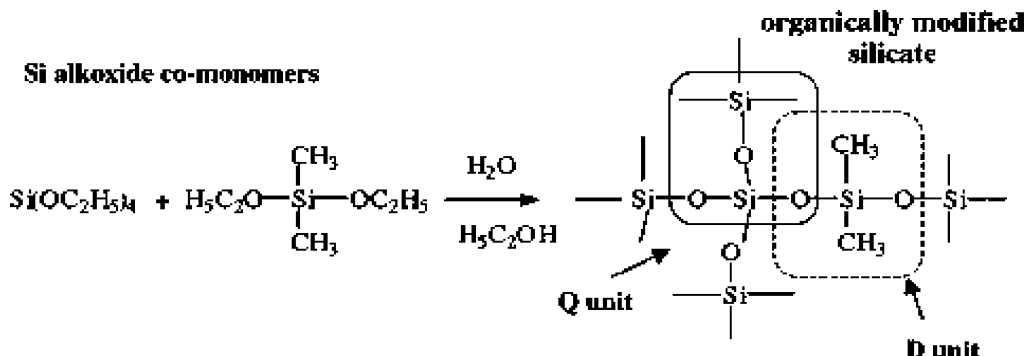


where R is an alkyl group, $\text{C}_n\text{H}_{2n+1}$. Subsequent condensation eliminates either water or alcohol to produce metal oxide or hydroxide linkages. In this process, two mononuclear complexes of M, each comprising only one metal M, can react with one another to form a polynuclear complex consisting of two metal atoms. Condensation occurs only when at least one hydroxo ligand is bonded to the cation M, and is designated as M–OH for simplicity. Condensation can proceed via olation and oxolation reactions. Olation is a reaction by which hydroxo or “ol” bridge M–OH–M bond is formed between two cations whilst oxalation involves the formation of oxo bridges M–O–M between to metal cations M [245]:



The “ol” or “oxo” bridges between two metal atoms lead to the formation of condensed oxide or hydroxide species. Under acid conditions, three-dimensional solid phase networks consisting of extended linear M–O–M chain polymers are developed. Accordingly, silica, alumina, titania and zirconia particles can be prepared using respective metallic alkoxides, M(OR)_z , ($\text{M} = \text{Si}, \text{Ti}, \text{Zr}, \text{Al}$) [246]. In general, the relative chemical reactivity of metal alkoxides is different, and non-silicate metal alkoxides, including Ti, Zr and Al have higher reactivity than silicon, i.e. $\text{Zr(OR)}_4, \text{Al(OR)}_4 > \text{Ti(OR)}_4 \gg \text{Si(OR)}_4$.

One way of preparing organic–inorganic hybrids is to incorporate functionalized polymers into an inorganic network derived from metal alkoxides. This approach allows the mixing of inorganic and organic components in various ratios to obtain the desired properties. Wilkes et al. prepared hybrid nanocomposites termed “ceramers” by the incorporation of silanol-terminated poly(dimethyl siloxane) (PDMS) into a siloxane network derived from tetraethoxysilane (TEOS) [247,248]. The condensation reaction proceeds as [249]:



The hybrid can be described as a material made of D unit ($-\text{O}-\text{SiMe}_2-\text{O}-$) and Q unit (siloxane), and includes only a siloxane network as an inorganic component. The structure and mechanical of the hybrids are strongly influenced by the process condition such as acid content, TEOS content and molecular mass of PDMS elastomer. TEOS has been employed in most cases as the inorganic component due to its relatively slow and controllable rate of reaction. Moreover, the chemical and mechanical properties of the hybrids are altered by incorporating organofunctional transition metal alkoxides other than silicon [250–253]. The major shortcomings of sol-gel technique are the high cost of the alkoxides, and tedious processing steps as it requires several sequential steps to form nanocomposites.

Alternatively, the sol-gel synthesis is carried out in an organic monomer and is polymerized subsequently and concurrently. Hybrid materials can also be synthesized through the in situ formation of inorganic species within a polymer matrix. The formation and dispersion of silica nanoparticles in polyolefin matrix is considered of practical importance. PP-silica nanocomposites with no chemical bonding between the filler and matrix can be prepared by the sol-gel method. In the process, TEOS was added to PP in the reactor together with a base catalyst. The sol-gel reaction was carried out in the reactor at 60 °C under continuous stirring. On the other hand, chemical interaction between the PP and nanofiller can be established by combining solid-state transformation (SSM) via grafting vinyl triethoxysilane (VTES) on PP with a sol-gel method [254]. Grafting of vinyl monomers onto isotactic PP in the solid state, i.e. below the melting point, displays several advantages over melt or solution grafting processes, such as negligible degradation of the PP chains and absence of any solvent. The process consists of contacting porous PP powders with a free radical initiator and a vinyl monomer at temperatures of 60–125 °C [255]. The VTES grafted PP is then incorporated into the silica during the sol-gel reaction. TEM observations reveal that in situ formed silica particles having sizes in the range of 50–100 nm, are nearly spherical and uniformly distributed in the PP matrix (Fig. 76).

In situ polymerization involves the dispersion of nanofillers in monomer first and then the mixture is polymerized using a technique similar to bulk polymerization. The nanoparticles were generally pretreated with a chemical agent to improve their compatibility with the polymer matrix. Qu et al. reported on the preparation of PA6–silica nanocomposites via in situ polymerization, in which silica was pretreated with aminobutyric acid [51]. They indicated that silica was dispersed homogeneously in the PA6 matrix and the addition of silica increased the glass transition temperature and crystallization rate of the PA6 matrix. Mai and coworkers synthesized PVC–CaCO₃ nanocomposites by in situ polymerization of vinyl chloride in the presence of CaCO₃ particles. Their results also showed that CaCO₃ particles were uniformly distributed in the PVC matrix for low particle loading level. As unmodified CaCO₃ particles were used, and agglomeration of nanoparticles occurred above 5 wt.% filler loading. The glass transition temperature of PVC in the nanocomposites was slightly higher

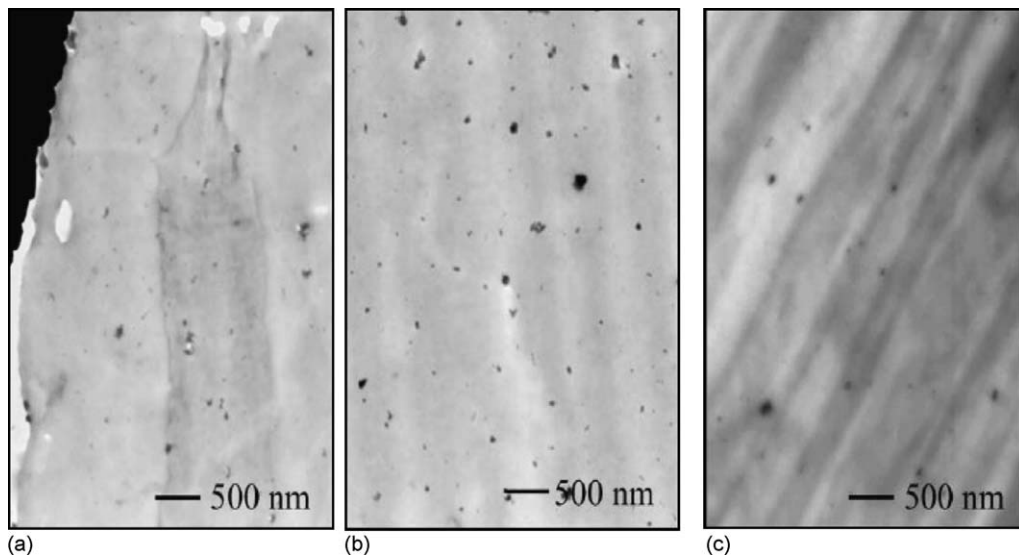


Fig. 76. TEM micrographs of PP–silica nanocomposite (5% silica): (a) edge, (b) center as well as (c) PP–g–silane–silica nanocomposite (reprinted from [254] with permission from Elsevier).

compared to pristine PVC due to the restriction of CaCO_3 nanoparticles on the chain mobility of the PVC phase [235]. Very recently, Liu et al. fabricated PET–silica nanocomposites by direct polymerizing PET monomer with organic modified silica nanoparticles [256]. Zhang and Simon prepared PE–alumina nanocomposites in which the alumina nanoparticles were chemically modified with an alkylaluminium compound and a vinyl alcohol for grafting vinyl groups to the surface. These species were then polymerized with ethylene using a late transition metal catalyst [257].

It appears that surface treatment of nanoparticles plays a key role to achieve homogeneous dispersion of inorganic nanoparticles in the polymer matrix. To decrease the surface energy of the nanoparticles, surface treatment of nanoparticles is necessary. In addition to the chemical treatment of particles, other approaches such as formation of core–shell particles and irradiation grafting of monomers have been reported. The encapsulation of inorganic particles with polymers is desirable in many applications in order to alter the surface characteristics of the cores, to enhance the stability of dispersions, and to improve the dispersibility in organic media [258]. Hergeth and coworkers [259] first applied emulsion polymerization method to encapsulate inorganic particles by a polymer layer, forming the so-called core–shell particles. Bourgeat-Lami et al. also functionalized silica nanoparticles (12 nm) by in situ emulsion polymerization [260]. Recently, Xie et al. coated micro-sized talc with polymethyl methacrylate (PMMA) via in situ polymerization of methyl methacrylate (MMA) monomer on the talc surface [261]. A similar process was adopted by them to form PMMA shell on antimony trioxide (Sb_2O_3) nanoparticles by in situ MMA polymerization. They reported that PMMA shell encapsulated Sb_2O_3 nanoparticles have enhanced interactions with PVC matrix, breaking down Sb_2O_3 agglomerates, improving their dispersion in the matrix and also increasing the particle–matrix interfacial adhesion [262]. Very recently Seul et al. also conducted the encapsulation of CaCO_3 nanoparticles with PMMA [263]. In another study, stable dispersions nanosilica were coated with tert-butyl acrylate monomer by in situ polymerization of monomer adsorbed on the particles in 2-propanol. To achieve a high coating efficiency, silica was first modified with 3-(trimethoxysilyl) propylmethacrylate (MPS) coupling agent. The encapsulation efficiency was governed by the degree of MPS grafting and by the initial concentration of the monomer [258].

It is noted that encapsulation of nanoparticles can also be carried out by melt compounding. Wu et al. have successfully encapsulated CaCO_3 nanoparticles (40 nm) with chlorinated polyethylene (CPE) via melt mixing of CPE and nanofillers in a two-roll mill at 130 °C for 10 min. The encapsulated CaCO_3 nanoparticles toughened the PVC effectively [264].

Friedrich and coworkers used the ^{60}Co γ -ray irradiation to modify the silica particle surfaces (15 nm) by grafting styrene or ethyl acrylate monomer onto the filler. During the process, a mixture of monomer/particle and solvent was irradiated with ^{60}Co γ -ray. The monomer was polymerized into polystyrene or polyethyl acrylate molecules. The irradiated nanoparticles were then compounded with polyolefin polymers. Different species of the grafting monomers resulted in different interfacial interactions and different ultimate properties of the composites [265–268]. PS-grafted SiC nanoparticles were also prepared via grafting polymerization of styrene and acrylamide monomers without γ -ray irradiation [269]. Grafting polymeric molecules onto inorganic nanoparticle surfaces exhibits distinct advantages over modification by surfactant or coupling agent. Owing to the low molecular weight nature, the grafting monomers can penetrate into the agglomerated nanoparticles easily and react with the activated sites of the nanoparticles. In addition, the polymer-grafted nanoparticles can possess desirable properties through a proper selection of the grafting monomers and grafting conditions [265].

For the melt-compounding route, homogeneous dispersion of nanoparticles in a polymeric matrix is also directly related to the surface treatment of particles. Gayman and coworkers reported that the dispersion in PP is more difficult for untreated CaCO_3 nanoparticles than stearic acid-treated nanoparticles during melt-mixing in a twin screw extruder [270]. More recently, Mai and coworkers also reported that the commercial CaCO_3 nanoparticles had a poor dispersion in PP matrix. However, the addition of a small amount of a non-ionic modifier improved the dispersion of CaCO_3 nanoparticles during melt extrusion [271]. The polyoxyethylene nonyphenol modifier had a long alkyl chain with one hydroxyl end group. The polar group is adsorbed on the surface of CaCO_3 nanoparticles and the long alkyl chain is compatible with PP molecular chains. The addition of such modifier reduces the particle–particle interaction by lowering the surface energy of CaCO_3 , leading to better dispersion of CaCO_3 nanoparticles.

3.2. Crystallization

Generally, inorganic nanoparticles tend to act as heterogeneous nucleation sites for the polymer chains as evidenced by higher peak crystallization temperature and lower $t_{1/2}$ values from the DSC measurements [272,273]. This behavior is similar to that of the thermoplastics reinforced with silicate clays as discussed previously. The non-isothermal crystallization behaviors of PP– SiO_2 nanocomposites were conducted by Qian et al. [273] and Jain et al. more recently [274]. Qian et al. reported that the Ozawa equation can be used to describe the non-isothermal crystallization of the nanocomposites very well. A series of almost nearly parallel lines for various temperatures are observed in the plots of $\ln[-\ln(1 - X_t)]$ versus $\ln \beta$ for both PP and PP–3 wt.% SiO_2 nanocomposite (Fig. 77). However, a linear relationship between $\ln[-\ln(1 - X_t)]$ versus $\ln \beta$ is not observed in the work of Jain et al. Accordingly, a combined Avrami–Ozawa approach developed by Liu et al. [275] is used by these two groups.

The well known Avrami equation for isothermal crystallization can be expressed as [276]:

$$X_t = 1 - \exp[-Kt^n] \quad (22)$$

where X_t is the fraction of material crystallized after time t , K a temperature-dependent constant that depends on nucleation rate and growth velocity, and n is an exponent describing the dimensionality of

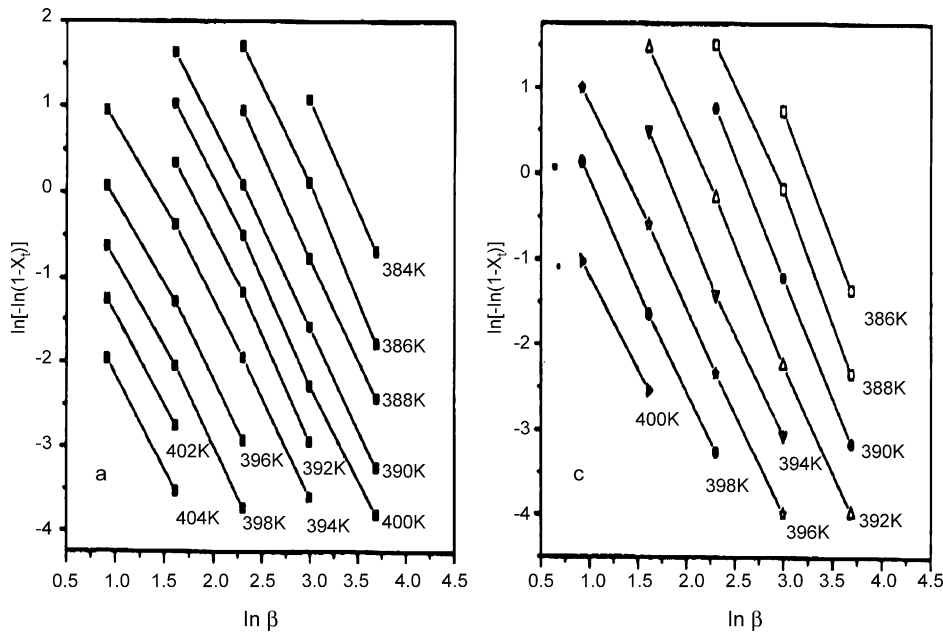


Fig. 77. Ozawa plots of $\ln[-\ln(1-X_t)]$ vs. $\ln \beta$ for crystallization of pure PP and PP-3 wt.% SiO_2 nanocomposite (reprinted from [273] with permission from Wiley).

crystal growth. Ozawa extended the isothermal crystallization to the non-isothermal case of controlled cooling rate, and derived the following relationship [277,278],

$$\frac{X(t)}{X_\infty} = 1 - \exp\left[\frac{-K_T}{\beta^m}\right] \quad (23)$$

where $X(t)$ is the crystallinity attained at temperature T , X_∞ the crystallinity at the termination of the crystallization process, β the cooling rate, K_T is a constant for a given cooling rate and m is the Ozawa index. This index is somewhat similar to the Avrami exponent, and it depends on the type of nucleation and the growth dimensions. By combining Eqs. (22) and (23), the following equation is obtained:

$$\ln K_t + n \ln t = \ln K_T - m \ln \beta \quad (24)$$

$$\ln \beta = \ln F(T) - b \ln t \quad (25)$$

where $F(T) = [K_T/K_f]^{1/m}$ and a is the ratio of the Avrami to Ozawa's exponent, i.e. $b = n/m$. $F(T)$ refers to the cooling rate at unit crystallization time, when the system has a definite degree of crystallinity. Fig. 78 shows the plots of $\log \beta$ versus $\log t$ for a given relative degree of crystallinity for the PP-1% SiO_2 nanocomposite. The values of $F(T)$ and B determined for each particular crystallinity are listed in Table 5. Apparently, the $F(T)$ values of PP-silica nanocomposites at a particular degree of crystallinity are lower than those of pure PP. This demonstrates that the nanocomposites achieve a value for the fractional crystallinity faster than the polymer, i.e. faster kinetics of crystallization. In this regard, silica nanoparticles facilitate the crystallization process. The activation energy of crystallization (ΔE) at different cooling rates can be determined from the Kissinger approach [279], based on

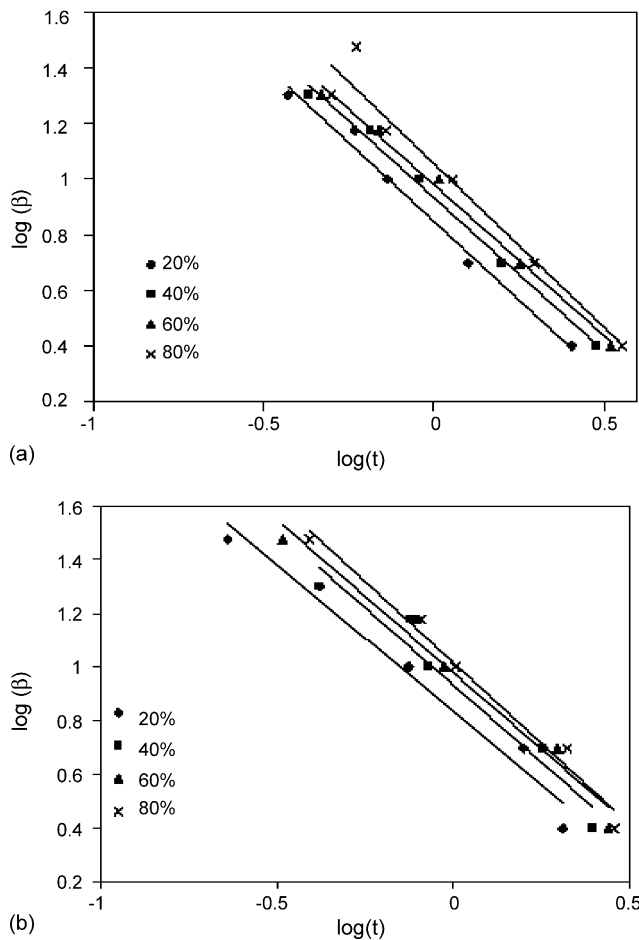


Fig. 78. Plots of $\ln \beta$ vs. $\ln t$ for crystallization of (a) PP and (b) PP– SiO_2 nanocomposite reinforced with 1 wt.% filler (reprinted from [274] with permission from Elsevier).

Table 5

The values of b and $F(T)$ at different degrees of crystallinity for PP and PP– SiO_2 nanocomposites (reprinted from [274] with permission from Elsevier)

	$X_c(t)$ (%)			
	20	40	60	80
Pure PP				
b	1.24	1.22	1.19	1.18
$F(T)$	7.56	9.31	10.46	11.35
PP/silica 0.2%				
b	1.2	1.26	1.3	1.13
$F(T)$	7.41	8.96	9.66	11.3
PP/silica 1%				
b	1.09	1.16	1.14	1.21
$F(T)$	6.58	8.6	9.51	10.45

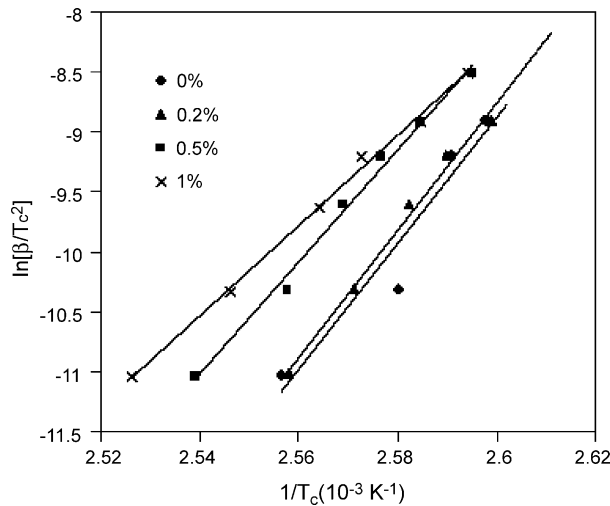


Fig. 79. Kissinger plot for calculating the non-isothermal crystallization activation energies for PP and PP–SiO₂ nanocomposites (reprinted from [274] with permission from Elsevier).

the following equation:

$$\frac{d[\ln(\beta/T_c^2)]}{d(1/T_c)} = \frac{-\Delta E}{R} \quad (26)$$

where R is the gas constant and T_c is the peak crystallization temperature. The crystallization activation energy of the nanocomposites determined from the slopes of linear lines in the plots of $\ln(\beta/T_c^2)$ versus $1/T_c$ are: 435, 322, 324, 311 and 358 kJ/mol for 0, 0.2, 0.5, 1 and 1.5 wt.% silica, respectively (Fig. 79). The activation energy of crystallization of nanocomposites is lower than that for neat PP and increases with increasing filler content. Thus silica nanoparticles act as heterogeneous nuclei and accelerate the crystallization rate of PP at a relatively low filler content during non-isothermal crystallization condition [274]. At high silica content, ca. 10 wt.%, the activation energy of the nanocomposite is higher than that of neat polymer. In this case, the SiO₂ nanoparticles tend to agglomerate, acting as a barrier to retard the crystallization by depressing the crystal growth [280].

3.3. Mechanical behavior

The use of rigid inorganic fillers as toughening agent is well recognized [240,241,270,281–284]. Kim and Michler studied the deformation behavior of the polymers filled with elastomers or rigid particles [240,241]. Based on the results of Kim et al., Gayman and coworkers [270] summarized the toughening process of rigid particles into three stages:

- (a) *Stress concentration*. The rigid particles act as stress concentrators owing they have different elastic properties compared to the matrix polymer.
- (b) *Debonding*. Stress concentration gives rise to build up of triaxial stress around the particles, leading to debonding at the particle–polymer interface.
- (c) *Shear yielding*. The voids resulting from debonding alter the stress state in the matrix polymer surrounding the voids. This reduces the sensitivity towards crazing and promotes shear yielding.

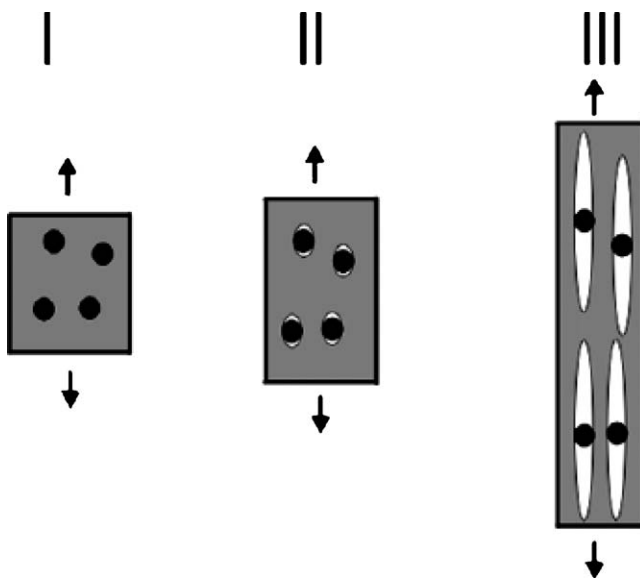


Fig. 80. Toughening mechanism with rigid particles (reprinted from [270] with permission from Elsevier).

The toughening mechanism with rigid particles is shown schematically in Fig. 80. In order for rigid particles to act as effective toughening agents, they must fulfill certain requirements. These include the particles should be of small size (less than 5 μm), otherwise the voids that are created would act as crack initiation sites; the aspect ratio must be close to unity to avoid high stress concentrations; the particles should be homogeneously distributed in the polymer matrix; the particles must debond prior to the yield strain of the matrix polymer [270]. From the volume strain measurements on PP–CaCO₃ composites, Lazzeri et al. indicated that debonding of rigid particles

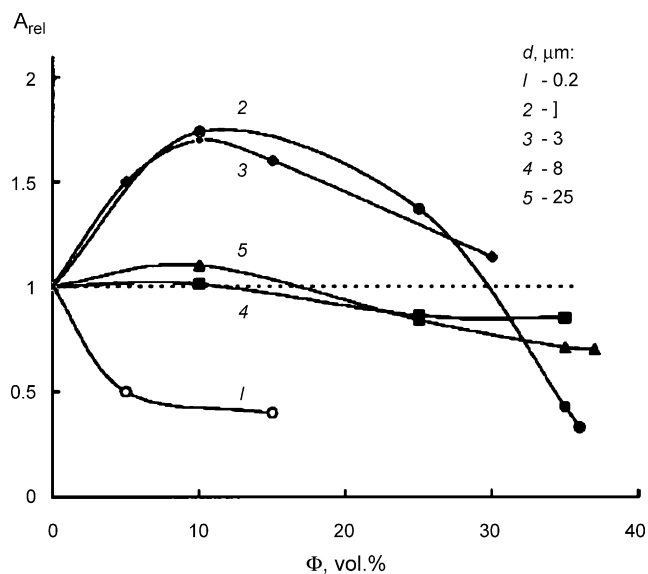


Fig. 81. Relative notched Izod impact strength of the PP composites (with respect to neat PP) vs. content of fillers having different sizes (reprinted from [283] with permission from Wiley).

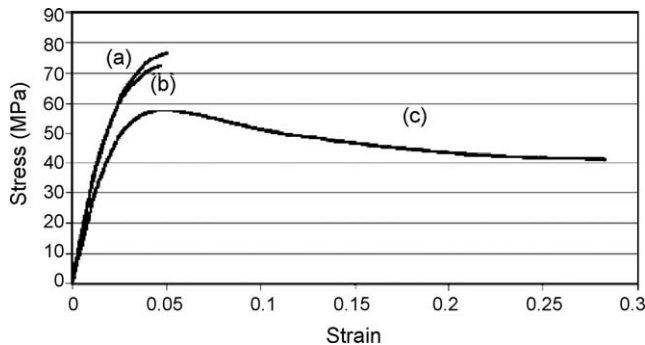


Fig. 82. Typical stress–strain curves for (a) neat PMMA, (b) 2 wt.% micrometer-sized alumina filled PMMA composite, and (c) 2.2 wt.% 38 nm alumina filled PMMA nanocomposite (reprinted from [48] with permission from The American Chemical Society).

from the matrix prior to macroscopic yielding triggers dilatational process of the composites. This behavior is similar to that observed in rubber-toughened polymers [282].

We now consider the effect of the particle size on the toughening behavior of polymer microcomposites. Fig. 81 shows the relative notched impact strength of PP composites filled with different sizes of rigid Al(OH)₃ particles (1–25 µm) and glass beads (0.2 µm). The introduction of rigid particles with diameters of 1 and 3 µm is very effective to toughen PP. A maximum toughening effect is observed when the content of such fillers reaches about 15–10 vol.%. Above this loading level

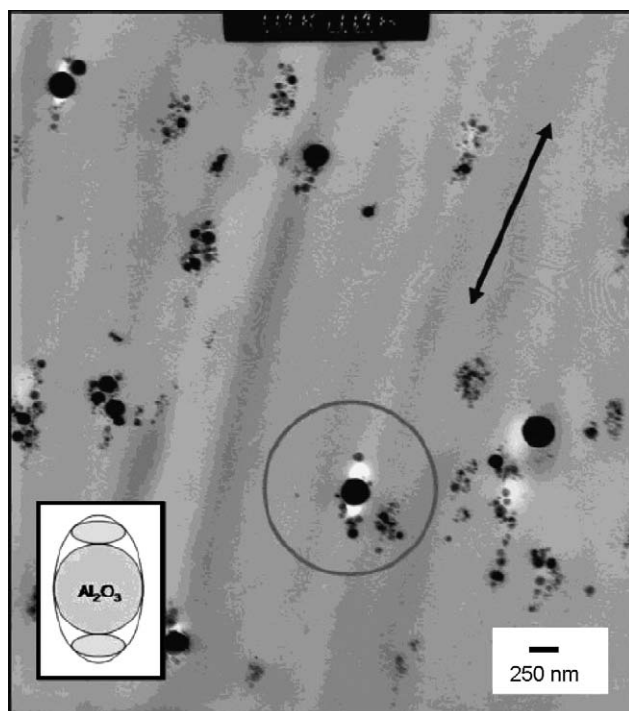


Fig. 83. TEM micrograph of the necked area in a 2.2 wt.% 38 nm alumina filled PMMA nanocomposite. The double-headed arrow indicates the direction of the tensile stress. *Inset:* Model of a single ellipsoidal void surrounding a nanoparticle and aligned in the tensile direction (reprinted from [48] with permission from The American Chemical Society).

to 30 vol.%, the composite toughness still remains higher compared to that for neat PP. However, glass-bead particles with an average diameter of 0.2 μm show no toughening effect for PP [283]. This is because the glass-beads tend to agglomerate into clusters during processing, thereby leading to poor impact toughness [281]. The toughness of the submicron filler reinforced composites can be enhanced when such particles are dispersed homogeneously in the polymer matrices.

Enhanced ductility in brittle amorphous PMMA polymer with rigid nanoparticles has been reported by Schadler and coworkers [47,48]. Fig. 82 shows the stress-strain curves of PMMA, PMMA–2 wt.% $\gamma\text{-Al}_2\text{O}_3$ (micrometer-sized) and PMMA–2.2 wt.% $\gamma\text{-Al}_2\text{O}_3$ (38 nm) samples [48]. Pure PMMA and its microcomposite fracture in brittle mode via craze formation and growth as expected. However, the nanocomposite displays ductile behavior as evidenced by a large increase of the strain-to-failure to about 30%. TEM micrograph reveals the formation of ellipsoidal voids on the poles (with respect to the tensile direction) of nanoparticles (Fig. 83). The micromechanical deformation mechanism of the nanocomposite involves debonding of particles from the matrix and associated shear yielding of polymer matrix with high-energy absorption.

As mentioned above, the toughness of brittle epoxy resins can be improved by the addition of rigid particles such as glass beads [224,225]. Very recently, Ragosta et al. prepared epoxy–silica nanocomposites by dispersing silica–organosol particles (10–15 nm) in TGDDM epoxy resin [284]. This epoxy was hardened with DDS. They determined the fracture toughness of the nanocomposites according to the ASTM D5045-99 standard method. Fig. 84(a) shows the load–displacement curves

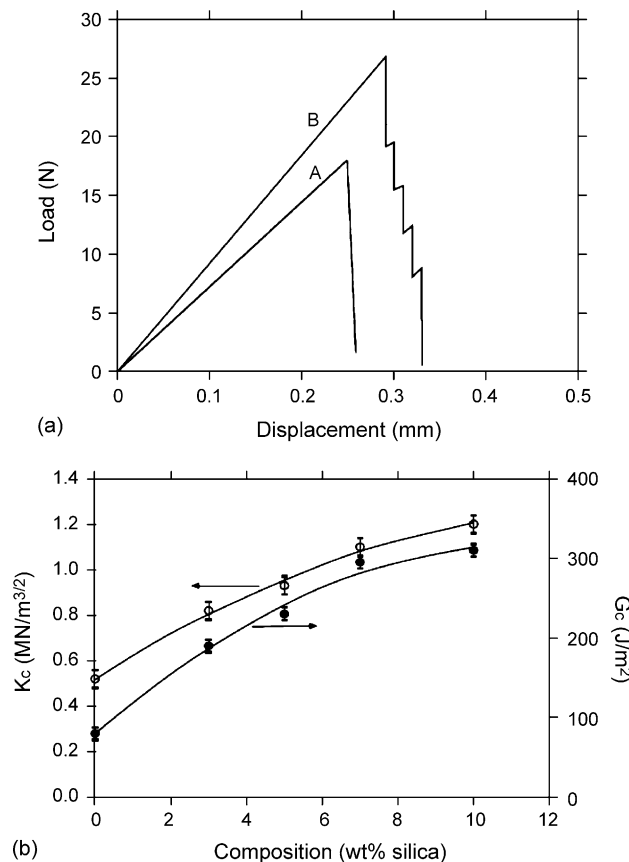


Fig. 84. (a) Load–displacement curves for pure epoxy (A) and epoxy–10 wt.% silica (B) SEN specimens. (b) Variation of K_{IC} and G_c as a function of silica content (reprinted from [284] with permission from Elsevier).

for the SEN specimens of pure epoxy and epoxy–10 wt.% silica. It can be seen that pure epoxy and nanocomposite fail in a brittle mode. However, a series of zigzag paths can be observed in the crack propagation stage of the nanocomposite, indicating that the crack propagates intermittently in a stick-slip fashion. The variations of fracture toughness (K_{IC}) and critical strain energy release rate (G_c) of the TGDDM/DDS epoxy resin with the silica content are shown in Fig. 84(b). It can be seen that the K_{IC} and G_c increase significantly with the addition of low amounts of silica. The K_{IC} of TGDDM/DDS resin has increased twofold by adding 10 wt.% silica. This level of enhancement is larger than it has been achieved with the microparticles [284].

The effect of nanofillers on the tensile and impact properties of polyamides is also very impressive. Fig. 85 shows the impact and tensile properties of PA6– SiO_2 nanocomposites as a function of filler content. The nanocomposites were prepared by in situ polymerization. Both unmodified and amino-butyric acid-treated silica nanoparticles were used [51]. Unmodified nanofiller additions only enhance the tensile stiffness of the composites; other mechanical properties remain unchanged or slightly deteriorated. In sharp contrast, the impact strength, tensile ductility and tensile strength of modified silica nanocomposites tend to increase with increasing silica content up to 5 wt%. Beyond this loading level,

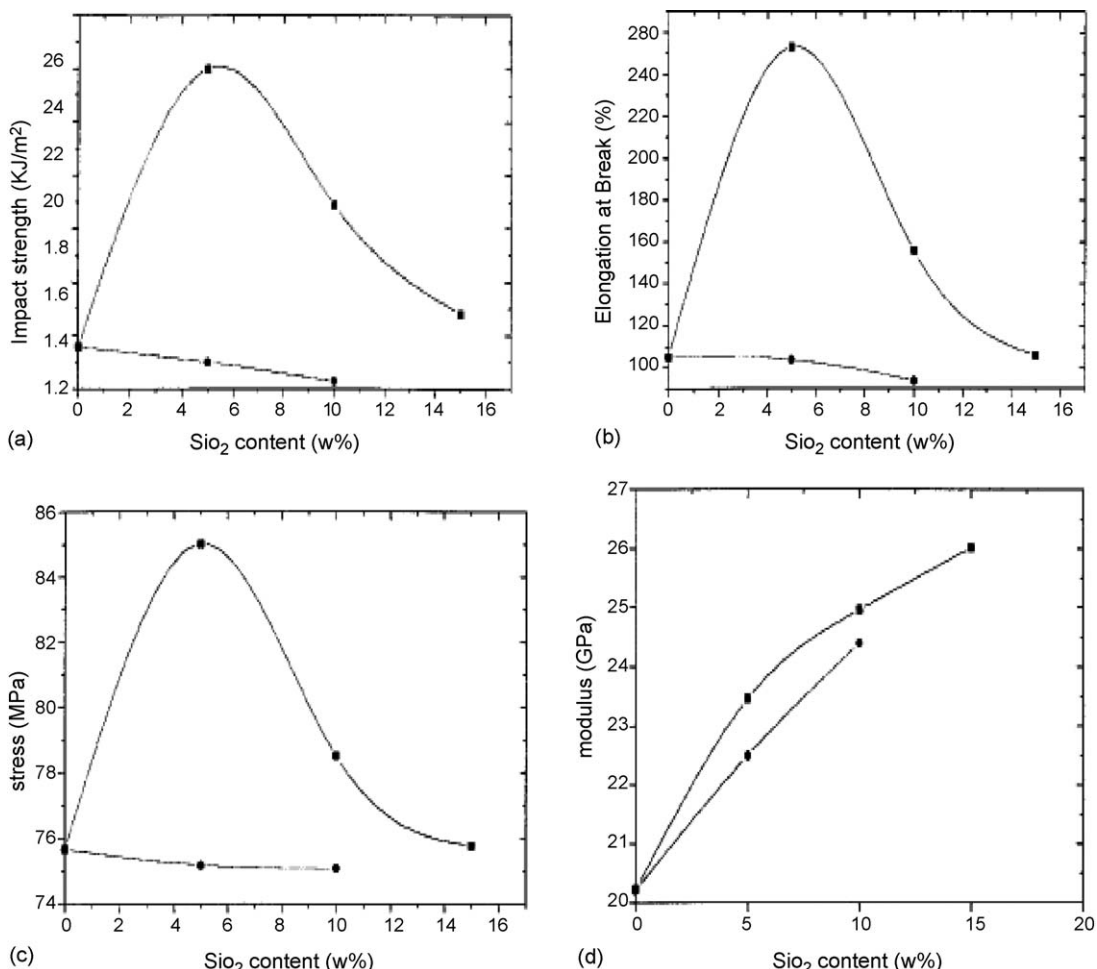
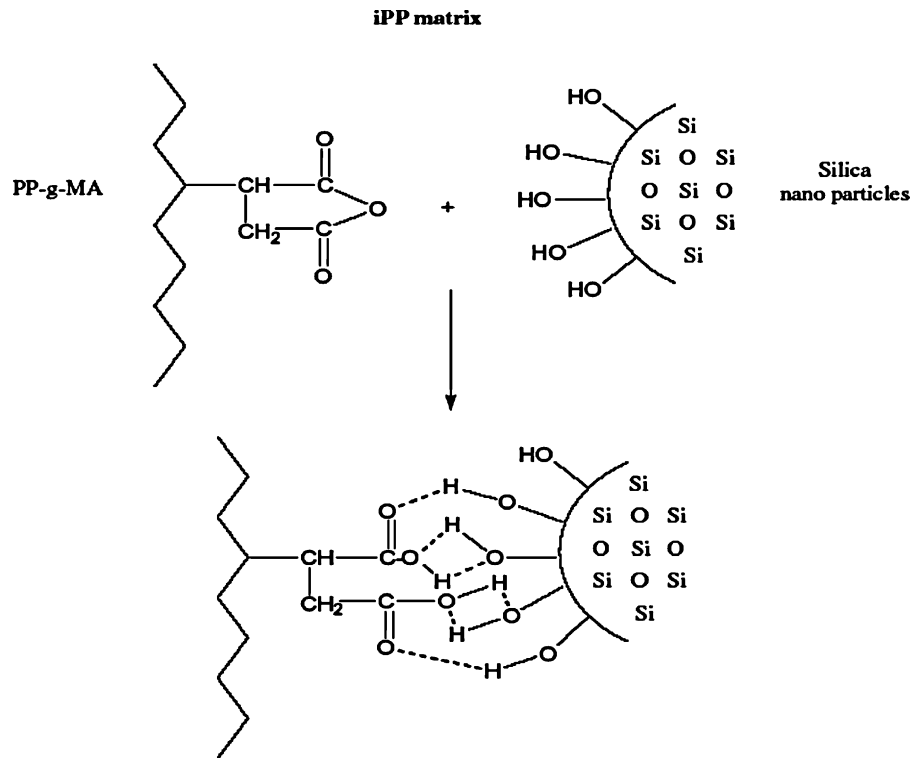


Fig. 85. Mechanical properties of PA6– SiO_2 nanocomposites as a function of nano- SiO_2 volume content: (a) impact strength, (b) elongation at break, (c) tensile strength, and (d) tensile modulus. (■) Modified silica-reinforced composites, (●) unmodified silica-reinforced composites (reprinted from [51] with permission from Wiley).

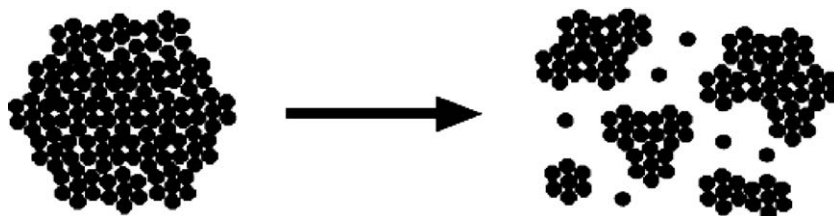


Scheme 1. Interaction between MA group of PP-g-MA and the surface hydroxyl groups of the silica nanoparticles.

the mechanical properties deteriorate dramatically. Qu et al. explained such remarkable improvement in the mechanical properties in terms of the matrix ligament thickness concept [51].

As hydroxyl group is resided on the surface of silica nanoparticles, homogeneous dispersion of silica in non-polar PP is more difficult to achieve. Bikaris et al. [285] indicated that the PP-g-MA can be used as a compatibilizer for the PP–SiO₂ nanocomposites. It is believed that the MA group can react with the surface hydroxyl group of SiO₂ nanoparticles. Thus the agglomerates can be destroyed or reduced in sizes. This is illustrated in the following Schemes 1 and 2.

Accordingly, they prepared a series of PP–SiO₂ nanocomposites containing 1–15 wt.% silica nanoparticles (average size of 12 nm) via melt mixing in a twin screw extruder. Fig. 86(a–d) shows the tensile and impact properties of such nanocomposites. It can be seen from Fig. 86(a) that the addition of PP-g-MA leads to a significant improvement of Young's modulus. Moreover, the stiffness of the nanocomposites tends to increase with increasing amounts of PP-g-MA. The tensile strength at break of the uncompatibilized nanocomposites shows a decrease with increasing silica content. However, the tensile strength of MA-compatibilized nanocomposites only displays a slight decrement with increasing



Scheme 2. Break up of large agglomerates into finer ones with the addition of PP-g-MA.

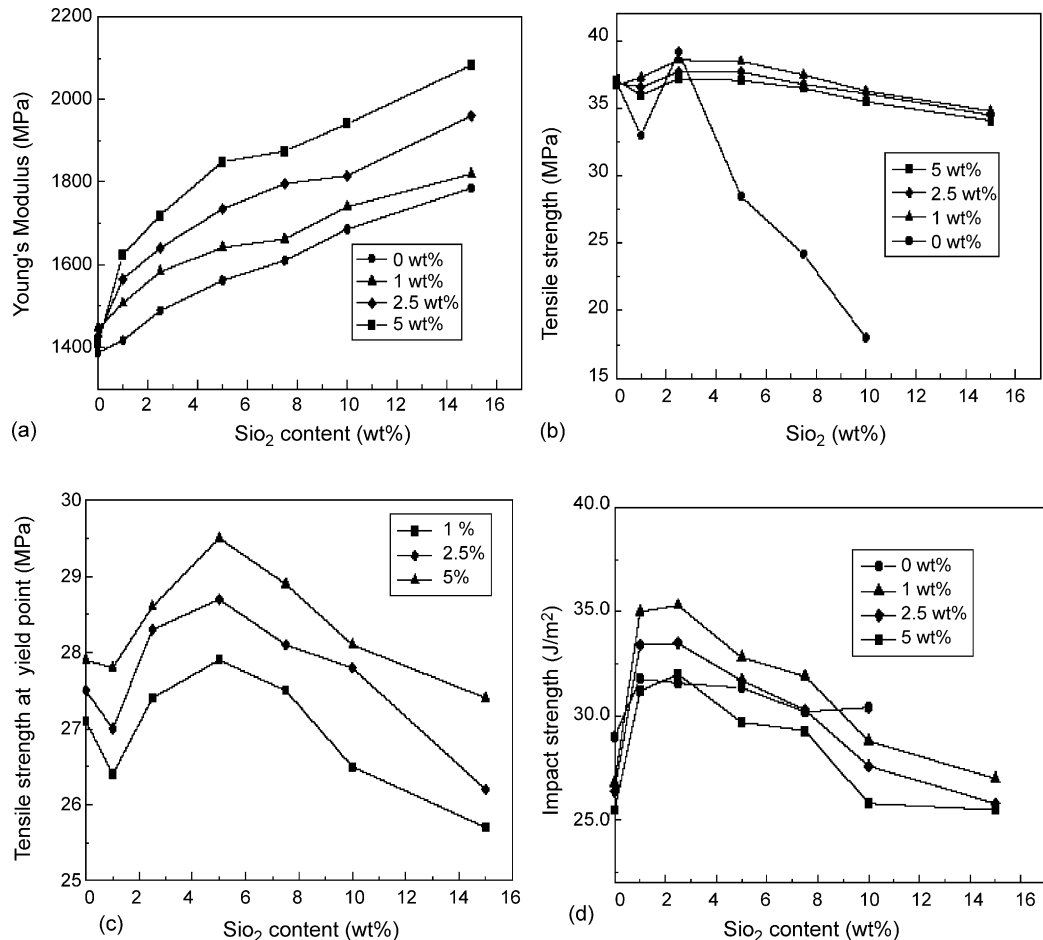


Fig. 86. (a) Young's modulus, (b) tensile strength at break, (c) yield stress, and (d) impact strength vs. silica content for melt-compounded PP- SiO_2 nanocomposites containing different amounts of PP-g-MA as a compatibilizer (reprinted from [285] with permission from Elsevier).

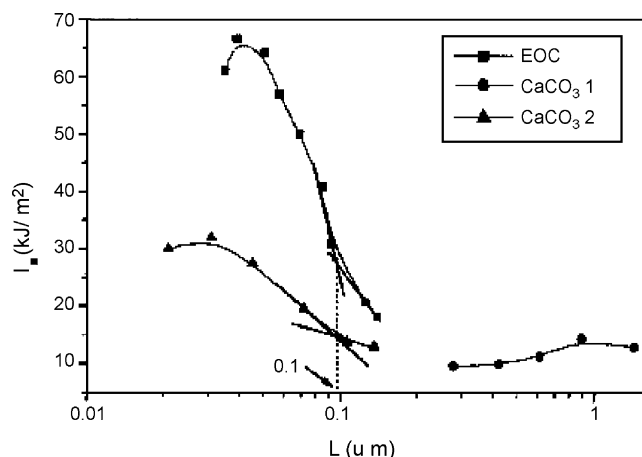


Fig. 87. Impact strength vs. matrix ligament thickness for brittle to ductile transition of PP- CaCO_3 and PP-elastomer systems. EOC is elastomer, CaCO_3 , 1 means CaCO_3 of 1 μm , and CaCO_3 , 2 implies CaCO_3 of 50 nm (reprinted from [287] with permission from Wiley).

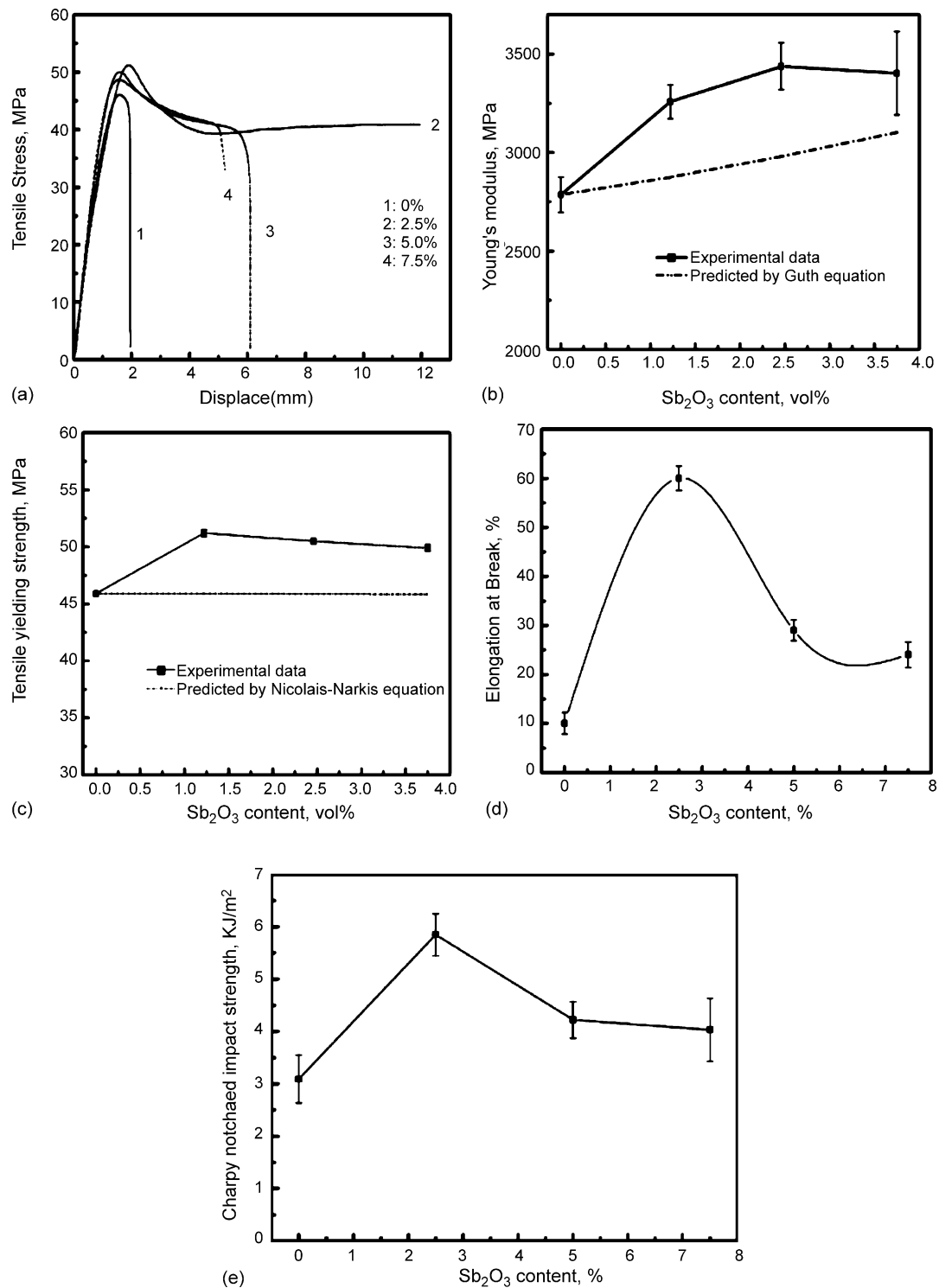


Fig. 88. Mechanical properties of PVC–Sb₂O₃ nanocomposites: (a) stress–strain curves, (b) Young's modulus vs. filler content, (c) yield strength vs. filler content, (d) elongation at break vs. filler content and (e) impact strength vs. filler content (reprinted from [262] with permission from Elsevier).

silica content (Fig. 86(b)). The yield stress versus silica content plots show an apparent maximum at 5 wt.% SiO_2 content. Above this concentration there is an almost linear decrease (Fig. 86(c)). For the impact strength, the toughening effect of silica nanoparticles is evident. A maximum appears at 2.5 wt.% SiO_2 content for both uncompatibilized and MA-compatibilized nanocomposites. The PP– SiO_2 nanocomposites generally exhibit higher impact strength than pure PP (Fig. 86(d)).

According to Wu's percolation theory, a polymer modified by elastomers shows a transition from brittle to tough behavior when the thickness of the interparticle matrix ligaments (τ) is smaller than a critical value (τ_c) [286]. Mathematically, the interparticle matrix ligaments can be expressed as:

$$\tau = d \left[\beta \left(\frac{\pi}{6\phi} \right)^{1/3} - 1 \right] \quad (27)$$

where d is the particle diameter, ϕ the particle volume fraction and β is a geometric constant, depending on the assumed packing of the particles (1.0 for cubic lattice, 1.09 for body-centered cubic and 1.12 for face-centered cubic packing). Bartczak et al. pointed out that the interparticle ligament of thickness less than τ_c possesses a structure of highly ordered lamellar crystallites having reduced

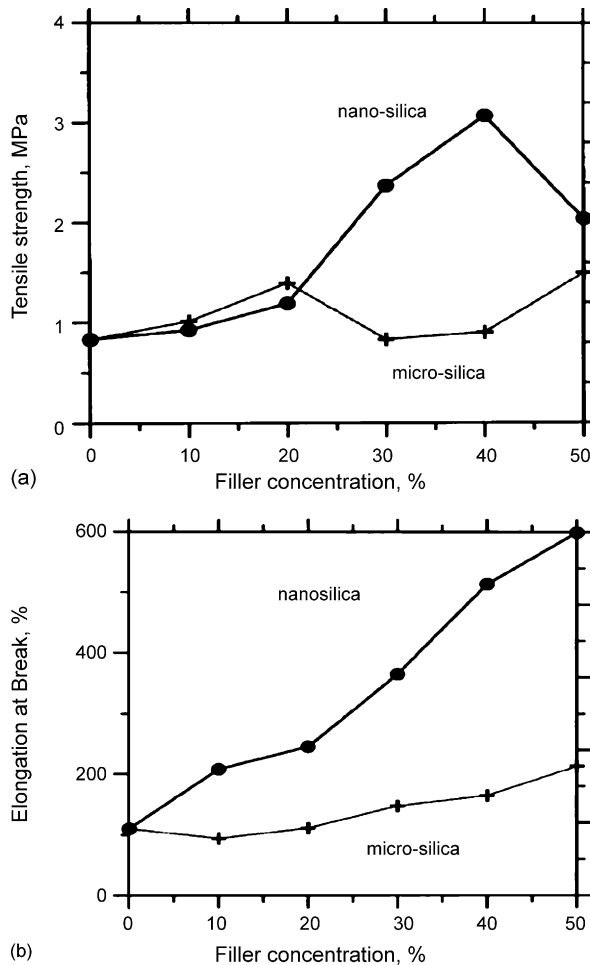


Fig. 89. Effect of filler concentration on (a) tensile strength and (b) elongation at break of filled PU (reprinted from [290] with permission from Wiley).

plastic resistance in certain orientations. When such material percolates throughout the structure the overall plastic resistance of the material is markedly reduced and brittle behavior is avoided [281]. On the basis of Wu's criterion, the ligament thickness dependence of the impact strength for the PP–CaCO₃ nanocomposite and PP–elastomer is determined by Zhang and Huang (Fig. 87) [287]. This figure demonstrates that the impact strength of the PP composites remains very low for large ligament thicknesses. When the ligament thickness decreases below approximately 0.1 μm, a sharp increase in the impact strength is observed for the PP–CaCO₃ nanocomposite. A similar ligament thickness

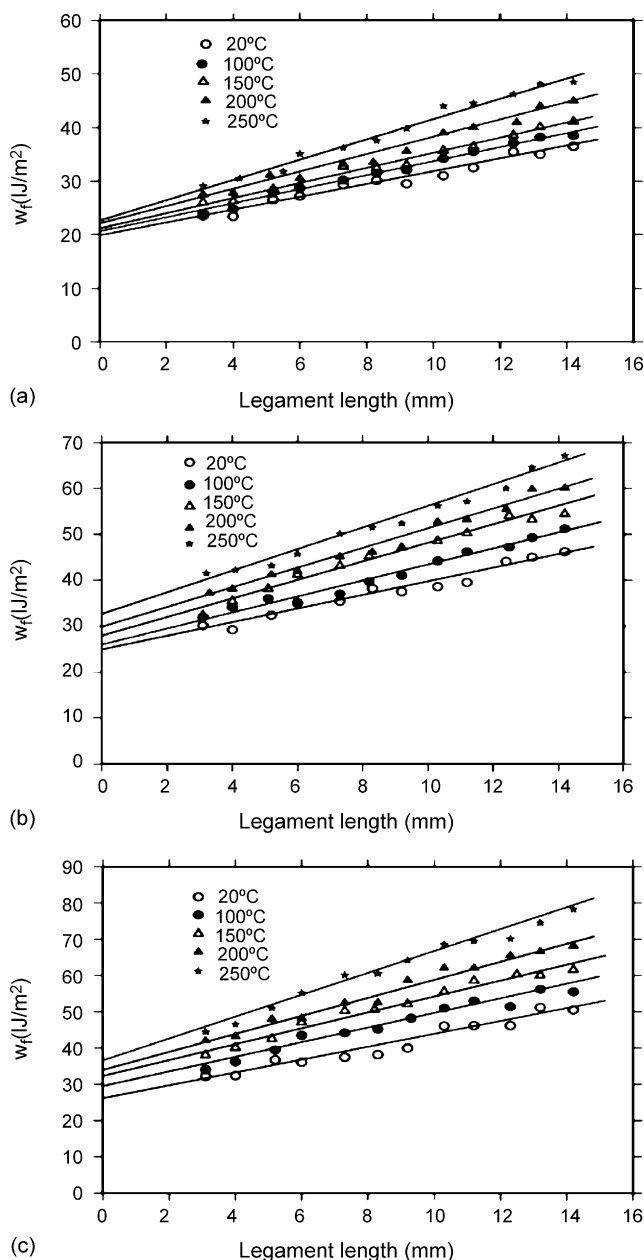


Fig. 90. Specific work of fracture vs. ligament length as a function of temperature: (a) polyimide, (b) polyimide–10 wt.% SiO₂ and (c) polyimide–15 wt.% SiO₂ samples (reprinted from [44] with permission from Elsevier).

dependence of the impact strength is observed for the PP–elastomer blend. At the same value of ligament length, the improvement in the toughness by the elastomer is obviously higher than that by CaCO_3 nanoparticle.

[Fig. 88\(a–e\)](#) shows the mechanical behavior of the PVC reinforced with PMMA encapsulated Sb_2O_3 nanoparticles [262]. PVC– Sb_2O_3 nanocomposites exhibit ductile behavior as evidenced by stress whitening and necking. From [Fig. 88\(b and c\)](#), the Young's modulus and yield strength of the nanocomposites appear to increase with increasing filler content. The experimental stiffness and yield strength are higher than those predicted from Guth equation [288]:

$$E_c = E_m(1 + 2.5\phi + 14.1\phi^2) \quad (28)$$

and Nicolais–Narkis equation [289]:

$$\sigma_{yc} = \sigma_{ym}(1 - 1.21\phi^{2/3}) \quad (29)$$

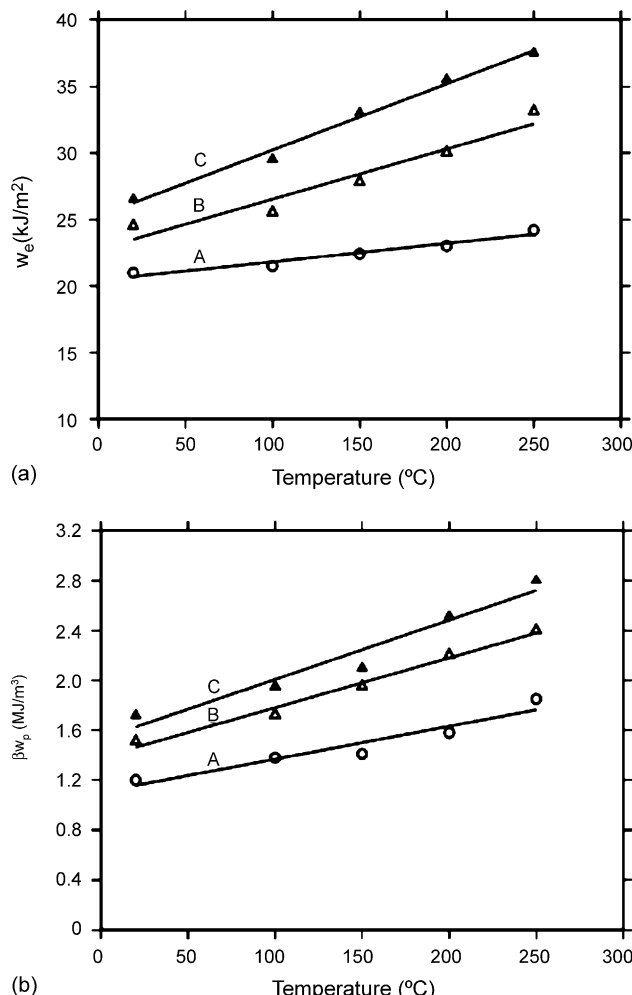


[Fig. 91.](#) (a) Essential work of fracture, w_e and (b) non-essential work of fracture, βw_p , as a function of temperature: (A) polyimide, (B) polyimide-10 wt.% SiO_2 and (C) polyimide-15 wt.% SiO_2 samples (reprinted from [44] with permission from Elsevier).

where σ_{yc} and σ_{ym} are yield strengths of composite and matrix, respectively. Moreover, the tensile ductility and impact strength of nanocomposite are higher than those of PVC. A maximum is reached when the loading level reaches 2.5 wt.% (Fig. 88(d and e)).

In the case of PU elastomer, Petrovic et al. [290] studied the effects of nanosilica (10–20 nm) and micro-silica (1.4 μm) additions on the tensile performance of PU composites (Fig. 89(a and b)). The strengthening and toughening effects of nanosilica can be readily seen. The tensile strength and elongation at break of the PU filled with nanosilica tend to increase with increasing the filler content. In contrast, the elongation at break of the micro-silica PU composites remains almost unchanged with increasing filler content up to 20%. Thereafter, it increases slightly with increasing microfiller concentration.

More recently, Musto et al. employed the essential work of fracture approach to determine the fracture toughness of polyimide–silica nanocomposites prepared by the sol–gel process [44]. The measurements were carried out from 20 to 250 °C. Fig. 90(a–c) shows specific work of fracture versus ligament length for polyimide and its nanocomposites at various temperatures investigated. The variations of w_e and βw_p parameters with temperature are shown in Fig. 91(a and b). Both w_e and βw_p parameters increase linearly with temperature. At any given temperature, the enhancement of

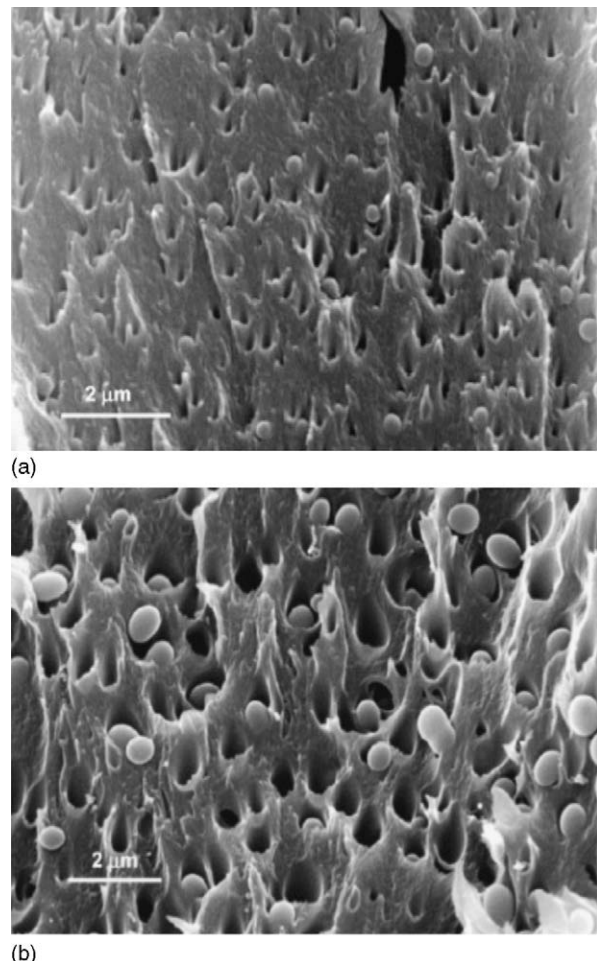


Fig. 92. SEM micrographs showing fracture surfaces of (a) polyimide–10 wt% SiO₂ and (b) polyimide–15 wt% SiO₂ samples tested at ambient temperature. The loading direction was vertical (reprinted from [44] with permission from Elsevier).

fracture toughness is related to the silica content. However, this temperature dependence is lower for the pure polyimide and increases with increasing silica content in the nanocomposites. SEM micrographs of the hybrids after EWF tests reveal that cavitation of silica particles and shear yielding of the polyimide matrix are dominant deformation fracture behavior of the nanocomposites (Fig. 92) [44].

4. Carbon nanotube reinforcement

4.1. Synthesis of CNTs and their nanocomposites

There are essentially three fundamental sources required for nanotube synthesis, i.e. carbon, heat and metal catalyst. The most commonly used catalysts are transition metals or alloys in the form of nanoparticles and thin films. SWNTs and MWNTs can be synthesized by means of the arc discharge [25], laser ablation [291–294] and chemical vapor deposition (CVD) from hydrocarbons [295–297]. Each technique has its specific merits and inevitable weaknesses. For the arc discharge and laser ablation, C vapor is produced by evaporation of an electrode or target. The catalytic growth of CNTs by CVD is an effective route to produce large amounts of nanotubes. The carbon vapor source is derived from the chemical vapor decomposition of various hydrocarbon gases on transition metal catalyst. Kong et al. reported that high quality SWNTs can be produced by chemical vapor decomposition of methane on supported transition metal oxide catalysts. Methane was used instead of acetylene or ethylene commonly used to produce MWNTs due to its kinetic stability at high temperatures [297]. In addition to the thermal stability of hydrocarbons, other factors such as higher temperature and finer catalyst particle also favor CVD formation of the SWNTs.

The arc discharge process involves the use of two high purity graphite rods acting as anode and cathode. A voltage is applied between these electrodes under helium atmosphere. To obtain SWNTs, the electrodes are doped with a small amount of metallic catalyst particles [298,299]. In the process, carbon neutrals (C and C_2) and ions (C^+) deposit and then coagulate with each other to form small clusters on the cathode surface. Through an accretion of carbon atoms and coalescence between clusters, nanoparticles and nanotubes develop ultimately [298]. It is generally known that the laser ablation can provide better control of the evaporation process by congruent evaporation of constituent elements of multi-component materials in a very short period of time. In this technique, an intense pulsed laser beam irradiates the target of interest, e.g. graphite, thereby vaporizing atoms and clusters from the target. The ablation rate is related to the total mass ablated from the target per laser pulse. To produce SWNTs, the graphite target was doped with Co and Ni catalysts [292]. The production yield of CNTs from both arc discharge and laser ablation is limited. In this regard, CVD is more attractive since CVD is a well established industrial process and the CNT production is easy to scale up. Depending on the activation sources for the chemical reactions, the deposition process can be categorized into thermally activated, laser-assisted and plasma-assisted CVD.

In conventional thermally activated CVD, resistive heating of hot wall reactors provides sufficiently high temperatures for dissociation of gaseous species. This leads to the entire heating of the substrate to a high temperature before the desired reaction is achieved. Conventional chemical vapor deposition of hydrocarbons over metal catalyst has been a typical method to produce various forms of carbon fibers, filaments and multi-walled nanotubes [295,296]. The first step in a CVD process involves the absorption and decomposition of hydrocarbon molecules on transition metal (Fe, Ni, Co) particles. The carbon atoms diffuse into the interior of the catalyst to form a metal–carbon solid-state reaction. Subsequent precipitation of carbon from the supersaturated catalyst particle then

occurs and leads to the formation of a carbon tube structure [295,296]. Thermally activated CVD process tends to produce CNTs with random and tangled structures of uncontrolled length and diameter.

Formation of SWNTs or MWNTs via CVD route is governed by the size of catalyst particle, growth temperature and hydrocarbon. When the particle size is a few nanometers, SWNTs form, whereas particles a few tens of nanometers favor the formation of MWNTs. Low temperature range (600–900 °C) tends to yield MWNTs, whereas a higher temperature range (900–1200 °C) favors SWNT growth. This implies that SWNTs can only be grown from selected hydrocarbons (e.g. CO, CH₄) that exhibit chemical stability in the higher temperature range of 900–1200 °C. Common effective precursors of MWNTs such as acetylene, benzene, etc. are unstable at higher temperatures, and lead to deposition of large amounts of carbonaceous compounds other than CNTs [299].

The vapor–liquid–solid (VLS) model is often used to explain the growth of CNTs. The VLS model was originally developed by Wagner and Ellis for the fabrication of micrometer-sized whiskers in 1960 [300]. The process involves the dissolution of gaseous reactants into nanosized liquid droplets of a metal catalyst, followed by the nucleation and growth of single crystalline rods and wires. This growth is mainly induced by liquid droplets. The droplet size remains essentially unchanged during the entire process of wire growth. Each liquid droplet serves as a catalyst to assist the subsequent growth and limits the lateral growth of an individual wire. The solubility of forming liquid alloy with the target material is a major requirement of this model. Once the liquid droplet is saturated, the growth can occur at the solid–liquid interface. The VLS model is a well established mechanism responsible for the growth of nanowires and nanotubes of various inorganic materials, e.g. semiconductors, oxides [301,302]. In the case of CNTs, the liquid metal catalyst acts as (a) catalyst for the decomposition of the carbon feedstock, (b) a solvent for the carbon atoms that are released from the feedstock and (c) a template for the nucleation and growth of the nanotubes [303,304]. However, CNTs can be produced at temperature far below the carbon-catalyst eutectic temperature. Recently, Dillon et al. reported that both MWNTs and SWNTs can be produced via hot-wire CVD at a temperature of 600 and 450 °C, respectively [305]. It is likely that the solid metal catalyst allows rapid surface diffusion of carbon atoms into the metal cluster before these atoms are incorporated into the growing CNTs [306].

In general, well-aligned carbon nanotube arrays are required for cold cathodes in field emission displays, and for reinforcing materials in polymers with superior mechanical strength and stiffness. This can be achieved with the use of the anodized aluminum oxide (AAO) template having uniform and straight channels with a diameter at the nanometer level [307,308], injection CVD [309–311], plasma-enhanced CVD (PECVD) [312–314] and simple pyrolytic [315] methods. In the former case, the template simply serves as a scaffold or a mold for directed synthesis of one-dimensional structures. Kyotani et al. have prepared unidirectional CNTs by pyrolysis of propylene at 800 °C in an AAO template. In another study, metal catalyst (Co) was initially electrodeposited into the bottom of the template channels. Multibranched CNTs were grown by pyrolysis of acetylene in an AAO template with and without catalytic Co particles at the pore bottom [268]. Recently, Xu and coworkers presented an overview for the formation of aligned CNTs via CVD template growth of acetylene gas. The process flow for forming the CNTs is shown in Fig. 93 [308]. The injection CVD route involves pumping or spraying a catalyst precursor into a suitable reaction furnace. The precursor is typically a metallocene–hydrocarbon solution such as ferrocene dissolved in toluene, benzene or xylene. In most cases, aligned nanotubes are grown on quartz substrates. Windle et al. prepared aligned MWNT films on quartz substrates by injecting a solution of ferrocene in toluene into a carrier gas. Aligned MWNTs grow within the temperature range 590–850 °C, with a maximum yield at 760 °C. At 940 °C, the alignment is lost and the quantity of nanotubes within the film decreases [309]. Windle et al. also produced spun fibers of CNTs directly from an aerogel formed during synthesis by chemical vapor deposition. Thus, these

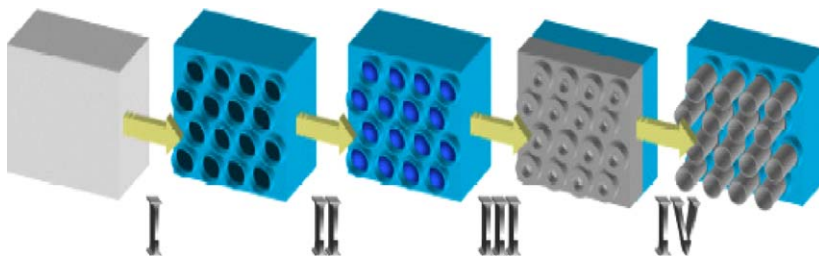


Fig. 93. Process flow for forming aligned CNTs: (I) formation of AAO template, (II) electrodeposition of catalyst, (III) CVD growth and (IV) post growth processing to expose the nanotubes (reprinted from [308] with permission from World Scientific).

fibers were produced from the dissociation of different hydrocarbons such as ethanol, ethylene glycol and hexane in the presence of an iron catalyst [316]. Dai et al. developed a pyrolytic method for producing micropatterns of perpendicularly aligned CNTs by simply pressing an adhesively sticky tape prepatterned with a non-adhesive layer onto a non-patterned carbon nanotube film, followed by peeling off the sticky tape from the quartz substrate in a dry state [315]. More recently, the research group of the University of Texas at Dallas has successfully fabricated multifunctional carbon nanotube yarns by introducing twist during spinning of MWNTs from nanotube forests. The tensile strength of MWNT

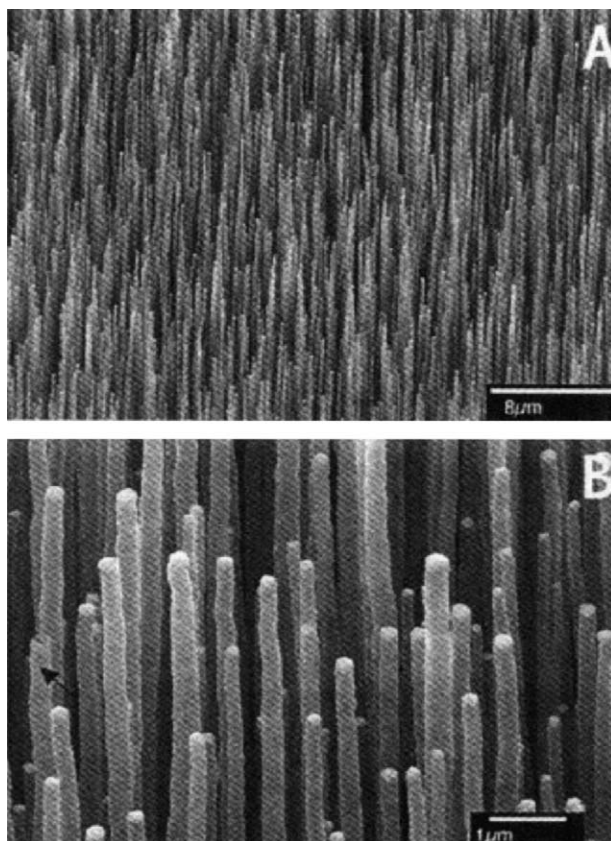


Fig. 94. SEM micrographs showing formation of aligned CNTs on nickel-coated glass using the plasma-enhanced hot filament CVD process under 1:2 C₂H₂:NH₃ gas flow. (A) Low magnification, and (B) high magnification view of the nanotubes where nickel cap on the tip of each nanotube can be clearly seen (reprinted from [312] with permission from AAAS).

yarns was reported to be greater than 460 MPa. Aligned nanotube forests comprising MWNTs were grown on an iron catalyst-coated substrate by CVD [317]. The continuous CNT yarns would find extensive applications as structural materials in industrial sectors.

PECVD is known to exhibit a distinct advantage over thermal CVD owing to its lower deposition temperature. Various types of energy resources, e.g. DC, RF, microwave and electron cyclotron resonance microwave (ECR-MW) radiation are currently used for plasma generation in CVD. The PECVD method has the advantages of producing well-alignment and selective growth on various substrates at lower temperatures. Fig. 94 shows the growth of straight and aligned CNTs on nickel-coated glass below 666 °C using the plasma-enhanced hot filament CVD technique. In the process, acetylene gas was used as the carbon source and ammonia gas was used as a catalyst and dilution gas [312]. More recently, microwave plasma-enhanced CVD has been used to grow well-aligned CNTs at a low temperature range of 600–800 °C [313,314].

CNTs prepared from the arc discharge, laser ablation and thermally activated CVD contain impurities of amorphous carbon, graphite particles and metal catalysts. Therefore, purification of CNTs is needed prior to blending with polymers. CNTs can be purified by oxidation [318], acid treatment [319] or combined oxidation and acid treatment [320–323]. Ebbesen et al. reported that oxidation of MWNTs in air at 700–750 °C would consume more than 95% of the nanotube material [318]. Liu et al. [319] treated the laser ablated SWNTs in the nitric acid or mixed 3:1 sulfuric/hydrochloric acid, then dipped in water containing a surfactant (pH 10), followed by filtering with polytetrafluoroethylene (PTFE). They reported that the SWNTs were converted from nearly endless and highly tangled ropes into short and open-ended pipes. Iijima and coworkers adopted various steps to purify SWNTs synthesized from metal catalyzed laser ablation [322,323]. These steps include heating the sample initially in air at 350 °C for 2 h in order to remove amorphous carbon. In the second

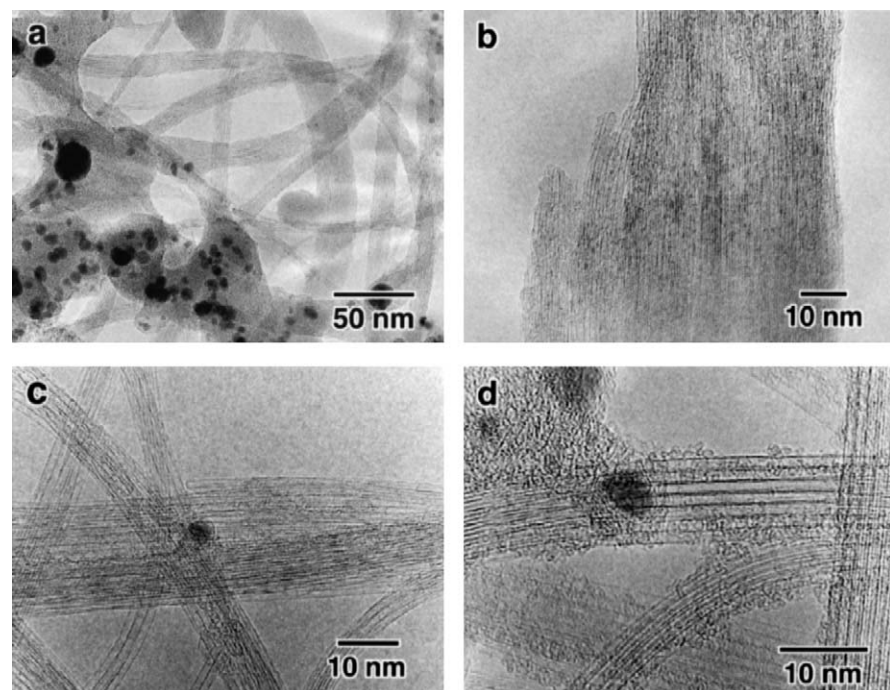


Fig. 95. High-resolution TEM micrographs of laser ablated SWNTs: (a) raw sample, (b) purified sample, (c) oxidized sample and (d) HCl acid treated sample (reprinted from [323] with permission from Elsevier).

step, the remaining soot was soaked in 36% HCl for 1 day and centrifuged for the removal of metal catalysts. In the last step, the sediment was washed with de-ionized water three times, dispersed in 0.2% benzalkonium chloride solution and filtered with PEFE membrane. Fig. 95(a–d) shows TEM micrographs of the raw SWTs prior to and after some purification steps. For the raw SWNTs, it can be seen that many metal particles are embedded in larger particles of amorphous carbon (Fig. 95(a)). However, amorphous carbon materials can be removed by oxidation (Fig. 95(c)), and part of the metal catalysts is removed by the acid treatment (Fig. 95(d)). After completion of the three-step purification process, most of the fullerenes, metal particles and amorphous carbon materials are removed. Bundles of SWNT are formed due to the aggregation of SWNTs during the filtration process; open-ended bundles can also be observed (Fig. 95(b)).

More recently, NASA–Johnson Space Center (JSC) has developed a protocol for the characterization of SWNT material quality and purity [324]. This JSC protocol standardizes the analytical procedures so that comparison of SWNTs can be done without less ambiguity. Different analytical techniques are used successfully to evaluate the homogeneity, purity and thermal stability both qualitatively and quantitatively (Table 6). For example, the amount of residual metal catalyst can be determined quantitatively from the techniques listed in this table. The numerical results are then used to assess the homogeneity, thermal stability and dispersability. Quantitative measurements of non-tubular carbon impurities still remains a problem, and have to rely on qualitative electron microscopy observations and Raman spectra analysis. In the latter case, Raman spectra of pristine SWNTs show tangential bands between 1500–1600 cm^{−1} and a broad band at ~1350 cm^{−1}, attributed to a convolution of the disorder-induced band (D band) of carbon impurities and the D-band of the SWNTs themselves [325]. As the full-width-at half-maximum (FWHM) intensity of the various carbon impurity D-bands is generally much broader than that of the nanotube D-band, an indication of the SWNT purity level can be obtained by simply examining the line-width of the D-band [324,325]. The oxygen residue in the CNT materials can be determined by Raman spectroscopy. Raman characterization is very sensitive to the presence of defects like oxygen. The D-band at around 1350 cm^{−1} is the first-order spectra of carbon nanotubes induced by disorder in a double resonant Raman process. To estimate the defect concentration, the D-mode intensity is generally normalized with respect to the intensity of the high-energy mode (G-mode) at ~1600 cm^{−1} [326].

Table 6

NASA–Johnson Space Center protocols for the characterization of SWNT quality and purity (reprinted from [324] with permission from Elsevier)

Parameter	Technique	Analysis
Purity	TGA	Quantitative—residual mass after TGA in air at 5 °C/min to 800 °C
	SEM/TEM	Qualitative—amorphous carbon impurities
	EDS	Qualitative—metal content
	Raman	Qualitative—relative amount of carbon impurities and damage/disorder
Thermal stability	TGA	Quantitative—burning temperature in TGA in air at 5 °C/min to 800 °C, dM/dT peak maximum
Homogeneity	TGA	Quantitative—standard deviation of burning temperature and residual mass taken on 3–5 samples
	SEM/TEM	Qualitative—image comparison
Dispersability	Ultra-sonication	Qualitative—time required to fully disperse (to the eye) low conc. SWCNT in DMF using standard settings
	UV/VIS/NIR	Quantitative—relative change in absorption spectra of sonicated low concentration SWCNT/DMF solution

The dispersion of CNTs in polymers is relatively poor due to the nanotubes have a strong tendency to agglomerate as a result of their high surface areas. Their very stable chemical characteristics and lack of functional sites on the surface also complicate the dispersion issue. Moreover, the length of CNTs prepared from thermally activated CVD ranging from 100 µm to several millimeters, which is undesirable for practical applications. Both physical and chemical approaches have been adopted to reduce the length of CNTs to certain extents that are suitable for blending. These methods also activate the CNTs at the open-ends via the formation of functional groups. Physical dispersion route generally includes ultrasonication, ball milling, grinding and high speed shearing [327–330]. Hading et al. reported that the physical dispersion methods can cause fragmentation of the nanotubes into shorter lengths [327]. Konya et al. reported that ball milling can effectively reduce the length of MWNTs [328]. Wang et al. demonstrated that physical methods such as ball milling, sonication and shearing can only break up large multi-agglomerates into small parts or single-agglomerates [329]. On the other hand, chemical treatment with a 3:1 concentrated sulfuric/hydrochloric acid mixture gives rise to a good dispersion by effectively severing the entangled CNTs. However, physical technique such as sonication can induce structural defects such as bending, buckling and fracture of graphene layers of CNTs. Prolonged sonication increases the defects of the carbon structures ultimately leading to the formation of amorphous carbon [330]. To prepare the nanocomposites, Qian et al. mixed the 1 wt.% CNTs with polystyrene in toluene via ultrasonication [331]. Watts et al. used a similar ultrasonication process to blend the polystyrene with CNTs [332]. As a result of the chemical and sonication treatments, the ends and the sidewalls of CNTs are covered with oxygen-containing groups such as carboxylate and ether groups. These groups serve as a starting point for tethering a variety of different chemical moieties onto CNT surfaces. Murphy et al. reported that the strong acid treatments of MWNTs cause an upshift of D and G Raman modes, due to intercalation of acid molecules, exerting pressure on the sp^2 -structure and an electron transfer from the π states in MWNTs to the oxygen atoms [333]. The oxygen content can be determined by normalizing the intensity of the first order D and G peaks with respect to the second order overtone mode D^* .

As mentioned above, Liu et al. [319] treated the laser ablated SWNTs in nitric acid or mixed 3:1 sulfuric/hydrochloric acid, and successfully converted the SWNTs from nearly endless and highly tangled ropes into short and open-ended pipes. The nanotube caps are more reactive because of their high degree of curvature can react readily with a strong acid. In this case, functional groups such as carboxylic ($-COOH$) and hydroxyl groups are bonded to the nanotubes at the open ends or the sidewall defect sites upon oxidative or acid treatments [319,334]. This implies that the CNTs can be solubilized through chemical modification or functionalization. Haddon and coworkers first used such carboxylic acid groups formed on SWNTs to interact with long-chain aliphatic amine octadecyl amine [$CH_3(CH_2)_{17}NH_2$] via amide linkages [335,336]. The carboxylic acid moieties at the defect sites can be used to link polymeric or oligomeric functional groups. This leads to an improvement in compatibility between the functional CNTs and polymer matrices of the nanocomposites. The solubilization of CNTs via chemical functionalization is considered as an effective way to achieve homogeneous dispersion of CNTs in polymer matrices of the nanocomposites [334–343]. For example, Mitchell et al. carried out functionalization of SWNTs with organic diazonium compounds, and such functionalized SWNTs were used to form polystyrene-based nanocomposites with better dispersion of the SWNTs in the matrix [237]. Tour and coworkers reported that the SWNTs can be solubilized in water by wrapping them with linear polymers such as polyvinyl pyrrolidone (PVP) and polystyrene sulfonate (PSS). This approach opens up the possibility of functionalization chemistry, both on the tubes themselves and on the wrapping polymer and solution-phase separation [344]. Hill et al. functionalized MWNTs and SWNTs with a polystyrene copolymer bearing hydroxyl moieties.

The functionalization reaction conditions were designed for the esterification of the carboxylic groups at the open ends of CNTs. The polymer-attached CNTs are soluble in common organic solvents [339]. Recently, they succeeded in functionalizing CNTs with poly(vinyl alcohol) (PVA) via esterification reactions. The resulting PVA–CNT films exhibit excellent homogeneity and optical quality [340]. Shaffer and Windle fabricated large PVA–CNT composite films based on the formation of a stable colloidal intermediate. In the process, oxidized CNTs were dispersed into the PVA solution followed by subsequent casting and controlled water evaporation [345]. In another study, Baughman and coworkers used solution spinning to synthesize the PVA–SWNT composite fibers that are tougher than spider silk [346,347]. The process uses an aqueous spinning solution in which SWNTs are dispersed using lithium dodecyl sulfate surfactant. The spinning solution is injected into a cylindrical pipe in which the coagulation bath (aqueous PVA solution) coaxially flows. A continuous gel fiber is then formed, and collected downstream on a rotating mandrel to produce the SWNT–PVA composite fibers of about 50 µm [347].

The preparation of aligned polymer–CNT bulk composites remains a scientific challenge for materials scientists. Enhanced mechanical and physical properties can be further achieved in the polymer–CNT composites provided that the CNTs are well aligned within the polymeric matrices. Very little information is available in the literature relating to this interesting topic. One approach to prepare aligned polymer–CNT composites is to infiltrate monomer into pre-aligned arrays of CNTs, followed by in situ polymerization. In a recent study, Feng et al. attempted to prepare well-aligned polyaniline–MWNT composite film by in situ polymerization (Fig. 96) [348]. The process involves dipping aligned MWNT filler in aniline/HCl solution for 12 h at 0 °C. A solution of ammonium peroxydisulfate (APS) (aniline:APS molar ratio 1:1) dissolved in HCl acid was added dropwise. The polymerization process was carried out at 0 °C for 4 h. Similarly, Raravikar et al. prepared the PMMA–MWNT composite film by infiltrating the pre-aligned MWNT arrays formed on the quartz substrate via CVD method with methyl methacrylate (MMA) monomer, followed by in situ polymerization as shown in Fig. 97 [349].

After polymerization, thermogravimetric analysis was performed for the aligned nanocomposite film. The weight fraction of MWNT in the composite is estimated to be ~4%. It is obtained as the ratio of the step height of the TGA curve at MWNT thermal degradation temperature to the initial weight of the composite film (Fig. 96(c)). Alternatively, alignment of CNTs in a polymer–CNT film can be achieved by mechanically stretching the sample above the glass transition temperatures of the polymer. When desired stretching ratio was attained, the sample was cooled down to room temperature then the load released [350,351].

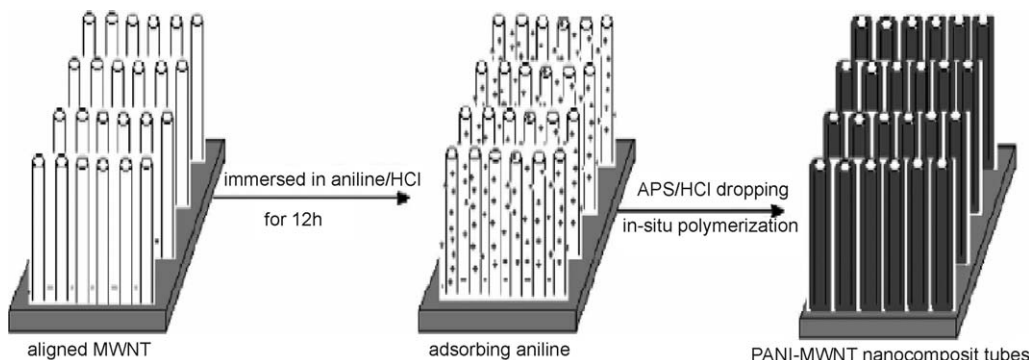


Fig. 96. Preparation of well-aligned polyaniline-MWNT composite film by in situ polymerization process (reprinted from [348] with permission from Elsevier).

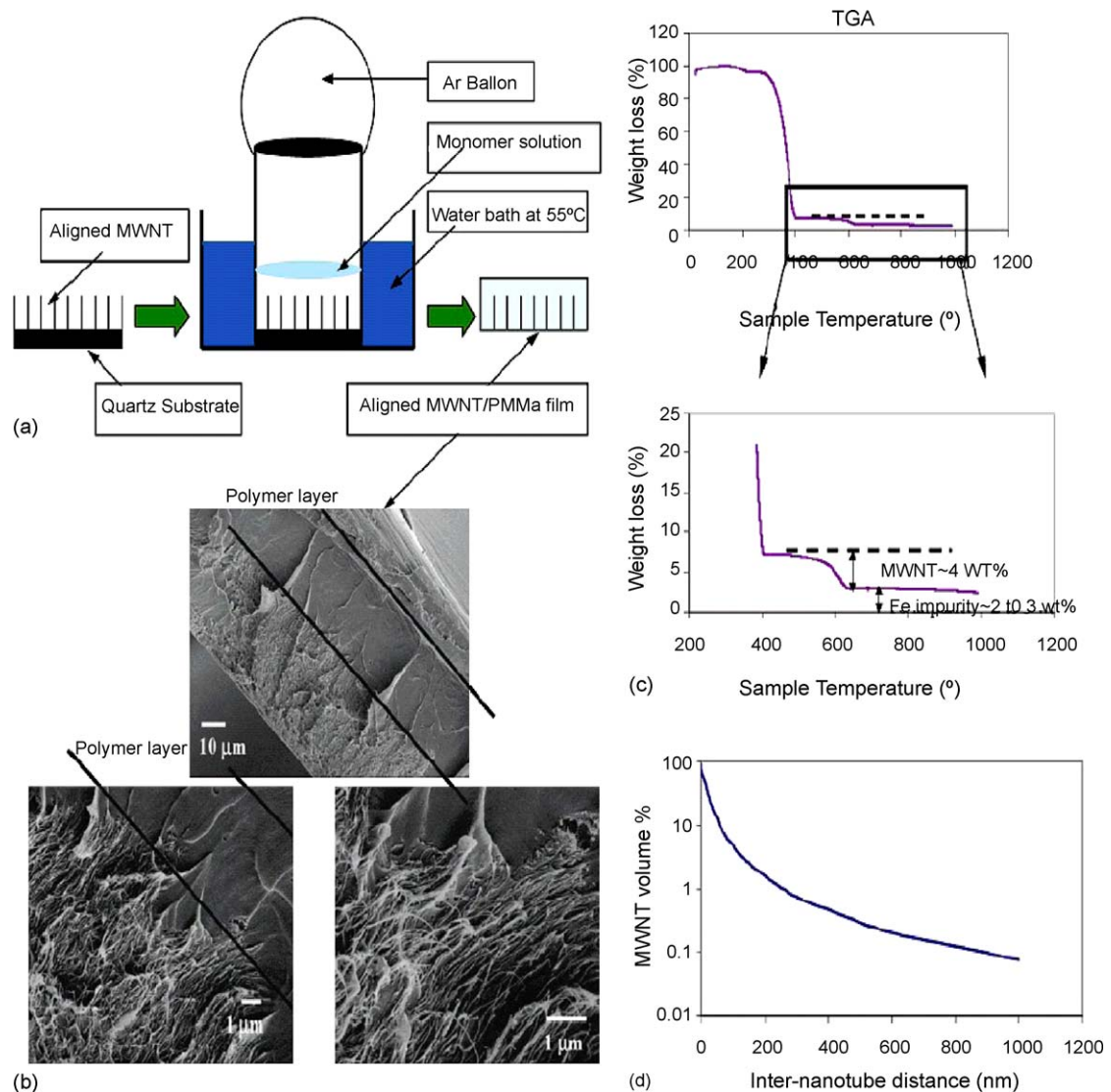


Fig. 97. Schematics of process for making thickness-aligned PMMA–MWNT film, (a) schematic of composite synthesis; (b) cross section of PMMA–MWNT film shows thickness-aligned MWNT ($\sim 30 \mu\text{m}$ long) in PMMA matrix. (c) Determination of weight fraction of MWNT by thermogravimetry (TGA); the inset in the TGA curve in (c) is magnified to reveal details. (d) A theoretical relationship between MWNT volume fraction with inter-nanotube distance (reprinted from [349] with permission from The American Chemical society).

As mentioned above, melt-compounding offers distinct advantages to produce larger volume and lower cost nanocomposites than *in situ* polymerization. The tendency of CNTs to form aggregates would be minimized by appropriate application of shear forces. McNally et al. [352] and Liu et al. [50,353] used twin-screw melt compounding to prepare the PE–MMT and PA6–MWNT composites. McNally et al. indicated that MWNTs of the PE composites appear to align along the flow direction. This is in contrast to the polymer–CNT composites prepared by solution mixing, where the CNTs tend to be randomly oriented [352]. More recently, Lopez Manchado et al. used shear mixing to disperse the SWNTs (0.25–1%) in PP. They reported that SWNTs can be dispersed uniformly in PP by shear mixing [354]. Similarly, Andrews et al. also reported well dispersed MWNTs in PP and PS using shear

mixing [355]. Other melt-compounded polymer–CNT composites include PC–MWNT [356], PE–(PC–2%MWNT) [357,358] and PMMA–MWNT [359].

4.2. Mechanical properties

The remarkable properties of CNTs offer the potential for improvement of the mechanical properties of polymers at very low concentrations. In practice, MWNTs are preferred over SWNTs as the reinforcing fillers for polymers due to their lower production cost. However, slippage between the shells of MWNTs would undermine the capability of the fillers to bear the external applied load. This is because only very weak van der Waals forces exist to link the individual grapheme shells together [360]. The inner shells can rotate and slide freely even without the presence of external stress [361,362].

Qian et al. mixed 1 wt.% MWNTs with polystyrene in toluene via ultrasonication [331]. They achieved about 36–42% increase in the elastic modulus and a 25% increase in the tensile strength of the PS–MWNT film compared to pure PS. Moreover, TEM was used to characterize the fracture behavior of the nanocomposite. They found that nanotube fracture and pullout are responsible for the failure of the composite. The fracture of MWNTs in a PS matrix implies that certain load transfer from the PS to the nanotubes has taken place. However, the pullout of MWNTs from the PS matrix indicating that the PS–nanotube interfacial strength is not strong enough to resist debonding of the fillers from the matrix. It is considered that some physical interactions exist at the PS–MWNT interface, thereby enabling load transfer from the matrix to the fillers. Generally, there are two types of interactions in a polymer–nanotube system, i.e. chemical bonding and mechanical interlocking of atoms. It is believed that local non-uniformity of a MWNT embedded in polymer matrix may result in mechanical locking of atoms [363]. Fig. 98 is a TEM micrograph showing non-uniform CNT diameter and kink at the PS–MWNT interface.

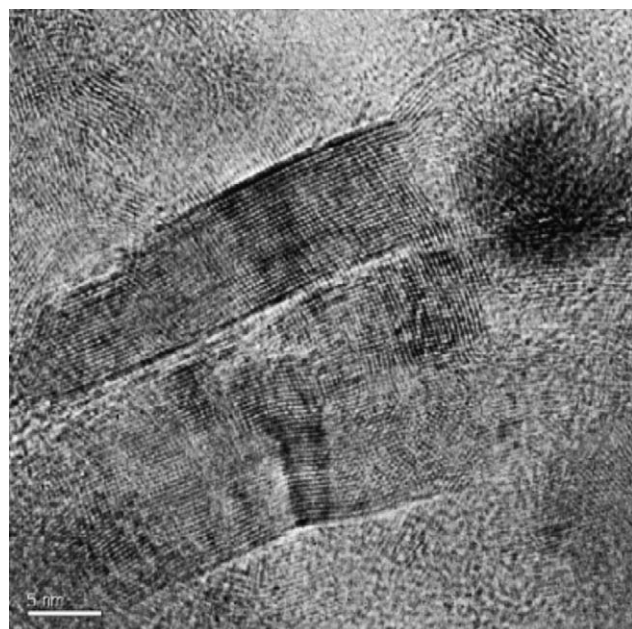


Fig. 98. TEM micrograph showing the interfacial region of the PS–MWNT nanocomposite. The kink and change in diameter of the MWNT is believed to promote mechanical interlocking (reprinted from [363] with permission from Elsevier).

The interfacial bonding between the polymer and MWNTs can be enhanced by functionalization of nanotubes as discussed above. The mechanical properties of melt-compounded of the PE–MWNT and PP–SWNT are well documented [352,354]. Lopez Manchado reported that the additions of 0.25–0.75 wt.% SWNTs to PP increase its tensile strength and stiffness as well as storage modulus considerably. The elongation at break reduces from 493 (PP) to 410% with the addition of 0.75 wt.% filler, corresponding to ~17% reduction in ductility. At 1 wt.% SWNT, both stiffness and strength are significantly reduced due to the formation of aggregates [354]. Liu et al. studied the morphology and mechanical properties of the melt-compounded PA6–MWNT nanocomposites [50]. The MWNTs were purified by dissolving the catalyst in hydrochloric acid followed by refluxing in 2.6 M nitric acid for increasing more carboxylic and hydroxyl groups. Fig. 99(a) shows the stress–strain curves for PA6 and its nanocomposites. The variations of tensile modulus and yield strength with the MWNT content are depicted in Fig. 99(b). With the addition of only 1 wt.% MWNTs, the tensile modulus and the tensile strength are greatly improved by ~115 and 120%, respectively compared to neat PA6. The tensile ductility drops slightly from 150 to 125%. They attributed the improvements of these mechanical properties to a better dispersion of MWNTs in PA6 matrix (Fig. 100(a and b)), and to a strong interfacial adhesion between the nanofillers and PA6 matrix (Fig. 100(c)). These lead to favorable stress transfer across polymer to MWNTs. Moreover, the MWNTs are sheathed by several small polymer beads (indicated by the arrows) (Fig. 100(d)). Such nanotubes bridge the microcrack

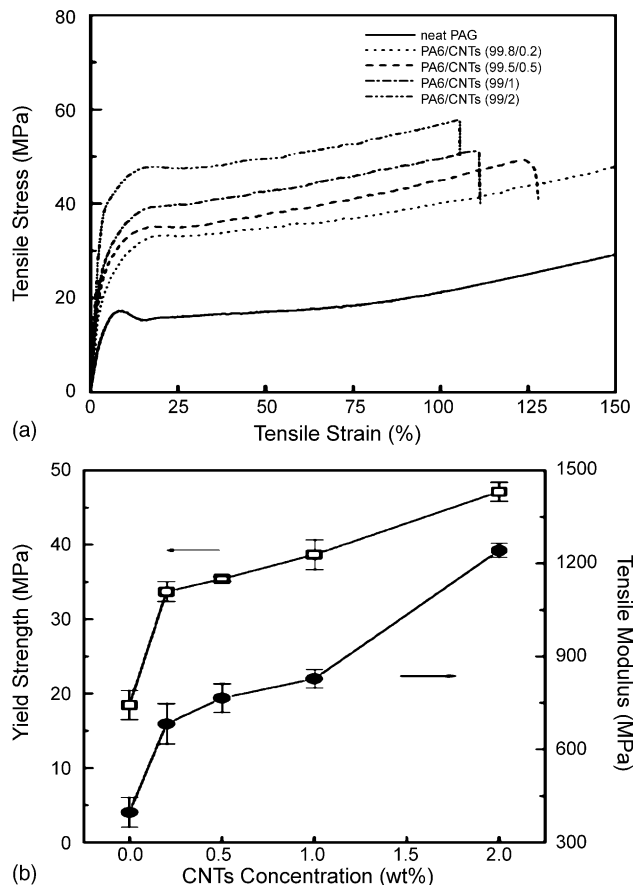


Fig. 99. (a) Typical stress–strain curves. (b) Yield stress and tensile modulus for PA6 and its nanocomposites as a function of MWNTs concentration (reprinted from [50] with permission from The American Chemical Society).

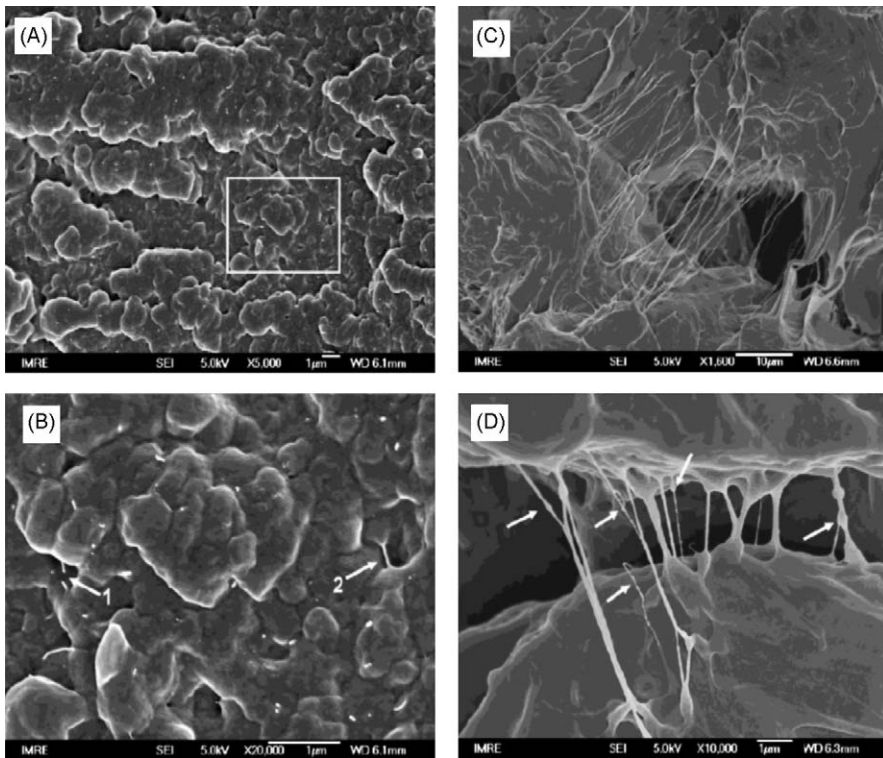


Fig. 100. (A) Low and (B) high magnification SEM images showing uniform dispersion of nanofillers in the matrix of PA6–MWNT nanocomposite reinforced with 0.5 wt.% MWNTs. (C) Low and (D) high magnification SEM images showing microcracks linked by stretched nanotubes (reprinted from [50] with permission from The American Chemical Society).

effectively. From these, it is evident that a very small addition of CNTs to thermoplastics improves their tensile strength and stiffness significantly; this is accompanied by a moderate reduction in tensile ductility. This behavior is in sharp contrast to the clay silicates that cause a very large reduction in tensile ductility of the semi crystalline thermoplastics.

For the amorphous polymers, the tensile ductility generally is similar and not impacted by CNT loading. Jia et al. prepared the PMMA–MWNT nanocomposites via in situ polymerization using raw and acid-treated nanotubes in the presence of free radical initiator (AIBN) [364]. They reported that the tensile strength of PMMA improves considerably with increasing content of treated nanotubes. The tensile toughness of the nanocomposites increases very slightly. However, the tensile strength and toughness of the composites filled with raw MWNTs decrease with increasing filler content. Gorga and Cohen investigated the effect of nanotube orientation on the mechanical properties of the PMMA–MWNT nanocomposites reinforced with 0.1–10 wt.% MWNT [365]. The nanotubes were oriented by drawing the extrudates at different draw ratios. The addition of 1 wt.% MWNT to PMMA (oriented nanocomposite) leads to the largest increase in tensile toughness with a 170% improvement over oriented PMMA. Fig. 101 shows the effect of extrudate ratio on the tensile toughness and modulus for PMMA and PMMA–1%MWNT nanocomposite. It can be seen that the tensile toughness and modulus increase with increasing draw ratio for both PMMA and filled composite. The tensile toughness is determined from the area of tensile stress–strain curve. Apparently, the tensile toughness of the nanocomposites is lower than that for PMMA in the unoriented case (draw ratio = 1) and is equivalent to PMMA at both draw ratios of 2.5:1 and 4.5:1. The tensile toughness of the nanocomposite is significant higher than that of PMMA under a draw ratio of 10:1. They attributed

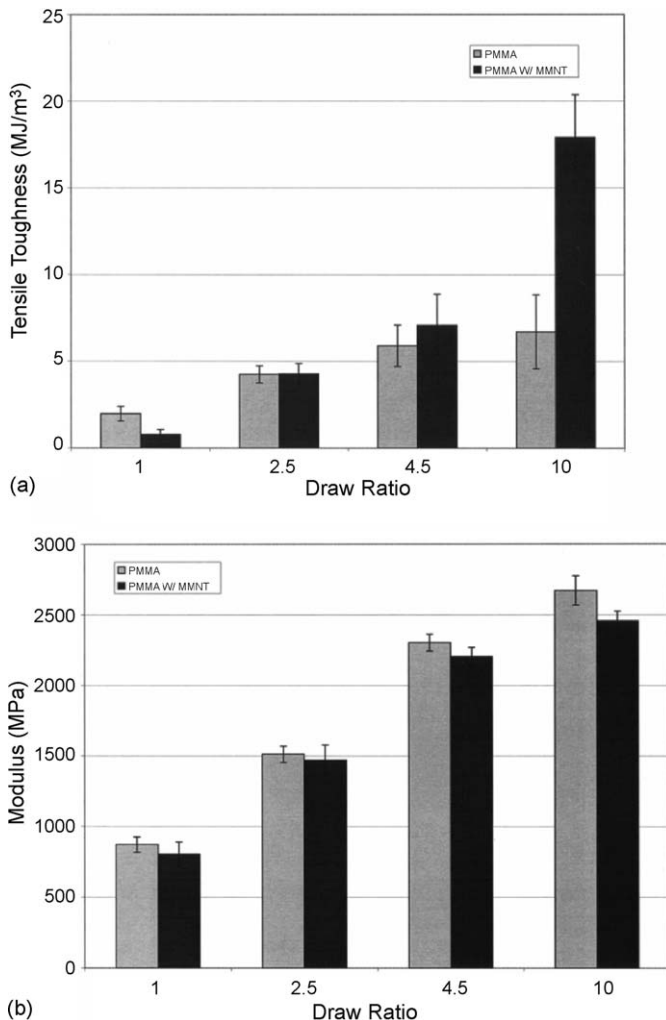


Fig. 101. The effect of extrudate draw ratio on (a) tensile toughness and (b) modulus for PMMA and PMMA-1 wt.% MWNT samples (reprinted from [365] with permission from Wiley).

this to the nanotubes oriented normal to the direction of craze propagation and crack development would bridge cracks that developed via craze precursors during the tensile tests on the basis of SEM observations (Fig. 102).

Very recently, Weidisch and coworkers studied the toughness behavior of melt-blended PC-MWNT nanocomposites using the EWF approach [366]. They reported that the addition of 2 wt.% MWNT to PC enhance its non-essential work of fracture (βw_p) considerably. Fig. 103(a) shows the typical force-displacement curves for the PC-2 wt.% MWNT nanocomposites having different ligament lengths. This figure clearly demonstrates the validity of the EWF approach as evidenced by self-similarity of the force-displacement curves. The effects of nanotube contents on the tensile behavior of PC and its nanocomposites are depicted in Fig. 103(b). The addition of 2 wt.% MWNT to PC leads to a slight reduction of the maximum displacement from 1.17 to 1.08 mm. On further increasing the MWNT contents to 4 and 6 wt.%, the maximum displacement decreases sharply to 0.82 mm, corresponding to a reduction of 24% in tensile ductility. Fig. 104(a) shows the plots of specific work of fracture versus ligament for pure PC and its nanocomposites. The βw_p values for these samples are

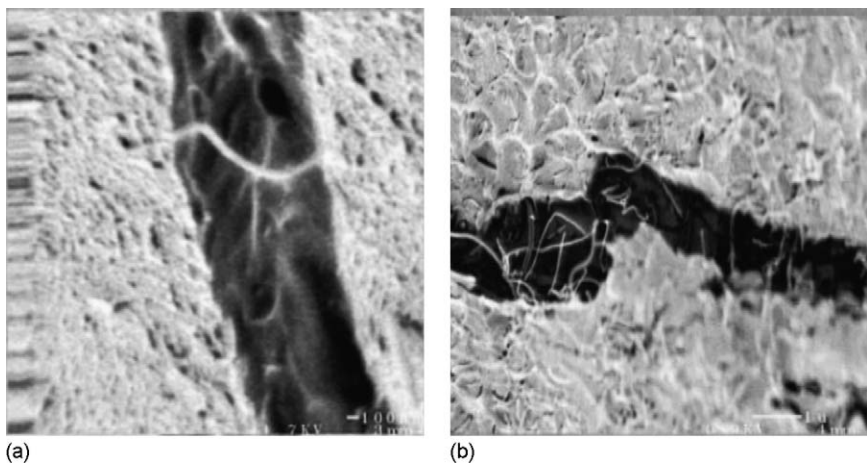


Fig. 102. SEM images of nanotubes bridging a crack in PMMA at the fracture surface: (a) PMMA–3 wt.% MWNT and (b) PMMA–5 wt.% MWNT nanocomposites with a 10:1 draw ratio (reprinted from [365] with permission from Wiley).

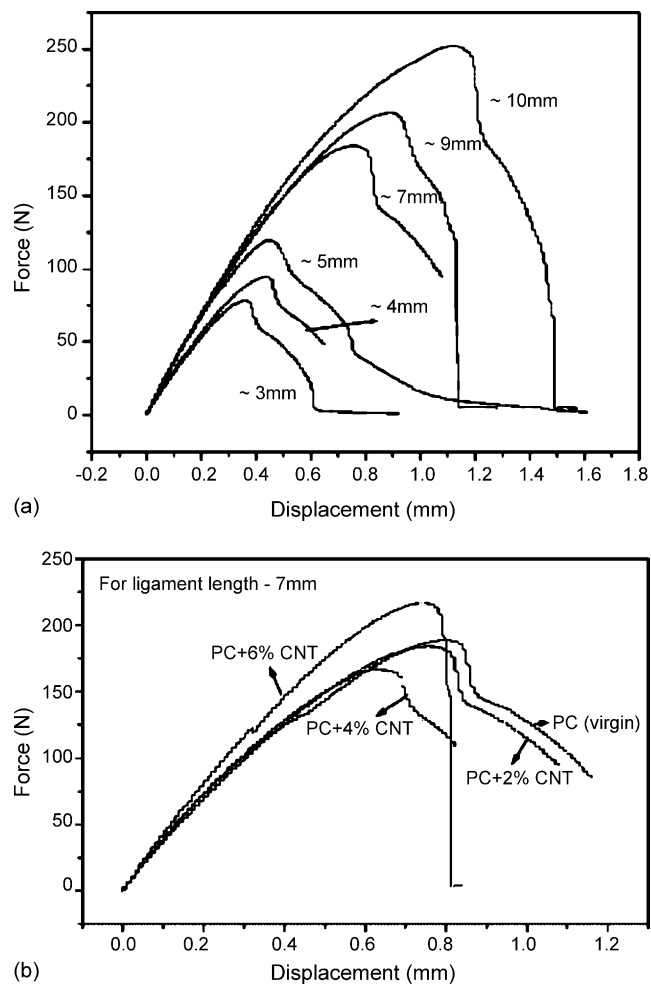


Fig. 103. Force–displacement curves for (a) PC–2 wt.% MWNT nanocomposite having different ligament lengths and (b) PC and its nanocomposites with a ligament length of 7 mm (reprinted from [366] with permission from Wiley-VCH).

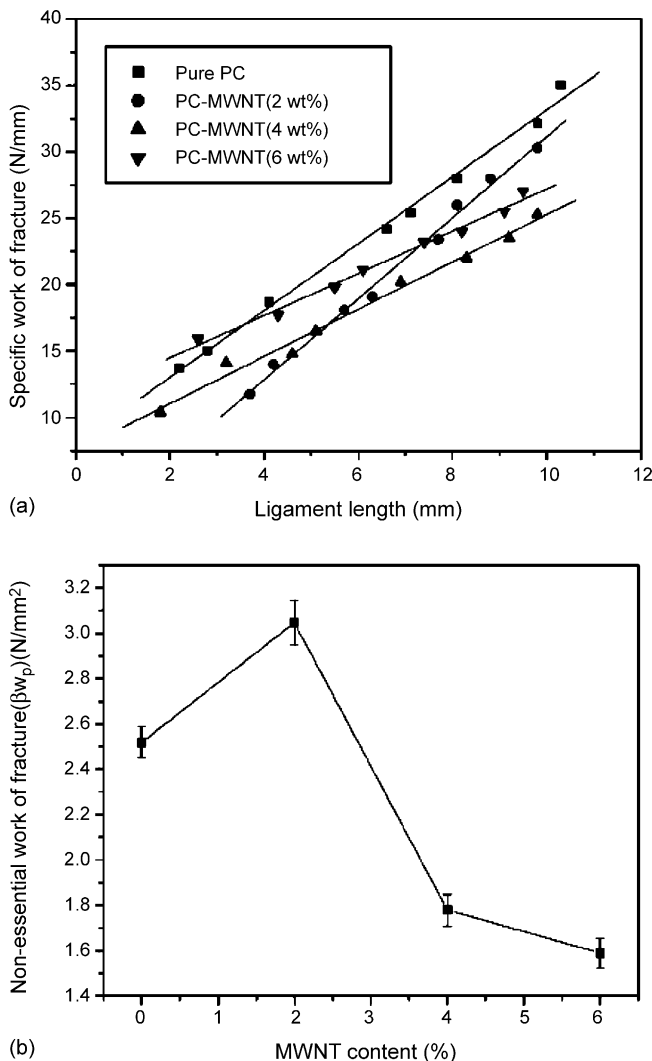
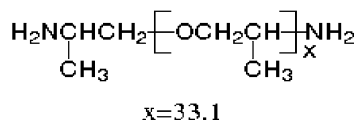
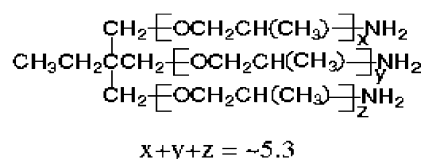


Fig. 104. (a) Specific work of fracture versus ligament length for PC and its nanocomposites. (b) Dependence of non-essential work of fracture on MWNT content (reprinted from [366] with permission from Wiley-VCH).

determined from the slope of linear regression lines; their dependency on nanotube content is shown in Fig. 104(b). The non-essential work of fracture is a measure of the resistance against crack propagation. It is evident that the plot reaches an apparent maximum at 2 wt.% MWNT content, indicating enhanced resistance to crack propagation compared to pure PC. The microcrack bridging effect is reported for the PC–2 wt.% MWNT nanocomposite. At 4 wt.% MWNT, a tough-to-brittle transition is observed.

Liu and Wagner investigated the mechanical properties of rubbery and glassy epoxy resins reinforced with MWNTs [367]. The morphology and mechanical behavior of these nanocomposites were compared and contrasted. Rubbery epoxy was prepared by curing Epon 828 resin with α,ω -polypropyleneoxide diamine (Jeffamine D-2000). Thus, the Epon 828/D-2000 has a sub-ambient T_g , i.e. the epoxy matrix was in a rubbery state at room temperature. Glassy epoxy was prepared by curing Epon 828 resin with glycolitic polypropyleneoxide triamine (Jeffamine T-403). As a result, Epon 828/T-403 with a T_g of ~80 °C was in a glassy state at room temperature. The chemical structures of curing agents are given as follows:

Jeffamine D-2000**Jeffamine T-403**

The pristine and functionalized MWNTs were used to reinforce these epoxy resins. MWNTs were functionalized with carboxylic groups by sonication in a 1:3 volume concentrated solution of $\text{HNO}_3/\text{H}_2\text{SO}_4$. Fig. 105(a–d) shows SEM fractographs of rubbery and glassy nanocomposites reinforced with 1 wt.% functionalized MWNTs. The MWNTs (bright dots) are found to disperse homogeneously in the rubbery Epon 828/D-2000 matrix. Moreover, these tubes are broken apart rather than pulling out from the matrix surface, indicating the existence of strong interfacial bonding between nanotubes and the matrix. In contrast, the nanotubes are dispersed non-uniformly in the glassy Epon 828/T-403 matrix (Fig. 105(c)). Careful examination of the fracture surface reveals that some nanotubes are curved or bent, as indicated by the arrows in the micrograph (Fig. 105(d)). The poor dispersion of nanotubes in the Epon 828/T-403 epoxy matrix is attributed to the relatively high viscosity of the matrix before curing. Homogeneous dispersion of MWNTs in the Epon 828/D-2000 matrix promotes better

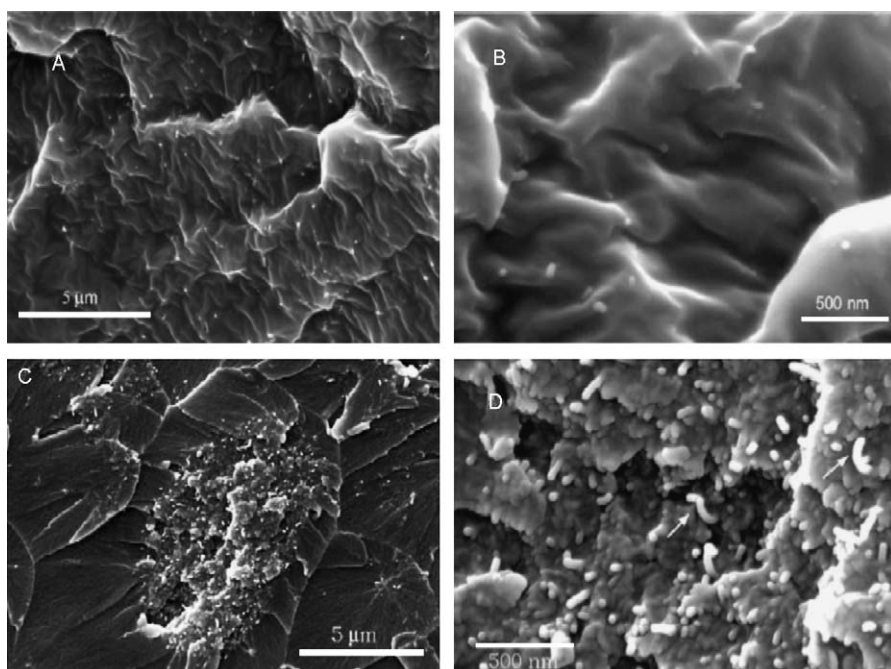


Fig. 105. SEM images of fracture surfaces of 1 wt.% *f*-MWNTs-epoxy resin nanocomposites. (A) Overall morphology of Epon 828/D-2000 composite; (B) detail of morphology from (A); (C) Morphology of Epon 828/T-403 composite; (D) detail of morphology from (C) (reprinted from [367] with permission from Elsevier).

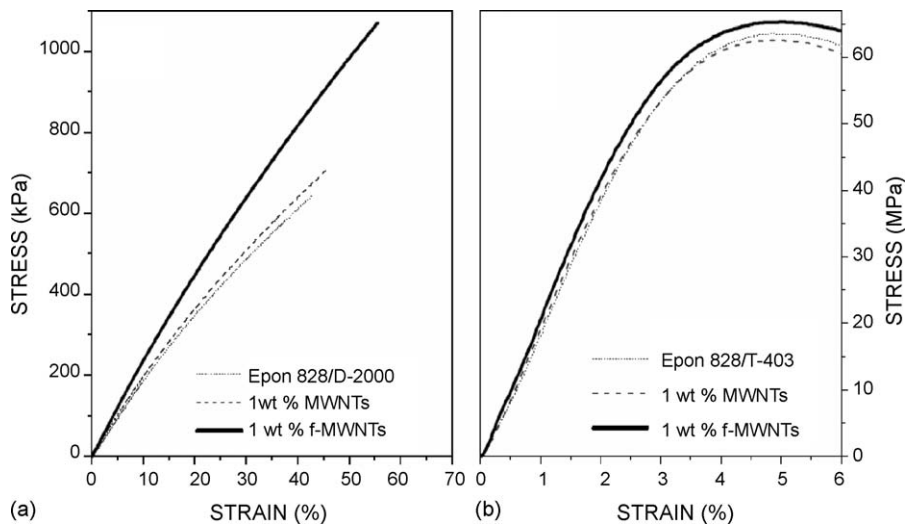


Fig. 106. Tensile stress–strain curves for (a) neat epoxy Epon 828/D-2000 and its nanocomposites; (b) neat epoxy Epon 828/T-403 and its nanocomposites (reprinted from [367] with permission from Elsevier).

mechanical performance as expected. Fig. 106(a and b) show the tensile stress–strain curves of rubbery and glassy nanocomposites reinforced with 1 wt.% pristine and functionalized MWNTs, respectively. The results of tensile tests are summarized in Table 7. Apparently, the rubbery Epon 828/D-2000 resin exhibits a much higher strain at break at room temperature compared to its brittle counterpart resin. The tensile modulus of rubbery resin increases from 1.89 to 2.41 MPa by adding only 1 wt.% *f*-MWNTs; this corresponds to a 28% improvement in stiffness. Moreover, the strain at break of this nanocomposite is 60% higher than that of its neat resin. In contrast, only a marginal improvement in modulus is observed for the 1 wt.% *f*-MWNTs–(Epon 828/T-403) composite compared to its neat epoxy resin. The strain at break of the nanocomposite is ~8% higher than that of neat epoxy resin. However, the impact strength of glassy Epon 828/T-403 resin is improved considerably with the addition of 1 wt.% pristine and functionalized MWNTs (Fig. 107). A significant

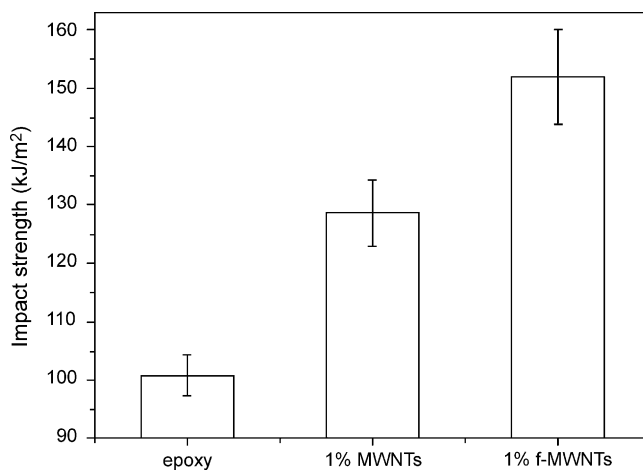
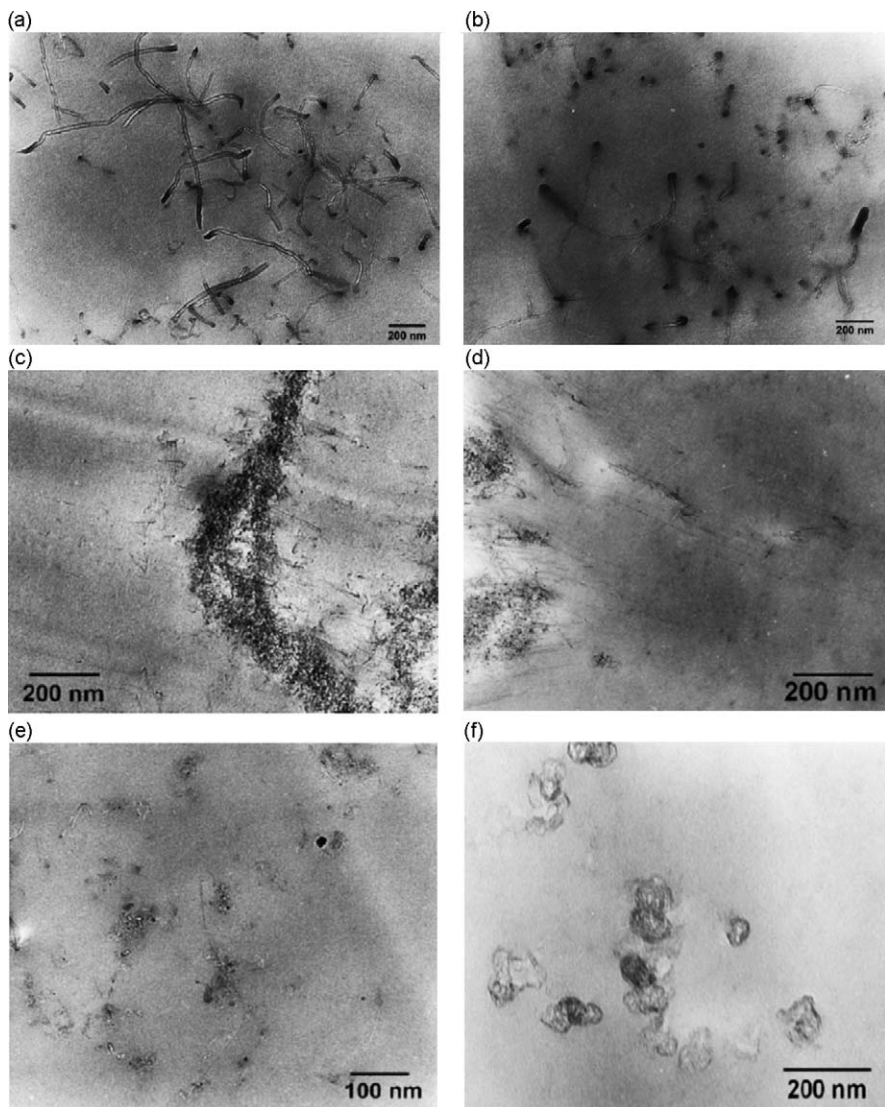


Fig. 107. Impact behavior of neat epoxy Epon 828/T-403 and its nanocomposites (reprinted from [367] with permission from Elsevier).

Table 7

Tensile properties of nanotube-based composites and pure epoxy resins (reprinted from [367] with permission from Elsevier)

Epoxy resin composites formulation	Tensile modulus (MPa)	Tensile strength (MPa)	Break strain (%)
1 wt.% MWNTs	1.97 ± 0.08	0.67 ± 0.11	43.6 ± 9.5
1 wt.% <i>f</i> -MWNTs	2.41 ± 0.09	0.98 ± 0.16	51.0 ± 11.1
Epon 828/D-2000	1.89 ± 0.05	0.48 ± 0.14	31.9 ± 1.3
1 wt.% MWNTs	2166.8 ± 60.3	63.99 ± 2.85	6.36 ± 0.99
1 wt.% <i>f</i> -MWNTs	2250.6 ± 25.2	64.05 ± 1.43	7.54 ± 0.92
Epon 828/T-403	2161.8 ± 53.4	64.67 ± 1.11	6.99 ± 0.66

Fig. 108. TEM images showing dispersion of nanofillers in matrices of the composites: (a) epoxy/MWCNT, (b) epoxy/MWCNT-NH₂, (c) epoxy/DWCNT, (d) epoxy/DWCNT-NH₂, (e) epoxy/SWCNT and (f) epoxy/CB (reprinted from [368] with permission from Elsevier).

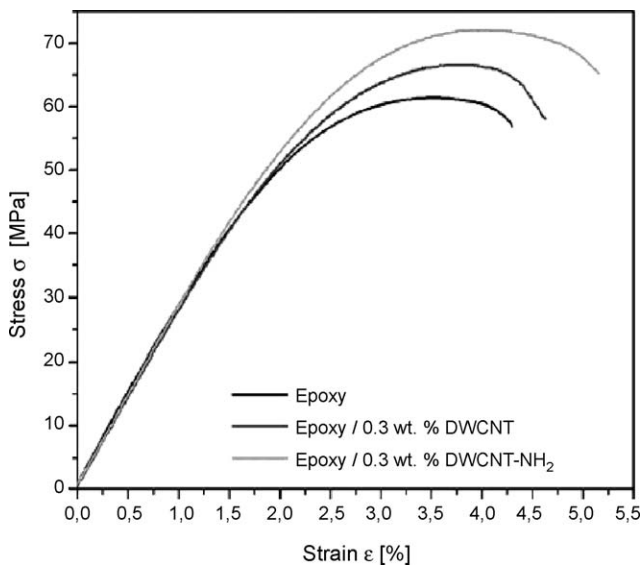


Fig. 109. Stress–strain curves of the neat epoxy and its nanocomposites containing 0.3 wt.% DWNTs and 0.3 wt.% DWCNT-NH₂ (reprinted from [368] with permission from Elsevier).

Table 8

Mechanical properties of CNT and CB reinforced composites (reprinted from [368] with permission from Elsevier)

	Filler type/content (wt.%)	Young's modulus (MPa)	Ultimate tensile strength (MPa)	Fracture toughness, K_{IC} (MPa m ^{1/2})
Epoxy	0.0	2599 (± 81)	63.80 (± 1.09)	0.65 (± 0.062)
Epoxy/CB	0.1	2752 (± 144)	63.28 (± 0.85)	0.76 (± 0.030)
	0.3	2796 (± 34)	63.13 (± 0.59)	0.86 (± 0.063)
	0.5	2830 (± 60)	65.34 (± 0.82)	0.85 (± 0.034)
Epoxy/SWCNT	0.05	2681 (± 80)	65.84 (± 0.64)	0.72 (± 0.014)
	0.1	2691 (± 31)	66.34 (± 1.11)	0.80 (± 0.041)
	0.3	2812 (± 90)	67.28 (± 0.63)	0.73 (± 0.028)
Epoxy/DWCNT	0.1	2785 (± 23)	62.43 (± 1.08)	0.76 (± 0.043)
	0.3	2885 (± 88)	67.77 (± 0.40)	0.85 (± 0.031)
	0.5	2790 (± 29)	67.66 (± 0.50)	0.85 (± 0.064)
Epoxy/DWCNT-NH ₂	0.1	2610 (± 104)	63.62 (± 0.68)	0.77 (± 0.024)
	0.3	2944 (± 50)	67.02 (± 0.19)	0.92 (± 0.017)
	0.5	2978 (± 24)	69.13 (± 0.61)	0.93 (± 0.030)
Epoxy/MWCNT	0.1	2780 (± 40)	62.97 (± 0.25)	0.79 (± 0.048)
	0.3	2765 (± 53)	63.17 (± 0.13)	0.80 (± 0.028)
	0.5	2609 (± 13) ^a	61.52 (0.19) ^a	^a
Epoxy/MWCNT-NH ₂	0.1	2884 (± 32)	64.67 (± 0.13)	0.81 (± 0.029)
	0.3	2819 (± 45)	63.64 (0.21)	0.85 (± 0.013)
	0.5	2820 (± 15)	64.27 (± 0.32)	0.84 (± 0.028)

^a High viscosity disabled degassing-composite contained numerous voids.

50% improvement in impact strength is observed in the nanocomposite reinforced with 1 wt.% functionalized nanotubes, compared to the unreinforced glassy epoxy resin.

Schulte and coworkers studied the effect different carbon nanotubes on the mechanical properties of epoxy resin [368]. The reinforcements included single-wall, double-wall (DWCNT) and multi-wall carbon nanotubes as well as carbon black (CB) particles. The DWNTs and MWNTs were functionalized with amino-groups. Fig. 108(a–f) is the TEM micrographs showing the dispersion of these reinforcing carbon materials in the DGEBA epoxy resins. Both pristine and functionalized MWNTS exhibit a high dispersibility in the epoxy matrix. The MWNTs exhibit the smallest specific surface area (SSA), i.e. $\sim 200 \text{ m}^2/\text{g}$ among the nanotubes investigated. Moreover, Fig. 108(b) indicates a very good matrix adhesion of the amino-functionalized MWNTs due to the amino groups can react with the epoxy resin to form covalent bonds. Other carbon nanotubes with larger surface areas tend to agglomerate in the epoxy matrix, and the degree of agglomeration depends on the type of carbon materials and surface functionalisation applied to the nanotubes (Fig. 108(c–f)).

Fig. 109 shows representative stress–strain curves of the neat epoxy and its nanocomposites containing 0.3 wt.% DWNTs and 0.3 wt.% DWNT-NH₂. Apparently, the incorporation of 0.3 wt.% DWNTs into neat epoxy leads to an increase in ultimate tensile strength (UTS) and strain to failure,

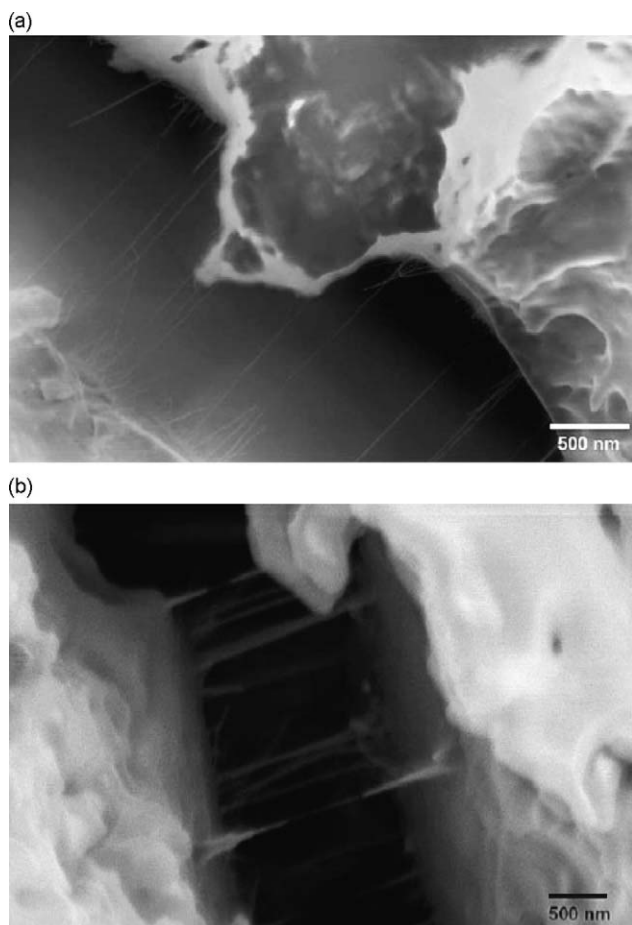


Fig. 110. SEM micrographs showing the crack bridging effect in epoxy/DWCNT nanocomposites reinforced with (a) amino-functionalized and (b) pristine nanofillers. The bridged gap length is about 500–1000 times the average diameter of the nanotubes (reprinted from [368] with permission from Elsevier).

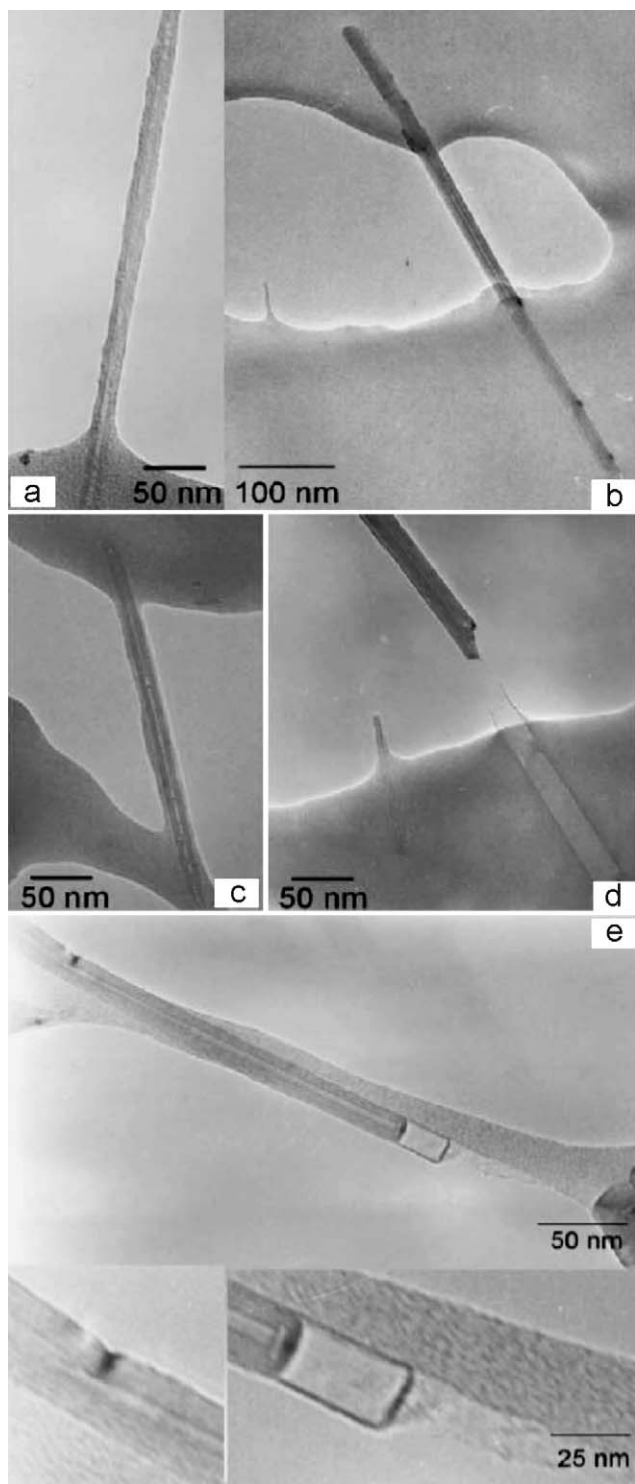


Fig. 111. TEM images of amine-functionalised MWNTs. (a) Matrix covers the surface of the carbon nanotubes which indicates an improved interaction, (b–d) show nanotubes bridge the microcracks and pores in the matrix. (e) Telescopic pull-outs substantiate the evidence of improved interactions (reprinted from [369] with permission from Elsevier).

particularly for amino-functionalized DWNT. The tensile and fracture toughness (K_{IC}) test results of the nanocomposites investigated are summarized in Table 8. This table reveals that the SWNTs exhibit the relatively large improvement in UTS due to their highest aspect ratio and SSA values. The DWNTs consisting of two concentric layers with a smaller SSA and lower aspect ratio than SWNTs yield a maximum UTS value of 67.8 MPa. The amino-functionalisation of the DWNTs generally results in an improvement of the UTS. The addition of 0.5 wt% DWNT-NH₂ leads to an increase in UTS from 63.8 (epoxy) to 69.1 MPa, corresponding to ~8.3% enhancement. The additions of pristine and functionalised MWNTs have little effect on the UTS. This is attributed to the absence of stress transfer to internal layers of MWNTs, only the outermost layer contributes to the tensile reinforcement. It is noted that the additions of pristine and functionalised carbon nanotubes and carbon black particles lead to relatively large enhancements in Young's modulus and fracture toughness. The most significant improvements stiffness (+15%), fracture toughness (+43%) and tensile strength (+10%) can be attained in the nanocomposite containing 0.5 wt.% amino-functionalised DWNTs. The improvement in the fracture toughness of epoxy resin due to the CNT additions can be explained in terms of the crack-bridging mechanism as shown in Fig. 110. The high strain to failure of CNTs [28,52] compared

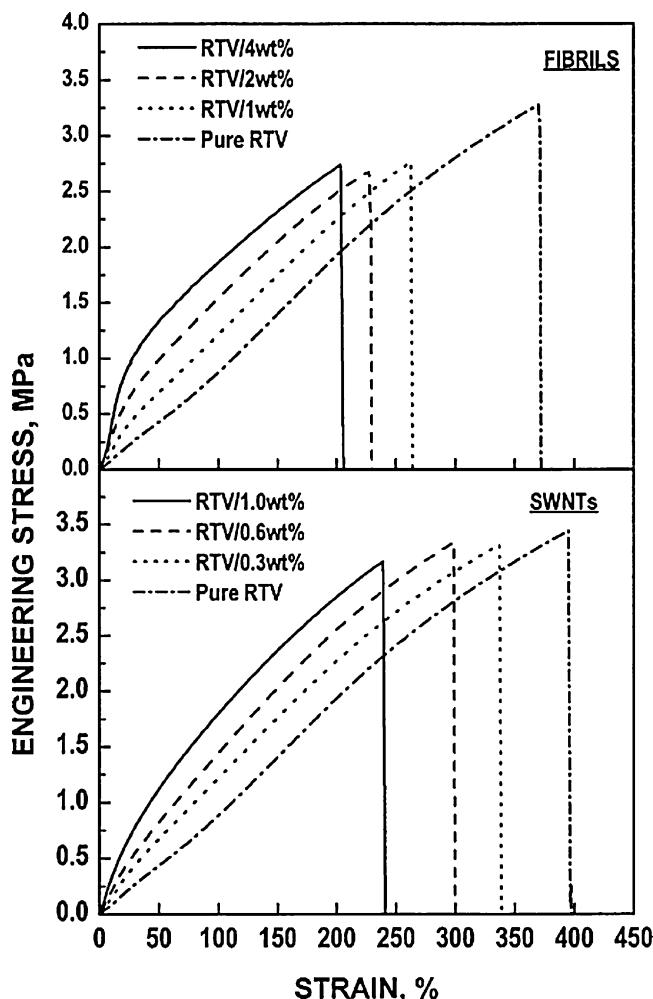


Fig. 112. Stress–strain curves for silicone rubber and its composites reinforced with various carbon fiber and SWNT weight fractions (reprinted from [55] with permission from Elsevier).

to the epoxy enables extended deformation of nanotubes during mechanical loading. This allows the pristine and functionalized CNTs undergo crack bridging during deformation. In another study using TEM technique [369], Schulte and coworkers demonstrated that the amine-functionalised MWNTs improve the fracture toughness of epoxy resin by bridging the microcracks and pores in the matrix (Fig. 111). The nanotubes are sheathed in a polymer material (Fig. 111(a)) due to strong interactions between functionalised nanotubes and matrix. Consequently, telescopic pull-out associated with improved interactions can be readily seen in the TEM micrographs (Fig. 111(e)). Telescopic pull-out is resulted from the fracture of the outer layer due to a strong interfacial layer and pull-out of the inner tube.

Wagner and coworkers studied the influence of SWNT and carbon nanofiber additions on the mechanical performances of silicone rubber, i.e. PDMS [55]. They reported that SWNTs are effective reinforcements for silicone rubber due to their large aspect ratio and low density. Fig. 112 shows representative stress-strain curves for pure silicone rubber (denoted as RTV) and its nanocomposites reinforced with different contents of carbon nanofiber and SWNT, respectively. For the RTV-SWNT nanocomposites, the initial modulus (measured by fitting a straight line to the data below 10% strain) tends to increase almost linearly with increasing filler content. The variation of initial modulus of the composites as a function of filler weight fraction is shown in Fig. 113. Taking the aspect ratio (f) of stiff particles into account, Guth theory (Eq. (28)) can be modified to the following equation:

$$E_c = E_m(1 + 0.67 f\phi + 1.62 f^2\phi^2) \quad (30)$$

It can be seen from this figure that the Guth equation agrees reasonably with the experimental data using $f = 120$ for the SWNTs and $f = 70$ for the carbon nanofibers. The dash curve is typical of conventional fillers such as carbon black particles. The SWNTs are recognized to possess a very large aspect ratio value of over 1000. However, theoretical prediction for the SWNTs with $f = 1000$ does not agree with the experimental data. This is because the theory ignores an increase in the surface-area-to-volume ratio for the nanofillers. The poorer dispersion and bending of CNTs in the polymer matrix also contribute to a discrepancy between estimated and actual data. Fig. 113 also shows that the SWNTs exhibit a much higher reinforcing effect than the carbon fiber and carbon black particles.

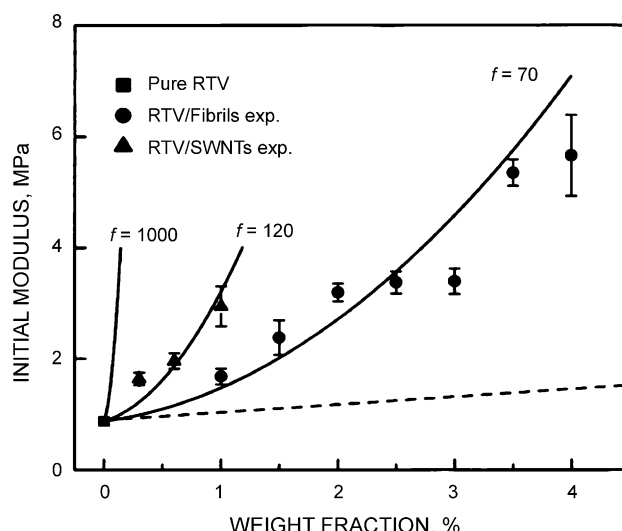


Fig. 113. Initial modulus of the silicone rubber composites as a function of filler weight fraction. The solid curves are theoretical predictions based on Guth equation with different filler aspect ratios (reprinted from [55] with permission from Elsevier).

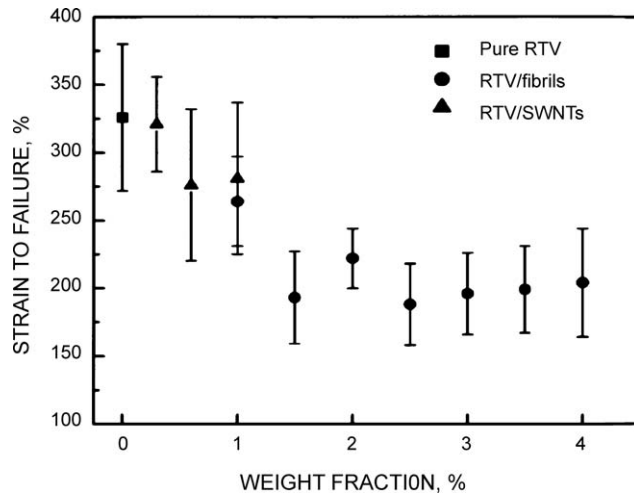


Fig. 114. Strain to failure as a function of filler weight fraction for the silicone rubber composites (reprinted from [55] with permission from Elsevier).

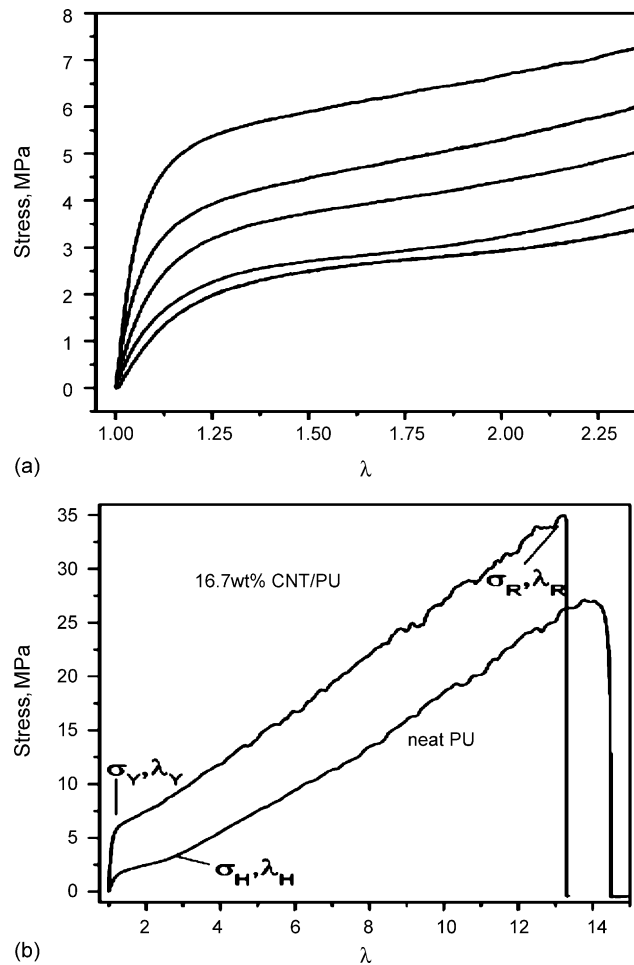


Fig. 115. Engineering stress-deformation behavior for various PU–CNT nanocomposites up to (a) $\lambda = 2.35$ and (b) to failure. Increasing volume fraction of CNT is 0, 0.57, 2.9, 5.9 and 10.2% (reprinted from [370] with permission from Elsevier).

The effect of SWNT and carbon fiber additions on the tensile ductility of silicone rubber is shown in Fig. 114. The strain to failure drops from 325 (RTV) to 275% upon loading with 1 wt.% SWNTs, corresponding to ~15% reduction.

Vaia and coworkers studied the deformation behavior of thermoplastic PU–MWNT nanocomposites [370]. They demonstrated that the carbon nanotube additions to PU improve the mechanical properties such as increased modulus and yield stress, without loss of the ability to stretch the elastomer above 1000% before final failure (Fig. 115). The results of tensile test parameters such as the initial modulus, engineering stress (σ_y), and elongation (λ_y) at the apparent yield, engineering stress

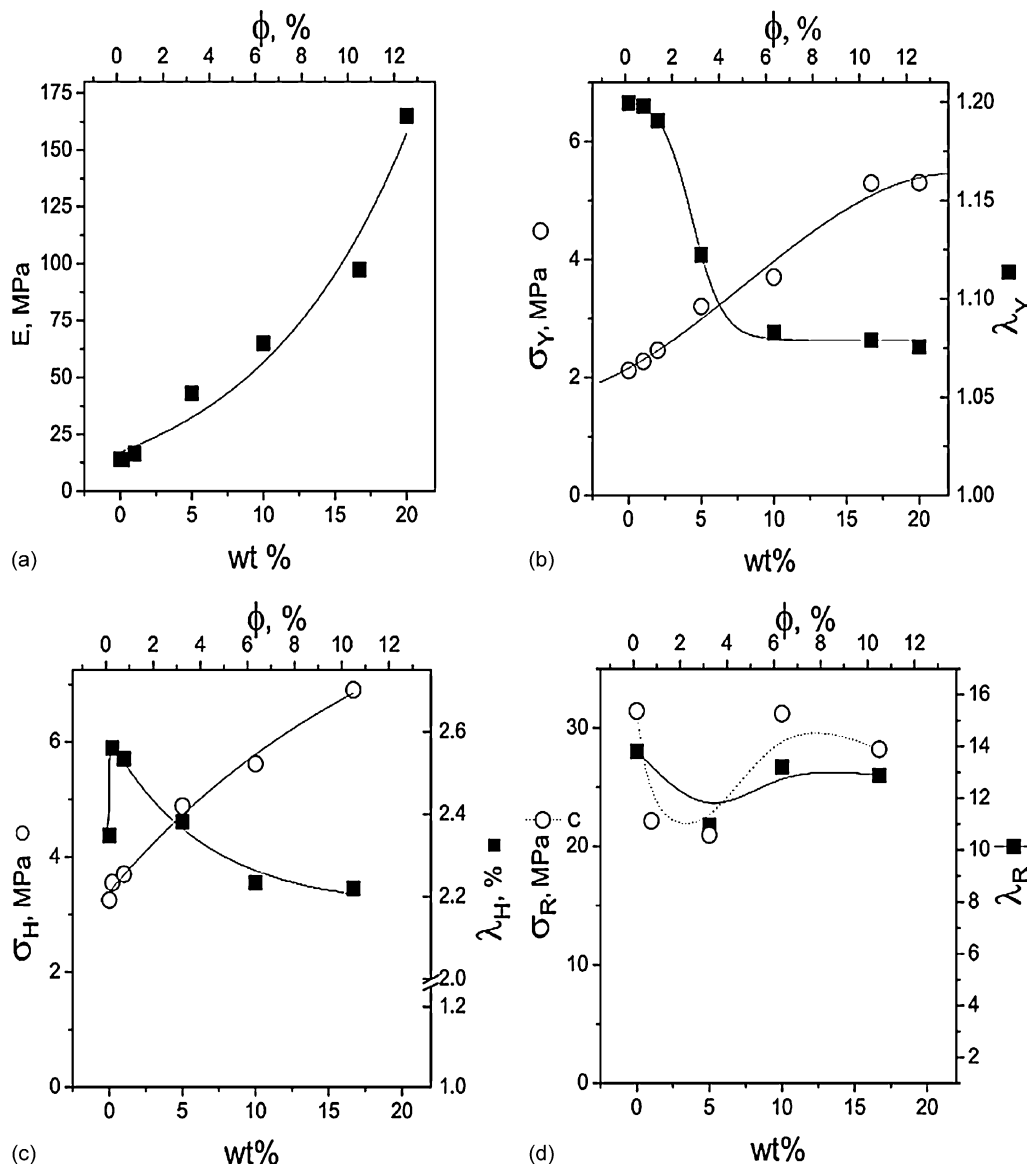


Fig. 116. Mechanical characteristics of the PU–CNT nanocomposites: (a) Initial Young's moduli, E ; (b) stress (σ_y) and elongation (λ_y) at yield; stress (σ_H) and elongation (λ_H) at hardening; (d) stress (σ_R) and elongation (λ_R) at rupture. Lines express qualitative data trends. Open circles are stress (σ) data and filled squares are elongation (λ) values (reprinted from [370] with permission from Elsevier).

(σ_H), and elongation (λ_H) at the onset of strain hardening and the elongation at rupture (λ_R) are summarized in Fig. 116(a–d). Generally, the addition of CNTs increases the modulus and strength of PU without degrading deformability. The elongation at break decreases very slightly with CNT loading up to 17 wt %. At this filler loading, the nanocomposite still maintains a very high value of elongation at rupture, i.e. 1200% (Fig. 116(d)).

For the purpose of comparison, the moduli of different elastomers (e.g. PDMS, PU and rubbery epoxy) reinforced with MWNT and clay as a function of filler content are shown in Fig. 117. These include the PU–MWNT data from Vaia, rubbery epoxy (Epon 828/D-2000)–MMT data from Shi [143], PDMS–MMT data from Burnside [167], PDMS–clay data from LeBaron and Pinnavaia [168] and PU–MMT data from Wang [169]. In this figure, the upper- and lower bounds to modulus enhancement derived from axial (Voigt model) and transverse (Reuss model) loading of an infinite, uniaxial arrangement of reinforcement with a respective modulus ratio of 100 and 500 are also shown [371]. It appears that the aspect ratio of nanofillers is the most critical factor for enhancing the reinforcement in elastomers. Therefore, MWNTs with a higher aspect ratio produce a larger reinforcing effect in elastomers than the silicate platelets. All experimental data can be described satisfactorily with Guth equation using an aspect ratio of 25.

As mentioned previously, the mechanical behavior of composites can be predicted from the theoretical models. Using micromechanical models for the microcomposites, several researchers have attempted to examine how the nanofiller structural parameters such as shape, aspect ratio and orientation would affect the mechanical properties of polymer nanocomposites. The Halpin–Tsai equation can be used to the polymer–clay nanocomposites by taking the hierarchical morphology of the clay platelets into consideration. The Halpin–Tsai equation generally yields a better prediction for the modulus of clay-reinforced polymers because the clay platelets are rigid. However, micromechanical models cannot be used to fully account for the exact mechanical behavior of polymer–CNT nanocomposites due to their structural complexity. The CNTs are flexible rather than rigid rods. The aspect ratio of curved or bent nanotubes is reduced considerably compared to that of rigid counterparts. This implies that the reinforcement efficiency of curved nanotubes would be reduced accordingly. Moreover, the load transfer mechanism in the MWNT reinforced polymers is different, i.e. only external layer of the nanotubes bears the applied load.

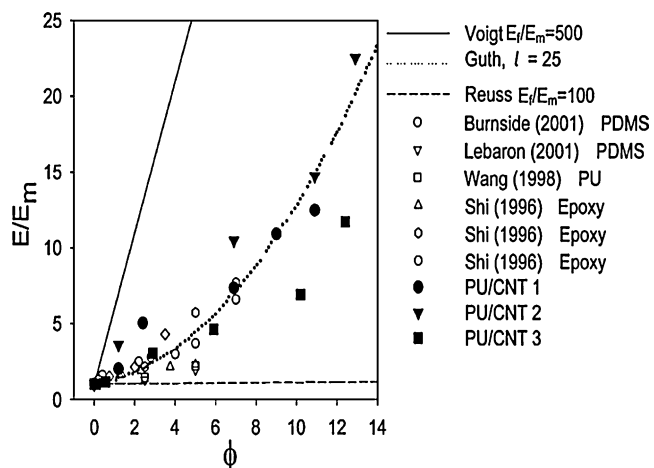


Fig. 117. Comparison of relative initial moduli of nanocomposites (E = modulus of nanocomposite, E_m = modulus of polymer matrix, E_f = modulus of fiber). For reference, the upper and lower bounds to modulus enhancement driven from axial (Voigt model) and transverse (Reuss model) loading of an infinite, uniaxial arrangement of reinforcement and filler with a moduli ratio of 100 and 500 are included (reprinted from [370] with permission from Elsevier).

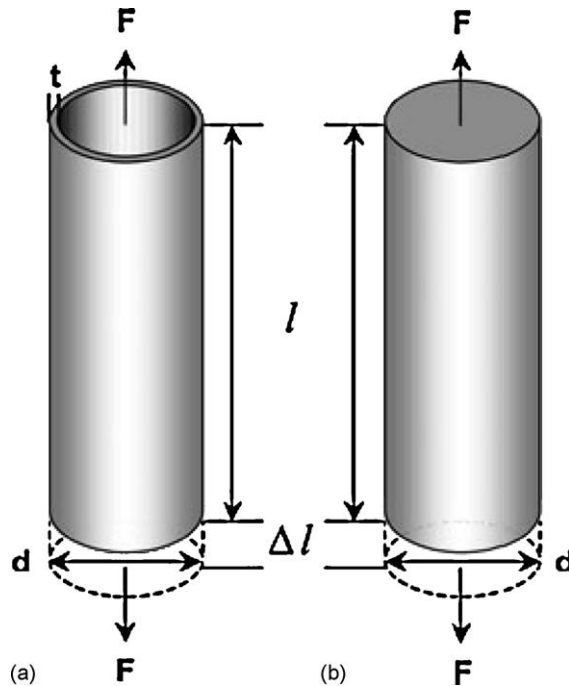


Fig. 118. Schematic of (a) nanotube and (b) effective fiber used to model the elastic properties of a nanotube embedded in a composite (reprinted from [372] with permission from Institute of Physics Publishing Ltd. (U.K.)).

Thostenson and Chou modified the Halpin–Tsai equation to account for the structure of the MWNT reinforcement in the polymer matrix [372]. The elastic modulus of the MWNT is modeled by considering that the outer wall of the nanotube acts as an effective solid fiber with the same deformation behavior and same diameter (d) and length (l) as shown in Fig. 118(a and b). An effective modulus (E_{eff}) is deduced assuming that the outer shell carries essentially all the load such that the nanotube modulus, E_{NT} , is reduced in proportion to the ratio of the area of the outer shell to the entire cross-sectional area of the nanotube. E_{eff} is expressed in terms of the nanotube outer layer thickness (t) and the nanotube diameter (d) as:

$$E_{\text{eff}} = \frac{4t}{d} E_{\text{NT}} \quad (31)$$

Fig. 119 shows a TEM micrograph of a MWNT having a diameter (d) and thickness (t) that can be determined from the image analysis. By substituting Eq. (31) into the Halpin–Tsai equation, they obtained the following equation:

$$\begin{aligned} E_{11} &= E_{\text{M}} \left(1 + 2 \left(\frac{l}{d} \right) \left(\frac{(E_{\text{NT}}/E_{\text{m}}) - (d/4t)}{(E_{\text{NT}}/E_{\text{m}}) - (l/2t)} \right) V_{\text{NT}} \right) \\ &\times \left(1 - \left(\frac{(E_{\text{NT}}/E_{\text{m}}) - (d/4t)}{(E_{\text{NT}}/E_{\text{m}}) - (l/2t)} \right) V_{\text{NT}} \right)^{-1} \end{aligned} \quad (32)$$

Eq. (32) is valid for $l > d > 4t$. Considering $E_{\text{NT}} = 1 \text{ TPa}$, $E_{\text{M}} = 2.4 \text{ GPa}$ for PS, the predicted elastic modulus of the PS–MWNT composite from the Eq. (32) is shown in Fig. 120. It is apparent that the nanotube diameter plays a key role in the composite elastic modulus.

In general, the MWNTs embedded in a polymer are not straight and aligned along the loading direction. Instead, coiled MWNTs are randomly distributed in the polymeric matrix. Fisher et al.

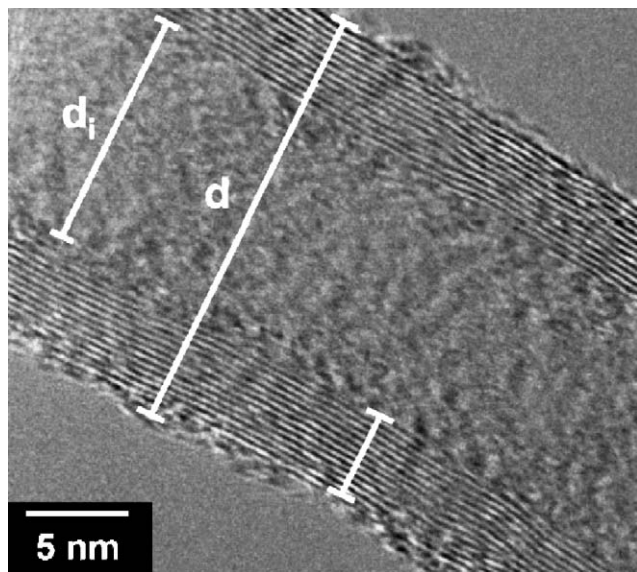


Fig. 119. TEM micrograph of a MWNT with measurements of outside diameter, inside diameter and wall thickness indicated (reprinted from [372] with permission from Institute of Physics Publishing Ltd. (U.K.)).

developed a model combining finite element result and micromechanical method (Mori–Tanaka) to determine the effective reinforcing modulus of a wavy embedded nanotube [373]. They considered that the CNT has a solid cross-section, is infinitely long and its centerline path is sinusoidal in the y - z plane at $x = 0$, i.e.

$$y = a \cos\left(\frac{2\pi z}{\lambda}\right) \quad (33)$$

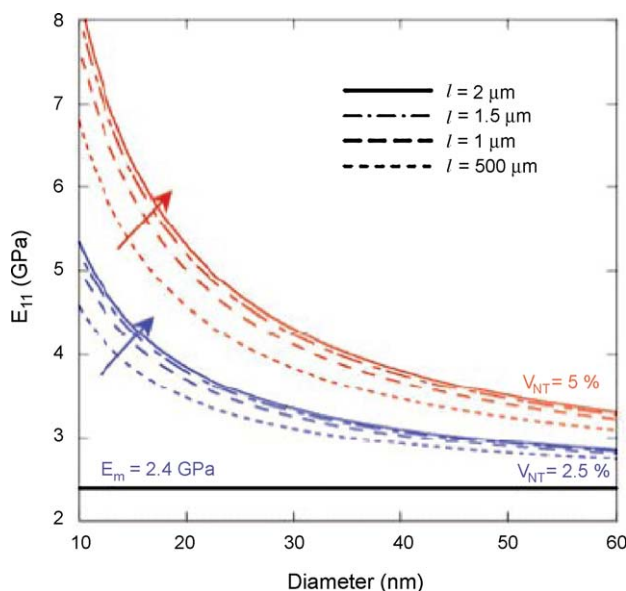


Fig. 120. Influence of nanotube diameter, volume fraction and length on the elastic properties of an aligned nanocomposite system (reprinted from [372] with permission from Institute of Physics Publishing Ltd. (U.K.)).

where a and λ are the amplitude and wavelength of the CNT waviness. The effect of waviness is incorporated using a reduced effective nanotube modulus (E_{ERM}) determined via finite element method as shown in Fig. 121. Since the wavy CNT is modeled as a straight CNT with a reduced modulus, the dilute strain concentration tensor could be determined analytically via Elshelby's solution for an ellipsoidal inclusion in an infinite matrix. E_{ERM} is dependent on three variables: the waviness ratio ($w = a/\lambda$) and wavelength ratio (λ/d) of the nanotube as well as the ratio of the phase moduli ($E_{\text{ratio}} = E_{\text{NT}}/E_{\text{matrix}}$). Given the E_{ERM} of each nanotube phase, $r = 1, 2, 3, \dots, N$, the effective stiffness tensor C_2 of each phase is determined assuming an isotropic, ellipsoidal inclusion. A^{dil} is then calculated from each CNT phase using Eq. (5). The overall effective modulus of the composite is obtained from the multiphase Mori–Tanaka analysis using Eqs. (4) and (6).

Fig. 122(a and b) shows the Mori–Tanaka predictions for the effective modulus versus nanotube volume fraction of the polymer–CNT composites for the 3D and 2D random orientation of straight and wavy nanotubes. The predictions are based on the nanotube wavelength ratio (λ/d) of 100, E_{NT} of 450 GPa, Poisson ratio of 0.3 for the nanotube and the matrix as well as the phase moduli ratio (E_{ratio}) of 200. Both the minimal waviness (wavy distribution 1 in which the w values ranged from 0 to 0.1) and moderate waviness (wavy distribution 2 in which the w values ranged from 0 to 0.5) are simulated. The experimentally measured moduli of the PS–MWNT are taken from the results of Andrew et al. [355]. These figures reveal that the waviness of embedded CNTs significantly reduced their reinforcement efficiencies compared to straight and aligned CNTs. Moreover, the experimental

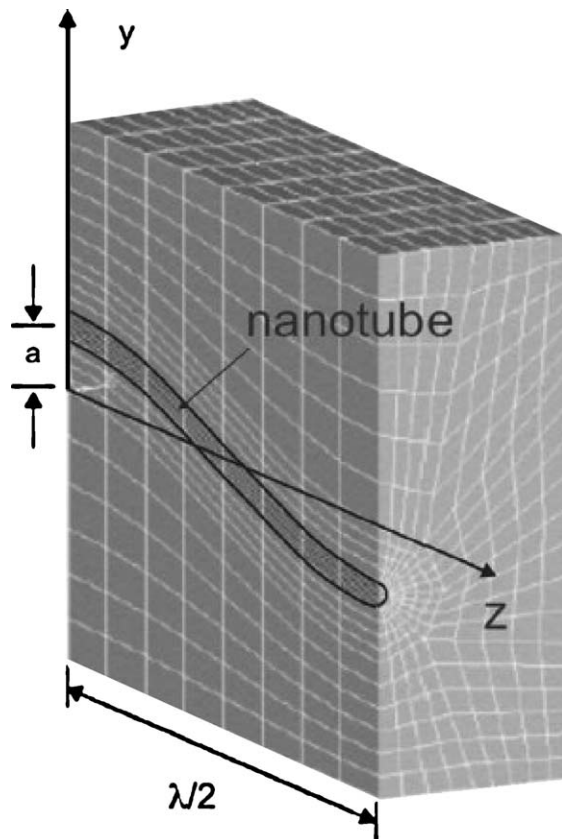


Fig. 121. Schematic of the finite element cell model of an embedded wavy nanotube. For the particular model shown $w = a/\lambda = 0.1$ and $\lambda/d = 35$ (reprinted from [373] with permission from Elsevier).

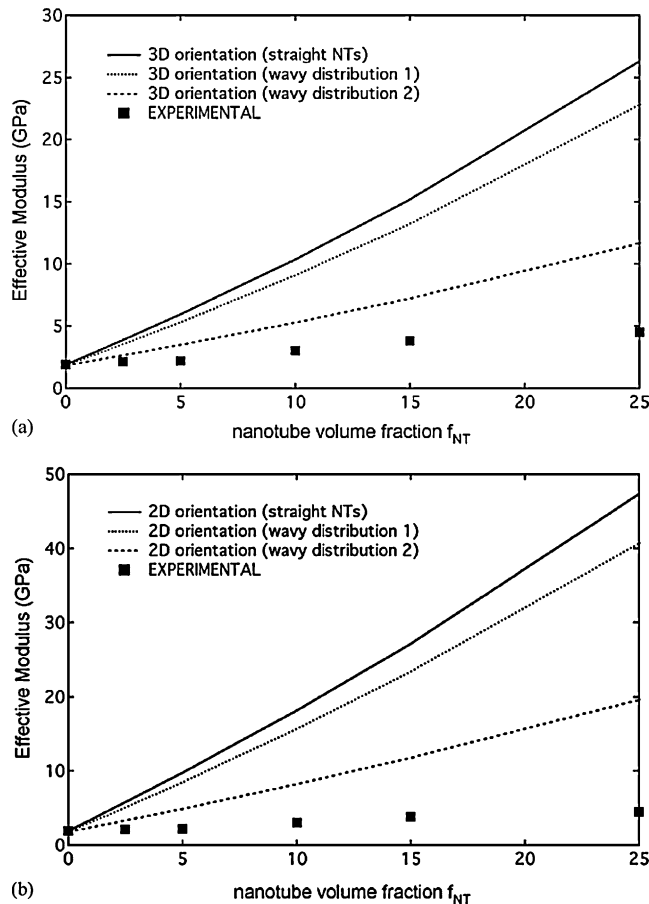


Fig. 122. Experimental data for MWNT in PS and micromechanical predictions of effective moduli of PS–MWNT composite assuming a (a) 3D random orientation of staright and wavy nanotubes and (b) 2D random orientation of staright and wavy nanotubes; $E_{NT} = 450$ GPa (reprinted from [373] with permission from Elsevier).

moduli of the PS–CNT composites are much lower compared than those predicted from the Mori–Tanaka approach incorporating the nanotube waviness.

5. Conclusions

The demand for high-performance and low cost polymer composites poses new challenges for materials scientists. Nanoclays, nanoceramic particles and carbon nanotubes with their nanometer size, large surface area, high mechanical strength and stiffness have been shown to be effective reinforcement materials for the polymer nanocomposites. The flexibility in selecting appropriate nano building blocks allows one to design novel materials properties and to optimize them for each desired application. Substantial progress has been made in the development, processing and microstructural aspects of the polymers reinforced with low level loading of nanomaterials over the recent years. Structural and morphological changes in the polymers induced by nanomaterials could lead to significant enhancement in several aspects of their mechanical properties. Understanding the synthesis–structure–property relationship of nanocomposites is vital for the development of advanced polymer nanocomposites with enhanced mechanical strength, stiffness and toughness for structural engineering applications.

This paper provides a comprehensive review on the effects of silicate clay, ceramic nanoparticle and carbon nanotube additions on the structure and mechanical properties of semicrystalline and glassy thermoplastics, elastomers and epoxy resins. The mechanical performance of polymer–nanofiller composites depends greatly on the types of nanofillers and polymeric matrices used. Overall, carbon nanotubes provide the largest modulus enhancement in these polymer resins at a fixed filler loading compared to silicate clays and nanoceramic particulates. This is attributed to the large aspect ratio (over 1000), high mechanical strength and stiffness of the nanotubes. Apart from the strengthening and stiffening effects, CNT additions also enhance the toughness of epoxy resins significantly due to the high strain to failure of nanotubes. The tensile ductility generally is quite similar and not affected by the CNT loading for semicrystalline and glassy thermoplastics as well as elastomers. This is because flexible CNTs often bridge the microcracks in these materials during deformation. Rigid silicate platelets with an aspect ratio of ~200 also strengthen and stiffen the semicrystalline and glassy thermoplastics, elastomers and epoxy resins dramatically. However, the nature of polymer resins significantly affects the tensile ductility and toughness of the clay-reinforced polymer nanocomposites. The silicate filler additions are beneficial to improve both the stiffness and toughness of epoxy resins and elastomers. This is due to the nanoclay platelets are very effective to deflect the propagation of microcracks into tortuous paths, particularly for the epoxy resins with an exfoliated structure. In contrast, the clay additions reduce the tensile ductility and toughness of semicrystalline thermoplastics. The mechanisms for reduced tensile ductility remain unclear. To restore the toughness, elastomers particles are commonly incorporated into the semicrystalline polymers. In the case of glassy thermoplastics, the tensile ductility and impact toughness of nanocomposites depend on the extent of clay dispersion in the amorphous polymer matrices. A highly exfoliated clay structure is rather difficult to achieve in glassy thermoplastics prepared by melt-compounding. For melt-mixed glassy polymer nanocomposites, the clays tend to disperse as intercalated tactoids and agglomerated platelets in the polymer matrices. This leads to a reduction of the mechanical toughness as expected. However, a highly exfoliated structure is formed in the nanocomposites prepared via in situ polymerization.

Consequently, the impact toughness improves considerably with increasing clay loadings. It seems that exfoliated clay platelets dispersed in brittle thermoplastic matrices prepared via in situ polymerization can deflect the crack propagation as in the case of the epoxy–clay nanocomposites. Finally, nanoceramic particulates are effective to enhance both the stiffness and toughness of semicrystalline thermoplastics, elastomers and epoxy resins. The enhanced toughness is attributed to the nanoparticle induced cavitation and shear yielding of the polymer resins during mechanical deformation.

References

- [1] Y. Long, R.A. Shanks, *J. Appl. Polym. Sci.* 61 (1996) 1877.
- [2] Z. Bartczak, A.S. Argon, R.E. Cohen, M. Weinberg, *Polymer* 40 (1999) 2347.
- [3] R.K.D. Misra, P. Nerikar, K. Bertrand, D. Murphy, *Mater. Sci. Eng. A* 384 (2004) 284.
- [4] H. Unal, A. Mimaroglu and, M. Alkan, *Polym. Int.* 53 (2004) 56.
- [5] A. Takahara, T. Magome, T. Kajiyama, *J. Polym. Sci. Part B: Polym. Phys.* 32 (1994) 839.
- [6] A.T. Dibenedetto, *Mater. Sci. Eng. A* 302 (2001) 74.
- [7] P. Potschke, A.R. Bhattacharyya, A. Janke, *Polymer* 44 (2003) 8061.
- [8] P.C. LeBaron, T.J. Pinnavaia, *Chem. Mater.* 13 (2001) 3760.
- [9] M.F. Yu, O. Lourie, M.J. Dryer, K. Molor, T.F. Kelly, R.S. Ruoff, *Science* 287 (2000) 637.
- [10] M.F. Yu, B.S. Files, S. Areppalli, R.S. Ruoff, *Phys. Rev. Lett.* 84 (2000) 5552.

- [11] M. Alexandre, P. Dubois, Mater. Sci. Eng. R 28 (2000) 1.
- [12] S.C. Tjong, Y.Z. Meng, A.S. Hay, Chem. Mater. 14 (2002) 44.
- [13] S.C. Tjong, Y.Z. Meng, Y. Xu, J. Polym. Sci. Part B: Polym. Phys. 40 (2002) 2860.
- [14] S.C. Tjong, Y.Z. Meng, J. Polym. Sci. Part B: Polym. Phys. 41 (2003) 1476.
- [15] S.C. Tjong, Y.Z. Meng, J. Polym. Sci. Part B: Polym. Phys. 41 (2003) 2332.
- [16] S.C. Tjong, S.P. Bao, J. Polym. Sci. Part B: Polym. Phys. 42 (2004) 2878.
- [17] S.C. Tjong, S.P. Bao, J. Polym. Sci. Part B: Polym. Phys. 43 (2005) 253.
- [18] H. Fischer, Mater. Sci. Eng. C 23 (2003) 763.
- [19] K.P. Pramoda, T. Liu, J. Appl. Polym. Sci. 42 (2004) 1823.
- [20] J. Kotek, V. Kelnar, M. Studenovsky, J. Baldrian, Polymer 46 (2005) 4876.
- [21] K.E. Strawhecker, E. Manias, Chem. Mater. 12 (2000) 2943.
- [22] Z. Wang, T.J. Pinnavaia, Chem. Mater. 10 (1998) 1820.
- [23] E.P. Giannelis, R. Krishnamorti, E. Manias, Adv. Polym. Sci. 138 (1999) 108.
- [24] H. Wang, C. Zeng, M. Elkovich, L.J. Lee, K.W. Koelling, Polym. Eng. Sci. 41 (2001) 2036.
- [25] S. Iijima, Nature 354 (1991) 56.
- [26] <http://www.seas.upenn.edu/mse/research/nanotubes.html>.
- [27] <http://www.Nanoamor.com>.
- [28] <http://www.apsci.com>.
- [29] H.D. Wagner, O. Lourie, Y. Feldman, R. Tenne, Appl. Phys. Lett. 72 (1998) 188.
- [30] P. Kim, L. Shi, A. Majumdar, P.L. McEuen, Phys. Rev. Lett. 87 (2001) 215502.
- [31] C.Y. Li, T.W. Chou, Int. J. Solids Struct. 40 (2003) 2487.
- [32] E. Hernandez, C. Goze, P. Bernier, A. Rubio, Phys. Rev. Lett. 80 (1998) 4502.
- [33] E.W. Wong, P.E. Sheehan, C.M. Liber, Science 277 (1997) 1971.
- [34] B.I. Yakobson, M.P. Campbell, C.J. Brabec, J. Bernholc, Comp. Mater. Sci. 8 (1997) 341.
- [35] B.G. Demczyk, Y.M. Wang, J. Cumings, M. Hetman, W. Han, A. Zettl, Mater. Sci. Eng. A 334 (2002) 173.
- [36] Plast. Add. Compd. 4 (2002) 30.
- [37] R. Steward, Plast. Eng. 60 (2004) 23.
- [38] Focus on Pigments 6 (2003) 6.
- [39] S.C. Tjong, H. Chen, Mater. Sci. Eng. R 45 (2004) 1.
- [40] C.M. Chan, J. Wu, J.X. Li, Y.K. Cheung, Polymer 43 (2002) 2981.
- [41] D. Wu, X. Wang, Y. Song, R. Jin, J. Appl. Polym. Sci. 92 (2004) 2714.
- [42] Q.X. Zhang, Z.Z. Yu, X.L. Xie, Y.W. Mai, Polymer 45 (2004) 5985.
- [43] P. Musto, G. Ragosta, S. Scarinzi, L. Mascia, Polymer 45 (2004) 1697.
- [44] P. Musto, G. Ragosta, S. Scarinzi, L. Mascia, Polymer 45 (2004) 4265.
- [45] Z.S. Petrovic, I. Javni, A. Waddon, G. Banhegyi, J. Appl. Polym. Sci. 76 (2000) 133.
- [46] R.W. Siegel, S.K. Chang, B.J. Ash, J. Stone, P.M. Ajayan, R.W. Doremus, L.S. Schadler, Scripta Mater. 44 (2001) 2061.
- [47] B.J. Ash, D.F. Rogers, C.J. Wiegand, L.S. Schadler, R.W. Siegel, B.C. Benicewicz, T. Apple, Polym. Compos. 23 (2002) 1014.
- [48] B.J. Ash, R.W. Siegel, L.S. Schadler, Macromolecules 37 (2004) 1358.
- [49] P.J. Yoon, D.L. Hunter, D.R. Paul, Polymer 44 (2003) 5323.
- [50] T. Liu, I.Y. Phang, L. Shen, S.Y. Chow, W.D. Zhang, Macromolecules 37 (2004) 7214.
- [51] Y. Qu, F. Yang, Z.Z. Yu, J. Polym. Sci. Part B Polym. Phys. 36 (1998) 789.
- [52] J.H. Park, S.C. Jana, Polymer 44 (2003) 2091.
- [53] V. Skakalova, U. Dettlaff-Weglikowska, S. Roth, Synth. Met. 152 (2005) 349.
- [54] H. Xia, M. Song, J. Mater. Chem. 16 (2006) 1843.
- [55] M.D. Frogley, D. Ravich, H.D. Wagner, Compos. Sci. Technol. 63 (2003) 1647.
- [56] A. Pattanayak, S.C. Jana, Polymer 46 (2005) 3394.
- [57] Z. Wang, T.J. Pinnavaia, Chem. Mater. 10 (1998) 3769.
- [58] S.W. Bailey, Structures of layer silicates, in: G.W. Brindley, G. Brown (Eds.), Crystal Structures of Clay Minerals and Their X-ray Identifications, Monograph No. 5, Mineralogical Society, London, 1980, pp. 1–123.
- [59] D.M. Moore, R.C. Reynolds Jr., X-ray Diffraction and the Identification and Analysis of Clay Analysis of Clay Minerals, Oxford University Press, Oxford, 1997, pp. 104–120 (Chapter 4).
- [60] M.A. Osman, M. Plotze, P. Skrabal, J. Phys. Chem. B 108 (2004) 2580.
- [61] T.D. Fornes, P.J. Yoon, D.L. Hunter, H. Keskula, D.R. Paul, Polymer 43 (2002) 5915.

- [62] S.S. Ray, K. Okamoto, M. Okamoto, *Macromolecules* 36 (2003) 2355.
- [63] R.A. Vaia, E.P. Giannelis, *Macromolecules* 30 (1997) 8000.
- [64] A.B. Morgan, J.F. Gilman, *J. Appl. Polym. Sci.* 87 (2003) 1327.
- [65] D.F. Eckel, M.P. Balogh, P.D. Fasulo, W.R. Rodgers, *J. Appl. Polym. Sci.* 93 (2004) 1110.
- [66] R.A. Vaia, D. Klaus, E.J. Kramer, E.P. Giannelis, *Chem. Mater.* 8 (1996) 2628.
- [67] <http://www.nanoclay.com/>.
- [68] <http://www.rheox.com/>.
- [69] <http://www.nanocor.com/>.
- [70] <http://www.sud-chemie.com/>.
- [71] T.D. Fornes, P.J. Yoon, D.R. Paul, *Polymer* 44 (2003) 7545.
- [72] S.S. Ray, M. Okamoto, *Prog. Polym. Sci.* 28 (2003) 1539.
- [73] S. Hotta, D.R. Paul, *Polymer* 45 (2004) 7639.
- [74] E. Manias, A. Touny, L. Wu, K. Strawhecker, B. Lu, T.C. Chung, *Chem. Mater.* 13 (2001) 3516.
- [75] Z.M. Wang, H. Nagajima, E. Manias, T.C. Chung, *Macromolecules* 36 (2003) 8919.
- [76] G. Lagaly, *Solid State Ionics* 22 (1986) 43.
- [77] R.A. Vaia, R.K. Teukolsky, E.P. Giannelis, *Chem. Mater.* 6 (1994) 1017.
- [78] E. Hackett, E. Manias, E.P. Giannelis, *J. Chem. Phys.* 108 (1998) 7410.
- [79] L.Q. Wang, J. Liu, G.J. Exarhos, K.Y. Flanigan, R. Bordia, *J. Phys. Chem. B* 104 (2000) 2810.
- [80] D.L. Ho, R.M. Briber, C.J. Glinka, *Chem. Mater.* 13 (2001) 1923.
- [81] D.L. Ho, C.J. Glinka, *Chem. Mater.* 15 (2003) 1309.
- [82] Y.S. Choi, H.T. Ham, I.J. Chung, *Chem. Mater.* 16 (2004) 2522;
R.F. Giese, C.J. van Oss, *Colloid and Surface Properties of Clays and Related Minerals*, Marcel Dekker, New York, 2002.
- [83] C.M. Hansen, *J. Paint Technol.* 39 (1967) 104.
- [84] C.M. Hansen, *J. Paint Technol.* 39 (1967) 505.
- [85] J.H. Hildebrand, R.L. Scott, *Solubility of Non-Electrolytes*, third ed., Reinhold, New York, 1950.
- [86] J.H. Hildebrand, R.L. Scott, *Regular Solutions*, Prentice-Hill, Englewood Cliffs, NJ, 1962.
- [87] K.L. Chasey, *Rubber World* 209 (1993) 35.
- [88] H.M. Lin, R.A. Nash, *J. Pharm. Sci.* 82 (1993) 1018.
- [89] Y. Li, H. Ishida, *Polymer* 44 (2003) 6571.
- [90] M. Zanetti, S. Lomakin, G. Camino, *Macro Mater. Eng.* 279 (2000) 1.
- [91] R.A. Vaia, H. Ishii, E.P. Giannelis, *Chem. Mater.* 5 (1993) 1694.
- [92] H.R. Dennis, D.L. Hunter, D. Chang, S. Kim, J.L. White, J.W. Cho, D.R. Paul, *Polymer* 42 (2001) 9513.
- [93] W. Xie, Z. Gao, W.P. Pan, D. Hunter, A. Singh, R. Vaia, *Chem. Mater.* 13 (2001) 2979.
- [94] R.A. Vaia, S. Vasudevan, W. Krawiec, L.G. Canlon, P. Giannelis, *Adv. Mater.* 7 (1995) 154.
- [95] A. Usuki, M. Kawasumi, Y. Kojima, A. Okada, T. Kurauchi, O. Kamigaito, *J. Mater. Res.* 8 (1993) 1174.
- [96] A. Usuki, Y. Kojima, M. Kawasumi, A. Okada, Y. Fukushima, T. Kurauchi, O. Kamigaito, *J. Mater. Res.* 8 (1993) 1179.
- [97] F.A. Bottino, E. Fabbri, I.L. Fragala, G. Malandrino, A. Orestano, F. Pilati, A. Pollicino, *Macromol. Rapid Commun.* 24 (2003) 1079.
- [98] X. Fu, S. Qutubuddin, *Polymer* 42 (2001) 807.
- [99] M.W. Weimer, H. Chen, E.P. Giannelis, D.Y. Sogah, *J. Am. Chem. Soc.* 121 (1999) 1615.
- [100] X. Qu, T. Guan, G. Liu, Q. She, L. Zhang, *J. Appl. Polym. Sci.* 97 (2005) 348.
- [101] M.W. Noh, D.C. Lee, *Polym. Bull.* 42 (1999) 619.
- [102] T.H. Kim, L.W. Jang, D.C. Lee, H.J. Choi, M.S. Jhon, *Macromol. Rapid Commun.* 23 (2002) 191.
- [103] Y.K. Kim, Y.S. Choi, K.H. Wang, I.J. Chung, *Chem. Mater.* 14 (2002) 4990.
- [104] M. Xu, Y.S. Choi, Y.K. Kim, K.H. Wang, I.J. Chung, *Polymer* 44 (2003) 6387.
- [105] G. Chen, Y. Ma, Z. Qi, *Scripta Mater.* 44 (2001) 125.
- [106] Y.S. Choi, M.H. Choi, K.H. Wang, S.O. Kim, Y.K. Kim, I.J. Chung, *Macromolecules* 34 (2001) 8978.
- [107] X. Huang, W.J. Brittain, *Macromolecules* 34 (2001) 3255.
- [108] Q. Kong, Y. Hu, L. Yang, W. Fan, *Polym. Compos.* 27 (2006) 49.
- [109] J. Tudor, L. Willington, D. O'Hare, B. Royan, *Chem. Commun.* (1996) 2031.
- [110] J. Heinemann, P. Reichert, R. Thomann, R. Mulhaupt, *Macromol. Rapid Commun.* 20 (1999) 423.
- [111] J.S. Bergman, H. Chen, E.P. Giannelis, M.G. Thomas, G.W. Coates, *Chem. Commun.* (1999) 2179.
- [112] H. Heinz, U.W. Suter, *Angew. Chem. Int. Ed.* 43 (2004) 2239.

- [113] A.C. Balazs, C. Singh, E. Zhulina, *Macromolecules* 31 (1998) 8370.
- [114] E. Zhulina, C. Singh, A.C. Balazs, *Langmuir* 15 (1999) 3935.
- [115] R.A. Vaia, E.P. Giannelis, *Macromolecules* 30 (1997) 7990.
- [116] D.L. Vanderhart, A. Asano, J.W. Gilman, *Chem. Mater.* 13 (2001) 3796.
- [117] N. Hasegawa, H. Okamoto, M. Kato, A. Usuki, N. Sato, *Polymer* 44 (2003) 2933.
- [118] Z.Z. Yu, G.H. Hua, J. Varlet, A. Dasari, Y.W. Mai, *J. Polym. Sci. Part B* 43 (2005) 1100.
- [119] T.D. Fornes, P.J. Yoon, D.L. Hunter, H. Keskkula, D.R. Paul, *Polymer* 43 (2002) 5915.
- [120] T.D. Fornes, P.J. Yoon, D.R. Paul, *Polymer* 45 (2004) 2321.
- [121] F. Chavarria, D.R. Paul, *Polymer* 45 (2004) 8501.
- [122] T.D. Fornes, D.L. Hunter, D.R. Paul, *Macromolecules* 37 (2004) 1793.
- [123] P.J. Yoon, D.L. Hunter, D.R. Paul, *Polymer* 44 (2003) 5341.
- [124] K.S. Minsker, S.V. Koselov, G.E. Zaikov, *Degradation, Stabilization of Vinyl Chloride Based Polymers*, Pergamon Press, New York, 1988, p. 76.
- [125] J. Trilica, A. Kalendova, Z. Malac, J. Simonik, in: Proceedings of SPE, ANTEC 2001, Dallas, TX, (2001), p. 2162.
- [126] C. Wan, X. Qiao, Y. Zhang, Y.X. Zhang, *J. Appl. Polym. Sci.* 89 (2003) 2184.
- [127] C. Wan, Y. Zhang, Y.X. Zhang, *Polym. Test.* 23 (2004) 299.
- [128] M. Kato, A. Usuki, A. Okada, *J. Appl. Polym. Sci.* 66 (1997) 1781.
- [129] N. Hasegawa, M. Kawasumi, M. Kato, A. Usuki, A. Okada, *J. Appl. Polym. Sci.* 67 (1998) 87.
- [130] N. Hasegawa, H. Okamoto, M. Kato, A. Usuki, *J. Appl. Polym. Sci.* 78 (2000) 1918.
- [131] P.H. Nam, P. Maiti, M. Okamoto, T. Kotaka, N. Hasegawa, A. Usuki, *Polymer* 42 (2001) 9633.
- [132] P. Maiti, P.H. Nam, M. Okamoto, N. Hasegawa, A. Usuki, *Macromolecules* 35 (2002) 2042.
- [133] P. Reichert, H. Nitz, S. Klinke, R. Brandsch, R. Thomann, R. Mulhaupt, *Macro. Mater. Eng.* 275 (2000) 8.
- [134] W. Xu, G. Liang, W. Wang, S. Tang, P. He, W. Pan, *J. Appl. Polym. Sci.* 88 (2003) 3225.
- [135] F.C. Chiu, S.M. Lai, J.W. Chen, P.H. Chu, *J. Polym. Sci. Part B Polym. Phys.* 42 (2004) 4139.
- [136] K.H. Wang, M.H. Choi, C.M. Koo, Y.S. Choi, I.J. Chung, *Polymer* 43 (2001) 9819.
- [137] M. Kato, H. Okamoto, N. Hasegawa, A. Tsukigase, A. Usuki, *Polym. Eng. Sci.* 43 (2003) 1312.
- [138] N. Ristolainen, U. Vainio, S. Paavola, M. Torkkeli, R. Serimaa, J. Seppala, *J. Polym. Sci. Part B Polym. Phys.* 43 (2005) 1892.
- [139] P.J. Yoon, D.L. Hunter, D.R. Paul, *Polymer* 44 (2003) 5323.
- [140] M.S. Wang, T.J. Pinnavaia, *Chem. Mater.* 6 (1994) 468.
- [141] T. Lan, P.D. Kaviratna, T.J. Pinnavaia, *Chem. Mater.* 7 (1995) 2144.
- [142] T. Lan, P.D. Kaviratna, T.J. Pinnavaia, *J. Phys. Chem. Solids* 57 (1996) 1005.
- [143] H. Shi, T. Lan, T.J. Pinnavaia, *Chem. Mater.* 8 (1996) 1584.
- [144] C.S. Triantafyllidis, P.C. LeBaron, T.J. Pinnavaia, *Chem. Mater.* 14 (2002) 4088.
- [145] C.S. Triantafyllidis, P.C. LeBaron, T.J. Pinnavaia, *J. Solid State Chem.* 167 (2002) 354.
- [146] D. Kong, C.E. Park, *Chem. Mater.* 15 (2003) 419.
- [147] C. Chen, M. Khobaib, D. Curliss, *Progr. Org. Coat.* 47 (2003) 376.
- [148] X. Kornmann, H. Lindberg, L.A. Berglund, *Polymer* 42 (2001) 4493.
- [149] I.J. Chin, T. Thurn-Albrecht, H.C. Kim, T.P. Russell, J. Wang, *Polymer* 42 (2001) 5947.
- [150] T.B. Tolle, D.P. Anderson, *Compos. Sci. Technol.* 62 (2002) 1033.
- [151] B. Jen, J. Liu, H. Chen, J. Wu, *Chem. Mater.* 16 (2004) 4864.
- [152] K. Wang, L. Wang, J. Wu, L. Chen, C. He, *Langmuir* 21 (2005) 3613.
- [153] S. Varghese, J. Karger-Kocsis, *Polymer* 44 (2003) 4921.
- [154] M. Arroyo, M.A. Lopez-Manchado, B. Herrero, *Polymer* 44 (2003) 2447.
- [155] K.Y. Lee, L.L.A. Goettler, *Polym. Eng. Sci.* 44 (2004) 1103.
- [156] H.S. Lee, P.D. Fasulo, W.R. Rodgers, D.R. Paul, *Polymer* 46 (2005) 11673.
- [157] J. Karger-Kocsis, C.M. Wu, *Polym. Eng. Sci.* 44 (2004) 1083.
- [158] T.K. Chen, Y.I. Tien, K.H. Wei, *Polymer* 41 (2000) 1345.
- [159] Y.I. Tien, K.H. Wei, *Macromolecules* 34 (2001) 9045.
- [160] S.Y. Moon, J.K. Kim, C. Nah, Y.S. Lee, *Eur. Polym. J.* 40 (2004) 1615.
- [161] M. Song, D.J. Hourston, K.J. Yao, D.Z. Luo, *J. Appl. Polym. Sci.* 90 (2003) 3239.
- [162] A. Usuki, A. Tukigase, M. Kato, *Polymer* 43 (2002) 2185.
- [163] B. Liu, Q. Ding, J. Zhang, B. Hu, J. Shen, *Polym. Compos.* 26 (2005) 706.
- [164] K.G. Gatos, J. Karger-Kocsis, *Polymer* 46 (2005) 3069.
- [165] H.A. Stretz, D.R. Paul, P.E. Cassidy, *Polymer* 46 (2005) 3818.

- [166] A. Ganguly, M.D. Sarkar, A.N. Bhowmick, *J. Appl. Polym. Sci.* 100 (2006) 2040.
- [167] S.D. Burnside, E.P. Giannelis, *J. Polym. Sci. Part B Polym. Phys.* 38 (2000) 1595.
- [168] P.C. LeBaron, T.J. Pinnavaia, *Chem. Mater.* 13 (2001) 3760.
- [169] Z. Wang, T.J. Pinnavaia, *Chem. Mater.* 10 (1998) 3769.
- [170] A.K. Kalkar, A.A. Deshpande, *Polym. Eng. Sci.* 41 (2001) 1597.
- [171] E. Di Maio, S. Iannace, L. Sorrentino, L. Nicolais, *Polymer* 45 (2004) 8893.
- [172] G. Zhang, D. Yan, *J. Appl. Polym. Sci.* 88 (2003) 2181.
- [173] T.D. Fornes, D.R. Paul, *Polymer* 44 (2003) 3945.
- [174] D.M. Lincoln, R.A. Vaia, R. Krishnamoorti, *Macromolecules* 37 (2004) 4554.
- [175] S. Hambir, N. Bulakh, J.P. Jog, *Polym. Eng. Sci.* 42 (2002) 1800.
- [176] P.H. Nam, P. Maiti, M. Okamoto, T. Kotaka, *Polym. Eng. Sci.* 42 (2002) 1864.
- [177] T.G. Gopakumar, J.A. Lee, M. Kontopolou, J.S. Parent, *Polymer* 43 (2002) 5483.
- [178] Y. Ke, C. Long, Z. Qi, *J. Appl. Polym. Sci.* 71 (1999) 1139.
- [179] B.J. Chisholm, R.B. Moore, G. Barber, F. Khouri, A. Hempstead, M. Larsen, *Macromolecules* 35 (2002) 5508.
- [180] D.F. Wu, C.X. Zhou, F. Xie, D.L. Mao, B. Zhang, *J. Appl. Polym. Sci.* 99 (2006) 3257.
- [181] H.D. Wu, C.R. Tseng, F.C. Chang, *Macromolecules* 34 (2001) 2992.
- [182] L. Priya, J.P. Jog, *J. Polym. Sci. Part B Polym. Phys.* 40 (2002) 1682.
- [183] D. Shah, P. Maiti, E. Gunn, D.F. Schmidt, D.D. Jiang, C.A. Batt, E.P. Giannelis, *Adv. Mater.* 16 (2004) 1173.
- [184] D.R. Dillon, K.K. Tenneti, C.Y. Li, F.K. Ko, I. Sics, B.S. Hsiao, *Polymer* 47 (2006) 1678.
- [185] K.E. Strawhecker, E. Manias, *Chem. Mater.* 15 (2003) 844.
- [186] D.M. Lincoln, R.A. Vaia, Z. Wang, B.S. Hsiao, *Polymer* 42 (2001) 1621.
- [187] L. Incarnato, P. Scarfato, G.M. Russo, L. Di Maio, P. Iannelli, D. Arcierno, *Polymer* 44 (2003) 4625.
- [188] J. Ho, K. Wei, *Macromolecules* 33 (2000) 5181.
- [189] G. Guerra, F.E. Karasz, W.J. MacKnight, *Macromolecules* 19 (1986) 1935.
- [190] J.H. Lee, D. Jung, C.E. Hong, K.Y. Rhee, S.G. Advani, *Compos. Sci. Technol.* 65 (2005) 1996.
- [191] M.A. Osman, J.E.P. Rupp, U.W. Suter, *Polymer* 46 (2005) 1653.
- [192] J.C. Halpin, *J. Compos. Mater.* 3 (1969) 732.
- [193] J.C. Halpin, J.L. Kardos, *Polym. Eng. Sci.* 16 (1976) 344.
- [194] T. Mori, K. Tanaka, *Acta Metall. Mater.* 21 (1973) 571.
- [195] Y. Benveniste, *Mech. Mater.* 6 (1987) 147.
- [196] T. Mura, *Micromechanics of Defects in Solids*, second ed., Martinus Nijhoff, Boston, 1987.
- [197] G.P. Tandon, G.J. Weng, *Polym. Compos.* 5 (1984) 327.
- [198] D.A. Brune, J. Bicerano, *Polymer* 43 (2002) 369.
- [199] T.D. Fornes, D.R. Paul, *Polymer* 44 (2003) 4993.
- [200] J.I. Weon, H.J. Sue, *Polymer* 46 (2005) 6325.
- [201] N. Sheng, M.C. Bouce, D.M. Parks, G.C. Rutledge, J.I. Abes, R.E. Cohen, *Polymer* 44 (2003) 4993.
- [202] M.K. Akkapeddi, *Polym. Compos.* 21 (2000) 576.
- [203] S.C. Tjong, Y.Z. Meng, *J. Polym. Sci. Part B Polym. Phys.* 41 (2003) 2332.
- [204] S.C. Tjong, S.A. Xu, R.K.Y. Li, Y.W. Mai, *Compos. Sci. Technol.* 62 (2002) 831.
- [205] A. Dasari, Z.Z. Yu, Y.W. Mai, *Polymer* 46 (2005) 5986.
- [206] Y.C. Ahn, D.R. Paul, *Polymer* 47 (2006) 2830.
- [207] W.Y.F. Chan, J.G. Williams, *Polymer* 35 (1994) 1666.
- [208] C.A. Paton, S. Hashemi, *J. Mater. Sci.* 27 (1992) 2279.
- [209] S. Hashemi, *J. Mater. Sci.* 28 (1993) 6178.
- [210] S.C. Tjong, S.A. Xu, R.K.Y. Li, *J. Appl. Polym. Sci.* 77 (2000) 2074.
- [211] S.C. Wong, Y.W. Mai, *Polym. Eng. Sci.* 39 (1999) 356.
- [212] E.C.Y. Ching, R.K.Y. Li, Y.W. Mai, *Polym. Eng. Sci.* 40 (2000) 310.
- [213] D.E. Mouzakis, F. Stricker, R. Mulhaupt, J. Karger-Kocsis, *J. Mater. Sci.* 33 (1998) 2551.
- [214] J.S. Wu, Y.W. Mai, B. Cotterell, *J. Mater. Sci.* 28 (1993) 3373.
- [215] F. Martinatti, T. Ricco, in: J.G. Williams, A. Pavan (Eds.), *Proceedings of Impact and Dynamic Fracture of Polymers and Composites*, vol. 19, European Structural Integrity Society (ESIS), (1995), p. 83.
- [216] R.A. Kudva, H. Keskkula, D.R. Paul, *Polymer* 41 (2000) 335.
- [217] K.C. Chiou, F.C. Chang, Y.W. Mai, *Polym. Eng. Sci.* 41 (2001) 1007.
- [218] D.M. Laura, H. Keskkula, J.W. Barlow, D.R. Paul, *Polymer* 42 (2001) 6161.
- [219] S.C. Tjong, S.A. Xu, Y.W. Mai, *J. Polym. Sci. Part B Polym. Phys.* 40 (2002) 1881.

- [220] S.C. Tjong, S.A. Xu, Y.W. Mai, *Mater. Sci. Eng. A* 347 (2003) 338.
- [221] S.C. Tjong, B.S. Bao, G. Liang, *J. Polym. Sci. Part B Polym. Phys.* 43 (2005) 3112.
- [222] S.C. Tjong, S.P. Bao, *J. Polym. Sci. Part B: Polym. Phys.* 43 (2005) 585.
- [223] K. Wang, L. Chen, J. Wu, M.L. Toh, C. He, A.F. Yee, *Macromolecules* 38 (2005) 788.
- [224] J. Lee, A.F. Yee, *Polymer* 41 (2000) 8363.
- [225] J. Lee, A.F. Yee, *Polymer* 41 (2000) 8375.
- [226] M. Franco, I. Mondragon, B.C. Bucknall, *J. Appl. Polym. Sci.* 72 (1999) 427.
- [227] H. Harani, S. Fellahi, M. Bakar, *J. Appl. Polym. Sci.* 71 (1999) 29.
- [228] F.F. Lange, K.C. Radford, *J. Mater. Sci.* 6 (1971) 1197.
- [229] O. Becker, R. Varley, G. Simon, *Polymer* 43 (2002) 4365.
- [230] L.L. Pluart, J. Duchet, H. Sautereau, *Polymer* 46 (2005) 12267.
- [231] C. Zilg, R. Mulhaupt, J. Finter, *Macromol. Chem. Phys.* 200 (1999) 661.
- [232] H. Miyagawa, L.T. Drzal, *J. Adhesion Sci. Technol.* 18 (2004) 1571.
- [233] A.S. Zerda, A.J. Lesser, *J. Polym. Sci. Part B Polym. Phys.* 39 (2001) 1137.
- [234] A. Dasari, R.D.K. Misra, *Acta Mater.* 52 (2004) 1683.
- [235] X.L. Xie, Q.X. Liu, R.K.Y. Li, X.P. Zhou, Q.X. Zhang, Z.Z. Yu, Y.W. Mai, *Polymer* 45 (2004) 6665.
- [236] Y.Y. Yu, C.Y. Chen, W.C. Chen, *Polymer* 44 (2003) 593.
- [237] Y.L. Liu, C.Y. Hsu, K.Y. Hsu, *Polymer* 46 (2005) 1851.
- [238] A. Bansal, H. Yang, C. Li, K. Cho, B. Kilwon, C. Brian, S. Kumar, L.S. Schadler, *Nat. Mater.* 4 (2005) 693.
- [239] A. Lazzeri, C.B. Bucknall, *J. Mater. Sci.* 28 (1993) 6799.
- [240] G.M. Kim, G.H. Michler, *Polymer* 39 (1998) 5689.
- [241] G.M. Kim, G.H. Michler, *Polymer* 39 (1998) 5698.
- [242] J. Wen, G.L. Wilkes, *Chem. Mater.* 8 (1996) 1667.
- [243] U. Schubert, N. Husing, A. Lorenz, *Chem. Mater.* 7 (1995) 2010.
- [244] P. Judeinstein, C. Sanchez, *J. Mater. Chem.* 6 (1996) 511.
- [245] C.J. Brinker, J.W. Scherer, *Sol–Gel Science: The Physics and Chemistry of Sol–Gel Processing*, Academic Press, Boston, 1990.
- [246] C.J. Brinker, K.D. Keefer, D.W. Schaefer, R.A. Assink, B.D. Kay, C.S. Ashley, *J. Non-Cryst. Solids* 63 (1984) 45.
- [247] G.L. Wilkes, B. Orler, H. Huang, *Polym. Prepr.* 26 (1985) 300.
- [248] H. Huang, B. Orler, G.L. Wilkes, *Macromolecules* 20 (1987) 1322.
- [249] S.K. Young, K.A. Mauritz, *J. Polym. Sci. Part B Polym. Phys.* 40 (2002) 2237.
- [250] N. Yamada, I. Yoshinaga, S. Katayama, *J. Mater. Chem.* 7 (1997) 1491.
- [251] C. Guermeur, J. Lambard, J.F. Gerard, C. Sanchez, *J. Mater. Chem.* 9 (1999) 769.
- [252] J.M. Breiner, J.E. Mark, *Polymer* 22 (1998) 5483.
- [253] B. Alonso, C. Sanchez, *J. Mater. Chem.* 10 (2000) 377.
- [254] J.S. Jain, H. Goossens, F. Picchioni, P. Magusin, B. Mezrari, M. van Duin, *Polymer* 46 (2005) 6666.
- [255] F. Picchioni, J.G.P. Goossens, M. van Duin, P. Magusin, *J. Appl. Polym. Sci.* 89 (2003) 3279.
- [256] W. Liu, X. Tian, P. Cui, Y. Li, K. Zheng, Y. Yang, *J. Appl. Polym. Sci.* 91 (2004) 1229.
- [257] X. Zhang, L.C. Simon, *Macromol. Mater. Eng.* 290 (2005) 573.
- [258] I. Sondi, T.H. Fedynyshyn, R. Sinta, E. Matijevic, *Langmuir* 16 (2000) 9031.
- [259] W.D. Hergeth, P. Starre, K. Schmutzler, *Polymer* 29 (1988) 1323.
- [260] E. Bourgeat-Lami, Ph. Espiard, A. Guyot, *Polymer* 36 (1995) 4385.
- [261] X.L. Xie, B.G. Li, Z.R. Pan, R.K.Y. Li, S.C. Tjong, *J. Appl. Polym. Sci.* 80 (2001) 2105.
- [262] X.L. Xie, R.K.Y. Li, Q.X. Liu, Y.W. Mai, *Polymer* 45 (2004) 2793.
- [263] S.D. Seul, S.R. Lee, Y.H. Kim, *J. Polym. Sci. Part A Polym. Chem.* 42 (2004) 4063.
- [264] D. Wu, X. Wang, Y. Song, B. Jin, *J. Appl. Polym. Sci.* 92 (2004) 2714.
- [265] M.Z. Rong, M.Q. Zhang, Y.X. Zheng, H.M. Zeng, R. Walter, K. Friedrich, *Polymer* 42 (2001) 167.
- [266] M.Z. Rong, M.Q. Zhang, Y.X. Zheng, H.M. Zeng, K. Friedrich, *Polymer* 42 (2001) 3301.
- [267] C.L. Wu, M.Q. Zhang, M.Z. Rong, K. Friedrich, *Compos. Sci. Technol.* 62 (2002) 1327.
- [268] M.Q. Zhang, M.Z. Rong, H.B. Zhang, K. Friedrich, *Polym. Eng. Sci.* 43 (2002) 490.
- [269] Q.L. Ji, M.Z. Rong, M.Q. Zhang, K. Friedrich, *Polym. Polym Compos.* 10 (2002) 531.
- [270] W.C.J. Zuiderduin, C. Westzaan, J. Huetink, R.J. Gaymans, *Polymer* 44 (2003) 261.
- [271] Q.X. Zhang, Z.Z. Yu, X.L. Xie, Y.W. Mai, *Polymer* 45 (2004) 5985.
- [272] C. Saujanya, S. Radhakrishnan, *Polymer* 42 (2001) 6723.
- [273] J. Qian, P. He, K. Nie, *J. Appl. Polym. Sci.* 91 (2004) 1013.

- [274] J.S. Jain, H. Goossens, M. van Duin, P. Lemstra, *Polymer* 46 (2005) 8805.
- [275] T. Liu, Z. Mo, S. Wang, H. Zhang, *Polym. Eng. Sci.* 37 (1997) 568.
- [276] M.J. Avrami, *Chem. Phys.* 7 (1939) 1130.
- [277] T. Ozawa, *Polymer* 7 (1971) 1103.
- [278] T. Ozawa, *J. Therm. Anal.* 9 (1976) 369.
- [279] H.E. Kissinger, *J. Res. Natl. Inst. Stand.* 57 (1956) 217.
- [280] Z. Peng, L.X. Kong, S.D. Li, *Polymer* 46 (2005) 1949.
- [281] Z. Bartczak, A.S. Argon, R.E. Cohen, M. Weinberg, *Polymer* 40 (1999) 2347.
- [282] A. Lazzeri, Y.S. Thio, R.E. Cohen, *J. Appl. Polym. Sci.* 91 (2004) 925.
- [283] I.L. Dubnikova, S.M. Berezina, A.V. Antonov, *J. Appl. Polym. Sci.* 94 (2004) 1917.
- [284] G. Ragosta, M. Abbate, P. Musto, G. Scarinzi, L. Mascia, *Polymer* 46 (2005) 10506.
- [285] D.N. Bikirias, A. Vassilou, E. Pavlidou, G.P. Karayannidis, *Eur. Polym. J.* 41 (2005) 1965.
- [286] S. Wu, *Polymer* 26 (1985) 1855.
- [287] L. Zhang, C. Li, R. Huang, *J. Polym. Sci. Part B Polym. Phys.* 42 (2004) 1656.
- [288] E. Guth, *J. Appl. Phys.* 16 (1945) 20.
- [289] L. Nicolais, M. Narkis, *Polym. Eng. Sci.* 11 (1971) 194.
- [290] Z.S. Petrovic, I. Javni, A. Waddon, G. Banhegyi, *J. Appl. Polym. Sci.* 76 (2000) 133.
- [291] A. Thess, R. Lee, P. Nikolaev, H. Dai, P. Pettit, J. Robert, C. Xu, Y.H. Lee, S.G. Kim, A.G. Rinzler, D.T. Colbert, G.E. Scuseria, D. Tomanek, J.E. Fischer, R.E. Smalley, *Science* 273 (1996) 483.
- [292] A.G. Rinzler, J. Liu, H. Dai, P. Nikolaev, C.B. Huffman, F.J. Rodriguez-Macias, *Appl. Phys. A* 67 (1998) 29.
- [293] P.C. Eklund, B.K. Pradhan, U.J. Kim, Q. Xiong, J.E. Fischer, A.D. Friedman, B.C. Holloway, K. Jordan, M.W. Smith, *Nano Lett.* 2 (2002) 561.
- [294] Z.P. Huang, J.W. Xu, Z.F. Ren, J.H. Wang, M.P. Siegel, P.N. Provencio, *Appl. Phys. Lett.* 73 (1998) 3845.
- [295] G.G. Tibbetts, *J. Cryst. Growth* 66 (1984) 632.
- [296] G.G. Tibbetts, *Carbon Fibers, Filaments and Composites*, Kluwer Academic, Amsterdam, 1990, pp. 73–94.
- [297] J. Kong, A.M. Cassell, H. Dai, *Chem. Phys. Lett.* 292 (1998) 567.
- [298] C. Journet, W.K. Masser, P. Bernier, A. Loiseau, M.L. de la Chapelle, S. Lefrant, P. Deniard, R. Lee, J.E. Fischer, *Nature* 388 (1997) 756.
- [299] Y. Saito, *Carbon* 33 (1995) 979.
- [300] R.S. Wagner, W.C. Ellis, *Appl. Phys. Lett.* 4 (1964) 89.
- [301] M. Morales, C.M. Lieber, *Science* 279 (1998) 208.
- [302] C.L. Cheung, A. Kurtz, H. Park, C.M. Lieber, *J. Phys. Chem. B* 106 (2002) 2429.
- [303] Y. Wu, P. Yang, *J. Am. Chem. Soc.* 123 (2001) 3165.
- [304] H. Kim, W. Sigmund, *Carbon* 43 (2005) 1743.
- [305] A.C. Dillon, A.H. Mahan, J.L. Alleman, M.J. Heben, P.A. Parilla, K.M. Jones, *Thin Solid Films* 430 (2003) 292.
- [306] F. Ding, A. Rosen, K. Bolton, *Carbon* 43 (2005) 2215.
- [307] Y.C. Sui, D.R. Acosta, J.A. Gonzalez-Leon, A. Bermudez, J. Feuchtwanger, B.Z. Cui, J.O. Flores, J.M. Saniger, *J. Phys. Chem. B* 105 (2001) 1523.
- [308] C. Papadopoulos, B.H. Chang, A.J. Yin, J.M. Xu, *Int. J. Nanosci.* 1 (2002) 205.
- [309] C. Singh, M.S.P. Shaffer, A.H. Windle, *Carbon* 41 (2003) 359.
- [310] R. Andrews, D. Jacques, A.M. Rao, F. Derbyshire, D. Qian, X. Fan, *Chem. Phys. Lett.* 303 (1999) 467.
- [311] M. Mayne, N. Grobert, M. Terrones, R. Kamalakaran, M. Ruhle, H.W. Kroto, *Chem. Phys. Lett.* 338 (2001) 101.
- [312] Z.F. Ren, Z.P. Huang, J.W. Xu, J.H. Wang, P. Bush, M.P. Siegel, P.N. Provencio, *Science* 282 (1998) 1105.
- [313] H. Murakami, M. Hirakawa, C. Tanaka, Y. Yamakawa, *Appl. Phys. Lett.* 76 (2000) 1776.
- [314] C. Bower, O. Zhou, W. Zhu, D.J. Werder, S. Jin, *Appl. Phys. Lett.* 77 (2000) 2767.
- [315] J. Yang, L. Dai, R.A. Vaia, *J. Phys. Chem. B* 107 (2003) 12387.
- [316] Y.L. Li, I.A. Kinloch, A.H. Windle, *Science* 304 (2004) 276.
- [317] M. Zhang, K.R. Atkinson, R.H. Baughman, *Science* 306 (2004) 1358.
- [318] T.W. Ebbesen, P.M. Ajayan, H. Hiura, K. Tanigaki, *Nature* 367 (1994) 519.
- [319] J. Liu, A.G. Rinzler, H. Dai, J.H. Hafner, R.K. Bradley, P.J. Boul, A. Lu, T. Iverson, K. Shelimov, C.B. Huffman, F. Rodriguez-Macias, Y.S. Shon, T.R. Lee, D.T. Colbert, R.E. Smalley, *Science* 280 (1998) 1253.
- [320] E. Mizoguti, F. Nihey, M. Yudasaka, S. Iijima, T. Ichihashi, K. Nakamura, *Chem. Phys. Lett.* 321 (2000) 297.
- [321] A.R. Harutyunyan, B.K. Pradhan, J.P. Chang, G.G. Chen, P.C. Eklund, *J. Phys. Chem. B* 106 (2002) 8671.
- [322] Z. Shi, Y. Lian, F. Liao, X. Zhou, Z. Gu, Y. Zhang, S. Iijima, *Solid State Commun.* 112 (1999) 35.
- [323] Y. Zhang, Z. Shi, Z. Gu, S. Iijima, *Carbon* 38 (2000) 2055.

- [324] S. Areppalli, P. Nikolaev, O. Gorelik, V.G. Hadjieva, W. Holmes, B. Files, L. Yowell, Carbon 42 (2004) 1783.
- [325] A.C. Dillon, M. Yudasaka, M.S. Dresselhaus, J. Nanosci. Nanotechnol. 4 (2004) 691.
- [326] L. Zhang, H. Li, K.T. Yue, S.L. Zhang, X. Wu, J. Zi, Z. Shi, Z. Gu, Phys. Rev. B 65 (2002) 073401.
- [327] J. Hilding, E.A. Grulke, Z.G. Zhang, F. Lockwood, J. Disper. Sci. Technol. 24 (2003) 1.
- [328] Z. Konya, J. Zhu, K. Niez, D. Mehn, I. Kiricsi, Carbon 42 (2004) 2001.
- [329] Y. Wang, J. Wu, F. Wei, Carbon 41 (2003) 2939.
- [330] K.L. Lu, R.M. Lago, Y.K. Chen, M.L.H. Green, P.J.F. Harris, S.C. Tsang, Carbon 34 (1996) 814.
- [331] D. Qian, E.C. Dickey, R. Andrews and, T. Rantell, Appl. Phys. Lett. 76 (2000) 2868.
- [332] P.C.P. Watts, W.K. Hsu, G.Z. Chen, D.J. Fray, H.W. Kroto, D.R.M. Dalton, J. Mater. Chem. 11 (2001) 2482.
- [333] H. Murphy, P. Papakonstantinou, T.I. Okpalugo, J. Vac. Sci. Technol. B 24 (2006) 715.
- [334] M.A. Hamon, H. Hu, P. Bhowmik, S. Niyogi, S. Zhao, M.E. Itkis, R.C. Haddon, Chem. Phys. Lett. 347 (2001) 8.
- [335] J. Chen, M.A. Hamon, H. Hu, Y. Chen, A.M. Rao, P.C. Eklund, R.C. Haddon, Science 282 (1998) 95.
- [336] M.A. Hamon, J. Chen, H. Hu, Y. Chen, M.E. Itkis, A.M. Rao, P. Eklund, R.C. Haddon, Adv. Mater. 11 (1999) 834.
- [337] C.A. Mitchell, J.L. Bahr, S. Areppalli, J.M. Tour, R. Krishnamoorti, Macromolecules 35 (2002) 8825.
- [338] Y. Lin, A.M. Rao, B. Sadanandan, E.A. Kenik, Y.P. Sun, J. Phys. Chem. B. 106 (2002) 1294.
- [339] D.E. Hill, Y. Lin, A.M. Rao, L.F. Allard, Y.P. Sun, Macromolecules 35 (2002) 9466.
- [340] Y. Lin, B. Zhou, K.A.S. Fernando, P. Liu, L.F. Allard, Y.P. Sun, Macromolecules 36 (2003) 7199.
- [341] M.C. Paiva, B. Zhou, K.A.S. Fernando, Y. Lin, J.M. Kennedy, Y.P. Sun, Carbon 42 (2004) 2849.
- [342] I.C. Liu, H.M. Huang, C.Y. Chang, H.C. Tsai, C.H. Hsu, R.C. Tsiang, Macromolecules 37 (2004) 283.
- [343] S. Qin, D. Qin, W.T. Ford, D.E. Resasco, J.E. Herrera, Macromolecules 37 (2004) 752.
- [344] M.J. O'Connell, P. Boul, L.M. Ericson, C. Huffman, Y. Wang, E. Haroz, C. Kuper, J. Tour, K.D. Ausman, R.E. Smalley, Chem. Phys. Lett. 342 (2001) 265.
- [345] C. Singh, M.S. Shaffer, A.H. Windle, Carbon 41 (2003) 359.
- [346] A.B. Dalton, S. Collins, J. Razal, E. Munoz, B.G. Kim, J.N. Coleman, J.P. Ferraris, R.H. Baughman, J. Mater. Chem. 14 (2004) 1.
- [347] E. Munoz, A.B. Dalton, S. Collins, M. Kozlov, J. Razal, J.N. Coleman, B.G. Kim, M. Selvidge, J.P. Ferraris, R.H. Baughman, Adv. Eng. Mater. 6 (2004) 801.
- [348] W. Feng, X.D. Bai, Y.Q. Lian, J. Liang, X.G. Wang, K. Yoshino, Carbon 41 (2003) 1551.
- [349] N.R. Ravarikar, L.S. Schadler, A. Vijayaraghavan, Y. Zhao, B. Wei, P.M. Ajayan, Chem. Mater. 17 (2005) 974.
- [350] L. Jin, C. Bower, O. Zhou, Appl. Phys. Lett. 73 (1998) 1197.
- [351] C. Bower, R. Rosen, L. Jin, J. Han, O. Zhou, Appl. Phys. Lett. 74 (1999) 3317.
- [352] T. McNally, P. Potschke, P. Halley, M. Murphy, D. Martin, S.E. Bell, G.P. Brennan, D. Bein, P. Lemoine, J.P. Quinn, Polymer 46 (2005) 8222.
- [353] W.D. Zhang, L. Shen, I.Y. Phang, T. Liu, Macromolecules 37 (2004) 256.
- [354] M.A. Lopez Manchado, L. Valentine, J. Biagiotti, J.M. Kenny, Carbon 43 (2005) 1499.
- [355] R. Andrews, D. Jacques, M. Minot, T. Rantell, Macromol. Mater. Eng. 287 (2002) 395.
- [356] P. Potschke, I. Alig, S. Dudkin, Polymer 44 (2003) 5023.
- [357] P. Potschke, A.R. Bhattacharyya, A. Janke, Polymer 44 (2003) 8061.
- [358] P. Potschke, A.R. Bhattacharyya, A. Janke, Carbon 42 (2004) 965.
- [359] Z. Jin, K.P. Pramoda, G. Xu, S.H. Goh, Chem. Phys. Lett. 337 (2001).
- [360] M.F. Yu, O. Lourie, M. Dyer, K. Moloni, T. Kelly, Science 287 (2000) 637.
- [361] K.T. Lau, D. Hui, Carbon 40 (2002) 1597.
- [362] K.T. Lau, M. Chipara, H.Y. Ling, D. Hui, Composites Part B 35 (2004) 95.
- [363] M. Wong, M. Paramsothy, X.J. Xu, Y. Ren, S. Li, K. Liao, Polymer 44 (2003) 7757.
- [364] Z. Jia, Z. Wang, C. Xu, J. Liang, B. Wei, D. Wu, S. Zhu, Mater. Sci. Eng. 271A (1999) 395.
- [365] R.E. Gorga, R.E. Cohen, J. Polym. Sci. Part B Polym. Phys. 42 (2004) 2690.
- [366] B.K. Satapathy, R. Weidisch, P. Potschke, A. Janke, Macromol. Rapid Commun. 26 (2005) 1246.
- [367] L. Liu, H.D. Wagner, Compos. Sci. Technol. 65 (2005) 1861.
- [368] F.H. Gojny, M.H. Wichmann, B. Fiedler, K. Schulte, Compos. Sci. Technol. 65 (2005) 2300.
- [369] F.H. Gojny, J. Nastalczyk, Z. Roslaniec, K. Schulte, Chem. Phys. Lett. 370 (2003) 820.
- [370] H. Koerner, W. Liu, M. Alexander, P. Mirau, H. Dowty, R.A. Vaia, Polymer 46 (2005) 4405.
- [371] I.M. Ward, Mechanical Properties of Solid Polymers, Wiley, New York, 1971, p. 255.
- [372] E.T. Thostenson, T.W. Chou, J. Phys. D Appl. Phys. 36 (2003) 573.
- [373] F.T. Fisher, R.D. Bradshaw, L.C. Brinson, Compos. Sci. Technol. 63 (2003) 1689.